



# X-ray Absorption Spectroscopy Calculations From First Principles

Oana Bunau

## ► To cite this version:

Oana Bunau. X-ray Absorption Spectroscopy Calculations From First Principles. Atomic Physics [physics.atom-ph]. Université de Grenoble, 2010. English. NNT: . tel-01152465

**HAL Id: tel-01152465**

**<https://theses.hal.science/tel-01152465>**

Submitted on 13 Sep 2019

**HAL** is a multi-disciplinary open access archive for the deposit and dissemination of scientific research documents, whether they are published or not. The documents may come from teaching and research institutions in France or abroad, or from public or private research centers.

L'archive ouverte pluridisciplinaire **HAL**, est destinée au dépôt et à la diffusion de documents scientifiques de niveau recherche, publiés ou non, émanant des établissements d'enseignement et de recherche français ou étrangers, des laboratoires publics ou privés.

# Méthodes *ab initio* pour le calcul des spectroscopies d'absorption X

Oana Bunău

Thèse de doctorat en physique

Université de Grenoble

dirigée par Yves Joly

Christian Brouder	Rapporteur
Peter Krüger	Rapporteur
Dominique Chandesris	Examineur
Françoise Hippert	Examineur
Yves Joly	Examineur
Zoltan Neda	Examineur
Lucia Reining	Examineur

Soutenance : 22 novembre 2010

Institut Néel, CNRS/UJF  
25 rue des Martyrs, BP 166, 38042 Grenoble cedex 9



# X-ray Absorption Spectroscopy Calculations From First Principles

Oana Bunău

Thesis submitted to The University of Grenoble  
for the degree of Doctor of Philosophy

Yves Joly, Thesis Supervisor

November 2010



*Science must not impose any philosophy, any more than the telephone must tell us  
what to say.*  
G.K. Chesterton



## Acknowledgements

I am especially grateful to Yves, for having shared his knowledge with kindness, patience, good humor and great tact. Your deep involvement made this thesis possible and learning enjoyable.

I am also thankful to Stéphane Grenier, Aline Ramos, Helio Tolentino, the other members of the Surfaces, Interfaces and Nanostructures team and of the MCMF department, for fruitful discussions and exchange of ideas. Thank you Stéphane for helping me survive with the manganites and for all the good advice. I equally enjoyed working with Rose Marie Galéra, thank you for your always clear explanations and pleasant exchange of ideas.

During this Ph.D. period I had the chance to be surrounded by wonderful people. Thank you F401, I'll terribly miss you all, your jokes, our life, love and off-the-record discussions and the unbearable noise in the office. I am especially grateful to the *admis sous titre*, whose warmth and joy of living made me feel welcome, learn French and decide to stay. I had the opportunity to spend quality time with you fantastic people at the second floor of the E building, sharing ideas, partying, doing sports and talking physics. Thanks to the cheerful guys from the M building for the rich lunchtime talking and laughing and for teaching me lots of non academic vocabulary. Last but not least I am grateful to my old reliable Romanian friends, for being old and reliable friends.

Thank you, Yannick, for your support, understanding and never ending patience.





<b>1</b>	<b>Introduction</b>	<b>1</b>
1.1	About the present Ph.D. work . . . . .	1
1.2	Synchrotron radiation and the latest trends in material science . . . . .	2
1.3	X-rays for the study of materials . . . . .	4
1.4	The synchrotron techniques . . . . .	5
1.4.1	The X-ray sources . . . . .	5
1.4.2	X-ray Absorption Near Edge Structure . . . . .	6
1.4.3	Resonant X-ray Diffraction . . . . .	10
1.4.4	X-ray Magnetic Circular Dichroism . . . . .	10
1.5	State of the art in the calculations . . . . .	11
<b>2</b>	<b>Fundamental aspects of the interaction of x-rays with matter</b>	<b>21</b>
2.1	The quantum field theory description . . . . .	21
2.2	The tensor analysis . . . . .	24
2.2.1	The formalism . . . . .	24
2.2.2	Symmetries . . . . .	26
2.3	Solving the electronic structure . . . . .	27
2.3.1	The Schrödinger-like equation . . . . .	27
2.3.2	The finite difference method . . . . .	29
2.3.3	The multiple scattering theory . . . . .	29
2.3.4	The optical theorem . . . . .	32
2.3.5	The physical quantities . . . . .	33
<b>3</b>	<b>FDMNES and the one body picture</b>	<b>35</b>
3.1	The structure of the FDMNES code . . . . .	35
3.1.1	The atomic calculation . . . . .	35
3.1.2	The potential calculation . . . . .	37
3.1.3	Solving the radial Schrödinger equation . . . . .	38
3.1.4	Solving the electronic structure . . . . .	39
3.1.5	The tensor calculation . . . . .	40
3.1.6	The convolution . . . . .	40
3.1.7	Miscellaneous aspects . . . . .	42
3.2	Application: magnetic and orbital ordering in NdMg . . . . .	42
3.2.1	The context of the study . . . . .	42
3.2.2	Tensor analysis . . . . .	44
3.2.3	Results . . . . .	46
3.2.4	Conclusions . . . . .	49
<b>4</b>	<b>The self-consistent procedure</b>	<b>53</b>
4.1	Motivation . . . . .	53
4.2	Implementation . . . . .	54

4.3	Results . . . . .	57
4.4	Conclusions . . . . .	67
<b>5</b>	<b>The LSDA+U method</b>	<b>69</b>
5.1	Motivation . . . . .	69
5.2	Theoretical grounds . . . . .	70
5.3	Implementation . . . . .	72
5.4	Results . . . . .	73
5.5	Conclusions and perspectives . . . . .	74
<b>6</b>	<b>Beyond the one body picture</b>	<b>77</b>
6.1	The failure of the single particle approximation . . . . .	77
6.2	The time dependent density functional theory . . . . .	79
6.2.1	The formalism . . . . .	80
6.2.2	The linear response regime . . . . .	82
6.2.3	The ground state response function . . . . .	83
6.2.4	The kernel . . . . .	85
6.2.5	The local fields effect . . . . .	86
6.2.6	The adiabatic local density approximation . . . . .	87
6.2.7	The restricted adiabatic approximation . . . . .	88
6.2.8	The limitations of these kernels . . . . .	88
6.2.9	The spherical harmonics expansion . . . . .	89
6.2.10	The renormalisation of the response function . . . . .	90
6.2.11	Extensions of the adiabatic approximation . . . . .	91
6.3	Implementation . . . . .	96
6.4	Results . . . . .	98
6.5	Conclusions and perspectives . . . . .	111
<b>7</b>	<b>A study of the colossal magnetoresistive <math>\text{Pr}_{0.6}\text{Ca}_{0.4}\text{MnO}_3</math> perovskite</b>	<b>113</b>
7.1	The context of the study . . . . .	113
7.2	The resonant X-ray diffraction study . . . . .	115
7.3	Tensor analysis . . . . .	115
7.4	Results at the $K$ edge . . . . .	117
7.5	Results at the $L_{23}$ edges . . . . .	120
7.6	Conclusions and perspectives . . . . .	125
<b>8</b>	<b>Conclusions and Perspectives</b>	<b>127</b>
	<b>Résumé en français</b>	<b>129</b>
	<b>Appendices</b>	<b>133</b>

# Chapter 1

## Introduction

### 1.1 About the present Ph.D. work

**The purpose of this work** As far as X-ray absorption phenomena are concerned, the available theoretical descriptions and calculation methods are rather behind the experiments, in terms of performance. In other words, experimental data are often not fully understood or ill interpreted. The current Ph.D. work aims to reduce the gap between the experiments and the theory behind, in order to achieve a better agreement between the two. Within the FDMNES code, I contributed to the improvement of existing methods - the implementation of a self-consistent scheme - and to the development of new ones, like the LSDA+U and the time dependent density functional theory (TDDFT) methods. I performed numerous calculations on simple, model compounds to test the accuracy and the reliability of our new developments. We compared the output of the FDMNES calculations with the ones issued by other codes or methods. No calculation method is well-suited for all the possible materials. Another main direction of this work was to test the limits of each method and its range of applicability. Thanks to these studies, we were able to set some default settings and calculation methods which make FDMNES friendlier for less experienced users. Finally, I performed calculations on complex compounds and provided interpretation of experimental data.

**The aim of this manuscript** The aim of this manuscript is to introduce the reader to the *ab initio* (first principles) X-ray absorption calculation techniques. I provide simple physical pictures, I explain the formalism and the potential approximations or limitations, I detail the implementation of the methods and finally I give explicit examples. I shall focus on the single particle approach with an underlying self-consistent procedure, as well as on the LSDA+U and the TDDFT methods. I will show examples of success and failures of each method and discuss their range of applicability. For some specific compounds (NdMg, manganites) I will show results of various calculation methods and investigate which is the best one to fit the experiment and why.

**The structure of this manuscript** The first part of the manuscript (the first two chapters and the first section of the third one) is an introduction to the field and to the FDMNES calculation code. The remaining part (from section 3.2 to the end) contains the theoretical developments achieved during this Ph.D. degree.

This manuscript is organized as follows. In the remaining part of this chapter I shall review the use of core spectroscopy for material science and the corresponding numerical calculations. In chapter 2 I treat the interaction of X-rays with matter in the second quantization formalism, I provide a unified description of the related types of absorption spectroscopies and finally I explain the tensor treatment of these. In section 3.1 I give an overview and explain the underlying formalism of the features already implemented in the FDMNES package. The reason behind this choice is that their mastery is a pre-requisite, in order to understand the further developments in the code.

The remaining part of chapter 3 is dedicated to an application, i.e. a complete study of the resonant diffraction spectra of NdMg revealing magnetic and orbital orderings. The rest of the manuscript describes the numerical developments to the FDMNES code that were implemented during this Ph.D: the self-consistent procedure (chapter 4), the LSDA+U (chapter 5) and the TDDFT methods (chapter 6).

I chose to move the heavy formulae to the appendix, provided their absence in the main part of the manuscript does not impede the comprehension of the aspects that I treat. The topics in the appendix are listed in its beginning.

## 1.2 Synchrotron radiation and the latest trends in material science

The current advancements in technology stimulate a growing interest in the understanding of novel materials. Large efforts, at the same time theoretical and experimental, are being invested to gain insight into the fundamental physics governing these materials.

X-ray absorption spectroscopy are powerful tools for solving crystallographic structures (coordination numbers, local symmetries etc.) and investigating the properties of the sample, like the phase distribution, magnetism, orbital hybridisation or valence states. Moreover, the latter can equally be studied in a dynamic regime by the time-resolved core spectroscopies. Therefore the use of synchrotron radiation has become a milestone for material science.

In a first category of materials of major interest one finds those which are potentially interesting for microelectronics, computer and energy industries and concern the storage and reading of information. These materials are carriers of so-called extraordinary properties. Giant and colossal magnetoresistance compounds, multiferroics, magnetic nanostructures, dilute magnetic materials, molecular magnets, magnetic heterostructures and high  $T_c$  superconductors are just some of the classes of materials whose physics is still not well understood. One hopes that an exact knowledge of their ground state would both clarify the mechanisms driving these extraordinary effects and allow the elaboration of other materials exhibiting similar properties.

Perovskite-type manganites exhibit the colossal magnetoresistance effect for certain values of the doping (see section 7 for details). It is believed that colossal magnetoresistance is an outcome of the interplay of several electron correlation driven effects, i.e. charge, orbital and magnetic order [30]. To discover the exact mechanism, one needs to determine the ground state of these compounds. The synchrotron techniques

in diffraction mode are a very good candidate for this purpose, as one may gain insight into any of these breakings of symmetry by cleverly choosing the diffraction scattering vectors.

In the field of spintronics, the quest for new materials exhibiting spin dependant transport properties speeds up with the increasing demand of technological developments. Standard reading devices are made up of multilayers containing in-plane magnetic compounds separated by isolators. A more recent trend is to create heterostructures with an out of plane (perpendicular) magnetic anisotropy and several successful attempts have been reported. In this sense, there is a particular interest for the study of heterostructures exhibiting the exchange bias, i.e. a shift of the hysteresis loop due to the exchange coupling between a ferromagnetic and a antiferromagnetic layer [82]. To discover and synthesize new similar materials, one needs to thoroughly understand the physics at the layers' interface. Microscopically, this can be done by using X-ray absorption techniques [117].

The spin torque phenomenon (i.e. the coupling between a spin polarized current and the magnetization of a ferromagnetic layer) is a promising alternative to applying magnetic fields to reading and writing information in a spintronic device. The recently developed pulsed X-ray laser allow a time-resolved study of spin dynamics in such spin torque devices [18, 29].

Some very recent developments [17] involve the study of the behaviour of magnetic layers subjected to an external electric field, or to a spin polarised current. Such a layout would allow the study of multiferroics by resonant diffraction (RXD) techniques, which are insensitive to the electric field.

A new emerging field called "orbitronics" has been proposed as an alternative to the more conventional spintronics. For "orbitronics", angular momentum is the spintronics' equivalent to the spin. The orbitronic devices are some metal oxide/superconductor heterostructures whose electronic structure at the interface, in terms of the spatial orientation of hybridized orbitals, can be controlled with an electric field. Thus, the current running through the structure can be switched on and off, depending on whether the orbital moment carried by the conduction electrons penetrates the interface or not [28]. Once again, X-ray absorption spectroscopy are the best means to gain insight into the microscopical behaviour at the interface.

The control of transition metal oxides interfaces offers the opportunity to exploit strongly correlated systems for the development of new application devices. Efforts are needed for a quantitative understanding of the phenomena at the interface, and X-ray spectroscopy are a good candidate for this task [43].

Molecular magnets (i.e. molecules combining a large spin with an easy magnetization axis) are another system of high interest in modern physics, as they offer the possibility of spin-dependent transport. Characterizing the magnetic behaviour is fundamental to the field of molecular spintronics. As long as sub-monolayers of magnetic atoms or molecules are concerned, the X-ray magnetic circular dichroism (XMCD) technique is the only available tool for characterization [69].

A second large category of materials of major interest are the biological molecules studied by the life sciences - proteins, organic and metallo-organic compounds, nucleic acids, viruses etc. Given the potential pharmaco-medical applications of these materials, the field of macromolecular crystallography has become a major stream in material

science. Determining the structure of these macromolecules is a delicate issue, due to the huge number of atoms from which they are formed from and to the polymorphisms these compounds may be subjected to. Such a macromolecule often contains thousands, up to several hundreds of thousands of atoms in the case of viruses. The resolution of the structure proves to be a difficult task, even when several complementary synchrotron techniques are being employed.

Besides the structure resolution, *in situ* dynamics of reactions is another issue at stake in biological and chemical physics. These *in operando* (i.e. real time) studies allow the understanding and eventually the control of the chemical reaction. By performing time resolved X-ray absorption experiments one can explore the relationship between structure, kinetics and functionality [108]. In the very same spirit, a detailed monitoring of the catalysis reaction would ultimately help to improve this technique.

Synchrotron radiation may be used on samples subjected to special conditions (high temperatures, high pressures) in order to study their behaviour to such extreme exposure. This technique is particularly important for geological and mineralogical studies [53].

### 1.3 X-rays for the study of materials

Spectroscopy is the study of emission, absorption or scattering of radiation with respect to its energy. Currently, one deals with light - gamma rays, X-rays, ultraviolet, visible or infrared, depending on frequency - but one may equally use other particles, such as electrons, neutrons, muons etc. When performing a spectroscopic experiment, one expects to get information on the sample by analysing the outgoing particles (whose nature is not necessarily the same as the incident ones').

One can obtain different kinds of information on the sample, depending on the type and wavelength of the measured radiation. In the IR range, one probes the molecular (vibrational and rotational) energy states, UV and visible radiation probe the valence electron states, X-rays are sensitive to the core electronic levels whereas gamma radiation senses the energy levels of the nuclei. The mean free path of the detected particles indicates whether one measures a surface or a bulk effect.

To learn information at the atomic scale, and to determine the crystal structures, one needs to use either X-rays, electrons or neutrons in the range corresponding to interatomic distances.

Standard X-ray diffraction is a method for solving crystallographic structures. When the energy of the incoming photon beam is tuned as to fit the absorbing edge (the binding energy of a core level) of some chemical element in the sample, an anomalous, resonant effect appears on the diffraction spectra. Hence, diffraction intensities are severely modified. One might equally find a non zero signal for forbidden reflections, i.e. whose extinction in the off-resonant regime is ordered by the space group. This specific diffraction technique is called Resonant X-ray Diffraction (RXD).

Compared to RXD, neutron diffraction techniques are not directly sensitive to the asphericity of the electron cloud. Despite the wider impact and spread of the latter, the former is a more appropriate probe of the electronic structure when an electric quadrupole moment is expected.

One often argues that neutron-based techniques are universal in the sense that they are the best tool to solve crystallographic and magnetic structures. This is generally true at low atomic numbers or if one uses a single crystal with a large volume, an imperative for neutron studies. If this is not the case (difficulty to grow a single crystal, thin films and interfaces, high pressure studies, nano and one dimensional objects) the X-ray techniques are the best solution.

Insofar as magnetic studies are concerned, X-ray absorption techniques are a viable alternative to neutrons. In the early '70s, a pioneering study of Brunel and Bergevin [33] proved that photons can couple directly to electron spins *via* the interaction spin - magnetic field, and thus can reveal diffraction patterns of magnetic superstructures (for instance the antiferromagnets). Nevertheless, apart from the resonant regime, diffracted intensities are very small. The idea of performing magnetic scattering experiments at the absorption edge dates back to Blume in 1985 [16] and was accomplished by Namikawa the very same year [79]. Two years later, Schütz discovered the circular magnetic dichroic effect [100], i.e. absorption spectra for right and left circular polarized incident light are quantitatively different. The dichroic effect is expected to measure the spin and orbital momentum of the empty electronic state, hence the development of the so-called sum rules (see for instance [112]). A great theoretical effort is required to improve these rules.

RXD techniques mainly provide structural information, either crystallographic or magnetic. If one wishes to explicitly study excitations such as the lattice, charge and spin density waves (whose Fourier transforms are the phonons, plasmons and magnons, respectively), one must appeal to the Resonant X-ray Inelastic Scattering (RIXS). Up to now, it has been believed that inelastic neutron scattering is the only technique that could investigate these excitations. The very recent, high resolution RIXS gives very promising results [20,21], which are in good agreement with the neutron data [21,32]. We equally mention the recently established, hybrid XMCD-RIXS method [107] that allows the investigation of the 3d transition elements magnetic moment all by exploiting the advantages of hard (i.e. high energy) X-rays.

In principle one may perform a scattering experiment on a single molecule. In practice the scattered intensity is too small to allow any quantitative analysis. One needs to grow a periodic structure in order to enhance the scattering signal. This is no longer necessary if the diffraction experiment is performed with pulsed X-rays instead of a continuous beam - a breakthrough introduced by the last generation of X-ray sources [66].

## 1.4 The synchrotron techniques

### 1.4.1 The X-ray sources

The development of X-ray absorption spectroscopy has become experimentally possible (on a large scale) with the advent of synchrotrons. The discovery of synchrotron radiation was a major scientific breakthrough of the '80s. Synchrotron radiation is emitted by a bunch of electrons at constant energy ( $\approx$  GeV) which circles a storage ring. What was previously considered a waste product appears to be a high quality source of polarized X-rays.

Contrary to ordinary, laboratory X-ray sources, the synchrotron radiation's spectrum



is continuous, and thus allows extended energy scans. Its intensity is high enough to allow the observation of time dependent phenomena as well as the measurement of dilute samples. The synchrotron beam can be focused down to  $\mu\text{m}$  size, has small divergence and is tunable to a well defined polarization (linear, circular or elliptic). Here are some instructive figures: with the flux of the third generation synchrotron' radiation ( $10^{12}$  -  $10^{13}$  photons *per* second) one can acquire a diffraction pattern within one second.

The fourth generation of X-ray sources (most of them are still under construction) introduced the free electron laser (X-FEL) capability, which is based on a high quality electron beam and a long undulator. The X-FEL emitted radiation is coherent, thus leading to an increase of several orders of magnitude in brightness, as compared to the standard synchrotron radiation. From now on, it is possible to record a diffraction pattern in about  $10^{-13}\text{s}$  and efforts are being made to decrease this limit.

The coherence of X-FEL makes it possible to split the beam into short pulses, going from 1 femtosecond down to 1 attosecond. This facility gives the opportunity of taking snapshots of ultrafast dynamics all by keeping the atomic resolution [66].

The following sections aim to introduce the reader to the most common synchrotron experimental techniques, with a particular emphasis on the X-ray absorption Near Edge Structure (XANES), RXD and XMCD. We shall explain the edge and polarization indexing conventions, as they are referred to all through this manuscript.

### 1.4.2 X-ray Absorption Near Edge Structure

Photons (i.e. electromagnetic waves) interact with electrons in the matter and thus can provide information on the electronic properties.

When an incident beam hits a sample, according to the Beer-Lambert law, the percentage of the transmitted beam reads as:

$$\frac{I}{I_0} = e^{-\mu(E) l} \quad (1.1)$$

where  $I_0$  and  $I$  are the intensities of the incident and the transmitted beam, respectively,  $l$  is the thickness of the sample and  $\mu(E)$  is the energy dependent absorption coefficient of the sample. The link to the atomic cross sections is:

$$\mu(E) = \frac{1}{V} \sum_i \sigma_i \quad (1.2)$$

where  $V$  is the volume of the sample and  $\sigma_i$  the absorption cross section of atom  $i$ .

X-ray Absorption Near Edge Structure (XANES) and the closely related Extended X-ray Absorption Fine Structure (EXAFS) measure  $\mu$ 's variation with respect to the energy, through an absorbing edge. The difference between XANES and EXAFS is uniquely related to the energy range the spectra is measured in: up to 50 eV after the edge for XANES, whereas EXAFS designates the extended region, i.e. from 50 to approximately 2000 eV after the edge. XANES and EXAFS merge under the acronym XAS, standing for X-ray Absorption Spectroscopy.

The idea behind XAS is that by tuning the incident beam's energy through the absorption edge one gets to excite a core electron to an empty electronic state. Electronic

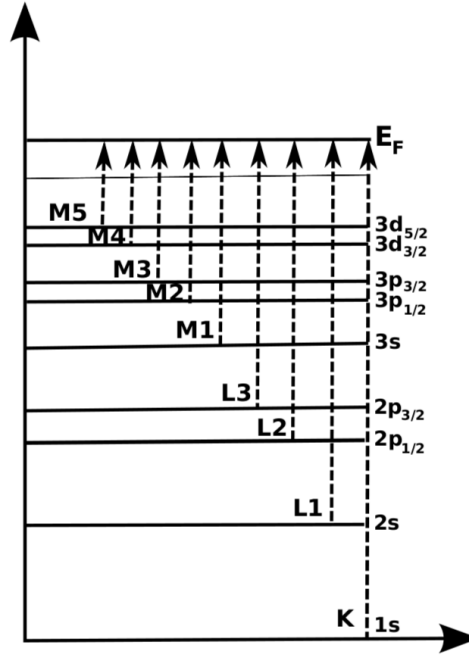


Figure 1.1: Each edge is named with a letter indicating the energy level and a figure designing the total angular momentum.

and geometric structures being entangled, XAS probes both of them. XAS is a selective technique, both chemically (each atomic species has well defined core level binding energies) and orbitally, through the selection rules. This means that from all the possible combinations, only a few transitions are allowed from a quantum mechanics point of view (see section 2.1).

The absorption spectrum of an isolated atom is a simple step function (sometimes containing simple atomic structures), i.e. one probes the density of electronic states of the vacuum. As we shall detail further in this manuscript (see section 2.3.3) the oscillations (the fine structures) in the XANES and EXAFS spectra are due to the atomic environment around the absorbing atoms. From an EXAFS spectra one can get quantitative information concerning the coordination number and atomic distances. The XANES spectra is more sensitive to the local symmetries around the absorbing atoms at the expense of atomic distances. More precisely, the information contained in the XANES region is used to refine the structure one has already fit with the EXAFS data. XAS techniques can be performed on either solids or fluids - as local probe spectroscopy, they do not require any long range order.

At an absorbing edge of a chemical species, the energy of the incident photon beam is such that a core electron is ejected out of the absorbing atom. Edges are indexed increasingly according to the energy and angular momentum quantum numbers describing the core level (figure 1.1). Each edge is named with a letter indicating the energy level -  $K$  for  $n = 1$ ,  $L$  for  $n = 2$  etc. - and a figure designing the total angular momentum -  $L_1$  for  $2s$ ,  $L_2$  for the  $2p_{1/2}$ ,  $L_3$  for the  $2p_{3/2}$  etc.<sup>1</sup>

<sup>1</sup>Historically, the spectroscopic notations showing the quantization of angular momentum have an intuitive meaning:  $s$  for simple,  $p$  for principal,  $d$  for diffuse and  $f$  for fundamental. All the rest ( $g, h, i$

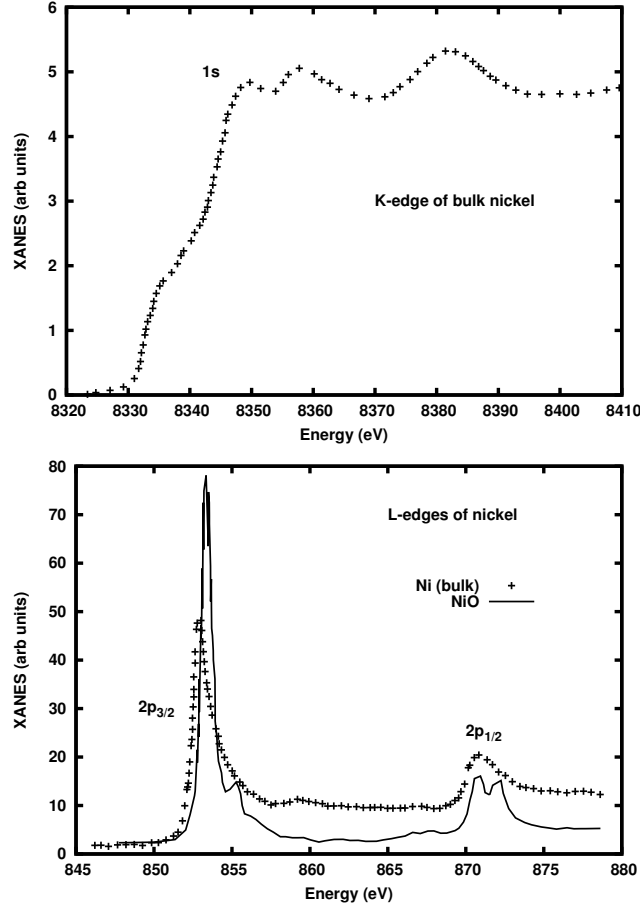


Figure 1.2: The experimental absorption spectra of nickel: above, the  $K$  edge of pure nickel; below, the  $L_{2,3}$  edges of pure nickel and of nickel in NiO. The form of the absorption edge depends strongly on both the core level and the atomic environment of the absorbing nickel.

In a first approximation, the XANES spectrum can be interpreted in terms of the Golden Rule, i.e. a result of the perturbation theory (see chapter 2.1):

$$\sigma(\omega) = \frac{\pi\omega e^2}{\epsilon_0 c \hbar^2} \sum_j \sum_{f,g} |\langle \psi_f | \vec{\epsilon} \cdot \vec{r} | \psi_g^{(j)} \rangle|^2 \rho(E) \delta(\hbar\omega - (E - E_g^{(j)})) \quad (1.3)$$

where  $\sigma(\omega)$  is the absorption cross section,  $\hbar\omega$  the photon energy and the other constants have the usual meaning. The absorption signal thus depends on  $\rho(E)$ , the density of states of the continuum. Absorption occurs when the photon energy  $\hbar\omega$  equals the difference of energy between the two concerned levels, a condition reflected in the Dirac  $\delta$  function. The initial state  $\psi_g$  and the final state  $\psi_f$  are coupled *via* the photon field, whose polarization is  $\vec{\epsilon}$ . Here the electromagnetic field has been described semiclassically, in the electric dipole approximation.  $\psi_g$  being an atomic-like, localized state, we thus introduced the  $j$  index to describe the absorbing atom.

---

etc.) are ordered alphabetically.

In the simplest (one body) picture, the absorption spectrum is a specific projection of the density of the unoccupied electronic states on the absorbing atom (eq. 1.3). According to the dipole allowed selection rule, at the  $K$  edge one probes the  $p$  states, whereas at the  $L_{2,3}$  edges one looks at the  $d$  states (and, to a lesser extent, the  $s$  ones). The general aspect of the spectrum is thus a signature of the localized ( $L_{2,3}$  edges of nickel in NiO), partially localized ( $L_{2,3}$  edges of bulk nickel) or delocalized ( $K$  edge of nickel) character of the final states (figure 1.2). The more localized the structures in the absorption spectrum, the more sensitive one is at the local electronic structure at the expense of the geometrical one.

The X-ray absorption spectroscopy are essentially anisotropic, i.e. one is sensitive to the orientation of the photon beam's polarisation with respect to the sample. Powders, as well as single crystals possessing cubic symmetry, and in the dipolar approximation (see section 2.1), give an isotropic signal. In the rest of this manuscript, all experimental and calculated XANES spectra are already spatially averaged, unless we explicitly specify otherwise.

In practice, the XANES signal is either obtained as  $\log I/I_0$  by a direct measurement of the transmitted beam, or by the measurement of a secondary decay effect. The latter can be fluorescence or emitted electrons. Fluorescence is the emission of a secondary photon during the re-arrangement of the electrons, as they are trying to fill the core hole. The Auger effect consists in the emission of electrons following the absorption of the secondary photon. The secondary effect measurement mode's resolution is less accurate, nevertheless for certain samples (opaque, diluted) the direct method cannot be used. Whatever the detection mode, the form of the recorded signal is globally the same, unless the self-absorption effects are strong. By self-absorption we mean the sample absorbing the X-ray fluorescent photons, which causes an alteration of the spectrum, in the sense that the strong absorption features are attenuated.

**Characteristic timescales of the absorption process** Modeling the absorption process becomes possible if one divides it into several subprocesses, governed by different timescales. The first step is the absorption of the photon, or, equivalently, the creation of the core hole ( $t_1 \approx 10^{-20}$  s). The core hole's lifetime is given by the probability of its filling ( $t_2 \approx 10^{-15} - 10^{-16}$  s). The electron cloud reacts to the advent of the core hole in the so-called screening process, within  $t_3 \approx 10^{-15} - 10^{-16}$  s. The ejected core electron travels out of the excited atom on a timescale depending on its kinetic energy ( $t_4 \approx 10^{-15} - 10^{-17}$  s). Once outside the atom, the photoelectron is subject to various elastic and inelastic (mainly plasmons) scattering mechanisms, with the latter limiting its lifetime ( $t_5 \approx 5 \cdot 10^{-15} - 10^{-16}$  s). The slowest dynamics involved is the interaction with the lattice (the scattering on phonons, with a characteristic time  $t_6 \approx 10^{-13} - 10^{-14}$  s). As  $t_5 \ll t_6$ , the photoelectron sees the lattice distortions only in the form of snapshots. Consequently, the inclusion of temperature effects in calculations reduces to a statistical averaging procedure.

**The screening process** The fact that several processes have characteristic timescales of the same order of magnitude makes it delicate to construct a theoretical model. Within the single particle approaches the screening of the core hole by the surrounding electron cloud is being taken into account in a static way, i.e. it remains unchanged

during the entire absorption process. In the XANES region, where the photoelectron has a low kinetic energy, *the final state rule* applies: the core hole is fully screened, i.e. one removes the core electron and places an extra one on the first available valence orbital of the absorbing atom. Physically, this means that the photoelectron has not yet quit the atom and still sees the core hole. In the EXAFS range *the initial state rule* applies: due to its high kinetic energy, the photoelectron's lifetime is longer than the hole's, thus it sees the ground state electronic structure. In some cases one has to perform a partial screening (0.8 - 0.9) to better fit the experiment. As we shall explain further, an accurate scheme for the core-hole screening can be achieved only in the framework of genuine many body calculation methods, with dynamical screening emerging naturally from the theory.

### 1.4.3 Resonant X-ray Diffraction

Resonant X-ray Diffraction (RXD) is a technique even more selective than XANES. Besides the chemical and orbital selectivity proper to every absorption spectroscopy technique, RXD may preferentially exploit specific atomic sites by an appropriate choice of the reflection. Increased selectivity can be obtained with a proper choice of the incoming and outgoing polarizations.

When far from the absorbing edge the scattering occurs on the whole electron cloud (which is nearly spherical) and not on a specific orbital state. Therefore the off-resonant (i.e. Thomson) diffraction is quasi-isotropic. When close to resonances, this is no longer the case and azimuthal (polarization) effects are generally strong. Equally, at resonance, the outgoing polarization may be different from the incoming one, contrary to the Thomson, charge scattering case. Note that the magnetic scattering generally has an azimuthal dependence, and may alter the orientation of the polarisation even in the off-resonant case.

Figure 1.3 illustrates the conventions for a RXD experiment.  $\vec{Q}$  is the scattering vector,  $\vec{k}_{in}$  ( $\vec{k}_{out}$ ) is the incoming (outgoing) wavevector and the plane defined by  $\vec{Q}$ ,  $\vec{k}_{in}$  and  $\vec{k}_{out}$  is called the diffraction plane. The polarization  $\vec{\epsilon}$  of the electric field is generally chosen as perpendicular to the diffraction plane ( $\sigma$  polarization) or contained in the plane ( $\pi$  polarization).  $\Psi$  is the azimuthal angle. The zero azimuth corresponds to the  $\sigma$  polarization along Oy.

### 1.4.4 X-ray Magnetic Circular Dichroism

Historically, the term "natural dichroism" (non-magnetic) points to a change of colour in a mineral's appearance when the linear polarization of the incident light is rotated. Microscopically, this phenomenon is due to a charge anisotropy within the sample. As charge and spin are coupled, dichroism will ultimately investigate the magnetism of the sample.

The incident photon's coupling to the electron spin, in the resonant regime, offers the opportunity to perform advanced X-ray magnetic studies. The X-ray Magnetic Circular Dichroism (XMCD) is based on the fact that a given spin orientation will scatter differently the right and left circular polarized light. The XMCD signal is given by the subtraction of the absorptions corresponding to the two circular polarizations.

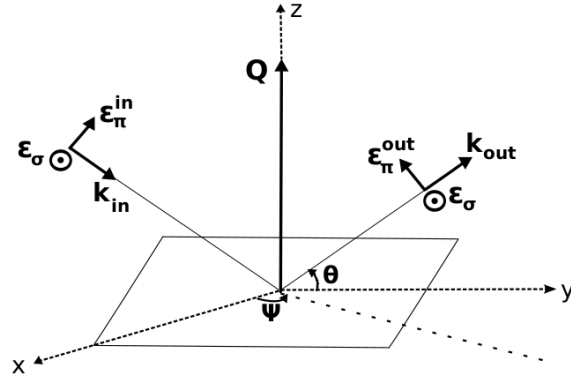


Figure 1.3: The conventional notations for a RXD experimental setup:  $\vec{Q}$  is the scattering vector,  $\vec{k}_{in}$  ( $\vec{k}_{out}$ ) the incoming (outgoing) wavevector. The polarization  $\vec{\epsilon}_\sigma$  is perpendicular to the diffraction plane, whereas  $\vec{\epsilon}_\pi$  is contained in the plane.

To have a signal, the sample must be spin-aligned. To see a XMCD signal the sample must not be antiferromagnetic, in which case the contributions from the two helicities cancel. Generally speaking, the time reversal breaking of symmetry makes XMCD even more selective than the related XANES technique.

One would not detect a XMCD signal if it weren't for the spin-orbit coupling. In the X-ray range, the interaction of the electromagnetic wave with the matter is entirely due to the electric field it carries. The electric field does not directly interact with the electron spin, but with its angular momentum. As the latter is coupled to the spin through the spin-orbit interaction, the incoming photons probe the magnetism of the sample.

XMCD allows one to trace the atomic magnetism, both in size and orientation, by means of the sum rules. In a simple physical picture, when absorption occurs, the photon transfers its angular momentum ( $+\hbar$  or  $-\hbar$  for right and left circular polarization, respectively) to the core electron, which will probe some continuum state. The transition amplitude is different whether the angular momentum of the final state is parallel or antiparallel to the photoelectron's. The XMCD  $L_2$  and  $L_3$  signals have opposite signs.

## 1.5 State of the art in the calculations

In some simple cases, X-ray absorption spectroscopic data can be interpreted by the comparison with reference spectra and by interpreting the chemical shift. This is no longer the case for complex, multi-phased compounds, or when one deals with new phases. In this instance a theoretical support is needed to interpret the spectra.

Theoretical spectroscopy aims to explain the origin of each structure in the spectrum and provide quantitative information on the sample: charge and magnetic moment of the atoms, inter-atomic distances, symmetries, phase or magnetic domain distribution

etc. Another target would be to suggest experimental setups the pursuit of which would reveal new information on the sample.

A realistic modelling of a many body system is a very difficult task, especially when excited states are involved. The many body system's evolution is governed by the Schrödinger-like equation (SE) - Schrödinger or Dirac equation -, whose solving is either *ab initio* or *via* a model Hamiltonian. The *ab initio* methods are often based on the density functional theory (DFT) plus a mean field approximation. We shall see in the following paragraphs that there exist more sophisticated *ab initio* calculations making less severe approximations. On the other hand, the model Hamiltonians simplify the exact one in a less crude way, but introduce parameters to quantify the relative strengths of the various interactions they aim to describe.

In either case, there is no exact analytical solution and one needs to construct a numerical one. Numerical solutions are basically electronic structure calculations that need to take into account the core hole. Therefore one finds the same plethora of methods as for the standard electronic structure calculations.

There is a great need of codes which are able to reproduce the near edge structure within a reasonable calculation time. Providing a satisfactory description of such complex electronic scattering phenomena is a theoretical challenge and numerous attempts have been reported. They are either well established, thoroughly tested methods - DFT or multiplet theory calculations [8, 13, 26, 34, 40, 56, 76, 80, 85] - or more recent works requiring further investigation - the multichannel method [62], the time dependent density functional theory (TDDFT) or the Bethe Salpeter equation (BSE) based methods [106].

## The one body methods

The DFT methods are *ab initio*, i.e. they are based on first principles and do not use essential, adjustable parameters. They are tailored for a multiatomic treatment and thus account for the influence of the distant atomic neighbourhood. The philosophy behind these methods is to solve the SE with the single particle potential suggested by the DFT description of exchange-correlation. The DFT methods provide a fair treatment of the extended states and in some sense of the partially delocalized ones (figure 1.2) but fail to describe the highly-correlated ones, where the interaction with the core hole is strong. This is due to the relatively long timescale associated to the localized level, as compared to the core hole's lifetime.

To solve the electronic structure, one can make approximations on the spacial range and distribution of the single particle potential. According to this criterion, the DFT methods are either full potential - the finite differences method (FDM) [56], the full potential multiple scattering theory (FP-MST) [9, 49], the full potential Korringa-Kohn-Rostoker (KKR) method [40], the full potential linear augmented plane waves method [85] - or subject to approximations. The ubiquitous muffin tin (MT) approximation assumes that the crystal potential has spherical symmetry around the atoms, within the so-called MT sphere, and is constant between adjacent spheres. The most common methods exploiting this approximation are the MT-MST [13, 56, 80], the linear muffin tin orbital (LMTO) [124] and the MT KKR [40] methods. The MT approximation provides fair results for the close-packed structures, but often fails to describe the

sparse materials. The more sparse the material, the more important it is to treat the scattering in the interstitial space and to consider other terms than the spherical one in the development of the potential inside the MT sphere.

DFT calculations can be performed either in the real space [8,13,56,62,80,118] or in the reciprocal one [26,40,85,124]. Note that for where absorption calculations are concerned, the real space basis seems to be a natural choice. First, these techniques can be performed on molecules or liquids, where no periodicity is involved. Second, even when performed on single crystals, the core hole breaks the periodicity. Third, the spacial range probed in X-ray absorption experiments is limited to the mean free path of the photoelectron ( $\approx 5\text{-}10\text{ \AA}$ ) and thus, in a real space description, the scattering problem is localized. Nevertheless reciprocal space calculations give similar results, provided a supercell has been built: the absorbing atom is treated as an impurity breaking the periodicity of the crystal [113]. The great majority of reciprocal space calculations are self-consistent [26,40,85,124]. The self-consistency for real space calculations is less trivial, due to technical reasons discussed in chapter 4. The only existing real space, X-ray absorption calculation codes are FDMNES [56] and FEFF [8].

**The exchange-correlation functionals** All the DFT methods of condensed matter physics use a local exchange-correlation functional, most often in the form of the local density approximation (LDA) or the semi-local one (GGA). Note that this is not the case of the DFT methods employed in quantum chemistry, which treat the FP case and employs more sophisticated, often parametrised descriptions of the correlation. The LDA approximates the exchange energy to that of a homogeneous electron gas (see for instance the beautiful explanations in [25]), whereas the correlation contribution is described by a local analytical form (see, for instance, reference [86]). Despite its reductionism, LDA gives good results when the physical system has a band behaviour. The LDA exchange - correlation functional has been improved based on the works of Hedin and Lundqvist [51], who proposed a parametrized, GW derived way to take into account the inelastic processes suffered by the photoelectron - the so-called self-energy correction to the exchange-correlation potential.

Note that the DFT methods support an extension of the LDA allowing the calculation of spin polarized energy bands, i.e. the so-called local spin density approximation (LSDA). In the absence of the spin-orbit coupling, two separate calculations are conducted for each spin. Magnetic behaviour can be described, since the exchange-correlation is a functional of both the density and the spin polarization.

**The self-energy corrections** The self-energy corrected exchange - correlation potentials have some energy dependence, unlike the LDA one. The locality of all these functionals leads to a decoupling of the equations of motion describing the electrons and maps the system into a non-interacting one yielding the same density. The emerging (non-interacting) quasiparticles feel an effective potential whose form depends on the functional. These kinds of approaches are called either the quasiparticle approximation (QA) or the independent particle approximation (IPA), depending on whether one uses an energy dependent functional or not. IPA and QA are generally referred to as the single particle (one body) approach.

A complete GW calculation [84] provides a more accurate treatment of the self-energy,



albeit an increased computational effort. For X-ray absorption one does not expect an improvement significant enough to justify the use of such a resource consuming method. For empty electron levels, the GW correction often reduces to a global energy shift [113]. Although this may correct the false offset of the absorption spectra predicted by the ground state DFT, we feel that a GW correction for the X-ray absorption calculations is no end in itself. Nevertheless, a GW calculation may be a good starting point for the implementation of more advanced features, as the BSE methods [106].

**The quasiboson model** There are structures in the spectra that cannot appear in an IPA calculation but are reproduced in a GW one: the plasmonic peaks and the multiple electron excitations (shake off and shake on processes). A way to include these in an X-ray absorption calculation would be to convolute the IPA spectrum with a spectral function that accounts for the many body processes. Such a function has been constructed based on a generalisation of the GW approach [27], the so-called quasiboson model. In this model, the electrons interact with the electron-hole excitations, which are treated as bosons. The quasiboson model goes beyond the GW approximation by making a distinction between the intrinsic inelastic losses (due to the instantaneous creation of the core hole) and the extrinsic ones (mainly the scattering on plasmons). As intrinsic and extrinsic losses are indistinguishable from a quantum mechanical point of view, they interfere. Contrary to the GW, the quasiboson model gets to treat this interference. The authors claim that its effects are particularly strong at the edge, where the two contributions cancel each other. Consequently, the quasiboson model would explain why the multiple electron excitations are scarce near the edge, where the intensity of the primary channel in the spectral function (the single particle peak) is enhanced at the expense of the broader queue describing the multiple electron excitations. The quasiboson model has been implemented in the FEF code [93].

**The shortcomings of the DFT methods** The one body approaches' major drawback is that they cannot handle accurately the electronic correlations. By correlations we mean all electron - electron interactions beyond the mean-field picture. Note that the generally accepted definition of correlation, in the sense of quantum mechanics, is that it contains all the effects beyond the Hartree-Fock approximation. Nevertheless, the Hartree-Fock calculation is usually not tractable for extended systems, as the DFT functional describing the exact exchange is highly non-local. Consequently, one cannot distinguish between pure correlation and exchange contributions, since we are not able to calculate the latter. Therefore when referring to correlation, we chose to include both effects: exchange and pure correlation. In this manuscript, the term "correlation" is used in the sense of the Dynamical Mean Field Theory.

In correlated materials, the DFT underestimates the gap at the Fermi level. This may be partially fixed by the adding of a Hubbard-like correction (the LDA+U method), as we shall see further (chapter 5). Another issue of the DFT-LDA based calculations is that they cannot correctly describe the excited states, as the DFT is a ground state theory. To account for the core hole some *ad hoc* prescriptions are used (see for instance the explanations for the final state rule in section 1.4.2). All these kinds of adjustments are static, i.e. they do not take into account the relaxation of the electron cloud surrounding the core hole. We shall come back to this point later in this very

section.

Some features in an experimental spectrum cannot be reproduced by single particle calculations, in particular the plasmonic and excitonic structures. Plasmons (i.e. the quanta of the collective oscillations of the electron gas) are correlation - driven effects that appear beyond the one body framework. Excitonic structures are equally missed by the single particle approximation, as they are due to the Coulomb interaction of electrons and holes, a two particle process. For bound excitons, the excitonic peak physically corresponds to the internal degrees of freedom of an interacting electron - hole pair, in the same way as a bound electron - positron system (the hydrogen atom) has discrete internal energy levels.

### The atomic methods

To improve the description of the X-ray absorption process one should leave behind the one body theories and explore the many-body framework. Correlations are particularly strong when the wavefunction of the core electron overlaps with those of the absorber's valence electrons, i.e. when the absorber's valence states have a pronounced atomic character (for instance, the transition metal oxides). In the case of open shell systems ( $S \neq 0$ ) this leads to the so-called multiplet effect (see, for instance, reference [34]). The multiplets are the discrete spectral structures appearing when correlations split a single particle state. Multiplets are a signature of the many-body effects.

**The multiplet methods** In the case of X-ray absorption, the transition of the photoelectron to an atomic-like unoccupied state can be described in terms of electron - hole configurations, whose multiplicity will depend on the initial and the final states' manifold. For instance, at the  $L_{2,3}$  edges of a metal in an oxide compound the dipolar signal is due to the  $2p^6 3d^N \rightarrow 2p^5 3d^{N+1}$  transitions [125]. The initial state rule IPA only treats the case where the  $d$  electrons are passive, i.e. no charge transfer from the oxygen atoms (also called ligands) occurs. Consequently, one of the strengths of the multiplet methods is that they can deal with the charge transfer effects, i.e. a phenomenon consisting in charge fluctuations in the initial and final state.

Secondly, within the multiplet methods, the arrival state  $3d^{N+1}$  is no longer degenerated: several configurations  $2p^5 3d^{N+1}$  are thus taken into consideration. Numerous interactions, like the spin-orbit coupling, the crystal field or other electron-electron interactions lift the degeneracy of the final state's configurations. This gives rise to a multiplet structure: a main line and its satellites. In zero external field, the lowest energy multiplet is indicated by Hund's rules. The multiplet effect may be masked by the core level's width, hence, except for the pre-edge structures, it is difficult to see a multiplet effect at  $K$  edges. The appearance of the multiplet structure is a consequence of having considered advanced correlations, whereas the energy position and the spectral weight of the multiplets depend on the strength of the various interactions described in the Hamiltonian. The ligand field theory gives a parametrized description of the localized electronic states but fails to describe the delocalized ones, which can no longer be characterized in terms of configurations. This method is limited in the number of atoms and it may disregard the effects due to the atomic neighbourhood.

Nevertheless efforts are underway to eliminate this shortcoming and one expects it to no longer be a problem in the near future. As the origin of multiplet structure lies in the localized states, one expects the atomic multiplet effect to be of the same order of magnitude in both atoms and solids. Note that the ligand field calculations are not *ab initio* as they use adjustable parameters whose values depend on the local symmetry of the absorbing site.

**The cluster many-body method** A very related, genuine many-body calculation technique is the so-called cluster many-body calculation. It consists in the solving of the parametrised, second quantization Hamiltonian [75]. Compared to the multiplet calculation, this method is less limited in terms of number of atoms. Its parameters are taken from experiments and are independent of the local symmetries [76].

**The configuration interaction method** The configuration interaction (CI) method is another *ab initio* method used to calculate X-ray spectra [55]. The CI methods scale very unfavourably with the system's size [84], thus one refers to them as atomic methods. One considers all the particle - hole excited configurations, with the hole lying on the core level concerned by the spectroscopy. Contrary to the multiplet method, which employs atomic orbitals, the CI uses the molecular ones (check reference [55] for a detailed comparison of the two methods). This method takes into account the mixing between the several transition channels (the so-called configuration interaction) and is naturally tailored to describe charge transfer. The CI method has been employed to calculate the  $L_{2,3}$  edge branching ratio of the  $3d$  elements [120]. The authors concluded that the  $L_2$  ( $L_3$ ) structure in the absorption spectrum does not correspond exclusively to transitions from the  $2p_{1/2}$  ( $2p_{3/2}$ ) core levels, as predicted by the single particle approaches. This conclusion will be later validated by all the TDDFT calculations of the X-ray absorption spectrum (see the discussion in chapter 6).

The essential shortcoming of the atomic methods (CI and multiplets) is that they ignore the band modulation of the continuum. This modulation is the effect of the non-zero size of the calculation cluster: the photoelectron suffers multiple scatterings on the neighbouring atomic shells and the backscattered wavefunctions interfere (see section 2.3.1). On the other hand, the complementary single particle DFT methods succeed in this, but fail to describe the eventual atomic features.

### The inclusion of many-body effects in the band description

**The LDA+U method** Correlations can be partially introduced in the one body calculation schemes by adding an on site, Coulomb repulsion corrective term  $U$  to a usual LDA calculation.  $U$  is often taken as a parameter, even if it may be calculated from first principles. Its value is element dependent and typically of several eV. The details of this method will be explained elsewhere (section 5). The LDA+U is a first attempt at merging an *ab initio* method (DFT-LDA) with a model Hamiltonian (the Hubbard Hamiltonian): delocalized states are treated within the former, whereas the localized ones are treated by the inclusion of a Hubbard-like term in the Hamiltonian. Note that although the LDA+U is successful in describing the Mott insulators [15], its application to weakly correlated metals is questionable [87].

**The Hamiltonian methods** One expects to override the one body approximations' limitations by taking explicitly into account the many-body effects in the Hamiltonian. A somehow rudimentary attempt to do so [89] is based on the theory developed by Nozières and De Dominicis [83]. They simplify the many body Hamiltonian by taking into account the Coulomb interaction only between the core electron and the valence ones, then apply the equation of motion technique. In this way both the itinerant electrons and the core hole are being considered. The authors get to validate the final state rule for the XANES spectroscopy and the initial state rule for the photoemission. Although this model makes a step beyond the single particle approaches and accounts for the core hole, at least to some extent, it is too rudimentary to reproduce multiplet structures, dynamic screening or excitonic effects.

**The time dependent density functional theory methods** TDDFT is a *ab initio* framework that can, in principle, account for some of these effects [84]. In theory TDDFT is an exact method. One is nevertheless brought to make assumptions on the form of the exchange correlation kernel, a key ingredient of the formalism. The kernel hides the richness of the physics that is reproducible by the TDDFT calculation. For instance, the time dependent equivalent of the LDA (TDLDA) inherits the same limitations as its ground state counterpart - for instance, it gives a wrong offset of the absorption spectra. Among its drawbacks, we note TDLDA's incapacity to describe the charge transfer and thus to treat the open-shells correctly. The TDLDA takes (partially) into account the core - hole: within this approach, the Coulomb interaction naturally mixes the transition channels, leading to a redistribution of intensities. More generally, this effect takes place when some two edges are close in energy ( $L_{23}$  or  $M_{45}$  edges). In a sense, this redistribution has the same origin with the one predicted by the CI calculations, but quantitatively it gives more reliable results than those of the atomic description. The advantage of the TDLDA over CI is that it can also handle the continuum states, which are ignored in the atomic approach.

A first attempt to implement a TDDFT method for X-ray absorption in extended systems has been reported by Schwitalla and Ebert in 1998 [101]. They propose a fully relativistic KKR method with a local kernel. As in the case of the multichannel method, they get a good agreement for the  $L_{2,3}$  branching ratio of the early transition metals and not such a good result for the late ones. A similar calculation method, fully relativistic and using the same TDLSDA formalism, has been reported the same year [64].

One should say that the TDDFT methods have been exploited more by the quantum chemists than by the condensed matter physicists. The reference in [111] contains a TDDFT study of the core electron excitations from the point of view of quantum chemistry. The authors used the TDDFT features in the ADF code to calculate the  $L_{2,3}$  edges of Ti in the  $\text{TiCl}_4$  molecule by considering no spin-orbit coupling, neither for the core states, nor for the final ones. Surprisingly, they succeed in reproducing the experimental data despite such a drastic assumption. Quantum chemistry calculations employ basis sets that are more refined than the ubiquitous Hartree-Fock atomic wavefunctions used in solid state physics. By increasing the accuracy in the choice of basis sets, the  $L_3$  structure is not altered, but the higher energy  $L_2$  peak is. The same behaviour occurs when choosing various forms of the exchange-correlation potential for

the ground state calculation, a pre-step of the TDDFT one. Whether these features would hold for extended systems, and by considering the spin-orbit coupling, remains an open question.

In 2003, Ankudinov, Nesvizhskii and Rehr reported the implementation of a TDDFT-MST method [7], which was later integrated in the FEFF package [92]. They made several choices of the kernel, including the random phase approximation with local field effects (RPA-LF), the TDLDA and an extension of the latter. Note that a static (i.e. no explicit time or energy dependence) kernel cannot describe the relaxation of the electron cloud. With an appropriate choice of the kernel, the authors apparently succeed in reproducing the experimental branching ratio for the  $L_{2,3}$  edges of the  $3d$  elements. For an extended discussion, please refer to section 6.4.

In 2005, Scherz et al. went the other way around: they used the values of the above mentioned experimental branching ratios to deduce the exact form of the kernel [99]. They concluded that the branching ratio anomaly of the early  $3d$  elements is not entirely due to the mixing of the  $L_2$  and  $L_3$  transitions, but to an effective reduced spin-orbit coupling of the initial state.

The latest news in the field concerns the derivation of the LDA+U kernel for the TDDFT - the non-local TDLDA+U functional by Lee, Hsueh and Ku [63]. Contrary to the TDLDA, or to the TDLDA coupled to a LDA+U calculation, the innovative TDLDA+U successfully generates excitons. Although the theory predicts a good excitonic energy range, it fails to detect their fine structure (the multiplet effect). The authors argue that in order to get it, it is imperative to construct an energy dependent (non-adiabatic) kernel.

**The two-body band methods** The BSE X-ray absorption calculations are a promising, yet computationally demanding option. Amongst the pioneers, we mention Shirley's performing the first BSE X-ray absorption calculation [106]. Ankudinov, Nesvizhskii and Rehr proposed a version of the TDLDA method with a kernel claimed to be derived from the BSE [7, 91]. Further advances have been reported by the same authors [9], who propose a claimed TDDFT-BSE calculation scheme. For a critical discussion of these approaches, please refer to chapter 6.

As the BSE formalism is based on the two particle Green's function, these methods naturally include the interaction between the electron-hole pairs, which is neglected by other *ab initio* methods. The inclusion of this interaction is crucial to reproduce the excitonic peaks and to treat the screening dynamically. The price to pay lies in the computation time - BSE calculations are extremely demanding. To this moment, such methods are not tractable for routine calculations and are not yet implemented at a large scale. Nevertheless, J.J. Rehr et al. have recently reported having developed an interface between the FEFF code and the BSE OCEAN code (to be published), but this attempt is still in an embryonic phase.

The BSE methods improve significantly the agreement between the band calculations and the experiment by adding the description of the two body effects (i.e. excitons). Nevertheless, some key features are still missing: the multiplet structures, which are a many body and not a two body effect. Correlation effects described by the BSE are not orbital dependent, and thus may not distinguish between the effect of the several atomic configurations.

## The coupled atomic-band methods

The Holy Grail of the X-ray absorption calculations is the union between the complementary *ab initio* and the atomic methods. The atomic approaches such as CI and the multiplet theory reproduce some complementary many body effects but neglect the band structure modulation of the continuum. On the other hand, one body calculations succeed in describing the band structure but not the multiplet one. To get an accurate picture of X-ray absorption, one should merge the atomic and the band methods.

**The multichannel method** Such an *ab initio* attempt is the multichannel MST method [61,62]. It is a real space method exploiting the standard multiple scattering theory (MST) formalism and the CI. The CI allows an explicit treatment of the core hole, whereas the band behaviour is handled by the MST. Given the atomic character of the CI, the multichannel method holds as long as the correlation effects are confined to the absorbing atom. The multichannel method gives more satisfactory results for the  $L_{2,3}$  absorption edges of the early transition metals as compared to the TDDFT ones [101].

**The dynamical mean field theory based methods** An example of such a combination is the use of the dynamical mean field theory (DMFT) [59] coupled to a LDA calculation. DMFT is suited for strongly correlated materials, i.e. in between the DFT-LDA (no correlations) and the LDA+U (Mott insulator) descriptions. The idea behind this method is to map (self-consistently) the full many-body problem onto the Anderson impurity Hamiltonian. In DMFT one calculates a local, but energy dependent self-energy - "the dynamical mean field". For a review of DMFT, please check [67]. The hybrid LDA-DMFT scheme treats the correlated orbitals in a DMFT-like way and the remainder in the LDA framework. Recently, this method has been employed to calculate the  $M_{4,5}$  branching ratio of the actinides [104]. Its success is explained by the LDA-DMFT capability to describe accurately both the localized electron states and the itinerant ones. A very recent X-ray absorption study investigating the Mott transition in  $V_2O_3$  [95] uses a combined LDA+DMFT coupled to a multiplet cluster calculation to explain the experimental findings.

Few attempts to perform hybrid atomic - band calculations have been reported, and they are still in an early phase. As long as TDDFT calculations are concerned, the possibility of providing the complete many body description is dependent on the development of an orbital dependent exchange-correlation kernel that contains the multiplet effect. For the time being such kernel does not exist.

**FDMNES** To understand experiments, one needs easy to use and accurate tools. FDMNES (standing for Finite Difference Method Near Edge Structure) is a calculation code originally developed by Yves Joly since 1996 and which simulates XANES, RXD and XMCD spectra [56]. The containing package is user-friendly, free and open-source, and equally supports parallel architectures (the Message Passing Interface protocol). It is an *ab initio*, self-consistent [24], real space, symmetrised code, which solves the electronic structure either in the MT-MST frame, or by using the full potential FDM. It can rigorously treat magnetism by taking into consideration the exact spin-orbit

Table 1.1: An overview of the most known X-ray absorption calculation codes and their main features

Code	Main author	Method	Type	FP	Rel.	self-consistent	Fit	Ref.
CONTINUUM	C.R. Natoli	MST	cluster	✗	✓	✗	✗	[80]
MXAN	M. Benfatto	MST	cluster	✗	✓	✗	✓	[13]
FEFF	J.J. Rehr	MST, TDLDA	cluster	✓	✓	✓	✓	[8, 92]
FDMNES	Y. Joly	FDM, MST, TDLDA	cluster	✓	✓	✓	✓	[24, 56]
FPX	D. Foulis	MST	cluster	✓	✗	✗	✗	[42]
SPRKKR	H. Ebert	KKR	3D	✓	✓	✓	✗	[40]
WIEN2k	P. Blaha	FP-LAPW	3D	✓	✓	✓	✗	[85]
PARATEC modified	D. Cabaret	pseudopotentials	3D	✗	✓	✓	✗	[26]
XKDQ	R.V. Vedriinski	MST	cluster	✗	✗	✓	✗	[118]
Py-LMTO	A.N. Yaresko	LMTO	3D	✗	✓	✓	✗	[124]
ICXANES	D.D. Vvedensky	MST	cluster	✗	✗	✗	✗	[119]
ADF	M. Stener	TDDFT	Slater	-	✓	✓	✗	[111]
NBSE	E. Shirley	BSE	cluster	-	✓	✓	✗	[106]
TT-MULTIPLETS	T. Thole	multiplets	cluster	-	✓	-	✗	[34, 35]
AMACORD	A. Mirone	multiplets	cluster	-	-	-	✗	[76]

coupling. FDMNES uses the Hedin-Lundquist energy corrections [51, 52] for the DFT exchange-correlation kernel [86]. The package allows an advanced analysis of both cartesian and spherical tensors describing the absorption process [57]. Recently we have extended the calculation behind the single particle approach, by implementing a TDLSDA method. Another recent development includes the adding of the LSDA+U calculation scheme.

## Chapter 2

# Fundamental aspects of the interaction of x-rays with matter

### 2.1 The quantum field theory description

For a scattering problem, the system under study contains both the cluster and the electromagnetic field. The purpose of this section is to calculate the absorption and the scattering cross sections in the second quantization formalism. This framework is necessary for rigorous analytical calculations. The general formulae are deduced in the single particle picture, i.e. the mean field approximation for the electronic problem.

**The Hamiltonian of the system** The main idea behind this calculation is to apply the time dependent perturbation theory's prescriptions to calculate the effects of the interaction of light with matter, all by considering the electromagnetic field as a perturbation. Let  $\mathcal{H}_0$  be the mean-field Hamiltonian of the unperturbed system, i.e. in the absence of the photon - matter interaction:

$$\mathcal{H}_0 = \sum_k \left( \frac{\hbar^2 k^2}{2m} + V^{MF}[n] \right) c_k^\dagger c_k + \sum_{\vec{q}, \epsilon_{\vec{q}}} \hbar \omega_q \left( a_{\vec{q}, \epsilon_{\vec{q}}}^\dagger a_{\vec{q}, \epsilon_{\vec{q}}} + \frac{1}{2} \right) \quad (2.1)$$

where  $\theta$  is the step function and  $\epsilon_k$  is the energy (calculated in the density functional theory) of the level  $k$ .  $V^{MF}[n]$  is the effective one body potential suggested by the density functional theory (see section 3.1).  $c_k^\dagger$  and  $c_k$  are the operators describing the creation and the annihilation of an electron of momentum  $k$ , whereas  $n_k = \sum c_k^\dagger c_k$  is the density operator.  $a_q^\dagger$  and  $a_q$  describe the creation and the annihilation of a photon of energy  $\hbar \omega_q$  and polarisation  $\vec{\epsilon}_{\vec{q}}$ . The choice of this mean field approximation for the electronic part of the Hamiltonian is motivated by the fact that in perturbation theory, the response to the perturbation is expressed in terms of the eigenfunctions of the unperturbed Hamiltonian. Therefore one needs a  $\mathcal{H}_0$  that one is able to solve. The electromagnetic field is described by the vector potential  $\vec{A}(\vec{r})$  [22]:

$$\vec{A}(\vec{r}) = \sum_{\vec{q}, \epsilon_{\vec{q}}} \sqrt{\frac{\hbar}{2\epsilon_0 \omega_q \mathcal{V}}} \left( a_{\vec{q}, \epsilon_{\vec{q}}}^\dagger e^{-i\vec{q}\vec{r}} \vec{\epsilon}_{\vec{q}}^* + a_{\vec{q}, \epsilon_{\vec{q}}} e^{i\vec{q}\vec{r}} \epsilon_{\vec{q}} \right) \quad (2.2)$$



where  $\mathcal{V}$  is the normalization volume. In the Coulomb gauge ( $\vec{\nabla} \vec{A} = 0$ ) the single particle Hamiltonian becomes:

$$\mathcal{H} = \sum_k \left( \frac{(\hbar k + e\vec{A})^2}{2m} + V^{MF}[n]\theta(E_F - \epsilon_k) \right) c_k^\dagger c_k + \hbar\omega_q \left( a_{\vec{q}, \epsilon_{\vec{q}}}^\dagger a_{\vec{q}, \epsilon_{\vec{q}}} + \frac{1}{2} \right) \quad (2.3)$$

We chose to show a simplified form of  $\mathcal{H}$ , where neither the spin-orbit interaction nor the coupling with the external magnetic field were included. The reason for the former choice is the simplicity (for the details of the spin orbit case please refer to the appendix), whereas the latter has negligible values in the linear regime. The perturbation  $\hat{V} = \mathcal{H} - \mathcal{H}_0$  gives:

$$\hat{V} = \sum_k \left( \frac{e\hbar}{m} \vec{k} \vec{A} + \frac{e^2}{2m} A^2 \right) c_k^\dagger c_k \quad (2.4)$$

and physically corresponds to the coupling between the electromagnetic field and the electronic system.

**The transition amplitude** To calculate the absorption cross section, one needs to know the probability *per* unit time  $W_{gf}$  that the system evolves from state  $|\Phi_g\rangle$  (electronic ground state + one photon) to  $|\Phi_f\rangle$  (electronic excited state + zero photons). Both  $|\Phi_g\rangle$  and  $|\Phi_f\rangle$  are eigenstates of the unperturbed Hamiltonian  $\mathcal{H}_0$ . Consequently, they can be factorised in pure electron ( $|\phi_f\rangle$  and  $|\phi_g\rangle$ ) and photon states ( $|1_{\omega_q}\rangle$  and  $|0_{\omega_q}\rangle$ ):

$$|\Phi_g\rangle = |\phi_g\rangle |1_{\omega_q}\rangle \text{ and } |\Phi_f\rangle = |\phi_f\rangle |0_{\omega_q}\rangle \quad (2.5)$$

In time dependent perturbation theory, the transition amplitude is given by:

$$W_{gf} = \frac{2\pi}{\hbar} \left| \langle \Phi_f | \hat{T} | \Phi_g \rangle \right|^2 \rho(E) \quad (2.6)$$

where  $\hat{T}$  is the transition operator. The absorption (or emission) problem is a one photon problem, in the sense that only one scattering process is involved. Therefore, to describe this first order process, it is sufficient to perform the first order approximation i.e.  $\hat{T} = \hat{V}$ . In this case, by replacing (2.4) in the Golden Rule (2.6), one obtains:

$$W_{gf} = \frac{2\pi}{\hbar} \left( \frac{e\hbar}{m} \right)^2 \left| \langle \Phi_f | \vec{k} \vec{A} | \Phi_g \rangle \right|^2 \rho(E) \quad (2.7)$$

Note that the term in  $A^2$  from (2.4) drops out, as it corresponds to a second order, two photon process. Moreover, in (2.2), the first term describes the emission process (creation of a photon) whereas the second describes the absorption. We replace the latter in (2.7) and we sum over all the available (empty states)  $|\phi_f\rangle$ , whose density of states is  $\rho(E)$ :

$$W = \sum_{g,f} \frac{\pi}{\epsilon_0 \mathcal{V}} \left( \frac{e\hbar}{m} \right)^2 \sum_{\vec{q}, \epsilon_{\vec{q}}} \frac{1}{\omega_q} \left| \langle \Phi_f | \vec{k} \vec{\epsilon}_q a_{\vec{q}, \epsilon_{\vec{q}}} e^{i\vec{q}\vec{r}} | \Phi_g \rangle \right|^2 \quad (2.8)$$

There exists one only mode  $q$  that couples  $|\Phi_g\rangle$  and  $|\Phi_f\rangle$ , thus the sum over the modes drops out:

$$W = \sum_{g,f} \frac{\pi}{\epsilon_0 \mathcal{V}} \left( \frac{e}{m} \right)^2 \frac{1}{\omega} \delta(E - E_g - \hbar\omega) \left| \langle \phi_f | \vec{p} \vec{\epsilon} e^{i\vec{q}\vec{r}} | \phi_g \rangle \right|^2 \rho(E) \quad (2.9)$$

where  $E$  is the eigenvalue corresponding to  $\phi_f$ . Moreover, it can be shown [31] that:

$$\langle \phi_f | \vec{p} \vec{\epsilon} (1 + i\vec{q}\vec{r}) | \phi_g \rangle = i \frac{m}{\hbar} (E - E_g) \left( \langle \phi_f | \vec{\epsilon} \vec{r} | \phi_g \rangle + \frac{i}{2} \langle \phi_f | \vec{\epsilon} \vec{r} \vec{q} \vec{r} | \phi_g \rangle \right) \quad (2.10)$$

where we kept only the first two terms in the expansion of the exponential in (2.9).

**The multipolar development of the potential** By definition, we call

$$\hat{O}(\vec{\epsilon}, \vec{r}) = \vec{\epsilon} \vec{r} \left( 1 + \frac{i}{2} \vec{q} \vec{r} \right) \quad (2.11)$$

the transition operator. It is obvious that its explicit form depends on the choice of the gauge and of the representation. This expansion is similar to the multipolar expansion of the classical electrodynamics and admits an infinity of terms, according to the expansion of the exponential function in (2.9). In practice, only the first two terms are necessary, as the contribution to the signal of the remainder is too small. When plugged into  $\langle \phi_f | \hat{O}(\vec{\epsilon}, \vec{r}) | \phi_g \rangle$ , the terms in (2.11) give, respectively, to the electric dipole (E1) and the electric quadrupole (E2) matrix elements.

**The absorption cross section** The absorption cross section is related to the transition probability:

$$\sigma(\omega) = \frac{W(\omega) \mathcal{V}}{c} \quad (2.12)$$

with  $c$  the speed of light in the vacuum. The final result for the absorption cross section is:

$$\sigma(\omega) = \frac{\pi\omega}{\epsilon_0 c} \left( \frac{e}{\hbar} \right)^2 \int_{E_F}^{\infty} dE \sum_{f,g} \delta(E - E_g - \hbar\omega) \left| \langle \phi_f | \hat{O}(\vec{\epsilon}, \vec{r}) | \phi_g \rangle \right|^2 \rho(E) \quad (2.13)$$

where  $f$  are all the empty states of energy  $E > E_F$  with  $E_F$  the Fermi energy.

**The scattering cross section** To describe the photon-in - photon-out processes one must expand the transition operator in second order in  $\hat{V}$ , i.e.  $\hat{T} = \hat{V} + \hat{V} \mathcal{G}_0(E_g) \hat{V}$ . By the aid of (2.4), for a given  $k$  and after suppressing the terms in power 1 (one photon process) or greater than 2 (high order excitations) of  $\vec{A}$ , we get:

$$T_k = \left( \frac{e\hbar}{m} \right)^2 \vec{k} \vec{A} \mathcal{G}_0(E_g) \vec{k} \vec{A} \quad (2.14)$$

From (2.6) and (2.14) one can deduce all the scattering amplitudes, resonant and non-resonant, elastic or inelastic. For the detailed calculation, please refer to [57, 103]. In

this work, we will be interested in the resonant elastic scattering cross-section (the structure factor):

$$f'(\omega) - if''(\omega) = \frac{m\omega^2}{\hbar^2} \int_{E_F}^{\infty} dE \sum_{f,g} \frac{\langle \phi_g | \hat{O}^\dagger(\vec{\epsilon}_{out}, \vec{r}) | \phi_f \rangle \langle \phi_f | \hat{O}(\vec{\epsilon}_{in}, \vec{r}) | \phi_g \rangle}{\hbar\omega - (E - E_g) + i\epsilon} \quad (2.15)$$

The sign convention for  $f''(\omega)$  requires it to be positive, whereas the limit  $\epsilon \rightarrow 0$  has been omitted for simplicity. Should one wish to describe the finite lifetime of the arrival states,  $\epsilon$  becomes finite (see section 3.1.6). The pre-factor is such that  $|\phi_f\rangle$  are normalized according to the procedure in the appendix.

**A unified description of the X-ray absorption spectroscopy** One can see that the connecting bridge of the absorption spectroscopies (XANES, RXD, RIXS, XMCD) is the transition matrix element of type  $\langle \phi_f | \hat{O}(\vec{\epsilon}, \vec{r}) | \phi_g \rangle$ . These spectroscopies are due to the same physical phenomenon and can be described by the same formalism. We recall that the proofs in this chapter have been conducted in the one body frame. Nevertheless, the strong connections between the several spectroscopies stay unaltered when the many body interactions are turned on.

**The selection rules** In the context of the spectroscopy calculation, the two matrix elements yield the E1-E1, E1-E2 or E2-E2 contributions. The main reason for this multipolar analysis is that it allows the precise identification of the probed orbital  $\phi_f$ . Depending on the term in the multipolar expansion (2.11) it comes from, the transition matrix elements are submitted to various selection rules [57]. As a rule of thumb, the spin is conserved during the transition, as the transition operator is purely electric. The orbital quantum number selection rule is  $\Delta l = \pm 1$  for the E1 transitions and  $\Delta l = 0, \pm 2$  for the E2 ones. In practice, almost all the signal comes from the  $\Delta l = 1$  for the dipole transitions and  $\Delta l = 2$  for the dipolar ones.

## 2.2 The tensor analysis

### 2.2.1 The formalism

As the X-ray absorption phenomena is generally anisotropic, both the physical origin and the azimuthal dependence of the spectra can be understood in terms of tensor algebra. Moreover, the tensor formalism provides a mathematically unified description of the core, related spectroscopy.

The tensor's rank depends on the order of the specific term in the multipolar expansion of the transition operator (2.11). Note that the expansion in (2.11) only considers the interactions of electrical origin. We therefore define the following atomic, electric tensors, whose energy dependent components describe the resonant process:

$$D_{\alpha\beta}^{(j)}(\hbar\omega = E - E_g^{(j)}) = \sum_{f,g} \langle \psi_g^{(j)} | r_\alpha | \psi_f \rangle \langle \psi_f | r_\beta | \psi_g^{(j)} \rangle \quad (2.16)$$

$$I_{\alpha\beta\gamma}^{(j)}(\hbar\omega = E - E_g^{(j)}) = -\frac{i}{2} \sum_{f,g} \langle \psi_g^{(j)} | r_\alpha | \psi_f \rangle \langle \psi_f | r_\beta r_\gamma | \psi_g^{(j)} \rangle \quad (2.17)$$

$$Q_{\alpha\beta\gamma\eta}^{(j)}(\hbar\omega = E - E_g^{(j)}) = \frac{1}{4} \sum_{f,g} \langle \psi_g^{(j)} | r_\alpha r_\beta | \psi_f \rangle \langle \psi_f | r_\gamma r_\eta | \psi_g^{(j)} \rangle \quad (2.18)$$

Here the  $f$  index accounts for the final states of same energy  $E$  whereas  $\alpha, \beta, \gamma$  and  $\eta$  run over the  $x, y$  and  $z$  space directions. All  $|\psi_f\rangle$  are normalized, according to the procedure described in the appendix.  $D_{\alpha\beta}$  is the electric dipole-dipole (also known as E1-E1),  $I_{\alpha\beta\gamma}$  the dipole-quadrupole (E1-E2) and  $Q_{\alpha\beta\gamma\eta}$  the quadrupole-quadrupole (E2-E2) tensor element.

The atomic tensor  $D$  is a tensor of rank 2 and has the form of a hermitian matrix:  $D_{\alpha\beta} = D_{\beta\alpha}^*$ .  $I$  and  $Q$  are of rank 3 and 4, respectively. Note that the atomic dipole-quadrupole term is zero if the point group of the corresponding atom contains the inversion. The reason behind this is that the selection rules impose that  $|\psi_f\rangle$  involved in the dipole-quadrupole is a mixture of states of opposite parity. This condition is not fulfilled if the material possesses the inversion symmetry. The dipole-quadrupole term is equally zero for linear polarizations in XANES (but not necessarily in RXD).

From a computational point of view working with tensors is extremely convenient, especially as far as the RXD calculations are concerned. Once we have the tensor describing a reflection, it is easy to multiply it by several sets of incoming and outgoing polarisations, in order to calculate the azimuthal scans and the polarization analysis:

$$f'(\omega) - if''(\omega) = \frac{m}{\hbar^2} \int_{E_F}^{\infty} dE \frac{(E - E_g)^2}{\hbar\omega - (E - E_g) + i\epsilon} \mathcal{T}(\hbar\omega = E - E_g) \quad (2.19)$$

where  $\mathcal{T}$  contains the contributions from the various terms in the multipolar expansion of the transition operator:

$$\begin{aligned} \mathcal{T}(\omega) &= \sum_{\alpha \beta} \epsilon_\alpha^* \epsilon_\beta D_{\alpha\beta}(\omega) + \sum_{\alpha \beta \gamma} \epsilon_\alpha^* \epsilon_\beta (k_\gamma I_{\alpha\beta\gamma}(\omega) + k_\gamma I_{\beta\alpha\gamma}^*(\omega)) \\ &+ \sum_{\alpha \beta \gamma \eta} \epsilon_\alpha^* \epsilon_\beta k_\gamma k_\eta Q_{\alpha\beta\gamma\eta}(\omega) \end{aligned} \quad (2.20)$$

Note that the atomic tensor  $T$  is invariant in the symmetry operations of the magnetic point group of the atomic site. One can re-write the absorption cross section (2.13) in a similar way:

$$\sigma(\omega) = \frac{\pi\omega}{\epsilon_0 c} \left(\frac{e}{\hbar}\right)^2 \int_{E_F}^{\infty} dE \sum_{f,g} \mathcal{T}(\hbar\omega = E - E_g) \quad (2.21)$$

By comparing (2.21) and (2.19) one can see mathematical evidence of the related character of the X-ray core spectroscopy. The reason why the density of states factor in (2.13) no longer appears in (2.21) should be looked for in the normalization procedure we previously mentioned.

The tensors of the transition matrix can be expressed either in a cartesian basis, or in the spherical one. The latter have a more straightforward meaning, as they link directly to physical quantities such as the charge, the magnetic moment, the quadrupolar electric moment etc. For instance, the isotropic contribution to scattering at the resonance is given by the trace of the tensor (a rotational invariant) normalized by a  $\sqrt{3}$  factor. The  $(D_{xx} + D_{yy} + D_{zz})/\sqrt{3}$  term is equal to the integrated (spatially) density of unoccupied

states *per* energy unit (the differential charge). The term  $D_{yz} - D_{zy} = i\sqrt{2}l_x$  (*idem* for circular permutations) where  $l_x$  is the projection of the atomic orbital momentum *per* energy unit on the Ox axis.

The FDMNES code is extremely powerful with respect to the analysis of the tensor. The calculation may be performed using the tensor elements of a specific rank, which allows the identification of the origin of each structure in the spectrum.

From now on, for simplicity, we shall only refer to the rank 2 atomic tensor and link it to the crystal. In periodic structures it is more convenient to deal with the crystal tensor  $\mathcal{D}$  given by:

$$\mathcal{D}_{\alpha\beta} = \sum_{j \in \text{unit cell}} D_{\alpha\beta}^{(j)} \quad (2.22)$$

The symmetry of  $\mathcal{D}$  is determined by the symmetries of the crystal. The crystal tensor  $\mathcal{D}$  is used for instance in the calculation of the absorption. One can assume a perfectly general form for the atomic tensor  $D_{\alpha\beta}^{(j)}$ :

$$\mathcal{D}_{\alpha\beta} = \sum_{\text{non equiv sym}} \sum_{\text{sym}} \left( D_{\alpha\beta}^{(j)} \right)_{\text{gen}} \quad (2.23)$$

where the first sum is over all the non-equivalent atoms, whereas the second one concerns all the symmetry operations. One can also introduce a symmetry reduced form of  $D_{\alpha\beta}^{(j)}$ , i.e. summed over all the atom's point group symmetries operations:

$$\mathcal{D}_{\alpha\beta} = \sum_{\text{non equiv}} \sum_{\text{equiv}} \sum_{\text{sym at}} \left( D_{\alpha\beta}^{(j)} \right)_{\text{gen}} = \sum_{\text{non equiv}} \sum_{\text{equiv}} \left( D_{\alpha\beta}^{(j)} \right)_{\text{sym}} \quad (2.24)$$

To describe the diffraction it is necessary to introduce the structure factor tensor given by:

$$\mathcal{D}_{\alpha\beta}(\vec{Q}) = \sum_j e^{i\vec{Q}\vec{R}_j} D_{\alpha\beta}^{(j)} = \sum_{\text{non equiv}} \sum_{\text{sym}} e^{i\vec{Q}\vec{R}_j} \text{sym}(D_{\alpha\beta}) \quad (2.25)$$

where  $\vec{Q} = (hkl)$  is the scattering vector. FDMNES uses symmetries to reduce the computation time: only the tensors of the non equivalent atoms are calculated, then symmetry operations are used to deduce those of the other atoms.

### 2.2.2 Symmetries

FDMNES is a symmetrized code, i.e. it exploits the point symmetries of the absorbing sites to save calculation time. In practice one calculates explicitly only the non-equivalent atoms (from the point group point of view). The equivalent atoms are being accounted for by the use of an adapted procedure to solve the SE. For the technical details of the symmetrization please refer to [36]. We stress the fact that the final result is independent of whether one uses a symmetrised procedure or not.

After solving the SE we obtain atomic tensors whose form is tributary to the magnetic point group symmetries of each site. Let  $d$  be the tensor of a central atom. A second atom, related to the first one by symmetry, may be described by:

$$d' = \mathcal{R}^+ d \mathcal{R} \quad (2.26)$$

where  $\mathcal{R}$  is the transformation matrix corresponding to the symmetry operation that links the two atoms and  $\mathcal{R}^+$  its adjoint. If no magnetism is involved, these transformations are simple matrix transformations. If this is not the case, one should pay attention to the particular behaviour of spins when submitted to symmetry operations:

$$\begin{aligned} M_{\parallel}S &= -S; & TM_{\parallel}S &= S; & C_{\parallel}S &= S; & TS &= -S \\ M_{\perp}S &= S; & TM_{\perp}S &= -S; & TC_{\parallel}S &= -S \end{aligned}$$

where  $T$  is the time reversal.  $M_{\parallel}$  ( $M_{\perp}$ ) stands for the mirror operation whose axis is parallel (perpendicular) to the spin  $S$  direction.  $C_{\parallel}$  is a rotation around the spin direction. If the rotation is performed along an axis which is perpendicular to the spin direction, the spin undergoes a vector-like transformation. Note that provided they are parallel to a rotation axis, spins are invariant under inversion and that time reversal changes the sign of their projection.

**An example** Let two magnetic atoms related by a  $C_{2z}$  rotation. The first one is described by a tensor in the most general form:

$$d = \begin{pmatrix} d_{xx} & d_{xy} & d_{xz} \\ d_{yx} & d_{yy} & d_{yz} \\ d_{zx} & d_{zy} & d_{zz} \end{pmatrix} \quad (2.27)$$

whereas the second one gives:

$$d' = C_{2z}^+ d C_{2z} = \begin{pmatrix} d_{xx} & d_{xy} & -d_{xz}^* \\ d_{yx} & d_{yy} & -d_{yz}^* \\ -d_{zx}^* & -d_{zy}^* & d_{zz} \end{pmatrix} \quad (2.28)$$

Note that as  $S_z$  is invariant with respect to  $C_{2z}$  one has  $\Im(d_{yx} - d_{xy}) = \Im(d_{yx}' - d_{xy}')$ . On the other hand  $S_x$  changes sign, thus  $\Im(d_{yz} - d_{zy}) = -\Im(d_{yz}' - d_{zy}')$ .

## 2.3 Solving the electronic structure

### 2.3.1 The Schrödinger-like equation

All one body methods that solve the electronic structure are based on some stationary equation describing the spatial distribution of the wavefunction. More precisely, when the relativistic effects are not significant, one deals with the Schrödinger equation. If one calculates heavy atoms, or a spin-orbit coupling, one should appeal to the Dirac equation.

**The Schrödinger equation** In a single particle, non-relativistic picture one can generally write (in Rydberg units):

$$(-\nabla^2 + \hat{V} - E) |\Psi\rangle = 0 \quad (2.29)$$

with  $\hat{V}$  the one body potential. To describe the inelastic effects one should introduce the self-energy correction:

$$(-\nabla^2 + \hat{V} + \Sigma(E) - E) |\Psi\rangle = 0 \quad (2.30)$$

Here  $\Sigma(E)$  is the standard notation for self-energy. The Hamiltonian in (2.30) is no longer hermitian, due to the imaginary part of  $\Sigma$ . This means that the eigenstates of the system decay with a rate described by  $\Im\Sigma$ . In section 3.1.6 we show that  $\Im\Sigma$  is responsible for the broadening of the spectral lines.  $\Re\Sigma$  is responsible for an energy shift in the spectrum. A proper treatment of the self-energy, but still subjected to approximations, is achieved within the GW framework [84].

In the case of spin polarisation, one can still appeal to the Schrödinger equation provided there is no spin-orbit coupling. Two distinct, independent calculations are conducted, with an effective potential depending on the specific spin population.

**The Dirac equation** The spin-orbit coupling is a relativistic effect and emerges naturally from the Dirac equation, i.e. the covariant generalisation of the Schrödinger equation. The radial Dirac equation is solved with the use of no approximation and by the elimination of the small components. For a discussion and references, please refer to [71]. For the radial solution of the Dirac equation, please refer to the appendix.

### The final state wavefunctions

To apply the Golden Rule (1.3) for an absorption calculation one should apply (2.29) to both the calculation of the initial wavefunctions  $\Psi_g(\vec{r})$  and to the final ones  $\Psi_f(\vec{r})$ . The solution of the formal is trivial, as the initial states concerned by the X-ray spectroscopy are atomic. Therefore, solving the electronic structure reduces to the calculation of the final states, or to some related quantities (the propagator  $\mathcal{G}$ ).

**Zero spin-orbit coupling** All through this manuscript, by spin-orbit coupling we mean the spin-orbit coupling of the final states, as for the initial ones it is included in the calculations under all circumstances. In the zero spin-orbit coupling limit we can treat magnetism provided we perform two separate calculations (with different potentials) for the two spins populations. Provided the transition operator is of an electrical nature (see chapter 2), the transition channels for the two spins do not mix, i.e. no spin-flip processes are possible. Consequently, the eigenfunctions of (2.29) can be expanded in:

$$\Psi_f(\vec{r}; E) = \sum_{\sigma} \sum_{l,m} a_{l,m}^{f,\sigma}(E) b_l^{\sigma}(r, E) Y_l^m(\hat{r}) \chi_{\sigma} \quad (2.31)$$

where the radial part is normalized according to the procedure described in the appendix and  $\chi_{\sigma}$  is the spin function.

**The spin-orbit coupling** The spin-orbit coupling links the  $|m, \uparrow\rangle$  and  $|m+1, \downarrow\rangle$  states ( $m$  of the complex spherical harmonics). The state vector  $\Psi_f$  is no longer a unique wavefunction, but the sum of two  $2 \times 1$  matrices in the spin vector space. The solutions  $s$  are indexed  $+\frac{1}{2}$  and  $-\frac{1}{2}$ , respectively. The final states have the following form [71]:

$$\Psi_f(\vec{r}) = \sum_{l,m} \sum_{s=\pm\frac{1}{2}} a_{l,m+\frac{1}{2}-s,s}^f(E) \begin{pmatrix} b_{l,m,\uparrow}^s(r) & Y_l^m(\hat{r}, E) \\ b_{l,m+1,\downarrow}^s(r) & Y_l^{m+1}(\hat{r}, E) \end{pmatrix} \quad (2.32)$$

We stress upon the fact that the spin-orbit coupling lifts the radial degeneracy, i.e. the solution  $b$  of the radial SE depends on both  $l$  and  $m$ . In the zero-coupling limit (2.31) one finds that  $b_{l,m+1,\downarrow}^{\frac{1}{2}}(r, E) = b_{l,m,\uparrow}^{-\frac{1}{2}}(r, E) = 0$  and the solution index is identical to the spin one. Moreover, one always has  $b_{l,l+1,\downarrow}^{\frac{1}{2}}(r, E) = b_{l,-l-1,\uparrow}^{-\frac{1}{2}}(r, E) = 0$ , which implies that the  $|m = -l, \uparrow\rangle$  and  $|m = l, \downarrow\rangle$  states are decoupled from the others.

Numerically, we assign  $\uparrow = +\frac{1}{2}$  and  $\downarrow = -\frac{1}{2}$  to the electron spin projections  $\sigma$ . If we keep the same values for the indices running over the solutions, one can re-write (2.32) under the more condensed form:

$$\Psi_f(\vec{r}) = \sum_s \sum_{\sigma} \sum_{l,m} a_{l,m+\frac{1}{2}-s,s}^f(E) b_{l,m+\frac{1}{2}-\sigma,\sigma}^s(r, E) Y_l^{m+\frac{1}{2}-\sigma} \chi_{\sigma} \quad (2.33)$$

where  $\chi_{\frac{1}{2}} = \begin{pmatrix} 1 \\ 0 \end{pmatrix}$  and  $\chi_{-\frac{1}{2}} = \begin{pmatrix} 0 \\ 1 \end{pmatrix}$  are the spin functions. Note that the use of real spherical harmonics in (2.32) and (2.33) is no longer possible.

If the potential  $V(\vec{r})$  can be factorized into a radial and an angular part, one may separate the two dependencies in the SE. In particular, this is the case for the potentials which have spherical symmetry, including the one of the MT approximation. We mention that the potential is rigorously symmetric only for the closed shells.

The radial SE is solved around each atom core and the solution is straightforward. Finding the angular distribution of the wavefunction is a more delicate issue, that we can address either in the MST or FDM frameworks.

### 2.3.2 The finite difference method

The FDM is a method to determine the electronic structure by the direct resolution of the SE equation. The FDM is full potential, i.e. it makes no approximation on the form of the potential. Moreover, FDM is the only full potential, real-space X-ray core spectroscopy calculation. It was implemented by Yves Joly in the FDMNES code [56]. The method consists in setting a mesh of points around each atom, discretising the SE and solving it at each point of the mesh.

### 2.3.3 The multiple scattering theory

The MST is a method to solve the electronic structure, all by avoiding the explicit calculation of eigenstates. The reason behind this choice is that the exact calculation of the real space, final state wavefunctions  $\Psi_f(\vec{r})$  require extended basis sets, that would be limiting from the numerical point of view. We do not intent to treat the issues of MST in detail (see [45] for a complete discussion or [74] for an introductory one) but to give an overview and focus on the specific features implemented in the FDMNES calculation.

**Phenomenologic interpretation of the multiple scattering** The idea behind the multiple scattering process is that the electron's wavefunction interferes with its reflections on the neighbouring atoms. Consequently, the origin of the modulations on a XAS, MST calculated, spectrum lies in the constructive interference between the



direct and the backscattered waves (figure 2.1): the spectrum of an isolated atom is smooth. This physical picture is appropriate only for the extended region in EXAFS. In the XANES energy range the wavelength of the photoelectron is larger than the distance to the first neighbouring shell and its propagation can no longer be described in the classical picture of a finite number of scattering events on separate atoms.

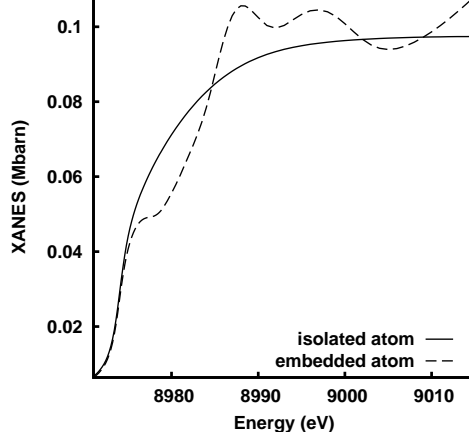


Figure 2.1: Absorption calculations at the  $K$  edge of copper: isolated *versus* embedded (175 atoms) absorber. The spectrum's fine structure is given by the environment around the absorbing atom

### The multiple scattering matrix

The MST treats the scattering of an electronic wave  $|\phi\rangle$  on a set of non overlapping atomic scatterers  $v_i$ . We only treat the MT case, where  $v_i$  have spherical symmetry in a region of finite radius. The propagation is described by the Hamiltonian:

$$\mathcal{H} = \mathcal{H}_0 + \hat{V} \quad (2.34)$$

where  $\mathcal{H}_0$  is the Hamiltonian in the free case, whose eigenfunctions  $|\phi\rangle$  have the eigenvalues  $E_0$ . The term  $\hat{V} = \sum_i v_i$  is the perturbation. One seeks the stationary solution  $|\psi\rangle$  of energy  $E$ :

$$\mathcal{H} |\psi\rangle = E |\psi\rangle \quad (2.35)$$

The formal solution of (2.35) is given by the Lippman-Schwinger equation, whose equivalent forms are:

$$|\psi\rangle = |\phi\rangle + \hat{\mathcal{G}}_0 \hat{V} |\psi\rangle \quad (2.36)$$

$$|\psi\rangle = |\phi\rangle + \hat{\mathcal{G}} \hat{V} |\phi\rangle \quad (2.37)$$

$$|\psi\rangle = |\phi\rangle + \hat{\mathcal{G}}_0 \hat{T} |\phi\rangle \quad (2.38)$$

where  $\hat{\mathcal{G}}$  and  $\hat{\mathcal{G}}_0$  are the retarded ( $\eta > 0$ ) propagators of the SE with and without the perturbation, respectively:

$$\hat{\mathcal{G}} = \lim_{\eta \rightarrow 0} \frac{1}{E - \mathcal{H} + i\eta}; \quad \hat{\mathcal{G}}_0 = \lim_{\eta \rightarrow 0} \frac{1}{E - \mathcal{H}_0 + i\eta} \quad (2.39)$$

and  $\hat{T}$  is the transition operator:

$$\hat{T} = \hat{V} + \hat{V}\hat{\mathcal{G}}_0\hat{T} \quad (2.40)$$

$$\hat{\mathcal{G}} = \hat{\mathcal{G}}_0 + \hat{\mathcal{G}}_0\hat{T}\hat{\mathcal{G}}_0 \quad (2.41)$$

The retarded propagator  $\hat{\mathcal{G}}$ , also called Green's function, describes the evolution of the outgoing solution.  $\hat{T}$  is sometimes referred to as the multiple scattering operator, and its representations are called the T-matrix. To solve the scattering problem in (2.38) one needs to determine the representations of either  $\hat{\mathcal{G}}$  or  $\hat{T}$ . To explain the physical meaning of  $\hat{T}$  we iterate equation 2.41 in infinite order (one is allowed to do that when the scattering is weak, i.e. in the EXAFS region):

$$\hat{T} = \hat{V} + \hat{V}\hat{\mathcal{G}}_0\hat{V} + \hat{V}\hat{\mathcal{G}}_0\hat{V}\hat{\mathcal{G}}_0\hat{V} + \dots \quad (2.42)$$

Consequently, the T-matrix describes the scattering on the potential  $\hat{V}$  at the infinite order (the  $n$  th term corresponds to the scattering process of order  $n-1$ ).  $\hat{T}$  pictures the effect of the ensemble of scatterers as a single unit. Note that the operators in (2.42) include the contributions from all the scatterers  $i$  in the cluster. More specifically one has:

$$\hat{T} = \sum_i \hat{t}_i + \sum_i \sum_{i_1 \neq i} \hat{t}_i \hat{\mathcal{G}}_0 \hat{t}_{i_1} + \sum_i \sum_{i_1 \neq i} \sum_{i_2 \neq i} \hat{t}_i \hat{\mathcal{G}}_0 \hat{t}_{i_1} \hat{\mathcal{G}}_0 \hat{t}_{i_2} + \dots \quad (2.43)$$

where the atomic multiple scattering operator  $\hat{t}_i$  is given by:

$$\hat{t}_i = v_i + v_i \hat{\mathcal{G}}_0 v_i + v_i \hat{\mathcal{G}}_0 v_i \hat{\mathcal{G}}_0 v_i + \dots \quad (2.44)$$

The expansion in (2.43) does not consider successive scatterings from the same atom  $i$ , as  $\hat{t}_i$  already accounts for the scatterings on  $v_i$  in infinite order (equation 2.44). At high kinetic energies  $E_0$  (EXAFS region) the series in (2.42) and (2.43) converge. Consequently, one can get  $\hat{T}$  by summing only the first terms in (2.42). This procedure is called the path expansion and it is employed by the codes specialized in the calculation of the extended region (for instance, the FEFF code [8]). At small  $E_0$  (the XANES region) the series diverges and the only way to get  $\hat{T}$  is to solve the matrix equation (2.41).

Due to the spherical symmetry of the problem, the resolution of (2.41) is performed onto the spherical harmonics basis. Subsequently, the free propagators  $\mathcal{G}_{0\,lm}^{ij\,l'm'}$  give the amplitude that a  $(l,m)$  wave issued on the scatterer  $i$  becomes of type  $(l',m')$  on the scatterer  $j$ :

$$\begin{aligned} \mathcal{G}_{0\,lm}^{ij\,l'm'} &= -4\pi i^{l-l'+1} \sum_{l'',m''} h_l^+(kr_{ji}) Y_{l''}^{m''}(\Omega_{ji}) \\ &\times \int d\Omega Y_l^m(\Omega) Y_{l'}^{m'}(\Omega) Y_{l''}^{m''}(\Omega) \end{aligned} \quad (2.45)$$

**Contractions in  $\tau$**  If the development in (2.31) is performed with real spherical harmonics, the T-matrix is symmetrical:  $\tau_{lm}^{l'm'} = \tau_{l'm'}^{lm}$ . Again, if no spin-orbit coupling, but by having used the complex harmonics in (2.31), one has  $\tau_{l,m}^{l',m'} = (-1)^{m+m'} \tau_{l',-m'}^{l,-m}$ . Either way, we draw attention upon the fact that  $\tau$  is not hermitian, i.e. it does not correspond to any observable.

## The Green function

The point in calculating the T-matrix is that it gives a complete description of the interacting system and can be used to calculate some more interesting quantities, such as the absorption cross section, the electronic DOS or the charge density. From now on we shall use  $\tau_{l,m}^{l',m'}(E)$ , the representation of the T-matrix in the spherical harmonics basis. We recall that in MST the final states are not calculated explicitly. Therefore, the use of the multiple scattering matrix avoids the complications arisen from the real space description of extended states.

The propagator  $\mathcal{G}$  and the multiple scattering matrix are closely related [116]:

$$\mathcal{G}_\sigma(\vec{r}, \vec{r}'; E) = \sum_{l,m} \sum_{l',m'} b_{l'}^\sigma(r', E) b_l^\sigma(r, E) Y_{l'}^{m'*}(\hat{r}') Y_l^m(\hat{r}) \tau_{l,m,\sigma}^{l',m',\sigma}(E) \quad (2.46)$$

or, equivalently:

$$\mathcal{G}_{lm\sigma}^{l',m',\sigma}(E) = \int dr \int dr' b_{l'}^\sigma(r', E) b_l^\sigma(r, E) \tau_{l,m,\sigma}^{l',m',\sigma}(E) \quad (2.47)$$

The purpose of calculating the propagator  $\mathcal{G}$  is that it provides the expectation value of any observable of the system. For an explicit link to the physical quantities, please refer to section 2.3.5. For real potentials the radial functions  $b_{l'}^\sigma(r', E)$  in (2.46) and (2.47) are real. We recall that if no spin-orbit coupling is involved,  $\mathcal{G}$  is diagonal in spin variables.

**The case of complex energies** The propagator changes its form if the scattering potential is complex. If this is the case, the radial SE has two admissible solutions and the MST formalism must account for both of them. If no spin-orbit coupling it has been shown [116] that:

$$\begin{aligned} \mathcal{G}_\sigma(\vec{r}, \vec{r}'; E) &= \sum_{l,m} \sum_{l',m'} b_{l'}^\sigma(r', E) b_l^\sigma(r, E) Y_{l'}^{m'*}(\hat{r}') Y_l^m(\hat{r}) \\ &\times \left( \tau_{l,m,\sigma}^{l',m',\sigma}(E) - \delta_{ll'} t_{l,m,\sigma}^{l',m',\sigma}(E) \right) - \sum_{l,m} t_{l,m,\sigma}^{l,m,\sigma}(E) \\ &\times s_l^\sigma(r_<, E) s_l^\sigma(r_>, E) Y_l^m(\hat{r}_<) Y_l^m(\hat{r}_>) \end{aligned} \quad (2.48)$$

where  $r_< = \min(r, r')$ ,  $r_> = \max(r, r')$ ,  $s_l$  the radial singular solution and  $t_{l,m}^{l',m'}$  is the atomic scattering matrix. In all cases  $t_{l,m}^{l',m'} = \delta_{ll'} t_{l,m}^{l',m'}$ , i.e.  $t$  is diagonal in  $l$ . If no spin-orbit coupling,  $t$  is equally diagonal in  $m$ . Note the absence of the complex conjugate factors in the first term of (2.48). For the spin-orbit case, please refer to the appendix.

### 2.3.4 The optical theorem

The optical theorem [37] connects the multiple scattering matrix element  $\tau_{l,m,\sigma}^{l',m',\sigma}(E)$  to the atomic amplitudes  $a^f(E)$ . This theorem is an expression of the conservation of the number of particles.

If no spin-orbit coupling, the optical theorem reads:

$$\left| \sum_f a_{l',m',\sigma}^{f*}(E) a_{l,m,\sigma}^f(E) \right| = -\Im \left( \tau_{l,m,\sigma}^{l',m',\sigma}(E) \right) \quad (2.49)$$

with  $f$  being the final states of the same energy  $E$ . Note that this form is valid only if the scattering potential is real.

When considering the spin-orbit coupling, but still in a real potential, the optical theorem becomes:

$$\Im \tau_{l,m+\frac{1}{2}-s,s}^{l',m'+\frac{1}{2}-s',s'}(E) = - \sum_f a_{l',m'+\frac{1}{2}-s',s'}^{f*}(E) a_{l,m+\frac{1}{2}-s,s}^f(E) \quad (2.50)$$

with  $f$  the final states of the same energy  $E$ .

If there is a spin-orbit coupling and if the potentials for the two spin populations are equal, one has:

$$\tau_{l,m,\sigma}^{l',m',\sigma'} = (-1)^{m+m'} \tau_{l',-m',-\sigma'}^{l,-m,-\sigma} \quad (2.51)$$

We draw attention to the fact that when considering the spin-orbit coupling spin-flip transitions are allowed, as the coupled  $|m, \uparrow\rangle$  and  $|m+1, \downarrow\rangle$  states carry opposite spins. Unlike the zero-coupling limit,  $\tau$  is no longer diagonal in the spin variables.

Note that (2.49) and (2.50) are valid whether one solves the electronic structure in the MST or in the FDM frames. For the former,  $\tau$  means the multiple scattering matrix, whereas for the latter only  $\Im \tau$  is obtained.

### 2.3.5 The physical quantities

The propagator in (2.46) and (2.47) gives access to all the one body physical quantities describing the system. For simplicity, in this section we shall discuss only the case of a real potential, within the limit of a zero spin-orbit coupling. For the similar quantities calculated in a complex potential, or including the spin-orbit coupling, please refer to the appendix.

We can easily get the density of states by taking the trace of the  $\mathcal{G}$  matrix:

$$\delta(E) = -\frac{1}{\pi} \sum_{\sigma} \Im \int d^3r \mathcal{G}_{\sigma}(\vec{r}, \vec{r}; E) \quad (2.52)$$

If no spin-orbit coupling, according to (2.52) and (2.47):

$$\delta(E) = -\frac{1}{\pi} \Im \int d^3r \sum_{lm\sigma} b_l^{\sigma}(r, E) \tau_{l,m,\sigma}^{l,m,\sigma}(E) b_l^{\sigma}(r, E) \quad (2.53)$$

For an atom, we are mostly interested in the representation of the occupation matrix in the spherical harmonics basis:

$$\rho_{l,m,\sigma}^{l',m',\sigma}(r) = -\frac{1}{\pi} \Im \int_{-\infty}^{E_F} dE b_{l'}^{\sigma}(r, E) \tau_{l,m,\sigma}^{l',m',\sigma}(E) b_l^{\sigma}(r, E) \quad (2.54)$$

The integral is taken over all the energies below the Fermi level  $E_F$ . We recall that:

$$\rho(r) = \sum_{\sigma} \int d\Omega \int d\Omega' Y_{l'}^{m'*}(\Omega') \rho_{l,m,\sigma}^{l',m',\sigma}(r) Y_l^m(\Omega) \quad (2.55)$$

The expectation value of the occupation number is obtained by taking the trace of the density of states matrix:

$$N = \int_{-\infty}^{E_F} dE \delta(E) = \int d^3r \sum_{lm\sigma} \rho_{l,m,\sigma}^{l,m,\sigma}(r) \quad (2.56)$$

The reformulation of the absorption cross section (2.13) gives [37, 81]:

$$\begin{aligned} \sigma(\omega) &= \frac{\pi\omega}{\epsilon_0 c} \left(\frac{e}{\hbar}\right)^2 \sum_g \sum_{\sigma} \sum_{lm} \sum_{l'm'} \Im \tau_{l,m,\sigma}^{l',m',\sigma'} \\ &\times \int dr \phi_g^{\sigma*}(r) O^*(\vec{\epsilon}, r) b_{l'}^{\sigma}(r) Y_{l'}^{m'}(\hat{r}) \int dr \phi_g^{\sigma}(r) O(\vec{\epsilon}, r) b_l^{\sigma}(r) Y_l^{m*}(\hat{r}) \end{aligned} \quad (2.57)$$

Note that if there is no spin-orbit coupling, the spin-flip processes are forbidden. Therefore, the summation over the spins is external. The fact that all the radial functions  $b_l(r, E)$  are real is a signature of the real potential. Identically, the structure factor (2.15), reformulated in the spherical basis, reads ( $\epsilon \rightarrow 0$ ):

$$\begin{aligned} f'(\omega) - if''(\omega) &= \frac{m\omega^2}{\hbar^2} \sum_{\sigma} \sum_g \sum_{lm} \sum_{l'm'} \int_{E_F}^{\infty} dE \frac{\Im \tau_{l,m,\sigma}^{l',m',\sigma'}}{\omega - (E - E_g) + i\epsilon} \\ &\times \int dr \phi_g^{\sigma*}(r) O^*(\vec{\epsilon}_{out}, r) b_{l'}^{\sigma}(r) Y_{l'}^{m'}(\hat{r}) \int dr \phi_g^{\sigma}(r) O(\vec{\epsilon}_{in}, r) b_l^{\sigma}(r) Y_l^{m*}(\hat{r}) \end{aligned} \quad (2.58)$$

## Chapter 3

# FDMNES and the one body picture

### 3.1 The structure of the FDMNES code

This section aims to describe the framework of FDMNES's calculation procedure (see figure 3.1). The details of the calculation steps are to be explained in the subsequent subsections.

**The space group symmetry analysis** FDMNES is a real-space code. Consequently, whether one deals with a molecule or with a periodic system, FDMNES builds a cluster of atoms around the absorber. If the cluster hosts two or more non-equivalent atoms (from the space group's point of view) of the absorbing species, several distinct calculations are conducted and one adds up the results.

**Building the cluster** One builds as many clusters as non-equivalent atoms. To get accurate results one must have a large enough calculation cluster. At the  $K$  edge, a cluster of about 8 Å is usually sufficient - one should check that by including extra atomic shells the form of the broadened spectrum remains the same. Note that at the  $L$  and  $M$  edges the convergence with respect to the radius is not necessarily faster, even if the  $d$  and  $f$  states are more localized than the  $p$  ones.

FDMNES is a symmetrized code: within the cluster, not all the atoms are solved, but only those which are non-equivalent in the magnetic point symmetry group of the central atom. Consequently, one can deduce the electronic structure of the rest, by applying the corresponding symmetry transformations (section 2.2.2). Note that this second symmetry analysis is completely separate from the one described above. The symmetrization procedure allows saving computation time: the more symmetric the material, the more calculation time and memory are saved.

#### 3.1.1 The atomic calculation

As input data, FDMNES only requires the atomic numbers and the positions of atoms. One should add the spin populations and the spin direction in the case of magnetic ordered materials. To begin with, we perform a self-consistent Dirac-Fock calculation of atomic densities and energies for all the chemical species of the atoms in

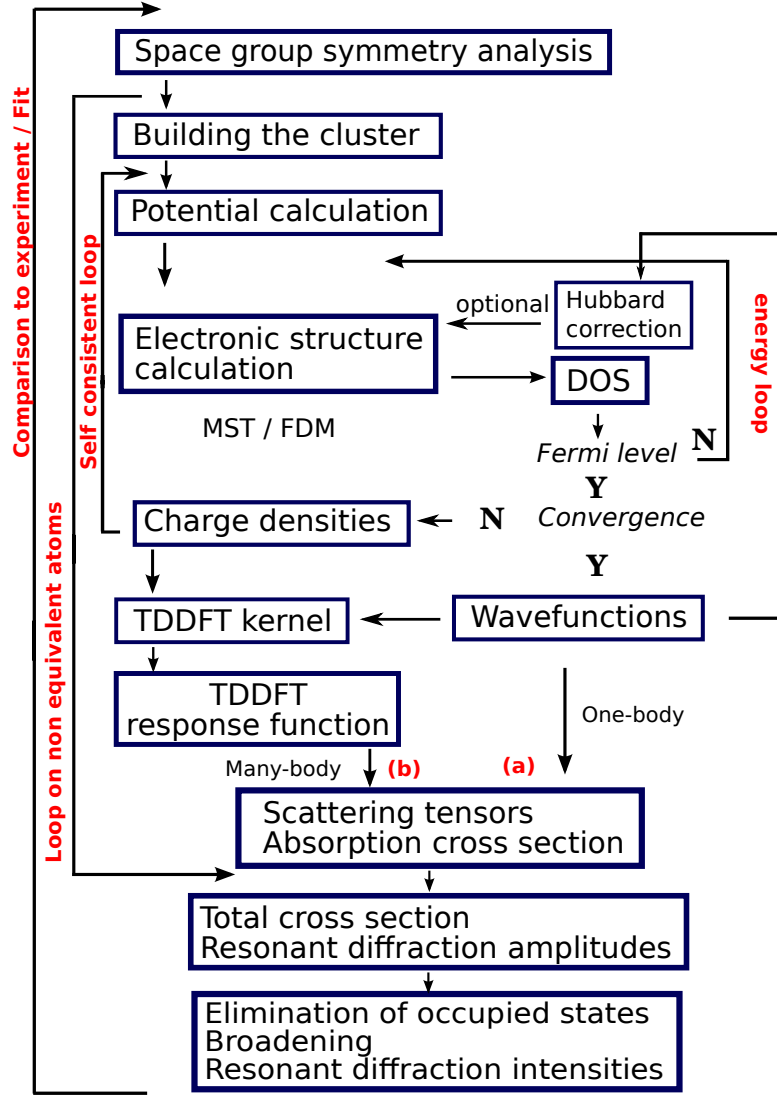


Figure 3.1: A simplified flow-chart of the FDMNES code

the calculation cluster. For the absorption calculation, we assume an excited electronic configuration for the absorbing atom. The default procedure is to place the core electron on the first available unoccupied level (we consider a full screening, according to the final state rule).

We use the atomic calculation to determine the initial state, i.e. the core level's wavefunction. The core states are deep, localized levels, thus there is no effective overlap between the ones belonging to adjacent atoms. Hence, the initial states have no band structure. We are therefore justified in describing the initial levels by using atomic wavefunctions.

For core levels, it is mandatory to introduce the spin-orbit coupling. Consequently, the eigenfunctions of the total Hamiltonian can no longer be characterized by the well known, atomic  $l$ ,  $m$ ,  $s$  and  $m_s$  quantum numbers, but may be indexed by  $l$ ,  $s$ ,  $j$  and  $m_j$ , where all notations obey the quantum mechanics standard (see, for instance, the

Table 3.1: The table contains the  $c_{\Lambda_g^\sigma}$  coefficients. When considering the spin-orbit coupling, the good quantum numbers that describe the electronic state are  $j$  and  $m_j$ . The  $c_{\Lambda_g^\sigma}$  coefficients connect this basis set to the one defined by  $l$ ,  $s$ ,  $m_l$  and  $m_s$ .

Initial state		$\sigma = 1/2$	$\sigma = -1/2$
1s, 2s	$j = 0, m_j = 0$	1	1
2p <sub>1/2</sub>	$j = \frac{1}{2}, m_j = -\frac{1}{2}$	$-\sqrt{\frac{2}{3}}$	$\sqrt{\frac{1}{3}}$
	$j = \frac{1}{2}, m_j = \frac{1}{2}$	$-\sqrt{\frac{1}{3}}$	$\sqrt{\frac{2}{3}}$
2p <sub>3/2</sub>	$j = \frac{3}{2}, m_j = -\frac{3}{2}$	0	1
	$j = \frac{3}{2}, m_j = -\frac{1}{2}$	$\sqrt{\frac{1}{3}}$	$\sqrt{\frac{2}{3}}$
	$j = \frac{3}{2}, m_j = \frac{1}{2}$	$\sqrt{\frac{2}{3}}$	$\sqrt{\frac{1}{3}}$
	$j = \frac{3}{2}, m_j = \frac{3}{2}$	1	0

dedicated chapter in reference [31]). This second basis  $|l, s, j, m_j\rangle$  can be obtained from the first one  $|l, s, m, m_s\rangle$  by an unitary transformation. We introduce the notations  $\chi_{1/2}$  and  $\chi_{-1/2}$  for the *up* and *down* spin wavefunction, respectively. The core level total (radial part included) wavefunctions  $\phi$  are of type:

$$\phi_g(r) = \sum_{\sigma} c_{\Lambda_g^\sigma} b_{\Lambda_g}(r) Y_{\Lambda_g}(\hat{r}) \chi_{\sigma} \quad (3.1)$$

where  $\Lambda_g^\sigma = (j, m_j)$  is the ensemble of quantum numbers describing the  $\sigma$  spin projection of the core state  $g$  and  $Y_{\Lambda_g} \equiv Y_{l_g}^{m_g}$  are the complex spherical harmonics.  $b_{\Lambda_g}(r)$  are the radial wavefunctions describing the core level. In practice, their dependence on  $m_j$  and  $\sigma$  is negligible and we shall consider it no further. Moreover,  $b_{\Lambda_g}(r)$  are always real quantities. The  $c$  coefficients (also called Clebsch-Gordon coefficients) correspond to the linear combinations in the above equations (see table 3.1).

For the  $K$  edge the core level has no dependence on the electron spin, nor on the angular variables:

$$\phi_{1s}^\uparrow(r) = \phi_{1s}^\downarrow(r) = \frac{1}{\sqrt{4\pi}} b_{1s}(r) \quad (3.2)$$

and the behaviour is similar for a  $L_1$  edge. The initial states for the  $L_2$  and  $L_3$  edges are twofold and, respectively, fourfold degenerated.

### 3.1.2 The potential calculation

To calculate the potential, one needs to know what is the charge distribution  $\rho_0(\vec{r})$  in the cluster. In a first approximation, one sums up all the individual, atomic charge densities  $|\Psi_0(r)|^2$  issued by the atomic self-consistent Dirac-Fock calculation (the so-called Mattheiss prescription [73]):

$$\rho_0(\vec{r}) = \sum_{i \in \text{cluster}} |\Psi_0^{(i)}(\vec{r})|^2 \quad (3.3)$$



The Poisson equation links the charge density to the potential  $v_H$  which generates it:

$$\frac{1}{r^2} \frac{d}{dr} \left( r^2 \frac{dv_H(r)}{dr} \right) = -4\pi\rho_0(r) \quad (3.4)$$

where we used the atomic units and assumed the spherical symmetry of both charge and potential.  $v_H$  is the Hartree, or the classical electrostatic potential. To get the total, one body scattering potential  $v$  we need to add some quantum mechanical correction  $v_{xc}$  that accounts for the exchange and the correlation effects, on one side, and for the inelastic scattering processes, on the other side:

$$v^\sigma(r, E) = v_H(r) + v_{xc}^\sigma(\rho_0^\uparrow(r), \rho_0^\downarrow(r), E) \quad (3.5)$$

where  $v_{xc}$  is suggested by Hedin, Lundqvist and Von Barth [51,52]. Their prescription was improved by Perdew and Wang [86], nevertheless this new parametrisation does not affect quantitatively the X-ray scattering potentials.

$V$  may be calculated separately for each spin. If any spin polarization (i.e.  $\rho_0^\uparrow(r) \neq \rho_0^\downarrow(r)$ ), the two spins scatter in two different effective potentials  $v^\uparrow \neq v^\downarrow$ . A magnetic ground state is an electron-electron driven correlation effect, and cannot emerge from a DFT calculation unless the breaking of the time reversal symmetry is described explicitly. In practice, this is done by imposing at the beginning different populations for the two spin channels, which gives  $v^\uparrow \neq v^\downarrow$ . Note that  $v_H$  has no spin dependence, as it issues from the classical theory.

Our exchange-correlation is described in a L(S)DA way: the corrective potential is local (i.e. it depends on the charge density at the very same point) and calculated in a simple model based on the homogeneous electron gas. Contrary to the Coulomb repulsion, the exchange-correlation correction is attractive (i.e.  $v_{xc} < 0$ ). Note that (3.5) is a mean field approximation for the electron-electron interactions in the system. No interaction with the nuclei has been considered, as  $|\Psi_0(\vec{r})|^2$  contains only the electronic charge distribution.

Hedin and Lundqvist [51] make a step beyond the LDA by considering the dependence of  $V_{xc}$  on the photoelectron's kinetic energy  $E$ . In a very simplified GW manner, they parametrize a self-energy correction which accounts for the inelastic scattering processes (mainly on plasmons) undergone by the photoelectron. The higher the kinetic energy, the lesser the probability that the photoelectron disturbs the electron cloud. Therefore the self-energy correction is positive, and applicable at the Fermi level and above.

### 3.1.3 Solving the radial Schrödinger equation

The radial solution of the SE is solved in the same way, whether one employs the MST or FDM methods. For spherical potentials with no spin-orbit coupling  $\tilde{b}_{lm}(r, E)$  does not depend on  $m$ . In this case the radial Schrödinger equation reads:

$$\left( -\frac{d^2}{dr^2} + V(r) - E + \frac{l(l+1)}{r^2} \right) u_l(r) = 0 \quad (3.6)$$

where  $u_l(r) = r\tilde{b}_l(r)$  is the solution of the radial SE, before the normalisation procedure. This equation admits two distinct solutions. Nevertheless, for real potentials, only

one of them is physical (the regular solution), whereas the second (the irregular one) diverges in  $r = 0$ . Note that for complex potentials this is no longer the case and both solutions are physically acceptable.

In practice, (3.6) is discretised within each atomic sphere and solved numerically. Next, the solutions are normalised according to the procedure described in the appendix. If relativistic effects are important, we solve the radial Dirac equation (see the appendix).

### 3.1.4 Solving the electronic structure

In practice we cut the wavefunction expansions in (2.31) and (2.33) at a maximum value  $l_{max} + 1$  of the  $l$  quantum number, which depends on the energy according to the rule:

$$\sqrt{l_{max}(l_{max} + 1)} = \sqrt{E} r_{MT} \quad (3.7)$$

where both the energy  $E$  and the muffin-tin radius  $r_{MT}$  are expressed in atomic units. Typical values of this cut-off are around 4 or 5 for up to 30 eV above the edge.

**The multiple scattering method** We use the spherical harmonics basis to represent all the operators. According to section 2.3.3, our procedure consists in calculating a multiple scattering matrix  $T_i$  for each atom in the cluster, where  $T = \sum_i T_i$ . We first calculate the atomic scattering matrix  $T_i$  in (2.44) and the free propagators  $\mathcal{G}_0^{ij l'm'}$  in (2.45).

Next we solve the following matrix equation in the  $(l, m)$  basis:

$$\hat{T}_i = [\hat{t}_i^{-1} - \hat{\mathcal{G}}_0]^{-1} \quad (3.8)$$

where the superscript indicates the inverse of the referred matrix. The MST calculation's most time demanding step is the matrix inversion required in (3.8), especially at high energies where the number of spherical harmonics considered when expanding the wavefunctions is increased (equation 3.7). In this case (100 eV above the edge or more) the path expansion (2.42) can be preferred.

We stress that although the MST requires non overlapping potentials, we get better results if we allow the MT spheres to overlap. This is a standard, although theoretically unjustified, procedure in the MST calculations community. It is primarily due to the fact that  $s$  and  $p$  orbitals' spatial range is wider than the MT radius. It is intuitive to understand that such a prescription allows a better treatment of the extended orbitals. Actually, it improves the description of the other orbitals also. Typically, FDMNES uses an overlap of 10 *per cent*.

**The finite difference method** In practice, the full potential method couples a MT sphere centred around the atoms, and whose radius is of the magnitude of an atomic unit, to an uniform mesh. We calculate the atomic amplitudes  $a_l(E)$  in every point of the mesh, and force the continuity with the solutions in the sphere. Subsequently, according to section 2.3.4, we can obtain the equivalent of the imaginary part of the multiple scattering matrix  $\Im\tau$ .

### 3.1.5 The tensor calculation

**The atomic tensors** Once  $\tau$  is available, we calculate the scattering tensors for each distinct (non-equivalent) absorbing atom in the cluster (equations 2.16, 2.17, 2.18) and for every energy. These differential tensors are necessary for the calculation of the XANES, RXD and XMCD spectra. At this step, we calculate the atomic spectra: we consider the polarisation terms and integrate over all the energies.

**The crystal tensors** We sum the atomic spectra over all the participating atoms. In the case of RXD, we multiply by the Bragg factors. Consequently, we obtain the total cross section and the RXD amplitudes.

### 3.1.6 The convolution

This step of the calculation is supposed to add some broadening to the XANES spectra and convolute the RXD amplitudes to get the total intensity on one hand, and to eliminate the occupied states according to (2.13), on the other hand.

The XAS spectrum in (2.13) requires the convolution with a lorentzian having an energy dependent width  $\Gamma(\omega)$  in order to account for the broadening due both to the core hole width  $\Gamma_{hole}$  and to the spectral width  $\gamma(\omega)$  of the final state:

$$\sigma^{conv}(\omega) = \int_{E_F}^{\infty} dE \sigma^{nonconv}(E) \frac{1}{\pi} \frac{\Gamma(\omega)}{\Gamma(\omega)^2 + (\hbar\omega - E)^2} \quad (3.9)$$

with

$$\Gamma(\omega) = \Gamma_{hole} + \gamma(\omega) \quad (3.10)$$

Here  $\sigma^{nonconv}(\omega)$  and  $\sigma^{conv}(\omega)$  are the unconvoluted and the convoluted absorption signal, respectively. In practice, one uses the standard, tabulated [60], edge dependent and energy independent (i.e. the screening is treated statically), values for  $\Gamma_{hole}$ . The energy dependence of the broadening is entirely due to  $\gamma$  and is a signature of the inelastic electron scattering phenomena. Note that  $\Gamma(E)$  is essentially a self-energy (equation 2.30) with no spacial dependence. We agree to set  $\gamma$  according to the arctangent model, an empirical model close to the Seah - Dench formalism [102]:

$$\Gamma(E - E_F) = \Gamma_{hole} + \Gamma_{max} \left( \frac{1}{2} + \frac{1}{\pi} \arctan \left( \frac{\pi \Gamma_{max}}{3 E_l} \left( e - \frac{1}{e^2} \right) \right) \right) \quad (3.11)$$

with

$$e = \frac{E - E_F}{E_{ctr}} \quad (3.12)$$

where  $E_F$  is the Fermi energy and the parameters describing the arctangent are: the total height  $\Gamma_{max}$ , the inflexion point  $E_{ctr} - E_F$  and the inclination  $E_l$  (figure 3.2). Their typical values for the K edge are 15 eV, 30 eV and 30 eV respectively. The deeper the edge, the larger the convolution. In figure 3.2, the inflexion point corresponds to the emergence of the plasmons. The energy scale is referenced to the Fermi level  $E_F$

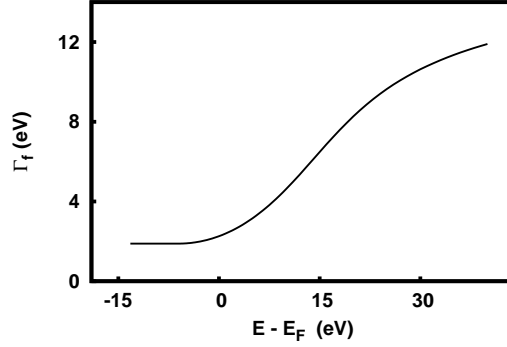


Figure 3.2:  $\Gamma$  has an arctangent-like form, centred at  $E_{ctr}$  and whose defining parameters are the slope  $\Gamma_{max}/E_l$  at  $E_{ctr}$  and the total height  $\Gamma_{max}$ .

whereas its zero points to vacuum energy. To have an indication on the energy of the photon, one should add the energy of the edge.

A similar procedure is used to obtain the RXD intensities from the corresponding amplitudes:

$$f'(\omega) - if''(\omega) = \frac{m\omega^2}{\hbar^2} \int_{E_f}^{\infty} dE \frac{\sum_g \sum_f \langle \phi_g | \hat{O}^\dagger(\vec{\epsilon}_{out}, \vec{r}) | \phi_f \rangle \langle \phi_f | \hat{O}(\vec{\epsilon}_{in}, \vec{r}) | \phi_g \rangle}{\omega - (E - E_g) + i\Gamma(E)} \quad (3.13)$$

We use the same  $\Gamma$  as the one for the XAS broadening, but we evaluate it at the photoelectron's energy  $E$ . The effect of  $\Gamma$  in (3.13) is no longer a broadening, like in the XAS case. The RXD spectrum is due to a coherent scattering process. The effect of the final state's finite lifetime (or width) is that it destroys this coherence. Consequently, the larger the  $\Gamma$  factor, the smaller the diffracted intensity (the surface below the curve diminishes).

Contrary to the convolution of the spectrum in (2.13), the convergence of (3.13) over the energies is sometimes extremely slow (for instance, the  $K$  edges). To overcome this problem, one uses the imaginary part of  $f(\omega)$  extrapolated to the atomic form factor up to 10000 eV above the highest calculated energy.

In the (1.3) and (3.13) summations over the states only unoccupied states appear. Consequently, one must eliminate the contribution of all  $\Psi_g^{(j)}$  corresponding to states whose energies are below the Fermi energy. The sum over the final states in (1.3) becomes:

$$\sum \equiv \int_{E_F}^{\infty} dE \sum_f \quad (3.14)$$

with  $f$  being the final states of the same energy  $E$ . In some cases the lower limit of this integral is different from the Fermi energy  $E_F$ , as we show in chapter 4.

**Interpretation of complex potentials** Numerically, one can prove that performing the convolution of (3.9) on the output of a real potential calculation is identical to the unconvoluted result for the equivalent complex energies calculation (i.e. the imaginary

part of the potential is equal to the  $\Gamma$  broadening of the former) in the limit  $E_F \rightarrow -\infty$ . Therefore the use of a complex potential is a synonym to the taking into account of some inelastic photo-electron scattering mechanisms which leads to damping (the self-energy correction, according to section 2.3.1).

### 3.1.7 Miscellaneous aspects

**Real versus complex spherical harmonics** From a computational point of view, it is often interesting to replace the standard, complex spherical harmonics  $Y_l^m$  with the real ones. The latter take half the memory space required by the former. The real harmonics are obtained as a linear combination of the complex ones:

$$Y_l^m|_{real} = \begin{cases} Y_l^m & , m = 0 \\ \frac{1}{\sqrt{2}} (Y_l^m + (-1)^m Y_l^{-m}) & , m > 0 \\ -\frac{i}{\sqrt{2}} (Y_l^{-m} - (-1)^m Y_l^m) & , m < 0 \end{cases}$$

We are allowed to use this unitary transformation under several restrictions. The expansions in (2.32) and (2.33) are no longer valid if the real harmonics basis is employed. Therefore, if one takes into account the spin-orbit coupling, one needs to work with the complex spherical harmonics. Secondly, if the calculation is not symmetrised (i.e. simplified thanks to the symmetry operations of the point group of the absorbing atom, according to the paragraph in the beginning of this section) we are allowed to use either the real or the complex harmonics in (2.31). We are equally allowed to do such if all the representations of the symmetrised calculation have a real character. In the opposite case of complex representations (for instance point groups containing the  $C_3$  symmetry operation) the use of complex harmonics in (2.31) is compulsory.

**The energy of the core level** For bulk and simple materials, the edge energies are well known, tabulated quantities [121]. When the very same absorbing chemical species is part of another compound, the different atomic environment induces a shift of the absorbing edge with respect to its tabulated value.

FDMNES estimates the value of the Kohn-Sham energy of the core level, by using the total potential  $V$  calculated above:

$$E_{edge} = \langle \psi_g | E_{kin} + V_{core} | \psi_g \rangle \quad (3.15)$$

where the  $V_{core}$  is the total electrostatic potential (including the attraction of the nucleus) at the core level and  $E_{kin}$  the kinetic energy.

## 3.2 Application: magnetic and orbital ordering in NdMg

### 3.2.1 The context of the study

At low temperatures, the  $4f$  electron cloud of the rare earths may lose its spherical symmetry and distort in the presence of crystal fields, provided  $L_{4f} \neq 0$ . This distortion can be described in terms of  $4f$  electric quadrupoles. Consequently, the electric quadrupolar moment becomes an order parameter and below the critical temperature

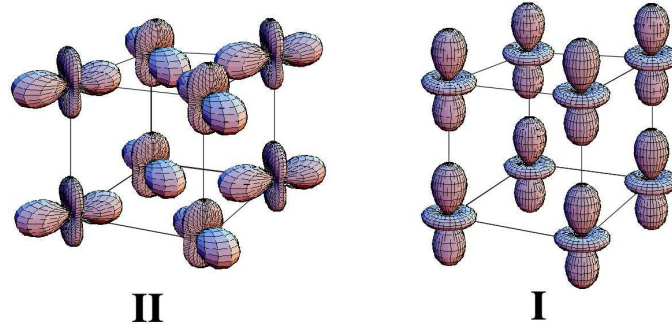


Figure 3.3: Sketches of the quadrupolar arrangement in NdMg. In phase I, between  $T_N = 61$  K and  $T_R = 35$  K, the single- $\mathbf{k}$  collinear antiferromagnetic structure is associated with a ferroquadrupolar arrangement of the quadrupolar moment. Below  $T_R$  in phase II, the double- $\mathbf{k}$  structure is associated with the antiferroquadrupolar arrangement. This figure was taken from reference [23].

one speaks of quadrupolar ordering. This ordering has either the periodicity of the lattice (ferroquadrupolar order) or forms a superlattice (antiferroquadrupolar order). When incidental to Jahn Teller distortions in insulator phases, the mechanism of the breaking of symmetry is mediated by the lattice (see chapter 7). In the metallic phases as the NdMg, the breaking of symmetry is a consequence of the indirect exchange.

The quadrupolar ordering cannot be identified straightforwardly by neutron studies, as neutrons are not sensitive to the charge cloud. In this chapter we will be investigating the alternative of the X-ray measurement, in terms of appropriateness for the study of quadrupolar ordering. NdMg is a suitable model compound for this purpose.

The quadrupolar ordering in NdMg was already identified by means of non-resonant X-ray techniques [2]. We recall that the non-spherical Thomson scattering signal is weak, thus delicate to measure. Before concluding on the appropriateness of the X-ray techniques for the study of quadrupolar ordering, one should consider working in the resonant regime, which enhances the diffraction signal. One chose to work at the  $L_{2,3}$  edges of neodym. Under these conditions the  $4f$  quadrupoles are not probed directly, but *via* their coupling to the  $5d$  states.

The quadrupolar ordering generally involves a magnetic ordering. In NdMg, the magnetism is due to the neodym atoms. Below the Néel temperature  $T_N = 61K$ , the consequent antiferromagnetic ordering drives a magnetostriction induced, tetragonal symmetry lowering with  $(a - c)/a < 1$ . At  $T_R = 35K$  a second phase transition occurs, and the magnetic structure becomes double- $\mathbf{k}$  (see figure 3.3). In the first phase, the antiferromagnetic structure is associated with a ferroquadrupolar arrangement of the electric quadrupoles. In the second phase, the double- $\mathbf{k}$  magnetic structure is associated with the antiferroquadrupolar placement of quadrupoles (see figure 3.3) and with a magnetoelastic strain of opposite sign  $(c - a)/a < 1$  [1]. In the first phase, the spins are vertical, whereas in the second one they lie in the horizontal plane.

The diffraction experiments were carried out at the ESRF-Grenoble on the ID20 beamline by R.M. Galéra and collaborators. For the details of the experimental setup please refer to reference [23]. The object of the study is the second low-temperature phase of NdMg. The measured reflections are of type  $(h/2 \ k \ l/2)$  and  $(h \ k \ l/2)$ , whose

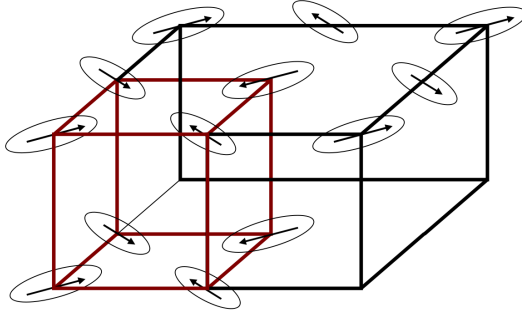
origins are quadrupolar and magnetic, respectively.

The tetragonal distortion is too small to allow the identification of the several magnetic domains, within the experimental resolution. In other words, one cannot resolve the three corresponding k-space spots for a given scattering vector. One therefore expects that the  $(h \ k \ \frac{l}{2})$  measured intensities come from the  $D_{xz}$  and from the  $D_{yz}$  domains, whereas the  $(\frac{h}{2} \ k \ \frac{l}{2})$  intensity is due to the  $D_{xz}$  exclusively.

### 3.2.2 Tensor analysis

In the following we will apply the prescriptions in sections 2.2.1 and 2.2.2 to the study of the azimuthal dependence of the RXD reflections in NdMg. Unless specified otherwise, we will be referring only to the  $D_{xy}$  domain, i.e. the magnetic moments lie in the xOy plane. The reflections revealing the magnetic ordering are of type  $(\frac{h}{2} \ 0 \ 0)$  and  $(0 \ \frac{k}{2} \ 0)$ . The quadrupolar reflections are of type  $(\frac{h}{2} \ \frac{k}{2} \ 0)$ . For convenience, we shall leave out from our discussion the more general  $(\frac{h}{2} \ k \ l)$  and  $(h \ \frac{k}{2} \ l)$  reflection (they can be treated in a similar way). To get the corresponding experimental indexes, one should perform the necessary circular permutations.

Figure 3.4: A sketch of the unit cell in NdMg. Only the Nd atoms have been considered, by using oriented arrows to describe spins and rounded, ex-centric shapes to model the electric quadrupoles. The quadrupolar order spans with the  $(\frac{1}{2} \ \frac{1}{2} \ 0)$  propagating vector, whereas the magnetic one is described by two propagating vectors:  $(\frac{1}{2} \ 0 \ 0)$  and  $(0 \ \frac{1}{2} \ 0)$ . The table contains the positions and symmetry operations that connect the equivalent atoms in the unit cell of NdMg.  $E$  stands for the identity,  $C_{4z}$  means a  $\pi/2$  rotation around the Oz axis and  $T$  stands for time reversal.



j	$\vec{R}_j$	Op. sym.
1	0 0 0	E
2	1 0 0	$C_{4z}$
3	0 1 0	$TC_{4z}$
4	1 1 0	TE

Figure 3.4 shows the symmetry operations that connect, in the unit cell of NdMg, the atoms in the plane where the magnetic moments lie. Let us consider the magnetic domain where the spins lie in the plane xOy. The corresponding magnetic point group is  $mtm\bar{m}$  and according to (2.24) the atomic, symmetry reduced tensor in the crystal basis set gives:

$$D = \begin{pmatrix} a & c & \text{id} \\ c & a & -\text{id} \\ -\text{id} & \text{id} & b \end{pmatrix} \quad (3.16)$$

The energy dependent components: a, b, c and d, are real numbers. We can note for instance that, as  $D_{xy} - D_{yx} = 0$  for all energies, the atomic orbital momentum along the Oz axis is zero.

We use (2.25) and (3.16) and the prescriptions in section 2.2.2, given the symmetry information in figure 3.4. We are led to the following form for the crystal tensor:

$$\mathcal{D} = 4 \begin{pmatrix} a & 0 & 0 \\ 0 & a & 0 \\ 0 & 0 & b \end{pmatrix} \quad (3.17)$$

In the same way the following forms are obtained for the amplitudes  $A^{(j)}$  for the  $(\frac{h}{2}00)$  and the  $(\frac{h}{2}\frac{k}{2}0)$  reflections:

$$A_{\frac{h}{2}00}^{(j)} \propto \epsilon_{out}^\dagger \begin{pmatrix} 0 & 0 & 0 \\ 0 & 0 & -4id \\ 0 & 4id & 0 \end{pmatrix} \epsilon_{in} \quad (3.18)$$

$$A_{\frac{h}{2}\frac{k}{2}0}^{(j)} \propto \epsilon_{out}^\dagger \begin{pmatrix} 0 & 4c & 0 \\ 4c & 0 & 0 \\ 0 & 0 & 0 \end{pmatrix} \epsilon_{in} \quad (3.19)$$

We draw the attention upon the fact that (3.18) and (3.19) involve only one value among the atomic tensor's elements. This implies that the global shape of the angular dependence is energy independent. The angular dependence gives a hint of the energy *via* an energy dependent multiplicative factor.

The components of the tensor in (3.18) being purely imaginary confirm the fact that the  $(\frac{h}{2}00)$  reflections are magnetic. In (3.19) the components of the tensor are real, thus the reflections at the  $(\frac{h}{2}\frac{k}{2}0)$  nodes are electrical. We note that the class of  $(0\frac{h}{2}0)$  reflections is equivalent to the  $(\frac{h}{2}00)$  ones as the site has the  $C_{4z}$  symmetry. Therefore in order to obtain its tensor amplitude it is enough to refer to (3.18) and perform the corresponding symmetry operations.

The tensor approach allows us to understand how the extinction of certain reflections appears for a specific combination between the incoming and the outgoing polarizations. For instance, the amplitude of the magnetic  $(\frac{h}{2}00)$  reflections in the  $\sigma - \sigma$  configuration gives (see equation 3.18):

$$\begin{pmatrix} 0 & -\sin \Psi & -\cos \Psi \end{pmatrix} \begin{pmatrix} 0 & 0 & 0 \\ 0 & 0 & -4id \\ 0 & 4id & 0 \end{pmatrix} \begin{pmatrix} 0 \\ -\sin \Psi \\ -\cos \Psi \end{pmatrix} = 0$$

where  $\Psi$  is the azimuthal angle. The experiment confirms the extinction of this specific reflection. The same reflection in the  $\sigma - \pi$  configuration is isotropic with respect to the azimuthal angle:

$$\begin{pmatrix} \sin \theta & \cos \theta \cos \Psi & -\cos \theta \sin \Psi \end{pmatrix} \begin{pmatrix} 0 & 0 & 0 \\ 0 & 0 & -4id \\ 0 & 4id & 0 \end{pmatrix} \begin{pmatrix} 0 \\ -\sin \Psi \\ -\cos \Psi \end{pmatrix} = 4id \cos \theta$$

where  $\theta$  is the Bragg angle. The lack of azimuthal dependence of the  $(\frac{h}{2}00)$   $\sigma - \pi$  reflection is in perfect agreement with the experimental observations. Note that the



$\sigma - \pi$  polarisation configuration does not necessarily yield the same results as the  $\pi - \sigma$  one. While the  $\sigma$  polarization is invariant, the  $\pi$  one has different forms for the incoming and outgoing cases. We obtain a periodicity of  $\pi$  for the  $(\frac{h}{2}\frac{k}{2}0)$   $\sigma - \pi$  reflections:

$$\begin{aligned} & (\sin \theta \cos \alpha - \cos \theta \sin \alpha \cos \Psi \quad \sin \theta \sin \alpha + \cos \theta \cos \alpha \cos \Psi \quad -\cos \theta \sin \Psi) \cdot \\ & \begin{pmatrix} 0 & 4c & 0 \\ 4c & 0 & 0 \\ 0 & 0 & 0 \end{pmatrix} \begin{pmatrix} \sin \Psi \sin \alpha \\ -\sin \Psi \cos \alpha \\ -\cos \Psi \end{pmatrix} = c(-4 \cos 2\alpha \sin \Psi + \cos \theta \sin 2\alpha \sin 2\Psi) \end{aligned}$$

with  $\alpha = \arctan(h/k)$

The calculations described above (diffraction amplitudes, crystal tensor, azimuthal dependence) are implemented in the FDMNES code and performed automatically. In comparison to the analytical calculations, the numerical ones provide the exact value of the atomic tensor components (a, b, c, d). For a single domain sample, this would allow a quantitative analysis of the angular dependence.

All the calculations in this section were validated by the experimental data. We cannot possibly know the distribution of the magnetic domains in the sample. Therefore, a quantitative analysis of the azimuthal dependence of the measured reflections is impossible.

### 3.2.3 Results

All calculations were performed with the FDMNES code: the magnetic reflections were calculated in the MST, whereas the FDM was used to simulate the quadrupolar ones. In rare earth compounds the spin-orbit coupling is essential and one cannot neglect it. On the other hand, FDM calculations including the spin-orbit coupling are extremely time consuming (several months for a small cluster calculation of NdMg). We were therefore forced to calculate the magnetism in the MST frame. The MST calculations were performed on a 8Å cluster, i.e. 65 atoms. The shortcoming of the MST is that it cannot describe the quadrupolar electric moment, which is erased in the MT approximation. We thus conducted the quadrupolar reflections calculations in the FDM, which is the ideal method for the situations where the non-sphericity plays an important role.

In NdMg, the final states of the dominant E1-E1 transitions at the neodymium  $L_{2,3}$  edges are the  $5d$  conduction band states. Consequently, the single particle approximation in FDMNES should be sufficient to describe the physics of the system. On the other hand, the energy positions of the peaks corresponding to the E2-E2 transitions to the  $4f$  localized states are satisfactory, but not their intensities.

The antiferroquadrupolar ordering of the  $4f$  electric quadrupolar moments introduces a periodic perturbation of the potential that affects the  $5d$  final states and gives rise to the resonant scattering at the  $(\frac{h}{2}0\frac{l}{2})$  nodes in the reciprocal space. The existence of the  $4f$  electric quadrupolar moment should be described through a convenient breaking of the  $4f$  orbital symmetry. This breaking of symmetry is driven by the correlation. More specifically, it is an effect of the crystal fields and cannot emerge naturally from a DFT calculation. Therefore, the breaking of symmetry must be described as an input of the calculations.

As far as the FDM calculations are concerned, the degeneracy is removed by imposing a specific extra population to a  $4f$  orbital, provided it possesses an axial symmetry along the local direction of the quantization axis defined by the local magnetic moment. The Coulomb repulsion of this non-spherical extra electric charge breaks the local symmetry and splits the  $5d$  levels. To obey the axial symmetry constraints, we chose the  $m_{4f} = 0$  orbital and rotated it to align it to the direction of the spins (see figure 3.3). Calculations were run on a cluster of radius 4 Å, centered on the absorbing atom and containing the first two neighboring shells *i.e.* 15 atoms. An extra population of 0.15 electrons was imposed on the  $m_{4f} = 0$  orbital but no magnetic information was introduced into the calculations.

To align the calculated and experimental spectra, we shift the former until the threshold position of the measured and theoretical absorption spectra coincide. We use the same energy shift for all the RXD spectra.

In the MST calculations the description of the magnetic arrangement is an input information, but no explicit description of the antiferroquadrupolar arrangement is given. Nonetheless MST calculations predict a scattered signal at the  $(\frac{h}{2}0\frac{l}{2})$  quadrupolar nodes, in the  $\pi - \pi$  channel. The magnetic scattering, that occurs only in the rotated  $\pi - \sigma$  or  $\sigma - \pi$  channels, is forbidden at these nodes. Such a result is quite unexpected, as in the MT approximation the electric potential is forbidden any asphericity. When the spin-orbit coupling is eliminated from the MST-MT calculations, no scattering at the quadrupolar nodes is predicted. One thus ascribes the emergence of this scattering to the spin-orbit coupling. The spin-orbit coupling enables the prediction of the non-spherical effects by means of the coupling of the magnetic moment to the electronic distribution. Figure 3.5 shows the  $L_2$  edge energy dependence of the calculated scattered signal at the  $(-\frac{1}{2}0\frac{5}{2})$  node in the  $\pi - \pi$  channel, within the MST-MT and FDM approaches. The global shape of the two spectra is the same, at both edges. In terms of intensities, the MST spectrum is underestimated by several orders of magnitude. This can be understood by the fact that the  $4f$  quadrupolar charge scattering (not described in the MST-MT) is several orders of magnitude stronger than the magnetic scattering implied by the spin-orbit coupling.

The experiment shows that the magnetic scattering occurs only in the rotated  $\pi - \sigma$  and  $\sigma - \pi$  channels, which is consistent with the analysis in section 3.2.2. The form of the measured magnetic spectra seems to depend on the edge and on the specular / off-specular character of the reflection. In figures 3.6 and 3.7 we show an example of each. For this specific experimental setup [23], the reflection  $(00\frac{5}{2})$  is specular, whereas  $(-\frac{1}{2}03)$ ,  $(\frac{1}{2}03)$  and  $(\frac{0}{5}02)$  are off-specular.

The spin-orbit MST calculations provide a qualitative interpretation of the measured reflections, but fail to reproduce the quantitative aspects (figures 3.6 and 3.7). At the  $L_3$  edge, in order to simulate the experimental peak at 6206 eV in the specular reflections, one has to lower the cut-off energy 2 eV down from the self-consistently calculated cut-off level. In the calculations, the appearing structure is unambiguously assigned to the E2-E2 electric quadrupole transitions towards the  $4f$  states. We recall that when many-body effects are present the concept of Fermi level loses its significance and a best description could be obtained by adjusting the cut-off energy. This is a reasonable procedure in the present case. While for the off-specular reflections no change occurs in the structure of the spectra, the peak of E2- E2 origin in the specular reflections

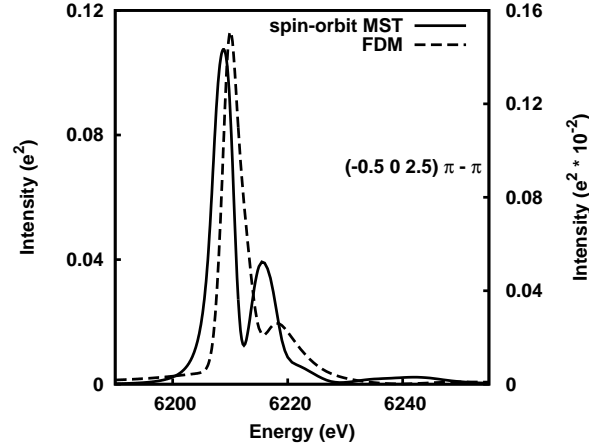


Figure 3.5: The calculations of the  $(-\frac{1}{2}0\frac{5}{2})$  quadrupolar reflection. The FDM spectrum (dashes) is issued from a non-magnetic calculation where the  $4f$  distortion was described explicitly. The spin-orbit MST calculation does not take into account the asphericity of the electron cloud. The common effect of the antiferroquadrupolar ordering and of the spin-orbit coupling is that they break the degeneracy of the  $4f$  electron cloud. Note that there is a difference of two orders of magnitude between the two: the charge scattering is stronger than the magnetic one.

is clearly resolved at the  $L_3$  and  $L_2$  edges, after having adjusted the cut-off level. Although the single particle approaches are not adapted to describe strongly correlated electrons, the reasonable agreement with the experiment allows to definitively ascribe the peaks observed at 6206 and 6715 eV in the spectrum of the  $(00\frac{5}{2})$  reflection to the E2-E2 electric quadrupole transitions.

The non-negligible intensity measured far below the  $L_{2,3}$  edges for the off-specular reflections is due to the interference between the non-resonant magnetic and non-spherical Thomson terms. The latter is not included in the FDMNES calculations, and thus the pre-edge background is absent from the calculations. The broad structure observed at both edges at  $\approx 6 - 7$  eV below the  $E_0$  peak in the energy spectra for the off-specular reflections is completely missing from the calculations. In our calculations, no available  $f$  or  $p$  states are calculated at this position in energy. The origin of the structure remains unclear, and we suspect it is an experimental artefact due to a misalignment issue.

The quantitative aspect of the agreement with the experiment for the magnetic reflections, in terms of calculated intensities, is particularly ill-suited. This is not entirely due to the many-body effects, but to the unknown domain distribution. For the two contributing magnetic domains, the polarization (azimuthal) conditions are not the same, for a given illumination. This is disturbing, provided the azimuthal dependence of a certain reflection is strong - the case of the off-specular reflections. Concerning the specular reflections, the calculations predict no azimuthal effect (see section 3.2.2 for an analytic proof).

Figure 3.8 shows the energy spectra of the  $(-\frac{1}{2}0\frac{5}{2})$  quadrupolar satellite in phase II at the neodym  $L_{2,3}$  absorption edges. In the  $\pi - \pi$  channel the quadrupolar scattering

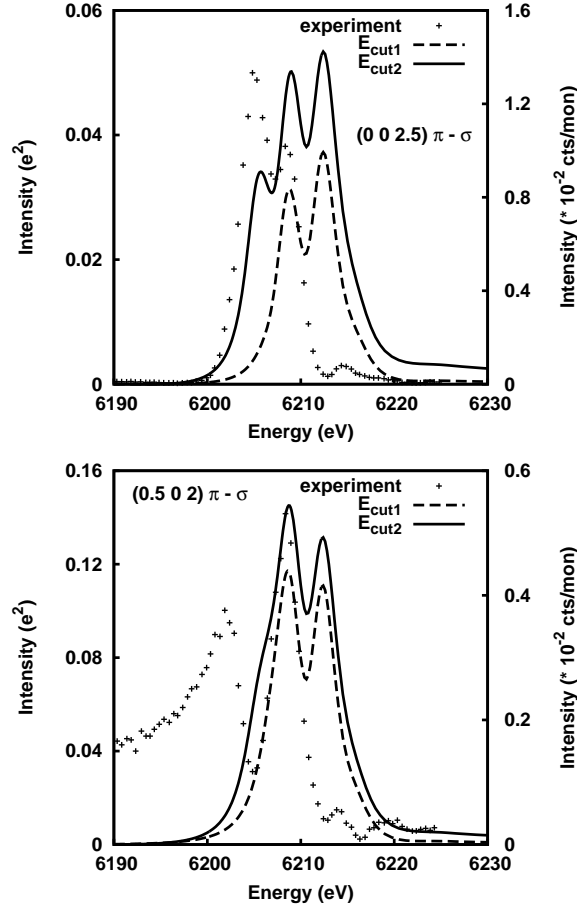


Figure 3.6: The magnetic specular (above) and off-specular (below) reflections at the  $L_3$  edge: calculations *versus* experiment. Two different cut-off energies were employed: the self-consistent Fermi level (dashes) and a cut-off shifted down by 2 eV from the previous value (solid).

presents a single-peak resonant structure centered around  $\approx 6724$  and  $\approx 6212$  eV for the  $L_2$  and  $L_3$  edges, respectively. Experimentally, the intensities at the  $L_2$  and  $L_3$  edge are not comparable. The statistics at the  $L_3$  edge are not very accurate, which could be a reason for the mismatch between the broadening of the experimental and calculated spectra. It appears clearly that the RXD may be used to investigate the quadrupolar ordering.

Quadrupolar scattering is straightforwardly related to the  $4f$  orbital asphericity, thus it is expected to be more intense than the magnetic scattering. However the experiment is observed to be one order of magnitude smaller. This discrepancy probably arises from an unfavorable domain partition in the probed surface crystal.

### 3.2.4 Conclusions

The present experimental and theoretical study of RXD at the  $L_{2,3}$  absorption edges of neodym confirms the existence of resonant scattering signals at the reciprocal space

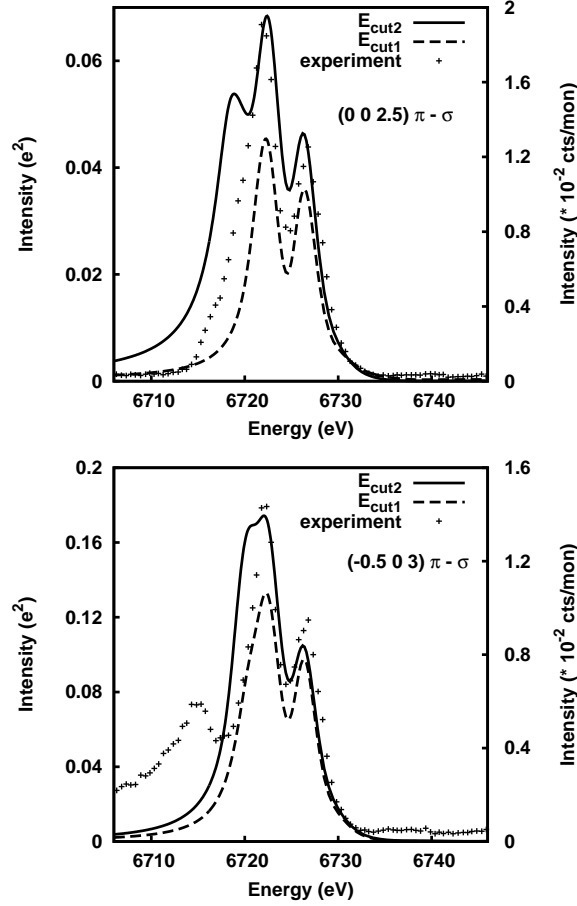


Figure 3.7: The magnetic specular (above) and off-specular (below) reflections at the  $L_2$  edge: calculations *versus* experiment. Two different cut-off energies were employed: the self-consistent Fermi level (dashes) and a cut-off shifted down by 2 eV from the previous value (solid).

positions associated with both the magnetic and the quadrupolar orderings in phase II of the NdMg compound. Experimentally, the polarization and azimuth dependencies of the  $(\frac{h}{2}0\frac{l}{2})$ -type satellites are fully consistent with the antiferroquadrupolar ordering in NdMg, ordering that was previously evidenced in non-resonant conditions. The calculations of the resonant quadrupolar scattering performed using the finite differences method predict the one peak structure of the energy spectra, the polarization and azimuth dependencies in noteworthy agreement with the observations.

The energy dependence of the magnetic satellites presents a multi-peak structure that depends on the edge and on the specular and off-specular character of the reflection. MST-MT calculations including the spin-orbit coupling allow these spectra to be interpreted. The E1-E1 electric dipole transitions toward the  $5d$  states give rise to the two peaks at and above the edge energy. Though the single particle approaches are not adapted to describe strongly correlated electrons, the position in energy of the E2-E2 electric quadrupole transitions toward the  $4f$  states in the calculated spectra is consistent with the experimental observations at least at the  $L_3$  edge.

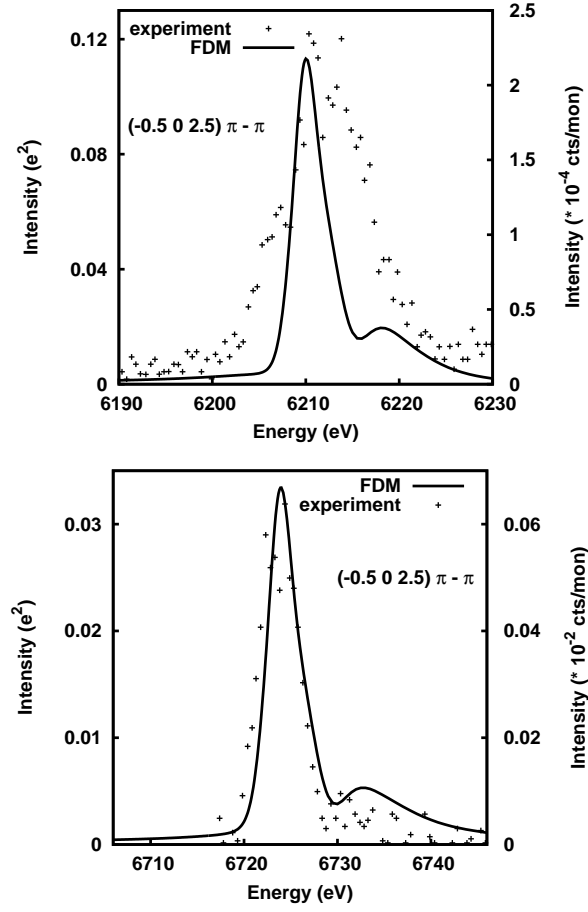


Figure 3.8: Experimental and FDM calculated spectra of the  $(-\frac{1}{2} 0 \frac{5}{2})$  quadrupolar reflection, at the  $L_3$  (above) and  $L_2$  (below) edges of neodymium.

One must nevertheless admit that the quantitative agreement between the calculations and the experiment is not satisfactory. These calculations could benefit from the inclusion of the spin-orbit coupling in the FDM calculations, which for the time being is prohibited for extended systems and within reasonable calculation times. One should equally tempt calculations behind the one body picture, which is obviously unsuitable to describe the correlated  $4f$  orbitals of the neodymium.



## Chapter 4

# The self-consistent procedure

### 4.1 Motivation

Given today's state of art of electronic structure calculations we feel that a reliable X-ray absorption calculation needs to support a self-consistent procedure. It is not customary for real space, MST absorption calculations to be self-consistent. Actually, FDMNES is the only self-consistent real-space code besides FEFF [8]. Whether the self-consistent results are better than the non self-consistent ones (and, eventually, to what degree) is another issue, that we will address later. In our view the development of a self-consistent procedure is not a goal in itself, but a layer to support further implementations. For instance, to perform a LSDA+U calculation one is required to know the occupation numbers for the correlated orbitals involved. Of even greater importance is the fact that we need a reliable procedure of counting the electrons in the cluster in order to determine the Fermi level in an unambiguous way. This feature emerges naturally provided one benefits from a self-consistent calculation scheme.

In the acceptance of the electronic structure calculation community, a self-consistent procedure consist in solving a non-linear equation (the mean field SE) by iteration. In other terms, we iterate on a certain ensemble of charge distributions in the cluster, until we are certain that the potential they generate is the closest to the real one. We recall that the default procedure is to calculate the potential starting from the superposition of the atomic charge densities in the cluster (see section 3.1.2). What self-consistency does is that beginning with the second iteration, the potential is calculated based on the charge density that was calculated at the previous iteration. After convergence, we should obtain a better potential than the one obtained with the Mattheiss prescription [73].

A more profound meaning of the self-consistency can be found in the very SE (in Hartree units):

$$\left(-\frac{1}{2}\nabla^2 + \hat{V}\right)|\Psi\rangle = E|\Psi\rangle \quad (4.1)$$

whose self-consistent feature is given by the fact that  $\hat{V}$  depends on  $|\Psi|^2$  (the cluster potential depends on the electronic density). This problem can be solved iteratively: we make a first assumption on  $\hat{V}$  (the Mattheis prescription), we solve the SE to get  $|\Psi\rangle$ , we calculate the new  $V = V[n]$  where the density  $n$  is directly linked to  $|\Psi|^2$ , we



Screening scheme	SCF cycle	Absorption calculation
(a) $\equiv$ SCF non-excited	<b>✗</b>	<b>✗</b>
(b) $\equiv$ SCF excited	<b>✓</b>	<b>✓</b>
(c) $\equiv$ SCF hybrid	<b>✗</b>	<b>✓</b>

solve again the SE etc.

In principle, the self-consistent procedure is mandatory in order to assure the relevance of the mean field solution of the exact Hamiltonian (in our case, the solution of the Kohn-Sham equations of the DFT in the local approximation). In this chapter, we will address the question whether the self-consistent loop is equally important from a practical point of view.

## 4.2 Implementation

The self-consistent procedure is independent of the actual method of resolution of the SE (MST or FDM in our case). Whatsoever, at the time being, the FDMNES self-consistency is performed strictly in the MST. We shall come back later to the reasons for this choice.

The details of the implementation are as follows. FDMNES self-consistency consists of two main steps. First we iterate to obtain the correct electronic density, in MST. Second, we perform a last iteration which calculates the absorption spectra (2.13), in either the MST or the FDM approach. We note that the cluster's radius for this last calculation is not necessarily the same as the one used in the previous step. In particular we can be interested in running an absorption calculation at a larger radius than the one used in order to get the electronic density in a self-consistent way.

We distinguish between three ways of performing the self-consistent procedure, which we will further reference by (a), (b) and (c), respectively. Scheme (a) assumes a non-excited electronic configuration for the absorber during the entire calculation (the ground state configuration). The second possibility (b) is to assume an excited absorber, i.e. in the presence of a core hole and with an extra electron on the first available valence level (solid state screening). Finally, there is a third scheme (c) corresponding to an intermediate situation between (a) and (b): the self-consistency is performed on a non-excited atom; it is only during the absorption calculation that we take into account the excited electronic structure of the absorber. In practice, at the beginning of the absorption calculation, we add the difference between the atomic density corresponding to an excited atom  $\rho_{\text{exc}}^{\text{atom}}(\vec{r})$  and the one for the non-excited case  $\rho_{\text{nonexc}}^{\text{atom}}(\vec{r})$  to the self-consistent electronic density of the absorber  $\rho^{\text{SCF}}(\vec{r})$ :

$$\rho^{\text{SCF}}(\vec{r}) = \rho_{\text{nonexc}}^{\text{SCF}}(\vec{r}) + (\rho_{\text{exc}}^{\text{atom}}(\vec{r}) - \rho_{\text{nonexc}}^{\text{atom}}(\vec{r})) \quad (4.2)$$

We note that both in (b) and in (c) we introduce by default a full screening to calculate absorption. Therefore, the many body effects due to the core hole are taken into account through the final state rule. The essential dissimilarity between the (b) and (c) procedures is linked to the difference in the time scales associated with the two main processes involved: the transit of the photoelectron out of the atom and the response of the electron cloud surrounding the absorber (see the dedicated paragraph in section

1.4.2). If the electrons adjust instantaneously to the perturbed structure scheme (b) is appropriate. If the photoelectron travels out of the atom before the other electrons have the time to readjust, scheme (c) is more accurate. In the results section we shall distinguish which is the most accurate procedure among the three.

We cycle on a wide range of electron energies (we set an energy step of 0.1 eV) and we calculate the  $a(E)$  and  $b_l(r, E)$  factors for each of these energies. The first energy of the calculation is chosen between those of the last core orbital and of the first valence one, in terms of the atomic energy levels of the atoms in the cluster. We define the core states as those atomic orbitals which are part of a full shell and are far enough from the potentially occupied states; the remainder are referred to as valence states. We recall that the atomic levels have no physical significance if the cluster contains several atoms; they still give us a fair indication of where the calculation should begin, in order not to miss the electrons we are interested in. We note that beginning the calculation at a rather low energy (at around 30 to 80 eV below the edge) is not very time consuming, because of the small number of spherical harmonics featured in the expansion, according to the rule in (3.7).

Calculation time is saved by means of the symmetrization. We recall that all calculations are symmetrized, but different symmetry constraints are applied according to the choice of the self-consistent scheme (a, b or c). Procedures (a) and (c) are consistent with the periodic description of a crystal. In this case we calculate electronic densities corresponding to the non-equivalent atoms in the unit cell and impose them on the rest of the atoms in the cluster, according to the space group symmetry. This scheme avoids the convergence problems due to border phenomena that concern the atoms far from the absorber. Within the scheme (b), when we deal with an excited absorber, the crystal symmetry is broken by the presence of the core hole which renders the calculation molecular-like. The space group symmetry is no longer relevant and we need to calculate the electronic structure of atoms independently, at most by taking into account the point group symmetry of the absorber. One straightforward consequence of this procedure is the fact that it induces artificial effects at the cluster's borders. The lack of constraints with regard to the distribution of electrons predisposes them to accumulate at the borders. This phenomenon does not prevent convergence.

In order to calculate the potential for the atoms at the border of the cluster, we use an auxiliary calculation cluster, whose radius is larger than that of the former. The additional atoms it brings are not calculated self-consistently. Their only purpose is to set the atomic levels used for the superposition of both the electronic densities and the atomic potentials.

To perform a real-space self-consistent calculation in solids the use of complex energies is mandatory. They are required in order to broaden the localized electronic levels, otherwise one would need an extremely small energy step to count properly the electrons in these orbitals. We therefore need to refer to equations (2.48) and (2.54) for the calculation of all the density-related quantities. The reason why we are limited to the MST scheme in order to perform the self-consistent procedure is that we cannot treat the singular solution with the FDM method. The energies of the calculation are chosen to have a small (0.1 eV) imaginary part.

The evaluation of the Fermi level demands the setting of a reference in terms of the number of valence electrons one can find in the cluster. Summing up the atomic

numbers is not exact, for two reasons. Firstly, we only count the electrons lying within the atomic spheres  $R_j$ , whose construction is explained in the following paragraph. Secondly, we fail to count some valence electrons localized beyond the cluster's borders and which belong to the next-to-the-border atoms.

To solve this, we assign a specific space extension to each atom. We consider spherical atoms  $j$  with radii  $R_j$ , chosen in such a way that the cluster is neutral. This procedure has been proved inappropriate for certain kinds of materials (i.e. sparse structures) as it implies a too large overlap between the atomic spheres. In this case we set an upper limit of 30 per cent of overlap with respect to the sum of the volumes of the spheres in the unit cell. We note that the atomic radii are usually larger than the MT radii. One calculates the spatial integrals in the following manner:

$$\int_{space} d^3r = \sum_j \int_0^{R_j} d^3r \quad (4.3)$$

by summing the relevant atomic sphere over all the atoms of the cluster.

Subsequently, we use (2.56) and (4.3) to calculate the number of electrons belonging to each atom and then the total electronic population of the cluster. The first calculation is stopped when this number reaches the reference electron number. We get the corresponding electron charge density. In practice, as usual, we perform a weighting of the charge density at the previous iteration (that we used in the beginning of the cycle in order to calculate the Coulomb potential) with the current one. The experience tells us that the current calculation needs to have a rather small weight (0.1 at most) for convergence to be achieved. The interpolation parameter is set up dynamically, i.e. we decrease it by a factor 2 in case of a beating convergence parameter, which we define later in (4.5). We inject the weighted charge density into the next cycle and we repeat the calculation until the convergence is achieved.

We note that the automatic setting of the Fermi level is a very convenient and user-friendly feature of the self-consistent calculation. For the codes where this is not the case, the Fermi level is set *ad-hoc* and thus the elimination of occupied states according to (3.14) is spurious. In the case of sparse structures (as one will see in the next section) the calculated Fermi level and the cut-off of the absorption spectrum may differ, nevertheless the former still gives valuable information (within  $\approx 1$ -2 eV).

Provided the non-spherical effects are not very significant, we observed that the calculated Fermi level suits well the cut-off value needed for a satisfactory agreement with the experiment, if schemes (a) or (c) are employed. If, on the contrary, we perform a full excited calculation of type (b), our experience tells that the cut-off value needs to be less (1-1.5 eV) than the calculated Fermi energy. Consequently, we developed an automatic procedure that estimates this new cut-off: we integrate the valence DOS for the absorber until it reaches the nominal number of electrons of the non-excited atom. For instance, let the case of a self-consistent, excited calculation on bulk titanium ( $Z = 22$ ). We integrate its atomic  $d$  DOS until it reaches the value 2 (i.e. the number of the  $3d$  electrons for the non-excited atom), and the limiting energy is taken as the cut-off for the spectrum. The reason that this value is less than the Fermi level is that the core hole lowers the energy of the (localized)  $d$  states, whereas the  $s$  and the  $p$  are less influenced.

The total energy of the cluster  $\mathcal{E}$  is calculated by integrating the multiple scattering

calculated quantities into the Kohn - Sham formula [58]:

$$\begin{aligned} \mathcal{E}[\rho(r)] = & \sum_{atoms} \int dE E \delta(E) + \sum_{atoms} \sum_{g \in core} \epsilon_g - \frac{1}{2} \int d^3r \rho(r) V_H(\rho(r)) \\ & + \int d^3r \rho(r) \epsilon_{xc}(\rho(r)) - \int d^3r \rho(r) V_{xc}(\rho(r)) \end{aligned} \quad (4.4)$$

where  $f$  are the final states of the same energy  $E$  and all quantities are in Rydberg units. The first term of (4.4) represents the sum over the occupied valence orbitals of the eigenvalues we got by solving the SE.  $V_H$  is the bare Coulomb potential (the Hartree term),  $V_{xc}$  the exchange-correlation potential and  $\epsilon_{xc}$  is the exchange correlation energy. The second term, which we do not calculate explicitly, is the energy of the core states, calculated in the single particle picture. What we calculate is the variation of this energy with respect to the first iteration value, under the assumption that this variation is entirely due to the changing potential and that the core wavefunction is the atomic one. Consequently, the energy in (4.4) is defined up to an additive constant.

The criterion to achieve convergence is to have a stable total cluster energy  $\mathcal{E}$ , i.e. the variation of this quantity from one iteration to the next must be inferior to a particular user-chosen value. In practice, we take into account the less favourable situation where the variations of energies of different atoms have different signs, from one iteration to the next. Hence we use a more severe criterion, as compared to the stability of  $\mathcal{E}$ :

$$\Delta\mathcal{E} = \sum_{eq}^p \mathcal{N}_p \cdot |E_p^i - E_p^{i-1}| < 1 \text{ eV} \times \sum_p N_p \quad (4.5)$$

where we sum on all the equivalent atoms  $p$ , with  $\mathcal{N}_p$  being their multiplicity and  $N = \sum_p N_p$  the total number of atoms in the cluster.  $E_p^i$  is the energy of such a prototype atom  $p$  at the  $i$  iteration. Once convergence is achieved we expect that  $\mathcal{E}$  reaches its minimum amongst all the iteration values.

In practice this is not the case. We suspect that the third term in (4.4), whose order of magnitude is largely superior to the others', masks the variations in the exchange-correlation contribution. We may be not precise enough to calculate an accurate total energy of the system. We think that this may be a limitation of the method. We nevertheless mention that when convergence is achieved, the total energy is definitely smaller than the one at the first iteration, and rather close to the minimum value recorded amongst all iterations. For comparison, we mention that the convergence criterion in the FEFF code is linked to the stability of the Fermi level and not to the total energy [8].

### 4.3 Results

In this section we aim to answer several questions linked to the pertinence of applying a self-consistent procedure to an X-ray absorption calculation. In particular, we are interested to detect what are the structures where a self-consistent calculation can improve the non self-consistent results. Another issue is whether one could afford a smaller calculation radius for the self-consistent part than for the absorption calculation,

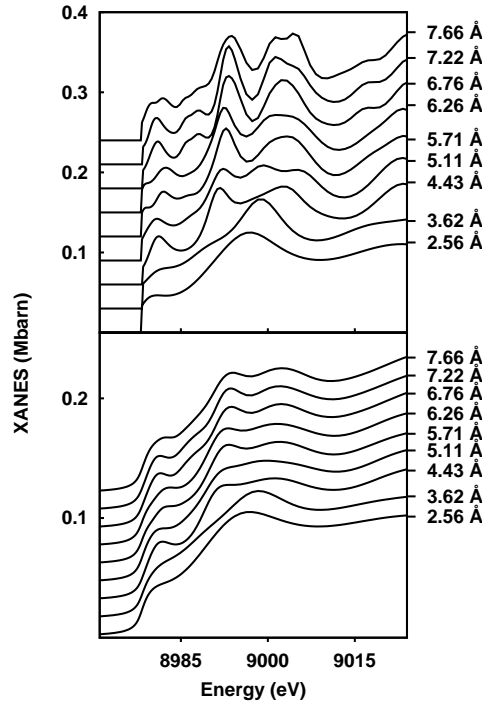


Figure 4.1: Evolution of the  $K$  edge absorption signal with respect to the cluster size: before (top) and after convolution (bottom). The cut-off in the unconvoluted spectra is a consequence of the elimination of the occupied states.

the purpose being to save computation time. Moreover, we wish to indicate what is the best self-consistent approach among the ones presented in the previous section. We shall mainly study the  $K$  edges, where the agreement with the experiments is satisfactory enough to enable us to state whether the self-consistent procedure is useful or not. To begin with, we shall study two textbook cases, the copper Cu (at both  $K$  and  $L_{2,3}$  edges) and the rutile  $\text{TiO}_2$ . We also discuss the results of calculations run on the boron nitrate BN and the calcium oxide CaO, as well as on the  $3d$  elements.

### The copper Cu

To begin with, we will show the self-consistent calculations run on copper, as a reference case. We show the absorption spectra at the  $K$  edge for several radii of calculation, each of them corresponding to an additional shell of atoms. Figure 4.1 shows the  $K$  edge absorption spectra, calculated within the MST frame, before and after the convolution. One should always appeal to the convoluted spectra when comparing with the experiment. One can see that in terms of calculation radii, convergence is achieved at 6.76 Å (i.e. 135 atoms). For this radius we superpose the spectra after convolution, for several self-consistent and for a non self-consistent calculation. The self-consistent calculations have been performed in several manners (a,b,c), according to the procedures described above (see section 4.2). Among these, one can see that procedure

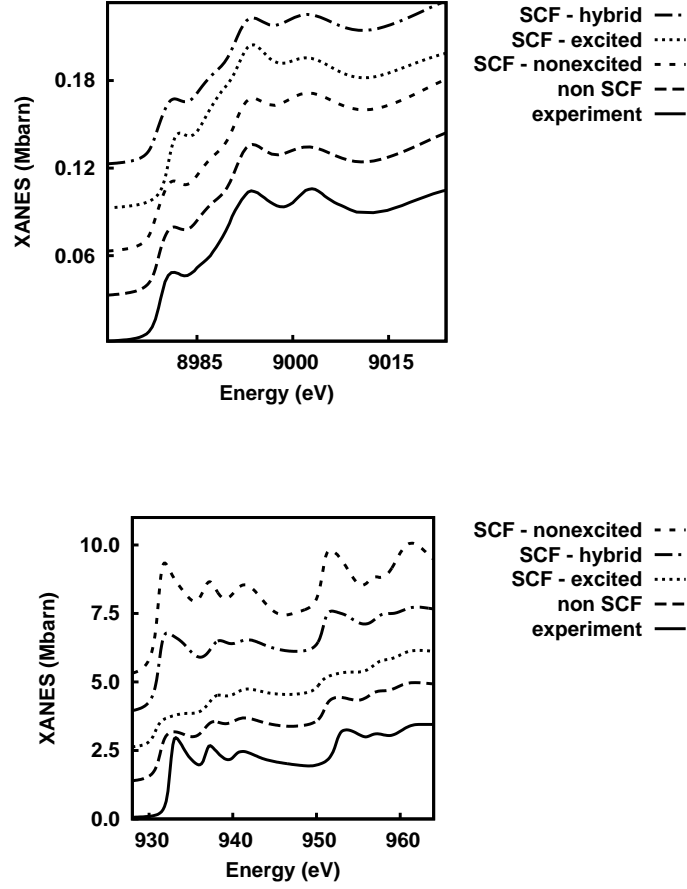


Figure 4.2: Calculation and experimental data for absorption of copper. Above, we show the  $K$  edge, for a  $6.76 \text{ \AA}$  cluster. Below, we show the  $L_{2,3}$  edges for a  $7.66 \text{ \AA}$  cluster. For what self-consistent calculations are concerned, we tested the three different procedures: full non-excited calculation (a), full excited calculation (b) and hybrid (c), i.e. self-consistency is performed on the non-excited absorber while the absorption takes into consideration the excited electronic structure.

(c) is the most appropriate with respect to the agreement with the experiments, as it improves the ratio of intensities of the structures after the edge. Unlike scheme (b), non-excited self-consistent procedures (a) and (c) do not influence the position of the structures preceding the main edge, as compared both to the non self-consistent case and to the experiment. We therefore conclude that the assumption we had made to get the (b) spectrum (i.e. the response of the electron cloud surrounding the absorber to the passage of the photoelectron is adiabatic) is not valid at the  $K$ -edge, as confirmed by our further examples. Note that in the particular case of copper, the  $L_{2,3}$  behaviour is similar to the  $K$  edge one. As the  $3d$  levels are completely filled for the excited atom, the orbitals probed by the photoelectron are the band like  $4d$  ones. We shall

discuss the issue whether the self-consistency (i.e. all but the last iteration) has to be performed at the same radius as the absorption (i.e. the last iteration) calculation. We ran a calculation where we used a cluster of 2.56 Å radius (13 atoms, i.e. the absorber surrounded by the first shell of copper atoms) for the self-consistency, while the absorption calculation was performed on a cluster of 6.76 Å. We compared the result with the one we had previously got (figure 4.2) for a full 6.76 Å calculation. We obtained practically no difference between the two, which encourages us to use a smaller cluster for the self-consistency part for the copper-like (i.e. compact, close packed) structures.

## The rutile TiO<sub>2</sub>

In this section we will show the results of calculations run on the TiO<sub>2</sub> compound. We calculate the absorption signal at the titanium's *K* edge, for two different polarisations. TiO<sub>2</sub> is an interesting structure to test our self-consistent procedure on, as it features several pre-edge peaks of both dipolar and quadrupolar origin, related to the 3*d* states of titanium. The MST non self-consistent calculations do not give a very good agreement with the experiments. *A priori* one would expect benefits from a self-consistent calculation, as it is supposed to act especially on the localized 3*d* states in the vicinity of the Fermi level.

In figure 4.3 we show the non self-consistent and the self-consistent calculations (according to the two different procedures (b) and (c) ) run on a 5.51 Å cluster and compare them to the experimental data of Poumellec et al. [88]. We note that a radius of 5.51 Å corresponds to 75 atoms and is enough to achieve convergence of the absorption signal with respect to the cluster size. We note that a condition *sine qua non* to obtain the pre-edge structures is that the cluster contains the first shell of TiO<sub>2</sub> octahedral surrounding the absorber, which is achieved for the 5.51 Å radius. All absorption calculations have been performed in the MST frame. We analyse the signal obtained for two different orientations of the polarisation and the wavevector:  $(\epsilon, k) = ([001], [110])$  and  $(\epsilon, k) = ([1-10], [110])$ . One can see that all calculations fail to describe the double structure at the edge (4980 - 4990 eV), for the second polarisation. This is a defect of the MT approximation. As far as the pre-edge structures are concerned, they are due to the overlap between the absorber's electronic states and the *e<sub>g</sub>* and the *t<sub>2g</sub>* of the titanium neighbours. As compared to the non self-consistent calculation, both procedures (b) and (c) succeed in shifting the pre-edge structures towards the smaller energies, nevertheless this shift is not enough to give a perfect agreement with the experiments. One should note that TiO<sub>2</sub> is a rather sparse material and the MST - MT is known not to give very good results for this particular kind of structure because of the approximations it introduces on the form of the potential. For what the self-consistent calculations are concerned, we checked that the converged result is the same if we choose different departure points in terms of the atomic electronic structure of the absorber (i.e. 3*d*<sub>1</sub> 4*s*<sub>2</sub> 4*p*<sub>1</sub> or 3*d*<sub>2</sub> 4*s*<sub>2</sub> 4*p*<sub>0</sub>), proving the robustness of our procedure. Moreover, in practice the result is nearly independent of the exchange correlation potential we used (i.e. Hedin-Lundquist [51,52] or Perdew and Wang [86]).

Another aspect to take into consideration when performing the self-consistent procedure is the evolution of the atomic charges during the iterations. We recall that we set the atomic radii *R<sub>j</sub>* in order to assure the neutrality of the unitary cell, or, equivalently,

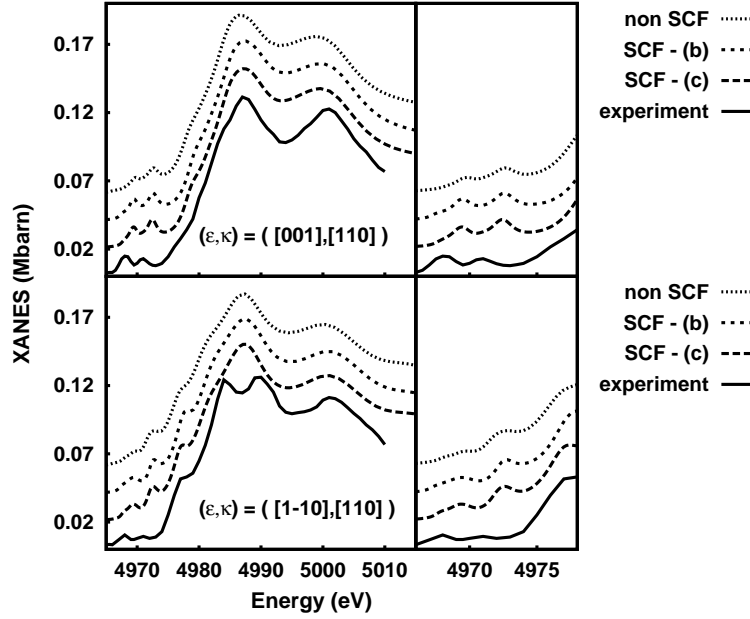


Figure 4.3: MST-MT calculations and experimental data [88] for absorption at titanium's K-edge, for a 5.51 Å cluster. Two polarisations are shown:  $(\epsilon, k) = ([001], [110])$  (top) and  $(\epsilon, k) = ([1-10], [110])$  (bottom). As far as the self-consistent calculations are concerned, we tested two different procedures: the full excited (b) and the hybrid (c) calculation. On the right hand side, we show a zoom on the pre-edge structures. One can see that as compared to the non self-consistent ones, self-consistent procedures reduce the disagreement with the experiment.

of the calculation cluster. We checked that when convergence is achieved, the modulus of the individual atom charges decreases as compared to its value at the beginning. In the particular case of  $\text{TiO}_2$ , by using the self-consistent scheme (c) we converge to negatively charged oxygen and positively charged titanium, which is consistent with the electrochemical picture. When convergence is achieved, we get an additional  $+0.7 e$  for the titanium and  $-0.35 e$  for the oxygen, with  $e$  being the modulus of the electron charge. At this point, the calculated atomic charges ( $0.256 e$  for the titanium and  $-0.128 e$  for the oxygen) are still very different from the formal ones ( $4e$  and  $-2e$ , respectively). This is partially due to the fact that the atomic radii  $R_j$  we used for the charge calculation ( $1.42 \text{ Å}$  and  $1.04 \text{ Å}$ ) are different from the ionic radii ( $0.86 \text{ Å}$  and  $1.4 \text{ Å}$ ).

In figure 4.4 we show a self-consistent calculation with the absorption calculation performed in the FDM frame. The main difference between the FDM and the MST-MT calculations occurs at the edge (4980 - 4990 eV), as the former is able to reproduce the double structure for the  $(\epsilon, k) = ([1-10], [110])$  polarisation. This is a consequence of having considered the full potential. As compared to its non self-consistent counterpart, the self-consistent FDM calculation shifts the quadrupolar signal towards the lower energies. Moreover, the ratio of the intensities of the pre-edge structures is improved.



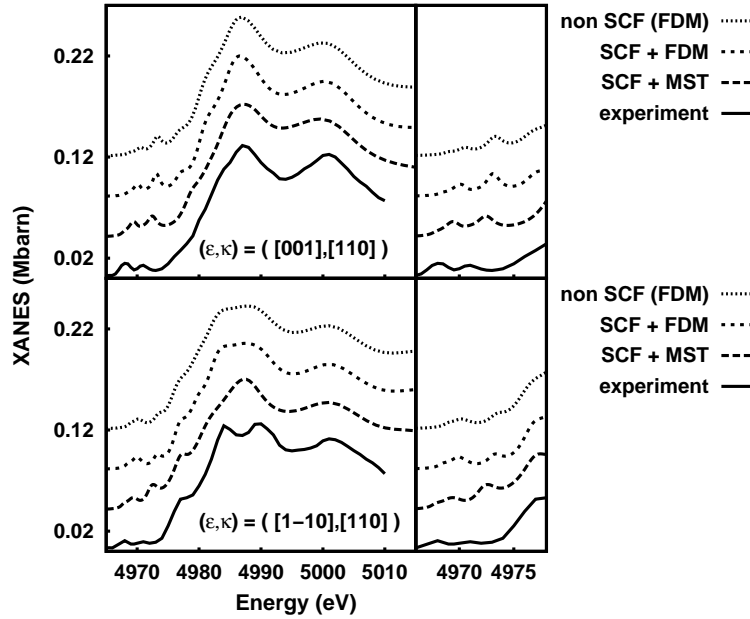


Figure 4.4: FDM calculations and experimental data [88] for absorption at titanium's  $K$  edge, for a  $5.51 \text{ \AA}$  cluster. Two polarisations are shown:  $(\epsilon, k) = ([001], [110])$  (top) and  $(\epsilon, k) = ([1-10], [110])$  (bottom). The self-consistent calculations are performed according to scheme (c). On the right hand side we show a zoom on the pre-edge structures. One can see that as compared to the non self-consistent ones, self-consistent procedures reduce the disagreement with the experiment.

The self-consistent scheme is still performed in the MST-MT frame; to get a better agreement with the experiments one should implement a full potential self-consistent calculation. We have studied the influence of the cluster's size for the self-consistent part, for a given radius ( $5.51 \text{ \AA}$ ) of the absorption calculation. We note that all the radii we tested upon are large enough to exhibit the pre-edge structures. Unlike the copper case, the results are very sensitive to the radius for the self-consistent part (figure 4.5). We therefore conclude that for oxides, whose structure is sparser, one should take the same cluster size for the self-consistent part as for the absorption calculation.

### The $3d$ and $4d$ series

We tested our procedure on numerous materials for which self-consistency brings little or no change with respect to its non self-consistent counterpart. In this section we focus on the results on the bulk  $3d$  and  $4d$  elements.

We ran  $K$  edge calculations on the  $3d$  and  $4d$  series by using the standard crystallographic structure. We encountered no particular difficulty, neither to achieve convergence, nor to obtain the correct cut-off for the convolution and, thus, the elimination of the occupied states. We chose to show the results we got for titanium, nickel, iron and silver (figure 4.6) and compare them to the experiment [72]. In the cases where the (b)

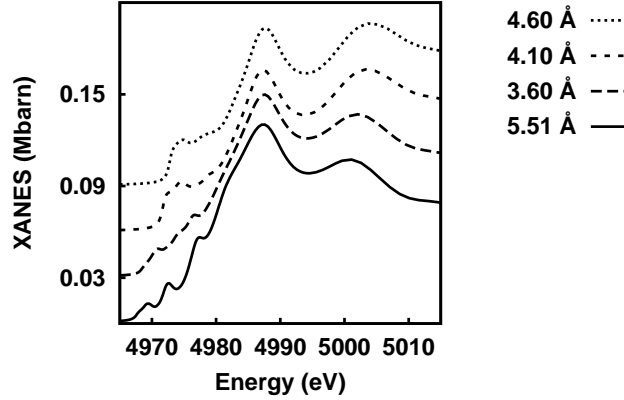


Figure 4.5: Self-consistent calculations of type (c), run for different sizes of the cluster. The absorption calculation is performed on a 5.51 Å cluster, in the MST-MT frame.

and (c) self-consistent schemes give different results (Ag,Ni,Cu), the best agreement is achieved by using the former procedure. In other cases (Fe,Ti) this difference is not at all noticeable. We inferred that the (b) self-consistent scheme is the best choice when dealing with the  $K$  edge. Our general conclusion is that the self-consistency brings no major change at high energies, as compared to the non self-consistent calculations. In some cases (Fe,Ni) one can see a shift in the position of the low energy peaks. This behaviour confirms our assertion that the self-consistent effects occur mostly in the vicinity of the Fermi level.

We note that in the case of transition metals one can allow the self-consistent calculation to run on a cluster of a lesser radius than the one for the absorption calculation. A cluster containing two atomic shells surrounding the absorber is large enough to render reasonable results for the self-consistent part of the calculation. We tested this feature on the transitional metals and we observed that the absorption calculation run for a given radius (of the order of 5 Å or more) is not sensitive to the previous self-consistent calculation step provided the latter contains two or more atomic shells. We equally calculated the  $L_{2,3}$  edges absorption spectra of the bulk  $3d$  elements (which we do not show in the manuscript). In this case, the agreement with the experiment is poor (including the non self-consistent calculation) to such extent that it does not allow us to distinguish what is the best screening scheme among the three. We cannot state clearly that for XANES spectra, the self-consistent calculation is better than its non self-consistent counterpart. A genuine improvement is brought by the corrections introduced by the TDDFT, as shown in section 6.

## Open structures

In the following paragraph we shall discuss the results we obtained for calcium oxide CaO and boron nitrate BN, some prototypical compounds where non-spherical effects are important. The experiments have been performed at the  $K$  edges of Ca and B, respectively. In both cases, we compared the self-consistent and the non self-consistent

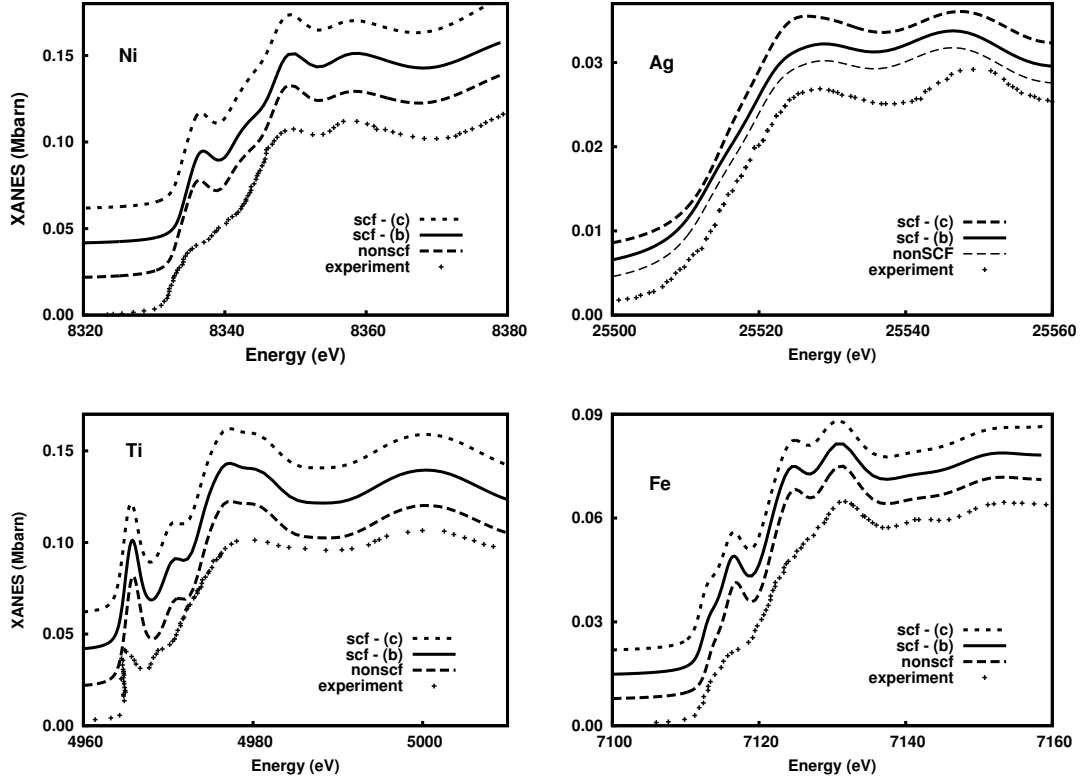


Figure 4.6: Calculations - nonSCF (long dashes), SCF - (b) (solid line), SCF - (c) (short dashes) and experimental data (with dots) for some transition elements. All calculations were performed on a  $7 \text{ \AA}$  cluster. The absorption units match the calculation and the experimental data is scaled for the comparison. Self-consistency does not bring significant change, nevertheless it allows a judicious estimation of the Fermi level. Among the several alternatives, the scheme (b) is to be preferred.

results (figures 4.7 and 4.8) with the experiment [8, 77]. Among the self-consistent calculations, schemes (b) and (c) give similar results and we chose to show the former one. For these particular materials, the calculated Fermi level is not the same with the cut-off we used for the convolution (for the quantitative information, see the captions of figures 4.7 and 4.8). We explain this inadequacy by the fact that our assumption of sphericity (the MT approximation) prevents us from counting all the electrons, given the fact that we are not allowed to exceed an upper limit of the overlap of the  $R_j$  integration spheres. This energy shift does not usually appear if the compound is a compact structure, as non-spherical effects are negligible, but may be significant if one deals with a sparse structure, like BN or CaO. We note that it is still the self-consistent calculation which gives a more reasonable result with respect to the Fermi level evaluation. In the case of BN, one can see practically no difference between the self-consistent and the non self-consistent calculations, whether the last iteration was performed in the FDM or in the MST-MT frame. Moreover, the agreement with the experiment is obviously better in the case of the FDM calculations. One concludes that

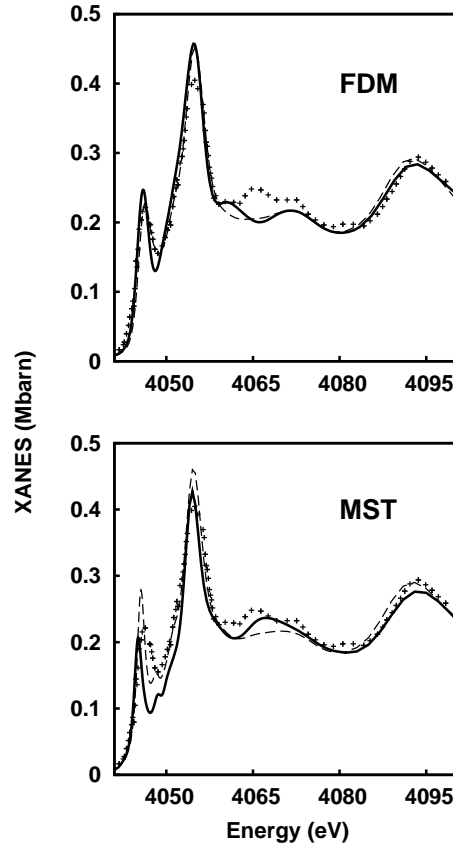


Figure 4.7: Comparison between the self-consistent (solid line) and non self-consistent (dashed line) calculations with the experimental data [77] (with dots), for the calcium oxide CaO, with the absorption calculation performed in the FDM (above) and in the MST-MT (below). We used a  $6.9 \text{ \AA}$  cluster, i.e. 93 atoms. The absorption units match the calculation and the experimental data is scaled for the comparison. The calculated Fermi level (4037 eV for the non self-consistent calculation and 4039.5 eV for the self-consistent one) is different from the cut-off we used for the convolution (4042 eV).

it is crucial for this particular material to be treated within a full potential method (FDM). The fact that the calculation is self-consistent or not (we recall that the self-consistency was implemented in the MST frame, due to computational limits) does not make any difference.

For what the CaO is concerned, one notices an improvement provided by the self-consistent calculations, in both MST-MT and FDM cases. Nevertheless we are still unable to get a perfect agreement for the modulations in the range 4060-4070 eV. One can see (figure 4.7) a better agreement in the case of a non self-consistent FDM absorption calculation than for the self-consistent MST-MT one. This leads us to the conclusion that the taking into account of the non spherical effects is more important than the improvement given by the self-consistent procedure, as implemented in the FDMNES (i.e. in the spherical potential approximation).

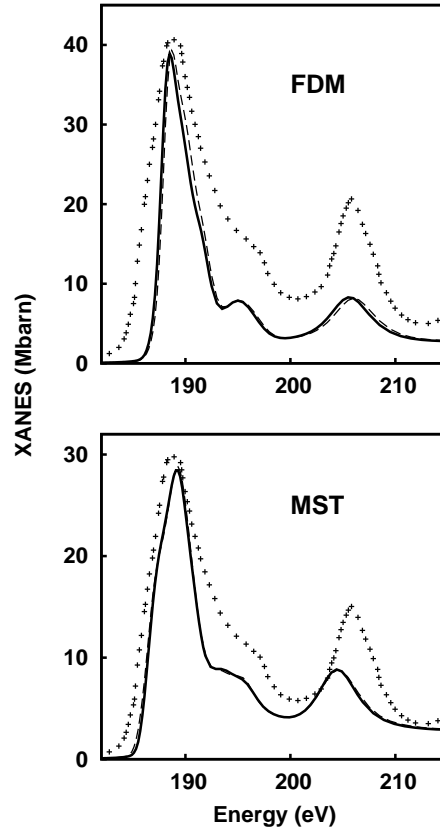


Figure 4.8: Comparison between the self-consistent (solid line) and non self-consistent (dashed line) calculations with the experimental data [8] (with dots), for the boron nitrate BN, with the absorption calculation performed in the FDM (above) and in the MST-MT (below). We used a 4.7 Å cluster, i.e. 87 atoms. The absorption units match the calculation and the experimental data is scaled for the comparison. The calculated Fermi level (178.2 eV for the non self-consistent calculation and 179 eV for the self-consistent one) is different from the cut-off we used for the convolution (186 eV).

### Comparison with other codes

We wish to validate our self-consistent procedure by comparing it to an equivalent band structure calculation. We chose to compare with the results of Moruzzi, Janak and Williams [78], who used the self-consistent, reciprocal space KKR method, leaning on the MT approximation. Our self-consistent scheme (a) is completely equivalent to a band structure result, as the absorber is supposed non-excited throughout the calculation. To insure a high resolution, we performed a calculation on a radius of 8.47 Å (225 atoms) taking the value of 0.025 eV both for the energy step and for the imaginary energy. In figure 4.9 we compare the total density of states (DOS) for the two calculations. One can see a very good agreement of the two, which testifies to the accuracy of our self-consistent scheme.

For comparison, we mention that the self-consistent procedure implemented in the

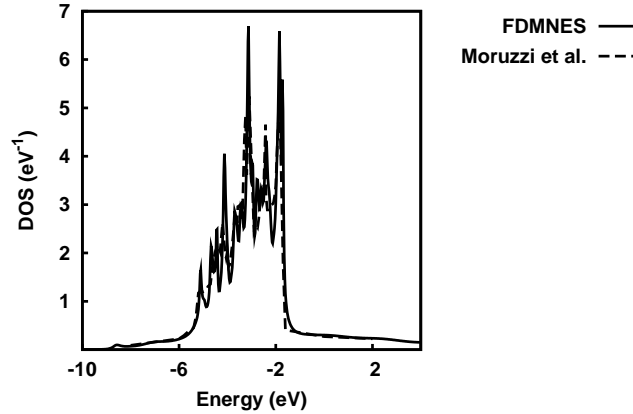


Figure 4.9: A comparison between the total density of states of copper calculated by FDMNES (a SCF - (a) procedure calculation) and the results of Moruzzi et al. [78]. The zero of the energy scale corresponds to the Fermi level [78].

FEFF code [8, 77] is automatically performed in the (b), i.e. excited scheme. According to our results for the  $K$  edge of copper, this is not the best scheme, as it overestimates the height of the main edge (see figure 4.2 and the first figure in reference [93]). We think that the choice of the hybrid self-consistent scheme (c) is a better solution.

For the rest, the applications of the self-consistent procedure implemented in the FEFF code [8, 77] suggest the same outcome as our's: self-consistency does not alter the global shape of the spectra, but it offers a more reliable, though not perfect, evaluation of the Fermi level.

## 4.4 Conclusions

One concludes that at the  $K$  edge most of the stringent effects of self-consistency, in terms of the positions of the peaks in the spectra, are restrained to the pre-edge structures, close to the Fermi level. Nevertheless, for certain materials, a slight redistribution of the intensities can be observed at high energies. These considerations apply to absorption spectra. We expect that XMCD calculations at the  $K$  edge will be rather sensitive to the self-consistent feature.

The value of the Fermi level is the most useful information one gets from a self-consistent calculation, as it is essential for the identification of the occupied states and thus for comparison with the experimental spectra. This cut-off of the spectra is correctly estimated for the compact structures, but is liable to adjustment (1-2 eV) in the case of materials where non-spherical effects are important.

We have proved that the self-consistency brings practically no change for the closed-packed structures, in which case one should content oneself to run the self-consistent part of the calculation at a lower radius than the one used for the absorption part. We recommend that the auxiliary calculation cluster's radius contains at least one atomic shells around the absorbing atom. Oxides require that one uses the same cluster sizes

for the two stages of the calculation for the purpose of improving the description of pre-edge structures.

The self-consistent procedure enables an *a posteriori* study of the screening of the core hole, as it allows us to distinguish which of the three possible screening schemes is the most appropriate one. Note that the full excited option, i.e. the (b) scheme, is inappropriate to the description of core spectroscopy, at least at the  $K$  edge. Our explanation to this fact is that the (b) scheme mistreats the screening phenomenon. At the  $K$  edge, we noticed that in most of the cases it is the (c) scheme that gives the best agreement to the experiment.

The self-consistent corrections are negligible at high photon energies (EXAFS region) where the shape of the spectrum depends on the position of the atoms and less on their electronic structure.

It has been argued [8] that for real space calculations the MT self-consistent procedure is more important than the full potential feature. We disagree with this statement (at least in the near-edge region), as proved by our results on CaO and BN compared to the ones in references [77] and [8], respectively. In our view and as proved by our results on CaO and BN, the most important ingredient of a single particle X-ray absorption calculation is the full potential feature. Full potential is far more important (at low energies) than self-consistency in the MT approximation.

To conclude upon the self-consistent effects at the  $L_{2,3}$  edges is a delicate task. Most often, the many body effects are important (the  $L_{2,3}$  edges of rare earths or transition elements) and the single particle calculations, whether self-consistent or not, give a poor agreement with the experiment. We believe that our self-consistent procedure does yield a more reliable density of states than its non self-consistent counterpart (this statement will be argued in chapter 5). The reason behind the disagreement with the experiments should be looked for in the inappropriateness of describing absorption based on the single particle density of states.

We conclude that the point in implementing self-consistency for the X-ray absorption real space calculations is that this procedure is a pre-step for other theoretical developments. One needs it to have a reasonable evaluation of the Fermi level, which is an important element of the TDDFT calculation scheme. One equally needs the electrons' count procedure in order to implement the LSDA+U.

## Chapter 5

# The LSDA+U method

### 5.1 Motivation

The LSDA+U calculation method is a hybrid scheme meant to improve the LSDA. Its introduction was motivated by the LSDA's failure to describe the strongly correlated systems. The reason behind this is that the LSDA picture is appropriate for band behaviour and misses completely the physics of localized (correlated) electrons. On the other hand, the LSDA+U reconciles, to some extent, the atomic behaviour of the correlated orbitals and the band behaviour of the remainder.

A textbook example of failure of the LSDA approximation to the DFT concerns the electronic structure calculations on materials containing ions with  $d$  or  $f$  open shells. In the case of several insulating transition metal oxides, the LSDA calculations predict a metallic character [114] and no gap in the  $3d$  DOS. In reality, the  $3d$  electrons are localized on the metal ion, which causes an energy gap between the occupied  $3d$  band and the continuum  $d$  states.





To solve this contradiction, one needs an orbital dependent DFT functional that selectively opens the gap for the  $3d$  like states and does not affect the delocalized orbitals. The DFT method employing such functional is called the LSDA+U scheme, with  $U$  the on-site  $3d$  repulsion. This functional has been constructed starting from the mean field approximation of the Hubbard model [5, 6, 39, 65].

The LSDA+U was originally introduced for ground state calculations. Nonetheless, successful calculations of X-ray absorption spectra have been reported [15, 50]. When applied to a compound whose Fermi level is already in the gap in a LSDA calculation (the  $3d$  degeneracy is lifted in octahedral or tetrahedral symmetries), the LSDA+U in practice enlarges this gap. For spectroscopy calculations, this is particularly important for the position of the calculated E2-E2 pre-peak: in the LSDA+U scheme, the pre-peak approaches the edge.

At the present moment, FDMNES is the first and only real space (MST) X-ray absorption calculation code to have the LSDA+U feature. The exchange-correlation functional contains the specific orbital's population, which requires at least one previous iteration. Therefore the self-consistent procedure is a pre-requisite of the practical implementation of the LSDA+U. Although the method is rather simple from a conceptual point of view, its implementation in a real space MST calculation is fastidious,



Table 5.1: The Hubbard parameter  $U$  is defined as the energy cost to bring two electrons to the same site.

N			$2\mathcal{E}(d^n)$
N+1			$\mathcal{E}(d^{n+1}) + \mathcal{E}(d^{n-1}) + U$

due to technical reasons that we shall develop in the following sections.

## 5.2 Theoretical grounds

LSDA+U is not just an unintentional approximation of the DFT exchange-correlation potential. The reasons for its success should be looked for in its ability to reconcile the band description (LSDA) with the atomic one (+U), as already discussed in section 1.5. In practice, the LSDA+U divides the Hilbert space into two distinct subspaces: the extended, delocalized electronic states, which are treated by the LSDA as usual, and the localized, correlated orbitals, whose corresponding LSDA result is corrected by a Hubbard-like term. Consequently, there is a close connection between the Hubbard model and the more recent LSDA+U method.

**The Hubbard model** The starting point in the construction of the LSDA+U functional is the Hubbard model, which treats the localized electrons embedded in the extended states. The corresponding Hamiltonian reads:

$$\mathcal{H} = -t \sum_{\langle i,j \rangle, \sigma} (c_{i\sigma}^\dagger c_{j\sigma} + c_{j\sigma}^\dagger c_{i\sigma}) + U \sum_i \rho_{i\uparrow} \rho_{i\downarrow} \quad (5.1)$$

Here  $t$  is the bandwidth (a measure of the kinetic energy),  $U > 0$  measures the on-site repulsion,  $i$  and  $j$  are the site indexes and the  $\langle i, j \rangle$  symbol stands for a summation on the nearest neighbours. The first term in (5.1) describes the hopping of an electron from site  $i$  to site  $j$ . Note that the hopping process conserves the spin - no spin-flips are allowed in the Hubbard model. The second term in (5.1) competes with the first one and is zero unless two electrons of opposite spins stand on the same site. In the limit  $U \rightarrow 0$  one retrieves the tight binding model, with  $t$  the overlap integrals.

In the Hubbard model,  $U$  is a parameter and it is defined as the energy cost to bring two electrons to the same site [6] (see table 5.1):

$$U = \mathcal{E}(d^{n+1}) + \mathcal{E}(d^{n-1}) - 2\mathcal{E}(d^n) \quad (5.2)$$

The Hubbard Hamiltonian has no exact solution for dimensions other than 1. Consequently, the mean field approximation of (5.1) gives [6]:

$$\mathcal{H}_{MF} = \mathcal{H}_{MF}^{LSDA} + \frac{U}{2} \sum_i \sum_{m\sigma \neq m'\sigma'} \rho_{i,m\sigma} \rho_{i,m'\sigma'} \quad (5.3)$$

**The LSDA+U exchange-correlation functional** The connection between the Hubbard Hamiltonian  $\mathcal{H}_{MF}$  and the LSDA+U exchange-correlation functional is made *via* the total energy of the system described by (5.3). One uses this procedure for the correlated orbitals only ( $d$  of the transition elements and  $f$  of the rare earths), whereas the remaining are described in the usual LSDA way. Therefore, one says that the LSDA+U exchange-correlation functional is orbital dependent.

One needs to calculate the total energy of a system described by the Hamiltonian in (5.3), by avoiding the double counting of the correlated electrons that are already included in  $\mathcal{H}_{MF}^{LDA}$ . These calculation steps are detailed in reference [6]. Next, the exchange-correlation potential is obtained as the functional derivative of the total energy with respect to the density.

Within the same philosophy, several forms of the exchange-correlation potential have been proposed [6, 39, 65]. In 1991, Anisimov et al. proposed the first correction to the LSDA for correlated orbitals [5, 6]. The shortcoming of the exchange-correlation potential they introduce is that it is basis set dependent (i.e. depends on the choice of the spherical harmonics basis  $m$ ). Nonetheless, this dependency is not crucial for the outcome of the LSDA+U calculations [4]. This flaw was corrected in 1995 by Liechtenstein et al., who proposed a rotationally invariant, orbital dependent exchange-correlation potential [65]. In the limit of a diagonal occupation matrix ( $\rho_{mm'} = \rho_m \delta_{mm'}$ ) the two approaches are equivalent. In 1998, Dudarev et al. propose a potential that has both the simplicity of the one in [6] and the rotational invariance of [65]:

$$V_{mm'}^\sigma = V_{mm'}^{\sigma, LSDA} + (U - J) \left( \frac{1}{2} - \rho_{mm'}^\sigma \right) \quad (5.4)$$

where  $V_{mm'}^\sigma$  is the orbital and spin dependent potential,  $V_{mm'}^{\sigma, LSDA}$  its LSDA counterpart and  $\rho_{mm'}^\sigma$  the occupation matrix.  $U$  and  $J$  stand for the spherically averaged on-site repulsion and exchange. They can either be accounted for as parameters (Hubbard  $U$  and the Stoner parameter  $J$ ) or may be calculated from first principles, by means of a constrained LSDA calculation [65] or based on a RPA scheme [11]. To grasp the meaning of (5.4), let us consider the diagonal case  $m = m'$ . The  $U$  correction takes the occupied orbitals  $\rho_m^\sigma = 1$  to lower energies, and the free orbitals to higher energies. Therefore one says that the  $U - J$  term opens the gap.

In this current work, we propose an improved form of the potential in (5.4). Instead of the  $\frac{1}{2}$  factor standing for the average occupancy number *per* orbital (for a complete shell) we use:

$$V_{mm'}^\sigma = V_{mm'}^{\sigma, LSDA} + (U - J) \left( \frac{\rho_0}{2} - \rho_{mm'}^\sigma \right) \quad (5.5)$$

where

$$\rho_0 = \frac{Tr\{\rho\}}{2(2l+1)} \quad (5.6)$$

the actual average occupancy *per* orbital.  $l$  is the orbital quantum number of the concerned correlated orbital ( $l = 2$  for the  $3d$ ) and  $Tr\{\rho\} = \sum_{m\sigma} \rho_{mm}^{\sigma\sigma}$  is the trace of the occupation matrix. The difference between (5.4) and (5.5) is that the latter keeps the correlated orbitals symmetric with respect to the Fermi level.

Formally, the orbital dependence of the potential in the LSDA+U method is synonymous with non-locality [4]. In this sense, the LSDA+U is a particular case of the GW approximation: the non-local, energy independent exchange-correlation potential is a contraction of the more general, non-local, energy dependent self-energy [4].

### 5.3 Implementation

As already mentioned, the implementation of a LDA+U method in a real space, symmetrized code is complicated from a technical point of view. Basically, the main difference between a LDA and a LSDA+U calculation is that the latter employs the  $V_{mm'}^\sigma$  in (5.5) instead of  $V_{mm'}^{\sigma \text{ LSDA}}$  to solve the radial SE. It therefore requires a previous LSDA iteration that returns the occupation matrix  $\rho_{mm'}^\sigma$ .

The technical difficulty resides in the fact that while the occupation matrix is a general matrix, the potential in the actual implementation of FDMNES is diagonal in  $m$  and  $m'$  (including the spin-orbit coupling case), and thus (5.4) requires a diagonal occupation matrix. There are two ways to reconcile the two. One may implement a radial SE resolution for un-spherical potentials and adapt the MST electronic structure resolution to deal with non-diagonal atomic scattering amplitudes. One may equally keep the diagonal formulation of the SE and MST and perform a basis set transformation from the crystal basis  $\mathcal{A}$  to an internal one  $\mathcal{B}$  where the occupation matrix is diagonal, and the other way around. It appeared to us that the latter is more convenient.

We perform a first iteration which employs the usual LSDA potential to calculate the occupation matrix  $\rho_{mm'}^\sigma$  according to (2.54). If  $\hat{\rho}$  is diagonal by symmetry, no basis set transformations are required. Otherwise we diagonalise  $\hat{\rho}$  for each atom in the cluster that contains a correlated orbital:

$$\hat{\rho}' = \mathcal{R}^\dagger \hat{\rho} \mathcal{R} \quad (5.7)$$

where  $\rho'$  is the diagonal occupation matrix and  $\mathcal{R}$  the transformation matrix from the crystal basis  $\mathcal{A}$  to the internal basis  $\mathcal{B}$ .  $\mathcal{R}$  contains on its columns the eigenvectors of  $\hat{\rho}$ . If the calculation is symmetrized, this transformation has to be done in blocks corresponding to irreducible representations. The reason for this is that the  $\mathcal{R}$  matrix must forbid the mixing of  $ms$  that do not belong to the same representation.

We inject both the diagonal matrix  $\hat{\rho}'$  and the transformation matrix  $\mathcal{R}$  into the next iteration. At this point we are in the local basis  $\mathcal{B}$ . We solve the radial SE in  $\mathcal{B}$ . We perform a unitary transformation towards  $\mathcal{A}$  and solve the electronic structure (either in MST or FDM) in the crystal basis. We therefore obtain  $\Im\tau$  in the  $\mathcal{A}$  basis, and transform it back to  $\mathcal{B}$ . The reason for this last change of basis set is the singular solution is diagonal in the internal  $\mathcal{B}$  basis only, and the MST formalism that treats it requires a diagonal form. Next, we calculate the atomic and crystal tensors in the internal basis  $\mathcal{B}$ , then transform them back to  $\mathcal{A}$ . Therefore the calculation of the density of states is performed in the crystal basis  $\mathcal{A}$ . We deduce the occupation matrix, and if necessary we re-iterate and start over all the procedure. If, on the other hand, the calculation is not self-consistent, we exit the loop and proceed with the convolution step.

Consequently, should one perform a self-consistent LSDA+U calculation, the first iteration is the usual LSDA one, and all the rest contain the  $U$  corrections. Our

LSDA+U procedure accepts complex energies. Compared to an usual LSDA calculation, the FDMNES implementation of the LSDA+U requires a similar amount of calculation time.

## 5.4 Results

We present preliminary results of the LSDA+U calculation scheme applied to X-ray absorption spectroscopy. As a model compound we chose the well known  $\text{LaMnO}_3$ , a Mott insulator belonging to the  $Pnma$  spacegroup. We performed calculations at the  $K$  and  $L_3$  edges of manganese by setting up  $U - J = 5$  eV (unless specified otherwise).

All the calculation we show here are self-consistent. Non self-consistent ones provide very bad results in the LSDA+U. It appears that LSDA+U is extremely sensitive to the calculated occupation numbers. Bad occupation numbers yield unphysical LSDA+U results. We performed calculations on a  $5\text{\AA}$  cluster. Note that in the LSDA+U case it is imperative to have the same cluster at all the calculation steps. We recall that in some cases one might want to perform the self-consistent loop at a smaller radius than the absorption calculation (see chapter 4).

All the calculations are in the ground state (non-excited, or, equivalently, no description of the core hole) for the occupation number calculation step. This procedure corresponds to the (a) and (c) calculation schemes introduced in chapter 4. The motivation for this choice is as follows. These results are preliminary and we do not intend to compare them to the experimental spectra yet. We are more interested in the fundamental differences between the LSDA and LSDA+U. This comparison is more natural in the non-excited case, as there is no ambiguity concerning the setting of the cut-off level of the spectra (we recall that the other calculation schemes often require an adjustment of the calculated cut-off). Second, the meaning of a self-consistently calculated core hole (scheme b) is less straightforward than the self-consistent calculation of the ground state electronic structure (schemes a and c). Third, we aim at obtaining a general view on the  $L_{2,3}$  edges calculation, by employing several tools (TDDFT, LSDA+U and the self-consistent procedure). As TDDFT is based on a ground state calculation, we prefer the same for the underlying self-consistent cycle of the LSDA+U to facilitate the comparison.

In figure 5.1 we show the self-consistent, ground state density of the manganese  $d$  states in  $\text{LaMnO}_3$ , with and without the Hubbard correction. The two calculations were shifted to superpose the Fermi levels, which are indicated by a thick vertical line. One can see that the LSDA predicts a metallic character, whereas the LSDA+U opens the gap around the Fermi level. It follows that the Hubbard  $U$  term corrects the LSDA prediction and describes the real physics of the  $\text{LaMnO}_3$  compound (a Mott insulator). Although the LSDA+U calculation in figure 5.1 shows some surviving electronic states around the Fermi level, the trend is definitely towards the description of an insulating state. Quantitatively, the gap opening is linked to the  $U - J$  parameter and to the calculated average occupation number of the  $d$  orbitals. Therefore one expects that increasing  $U - J$  will increase the gap of a similar value, weighted by the average population (see figure 5.2).

In figures 5.3 and 5.4 we show the absorption spectra of manganese in  $\text{LaMnO}_3$  within the two calculation schemes, LSDA and LSDA+U, at the  $K$  and  $L_3$  edges,

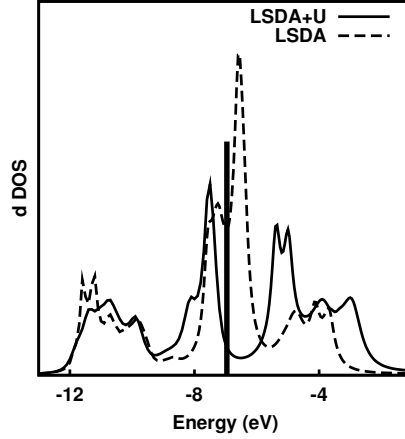


Figure 5.1: The self-consistent  $d$  DOS of the Mn atoms in  $\text{LaMnO}_3$ : with (solid) and without (dashes) the Hubbard  $U$ . The former was shifted by 1.9 eV to the higher energies, in order to superpose the Fermi levels in the two calculations (indicated by the thick vertical line). The energies are expressed in an internal energy scale of FDMNES. The  $U$  term opens the gap around the Fermi level.

respectively. At both edges, it appears that the effect of the Hubbard  $U$  correction is to change the form of the spectrum. At the  $L$  edges, this is due to the different position of the Fermi level relative to the edge jump (the Fermi levels are indicated by a vertical line). The change in the shape of the XANES signal is a general feature of the LSDA+ $U$  calculations at the  $L_{2,3}$  edges, where one probes directly the correlated  $d$  states. On the other hand, further tests are required before concluding whether the change at the edge jump in  $K$  edges is a universal behaviour in LSDA+ $U$  calculations or not. We recall that at  $K$  edges one probes the  $p$  states, which are sensitive to the  $U$  correction only *via* the coupling with the  $d$  states. At the  $K$  edge (figure 5.3) the LSDA+ $U$  decreases the energy distance between the pre-peak and the main edge. This is a general feature of the LSDA+ $U$  calculations at the  $K$  edge: as the empty  $d$  states are moved to the higher energies, the position of the pre-peak changes accordingly.

## 5.5 Conclusions and perspectives

The LSDA+ $U$  feature in the FDMNES code is supposed to allow an improved treatment of correlated orbitals, more precisely the  $3d$  orbitals of the transition metal compounds and the  $4f$  ones of the rare earths. We have shown that the LSDA+ $U$  results are very sensitive to the occupation numbers of the correlated orbital. Therefore the LSDA+ $U$  requires an accurate underlying electronic structure calculation, which can only be achieved within a self-consistent scheme. Non self-consistent LSDA+ $U$  calculations are often inaccurate, due to the badly calculated occupation numbers.

In practice, one should employ the LSDA+ $U$  for the  $K$  edge calculations in the cases where the LSDA calculated pre-peaks are placed at too low an energy with respect to the edge jump. If, on the other hand, the  $K$  edge pre-peaks' position is too high in energy, the LSDA+ $U$  can only worsen the agreement with the experiment.

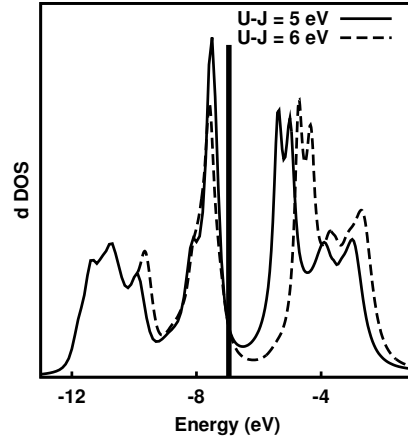


Figure 5.2: The self-consistent  $d$  DOS of the Mn atoms in  $\text{LaMnO}_3$  for two distinct values of the  $U - J$  parameter: 5 (solid) and 6 eV (dashes). The calculations were shifted to the same Fermi levels which is indicated by the thick vertical line. The energies are expressed in an internal energy scale of FDMNES. The value of the gap depends on  $U - J$  and on the average population.

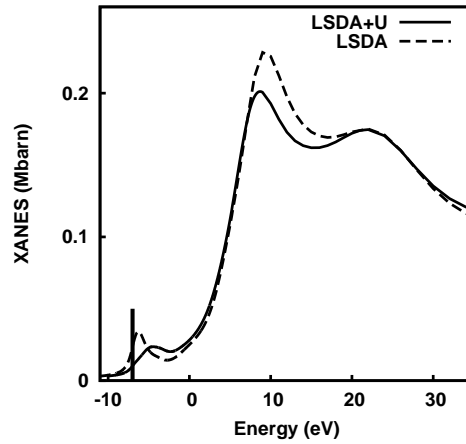


Figure 5.3: The Mn absorption spectra in  $\text{LaMnO}_3$  at the  $K$  edge: with (solid) and without (dashes) the Hubbard  $U$ . The former was shifted by 1.9 eV to the higher energies, in order to superpose the Fermi levels in the two calculations (indicated by the thick vertical line). The  $U$  term changes the shape of the spectrum and the position of the pre-peak.

One might think that the LSDA+ $U$  correction to the LSDA is more significant at the  $L_{2,3}$  and  $M_{4,5}$  edges, where one probes directly the  $d$  and  $f$  states, than at the  $K$  edge. Our results on  $\text{LaMnO}_3$  suggest the opposite: at both edges, the Hubbard correction is liable to change the shape of the XANES signal at the main jump. Nevertheless, further tests on different kind of compounds are needed before concluding upon the effects of the LSDA+ $U$  method at the  $K$  edges.

At the  $L_{2,3}$  edges, the LSDA+ $U$  leads to the reduction the  $L_{2,3}$  branching ratio (see

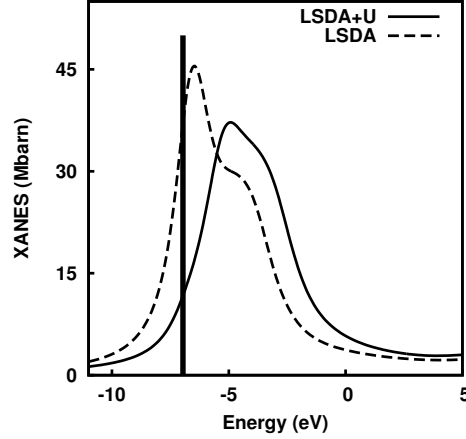


Figure 5.4: The Mn absorption spectra in  $\text{LaMnO}_3$  at the  $L_3$  edge: with (solid) and without (dashes) the Hubbard  $U$ . The former was shifted by 1.9 eV to the higher energies, in order to superpose the Fermi levels in the two calculations (indicated by the thick vertical line). The  $U$  term changes the off-set and the shape of the spectrum.

figure 5.4). Consequently, we are considering using a ground state LSDA+ $U$  calculation (instead of a LSDA one) as the first step of the TDLSDA procedure (see chapter 6) meant to calculate the  $L_{2,3}$  edges of correlated materials.

The present FDMNES implementation of the LSDA+ $U$  uses  $U - J$  as a parameter. In practice, we either take its first principles value from the literature, if available, or make an educated guess on its value. The value of  $U - J$ , weighted by the average population, is identical to the extra gap opening that it brings. Therefore one should be careful not to fit the experiment with unphysical assumptions. We are currently considering the implementation of a first principle, RPA based estimation of  $U$ , to remove these ambiguities.

The results of this chapter are preliminary. More tests and benchmarking are to be foreseen before coming to an ultimate conclusion on the influence of the  $U$  correction on the X-ray core spectroscopy.

## Chapter 6

# Beyond the one body picture

### 6.1 The failure of the single particle approximation

There are cases where the agreement between experimental data and single particle calculations is far from being satisfactory. In the following paragraphs we shall illustrate some typical cases where the single particle picture fails.

**The  $L_{2,3}$  branching ratio of 3d elements** One of the most cited examples when the single particle picture fails concerns the  $L_{2,3}$  edges of the transition metals. In figure 6.1 we show the experimental and calculated absorption at the  $L_{2,3}$  edges of bulk vanadium. Roughly, the experiments shows a 1:1 ratio between the  $L_3$  and the  $L_2$  features, which is obviously not the case in the one body calculation. In the single particle picture, according to the Golden Rule (2.13), one assumes that the  $L_2$  peak comes from the transitions from the  $2p_{1/2}$  core level, whereas  $L_3$  is due to the  $2p_{3/2}$  ones. The manifold of the corresponding initial states are 2 and 4, respectively. It follows that the  $L_3$  feature should be more or less twice as high as the  $L_2$  one. The calculated ratio moves away from this value, due to the spin-orbit coupling of the final

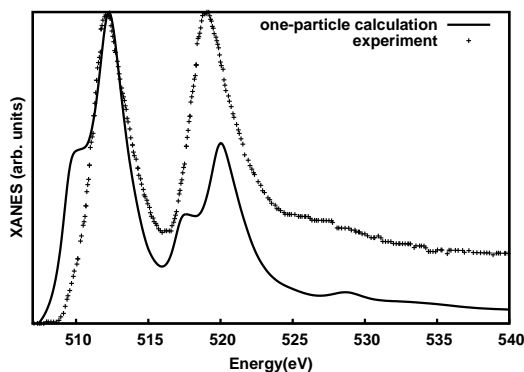


Figure 6.1: Experiment (dots) from reference [98] and FDMNES one body calculation (solid) for the absorption at the  $L_{2,3}$  edges of vanadium. The ratio between the  $L_3$  and the  $L_2$  intensities is ill calculated.



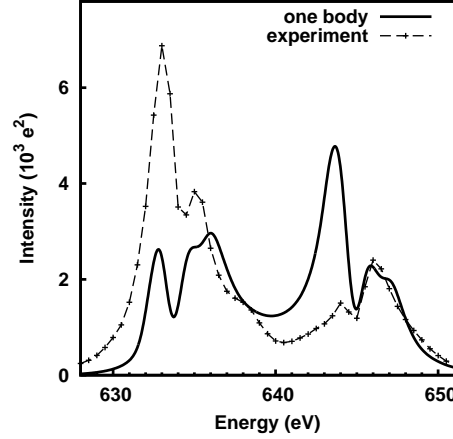


Figure 6.2: The (100) incoming  $\pi$  reflection at the  $L_{2,3}$  edges of manganese in  $\text{Pr}_{0.6}\text{Ca}_{0.4}\text{MnO}_3$ : the one body calculation (solid) *versus* the experiment (with points).

states and to the ratio  $\frac{\omega_{L_3}}{\omega_{L_2}}$  (see equation 1.3). The value  $\approx 2$  for the branching ratio is rigorously exact if one subtracts the continuum background signal. In so far as this work is concerned, we did not do this. Consequently, the actual value of the branching ratio in the one body calculations is  $\approx 1.5$ .

The reason for this disagreement is that the  $L_2$  and the  $L_3$  features cannot be assigned to one of the two core levels exclusively. The two transition channels mix, due to the many body effects. The closer the edges, the more important the mixing. In the language of quantum mechanics, the absence of mixing is indicated by the sum of the square modulus in (1.3). One sums over the probabilities (and not the probability amplitudes !) associated to each transition channel:

$$\sigma \propto \sum_f \sum_i |\langle \phi_f | \hat{O} | \phi_i \rangle|^2 \rho(E) \quad (6.1)$$

**The strongly correlated materials** As we stressed previously in chapter 1.5, the one body calculations are particularly ill-suited when strong correlation is involved. For illustration, we show a diffraction spectrum at the  $L_{2,3}$  edges of manganese in  $\text{Pr}_{0.6}\text{Ca}_{0.4}\text{MnO}_3$ .

**The absorption spectra of rare gases** The multiple electron excitations are a many-body effect which cannot be obtained in a one body picture. During a multiple excitation process, due to correlation effects, other electrons are promoted by the X-ray field, in addition to the usual photoelectron transition. If these extra electrons transit to a bound state, the process is called shake-up. If, on the contrary, the final state is a continuum one, the process is called shake-off. These effects are significant in closed-shell systems, like the rare gases. For some experimental examples, please refer to the references cited in [127].

Numerous attempts to go beyond the one body approximation have been reported (see section 1.5 for details and references). One has to mention the atomic methods (CI,

multiplets) which describe successfully the many body effects, but fail to account for the band modulation of the continuum. On the other hand, the band structure methods like TDDFT or BSE succeed in doing so, but fail to reproduce the localized electronic states. Great hope is placed in the advent of the coupled atomic - band like calculations, such as the multichannel method, the cluster calculations or the DMFT-LDA based methods. It is extremely difficult to build a methodology that works on whatever compound. Should one limit oneself to the delocalized and partially delocalized edges, the TDDFT methods give reasonable results. The rest of this chapter focuses on the formalism and on the implementation of a TDDFT method for X-ray absorption calculation in the FDMNES code, as well as on its successes and limitations.

## 6.2 The time dependent density functional theory

We argued the need to go beyond the single particle picture for electronic structure calculations, and particularly for the X-ray absorption spectroscopy simulations. We equally argued that one is interested in a method that is computationally reasonable for extended systems. Such a solution was first proposed by Zangwill and Soven in 1980 [126]. They proposed an efficient, LDA-based method to describe the local field effects in rare gases. The theoretical basis of this approach were established later in 1984, when Runge and Gross stated and proved the founding theorems of the time dependent density functional theory (TDDFT) [96].

**TDDFT *versus* DFT** The TDDFT integrates time dependence and thus can account for excited states. This feature, essential for spectroscopic calculations, propels TDDFT one step behind the ubiquitous density functional theory (DFT). DFT won recognition due to its success in describing the ground state properties (electronic configuration, atomic distances, ground state energies) of an electronic system. Nevertheless, DFT is not meant to describe the excited states of the system, nor to reproduce the excitation spectra. In spite of all this, the DFT might give a satisfactory agreement, under the limiting conditions discussed in chapter 1.5.

Both DFT and TDDFT are an alternative to the Schrödinger (many body) wavefunction formulation of quantum mechanics. They no longer rely on the many body wavefunction, but on the electron density. While the wavefunction depends on  $3N+1$  variables, with  $N$  the number of electrons in the system, the density depends on only four variables (three spacial + time). Consequently, the many body problem becomes computationally tractable.

**TDDFT for solids** TDDFT was initially used in quantum chemistry and applied to the study of the excitation of molecules under an external field (optical spectra, laser pulses etc.). The use of TDDFT in condensed matter studies is more recent [19, 84]. In the thermodynamic limit (in our case, for the extended systems) the exchange-correlation functionals of quantum chemistry lose their special behaviour and are no longer useful [70]. Solid state systems have a huge number of basis functions, which makes the engineering of an exchange-correlation functional adapted to the extended system impossible in practice. Therefore, exchange-correlation functionals in condensed matter studies are variations of the exchange-correlation of the uniform electron gas.

The limitations of this model makes TDDFT less successful for solids than it is for molecules.

**TDDFT and synchrotron radiation** We have already stated that the TDDFT is naturally tailored to describing spectroscopy. We shall see that, depending on the strength of the incoming radiation, TDDFT can be treated either within the linear response or by solving the full time propagation of the ground state. The latter, though extremely resource consuming, is mandatory when one deals with laser pulses or X-FELs, i.e. for fields whose intensity is of the same order of magnitude with electric fields inside the atom. In this manuscript only the standard (weak) fields of the third generation synchrotron are to be considered, which is where the perturbation theory works.

**TDDFT within this work** According to the overview in chapter 1.5, TDDFT has recently been applied to core spectroscopy [7, 64, 92, 101]. Although we do not claim to have developed an original theoretical framework, we consider this work to be an important study of the TDDFT applied the X-ray core spectroscopic frequency range, as the previous ones are not sufficiently well established. We propose our own implementation of the TDDFT method and perform a detailed study of its applicability and performance. We make numerous references to the existing TDDFT methods and reveal behaviour that has not previously been discussed in the literature. At the present time, the X-ray absorption community lacks an advanced study of the suitability of the various exchange-correlation kernels. Our work aims to fill in these gaps. Such a study is mandatory before attempting the implementation of more sophisticated many body methods.

### 6.2.1 The formalism

In the remainder of this section we shall present the founding principles of the TDDFT. For an extended discussion please refer to references [19, 70]. Let a system of  $N$  electrons, submitted to an external perturbation  $\hat{V}_{ext}$  (the electromagnetic field, for instance) acting from  $t = 0$ . The system is described by the Hamiltonian (in Rydberg units):

$$\hat{H} = - \sum_i^N \nabla^2 + \sum_{i \neq j}^N \frac{1}{|\vec{r}_i - \vec{r}_j|} + \hat{V}_{ext} \quad (6.2)$$

where the first term is the kinetic energy, the second one is the Coulomb repulsion and  $\hat{V}_{ext} = \sum_i^N v_{ext}(\vec{r}_i, t)$  is the problem specific, external potential. Note that this Hamiltonian ignores the nuclei, which are either considered fixed or treated classically (the Born-Oppenheimer approximation).

Similar to the DFT, TDDFT is based on a one to-one correspondence between the wavefunction of the system, the total potential and the density:

$$V(\vec{r}, t) \leftrightarrow \Psi(\vec{r}_1, \vec{r}_2, \dots \vec{r}_N, t) \leftrightarrow n(\vec{r}, t) \quad (6.3)$$

The milestone of the TDDFT is the Runge-Gross theorem [96], which yields the precise form of this mapping. This theorem states that for a given initial state  $\Psi(t = 0)$ , two

different external potentials  $v_{ext}(\vec{r}, t)$  and  $v'_{ext}(\vec{r}, t)$  yield different densities provided they differ by more than a purely function of time. Under these restrictions the external potential is a functional of the density.

We stress that the above argument can be formulated in terms of spin densities. With the same restrictions, there is a mapping between  $v_{ext}^\uparrow(\vec{r}, t)$  ( $v_{ext}^\downarrow$ ) and  $n^\uparrow(\vec{r}, t)$  ( $n^\downarrow$ ). It follows that the external potential is a functional of the two spin densities:  $v_{ext}[n^\uparrow, n^\downarrow]$ .

Since the many-body SE is not tractable, solving (6.2) is problematic. To overcome this impediment, one applies the same procedure as in the case of the DFT to reduce the complexity to that of a one body problem. One constructs a fictitious system of non-interacting particles (the so-called Kohn-Sham system) which yields a density identical to the one of the real system. The time evolution of the auxiliary system obeys the Kohn-Sham equations:

$$i \frac{\partial \phi_i(\vec{r}, t)}{\partial t} = [-\nabla^2 + v_{KS}[n](\vec{r}, t)] \phi_i(\vec{r}, t) \quad (6.4)$$

with

$$v_{KS}[n](\vec{r}, t) = v_{ext}(\vec{r}, t) + v_H(\vec{r}, t) + v_{xc}[n](\vec{r}, t) \quad (6.5)$$

the Kohn-Sham one body potential and

$$n(\vec{r}, t) = \sum_i^N |\phi_i(\vec{r}, t)|^2 \quad (6.6)$$

the genuine density, built from the Kohn-Sham single particle eigenstates  $\phi_i(\vec{r}, t)$ . Note that  $\phi_i(\vec{r}, t)$  are not the true eigenfunctions of the interacting system, and only their square modulus is meaningful. Here the notation  $v_{xc}[n](\vec{r}, t)$  signifies that the potential in  $(\vec{r}, t)$  is generally non-local, a functional of the density  $n$  in every point, and not necessarily in the  $(\vec{r}, t)$ .

From the Runge-Gross theorem one infers that the exchange-correlation potential  $v_{xc}[n](\vec{r}, t)$  is a functional of the density  $n(\vec{r}, t)$  and of the interacting and Kohn-Sham systems' initial wavefunctions,  $\Psi(0)$  and  $\Phi(0)$ , respectively. In practice we consider that the ground state is non-degenerate. Consequently, any dependence on the initial state drops out. This procedure is always applied for extended systems studies.

The philosophy behind the TDDFT is to alias the interacting system of interest with a non-interacting one (the Kohn-Sham system), which one is able to solve. The missing piece of the puzzle is the exchange-correlation potential  $v_{xc}[n](\vec{r}, t)$ . The Runge-Gross theorem guarantees that the exchange-correlation potential is a functional of the density, that is unique and independent of the specificity of the problem (i.e. of the external potential  $v_{ext}$ ). Nonetheless, no exact analytical form of  $v_{xc}[n](\vec{r}, t)$  is known and one has to approximate it.

One way to solve the many-body problem (6.2) would be to calculate the evolution operator of (6.4), propagate the initial state  $\Phi(0)$ , which can be factorized in terms of Kohn-Sham orbitals as  $\Phi(0) = \prod_i \phi_i(0)$ , and finally deduce the time evolution of the system from (6.6). This procedure is extremely costly and is not really necessary unless high external fields are employed. For small fields the perturbation theory is valid and one may work in the linear response approximation.

### 6.2.2 The linear response regime

The essence of the linear response (LR) theory is that it describes the response of a system to an external perturbation by employing ground state quantities. Such an approach is pertinent only if the external perturbation does not modify the density far from its ground state value.

The key quantity of the LR theory is the response function  $\chi$ , also called susceptibility, or the density - density correlation function of the Kubo theory. One defines:

$$n(\vec{r}, t) = n(\vec{r}, 0) + \int_{-\infty}^t dt' d^3r' \chi(\vec{r}, \vec{r}', t, t') \delta v_{ext}(\vec{r}', t') \quad (6.7)$$

$\chi$  shows in what way the perturbing potential of the electromagnetic wave  $\delta v_{ext}$ , acting in  $\vec{r}'$  at  $t'$ , changes the density  $n$  in  $\vec{r}$  and at the instant  $t$ . The response function  $\chi$  contains all the information on the first order response of the system. An equivalent form of (6.7) yields:

$$\chi(\vec{r}, \vec{r}', t, t') = \left. \frac{\delta n(\vec{r}, t)}{\delta v_{ext}(\vec{r}', t')} \right|_{n=n(t=0)} \quad (6.8)$$

Note that  $\chi$  is calculated from quantities belonging to the unperturbed system.

Equation (6.7) is written for the interacting many body system. One can write an analogue expression for the non-interacting Kohn-Sham system:

$$\begin{aligned} n(\vec{r}, t) = n(\vec{r}, 0) &+ \int_{-\infty}^t dt' d^3r' \chi_0(\vec{r}, \vec{r}', t, t') \\ &\times \left[ \delta v_{ext}(\vec{r}', t') + \delta v_H(\vec{r}', t') + \delta v_{xc}[n](\vec{r}', t') \right] \end{aligned} \quad (6.9)$$

Note that (6.7) and (6.9) involve the *same* density variation  $\delta n(\vec{r}, t) = n(\vec{r}, t) - n(\vec{r}, 0)$ , due to the very definition of the Kohn-Sham system: it is meant to yield the same density as the one of the interacting system.

**The Dyson-like equation** We wish to connect  $\chi$  to  $\chi_0$ . To do so, we take the functional derivative of (6.5):

$$\left. \frac{\delta v_{KS}(\vec{r}, t)}{\delta n(\vec{r}', t')} \right|_{n=n(t=0)} = \left. \frac{\delta v_{ext}(\vec{r}, t)}{\delta n(\vec{r}', t')} \right|_{n=n(t=0)} + \left. \frac{\delta v_H(\vec{r}, t)}{\delta n(\vec{r}', t')} \right|_{n=n(t=0)} + \left. \frac{\delta v_{xc}[n](\vec{r}, t)}{\delta n(\vec{r}', t')} \right|_{n=n(t=0)} \quad (6.10)$$

By employing (6.8) and (6.9) one gets an operatorial, Dyson-like renormalisation equation:

$$\begin{aligned} \hat{\chi}_0^{-1} &= \hat{\chi}^{-1} + f_H + f_{xc} \\ \hat{\chi} &= \hat{\chi}_0 + \hat{\chi}_0(f_H + f_{xc})\hat{\chi} \end{aligned} \quad (6.11)$$

$f_H$  and  $f_{xc}$  are the Hartree and the exchange-correlation kernel, respectively (see the appendix). Equation (6.11) is an operatorial equation. In the reciprocal space  $(k, \omega)$  it reduces to a simple product, whereas in the direct one it becomes an integral equation, as shown later in (6.25). Equation (6.11) is often referred to as the Dyson-like equation, due to the similarities to the Dyson equation (2.41) for the Green function of an interacting system.

**The absorption cross section** The imaginary part of the response function is directly connected to the absorption cross section [126]:

$$\sigma(\omega) = -\frac{4\pi\omega}{c} \sum_{\sigma\sigma'} \Im \int d^3r \int d^3r' \hat{O}^\dagger(\omega, \vec{r}') \chi^{\sigma\sigma'}(\omega, \vec{r}, \vec{r}') \hat{O}(\omega, \vec{r}) \quad (6.12)$$

where  $\hat{O}$  is the transition operator (2.11) corresponding to the (unscreened) external potential  $\delta v_{ext}$ . All through this chapter, we shall be using the atomic unit system. The analogous of (6.12) for the Kohn-Sham system reads [126]:

$$\sigma(\omega) = -\frac{4\pi\omega}{c} \sum_{\sigma\sigma'} \int d^3r \int d^3r' \hat{O}^\dagger(\omega, \vec{r}') \Im \chi_0^{\sigma\sigma'}(\omega, \vec{r}, \vec{r}') \hat{O}'(\omega, \vec{r}) \quad (6.13)$$

Note that  $\hat{O}' = \epsilon^{-1} \hat{O}$  describes the screening of the photon field, with  $\epsilon$  the dielectric matrix.

If one plugs in  $\chi_0$  instead of  $\chi$  in (6.12) one would expect a result identical to the absorption calculated in the MST framework, for a ground state (no core hole) cluster. In the terminology of chapter 4 this corresponds to the screening scheme (a).

To our knowledge, all the TDDFT calculations for X-ray absorption spectroscopy have been performed in the dipole approximation [7, 99, 101]. We stress the fact that our implementation of the TDDFT can account in principle for the matrix elements beyond the dipole approximation (E1-E2 and E2-E2 introduced in section 2.2.1) and make use of them for the calculation of the absorption signal (6.12).

Formally, the TDDFT implementation we propose is similar to the one of Schwitalla and Ebert [101] in the sense that the many body corrections are contained within  $\chi$  and the absorption cross section is calculated from (6.12). An equivalent way to do this, provided the potential takes real values, would be to plug the many body effects directly into the field operator, following the prescription of Zangwill and Soven [126]. This method was employed by Ankudinov, Nesvizhskii and Rehr [7], who calculate the absorption cross section from (6.13) and consider the screened photon field  $\hat{O}'$  instead of the external one  $\hat{O}$ . In principle, these two procedures are equivalent.

### 6.2.3 The ground state response function

To explain the formalism we chose the zero spin-coupling limit. Please refer to the appendix for the fully relativistic formulae. Concerning the wavefunctions, we shall be using the following notations ( $\hbar = 1$ ):

$$\phi_g^\sigma(\vec{r}) = c_{g\Lambda_g^\sigma}^\sigma b_{\Lambda_g}^\sigma(r) Y_{\Lambda_g}(\Omega) \quad (6.14)$$

$$\Psi_\Lambda^\sigma(\vec{r}, E) = b_\Lambda^\sigma(r, E) Y_\Lambda(\Omega) \quad (6.15)$$

$$\tilde{\Psi}_\Lambda^{\sigma f}(\vec{r}, E) = a_\Lambda^{\sigma f}(E) b_\Lambda^\sigma(r, \omega + E_g) Y_\Lambda(\Omega) \quad (6.16)$$

Here  $\Psi$  and  $\tilde{\Psi}$  are the final state wavefunctions, the latter being normalized to the square root of the density of states of the vacuum.  $\phi$  describe the initial states  $g$ . Let

the ground state susceptibility  $\chi_0$  ( $\epsilon \rightarrow 0$ ):

$$\chi_0^{\sigma\sigma'}(\vec{r}, \vec{r}', \omega) = \sum_{g(E_g < E_F)} \sum_{\Lambda\Lambda'} \sum_f \int_{E_F}^{\infty} \frac{\phi_g^{\sigma}(\vec{r}) \tilde{\Psi}_{\Lambda}^{\sigma f \dagger}(\vec{r}, E) \tilde{\Psi}_{\Lambda'}^{\sigma' f}(\vec{r}', E) \phi_g^{\sigma' \dagger}(\vec{r}')}{\omega - (E - E_g) + i\epsilon} \quad (6.17)$$

$$\chi_0^{\sigma\sigma'}(\vec{r}, \vec{r}', \omega) = -\frac{1}{\pi} \sum_{g(E_g < E_F)} \sum_{\Lambda\Lambda'} \int_{E_F}^{\infty} \frac{\phi_g^{\sigma}(\vec{r}) \Psi_{\Lambda}^{\sigma \dagger}(\vec{r}, E) \Im \tau_{\Lambda\Lambda'}^{\sigma\sigma'} \Psi_{\Lambda'}^{\sigma'}(\vec{r}', E) \phi_g^{\sigma' \dagger}(\vec{r}')}{\omega - (E - E_g) + i\epsilon} \quad (6.18)$$

We recall that  $\chi_0$  is the response function for a system of non-interacting particles. Equations (6.17) and (6.18) are simplified forms of the Adler-Wiser equation. Their equivalence is easy to see given the optical theorem (2.49). The Adler-Wiser equation [84] normally involves all the occupied ( $g$  index) and unoccupied (energy  $E$ ) states. Nevertheless, in the resonant case, and thus at high energies beyond the optical spectrum, one can assume that the only significant contribution is brought in by the levels whose energy  $E$  is close to the photon energy  $\omega$ , i.e. the concerned core levels. We stress the fact that the energies  $\omega$  and  $E$  are expressed into different scales: the former describes the photon, whereas the latter belongs to the photoelectron.  $E_g$  is the Kohn-Sham energy of the  $g$  state, i.e. the expectation value of the DFT local density approximation hamiltonian  $\mathcal{H}_{LDA}$ :

$$E_g = \frac{\langle \phi_g | \mathcal{H}_{LDA} | \phi_g \rangle}{\langle \phi_g | \phi_g \rangle} \quad (6.19)$$

$\chi_0$  is diagonal over the initial state index  $g$ , meaning that in a single particle picture the different channels available to the electronic transition do not mix. In the language of many body physics, inserting  $\chi_0$  into (6.12) provides the absorption cross section  $\sigma$  in the random phase approximation with no local field effects (RPA).

In the following we shall exploit the formalism developed by Schwitalla and Ebert in [101]. We are interested in a spherical harmonics representation for  $\chi_0$ . Consequently, we are considering an expansion of the following kind:

$$\begin{aligned} \chi_0^{\sigma\sigma'}(\vec{r}, \vec{r}', \omega) &= \sum_{gg'} \delta_{gg'} \sum_{\Lambda\Lambda'} \tilde{\chi}_{0gg', \Lambda\Lambda'}^{\sigma\sigma'}(\omega) \\ &\times \phi_g^{\sigma}(\vec{r}) \Psi_{\Lambda}^{\sigma \dagger}(\vec{r}, \omega + E_g) \Psi_{\Lambda'}^{\sigma'}(\vec{r}', \omega + E_{g'}) \phi_{g'}^{\sigma' \dagger}(\vec{r}') \end{aligned} \quad (6.20)$$

as if we were projecting  $\chi_0$  on the "set" of functions formed by the initial state wavefunctions  $\phi$  and the final state ones  $\Psi$ . We stress the idea that  $\phi_g$  and  $\Psi_{\Lambda}$  do not form a basis set, as they are not orthogonal. The peculiar feature of our calculation is that we do not use a fixed basis, but perform an exact solution of the electronic structure, yielding the energy dependence of  $\Psi_{\Lambda}$ . Consequently, the energy dependence of  $\Psi$  is bothering and needs to be counterbalanced by considering an energy dependence in the very form of  $\tilde{\chi}_{0gg', \Lambda\Lambda'}^{\sigma\sigma'}(\omega)$ . We suppose that a similar development is also valid for  $\chi$ .

**The connection to the multiple scattering amplitude** We are trying to establish the connection between  $\chi$  and  $\tau$ , the multiple scattering amplitude of the MST. Let us investigate the similarities between the results of the LR theory and the MST for the absorption cross section. We recall that in the MST and in the complex spherical harmonics basis:

$$\sigma(\omega) = -\frac{4\pi\omega}{c} \int d^3r \int d^3r' \sum_{\sigma\sigma'} \sum_{gg'} \int_{E_F}^{\infty} dE O(\omega, \vec{r}) O^*(\omega, \vec{r}') \phi_{g'}^{\sigma'\dagger}(\vec{r}') \sum_{\Lambda\Lambda'} \Im \tau_{\Lambda\Lambda'}^{\sigma\sigma'} \Psi_{\Lambda'}^{\sigma'}(\vec{r}', \omega + E_{g'}) \Psi_{\Lambda}^{\sigma\dagger}(\vec{r}, \omega + E_g) \phi_g^{\sigma}(\vec{r}) \quad (6.21)$$

One can treat the projection of the susceptibility  $\tilde{\chi}$  and the multiple scattering amplitudes  $\tau$  on equal footing:

$$\tilde{\chi}_{0gg',\Lambda\Lambda'}^{\sigma\sigma'} \equiv \tau_{\Lambda\Lambda'}^{\sigma\sigma'} \quad (6.22)$$

The equivalence is easy to see if one compares (6.21) to (6.13), all by using the definition of  $\tilde{\chi}_{0gg',\Lambda\Lambda'}^{\sigma\sigma'}$  in (6.21). This is a remarkable result and it was first suggested by Schwitalla and Ebert [101]. We recall that the equivalence does no longer hold if  $\tau$  is issued from a (mathematical) complex potential. The equivalence between  $\Im\tilde{\chi}$  and  $\Im\tau$  equally holds if the latter is calculated in the FDM. In this case,  $\Im\tau$  may be expressed in function of the atomic amplitudes (section 2.3.4) and keeps the same physical meaning. The advantage of coupling the TDDFT procedure to a full potential ground state calculation are obvious provided the non-spherical effects are significant.

Let:

$$\tilde{\chi}_{0gg',\Lambda\Lambda'}^{\sigma\sigma'}(\omega) = - \int_{E_F}^{\infty} \frac{dE}{\pi} \frac{\Im \tau_{\Lambda\Lambda'}^{\sigma\sigma'}(E) \delta_{gg'}}{\omega - (E - E_g) + i\epsilon} \frac{Z_{\sigma'}^{g'\Lambda'}(E) Z_{\sigma}^{g\Lambda}(E)}{Z_{\sigma'}^{g'\Lambda'}(\omega + E_g) Z_{\sigma}^{g\Lambda}(\omega + E_{g'})} \quad (6.23)$$

an equivalent form with (6.22), where

$$Z_{\sigma}^{g\Lambda}(E) = \int_0^R dr r^2 b_{\Lambda_g}^{\sigma}(r) b_{\Lambda}^{\sigma}(r, E) \quad (6.24)$$

is some energy dependent function that is supposed to account for the energy modulations in  $\Psi$ . In our actual implementation,  $Z$  has no dependence on the initial state  $g$ , as we consider that the radial wavefunctions describing the core levels depends on  $n$  and  $l$  only, and not on  $j$ . Note that the  $Z$  normalisation procedure in (6.23) is reasonable as long as the energy dependence in  $Z$ , and consequently in the radial final state wavefunctions, is weak. We stress upon the fact that this is the only approximation introduced by the method and otherwise the expansions in (6.20) and (6.23) would be exact.

#### 6.2.4 The kernel

We have already seen that in LR-TDDFT, the response function is renormalised to include the many body effects:

$$\begin{aligned} \chi^{\sigma\sigma'}(\vec{r}, \vec{r}', \omega) &= \chi_0^{\sigma\sigma'}(\vec{r}, \vec{r}', \omega) + \sum_{\sigma''\sigma'''} \int d^3r'' \int d^3r''' \\ &\times \chi_0^{\sigma\sigma''}(\vec{r}, \vec{r}'', \omega) K^{\sigma''\sigma'''}(\vec{r}'', \vec{r}''') \chi^{\sigma'''\sigma'}(\vec{r}''', \vec{r}', \omega) \end{aligned} \quad (6.25)$$



This expression is a form of the operatorial Dyson-like equation (6.11), projected on the  $|r\rangle$  basis. Ideally, the integral kernel  $K$  describes the many body effects, including the core hole interaction.  $\chi_0$  is the ground state response function and  $\chi$  is the one accounting for the many body corrections described by  $K$ .

The TDDFT is in principle an exact theory, provided the kernel integrates the full interactions. Whatsoever, as no exact analytical form of the exchange-correlation is available, one has to assume the form of  $K$ . The physics one may describe and the accuracy of the description are tributary to the choice of the *ansatz*.

To avoid the solving of the integral equation (6.25), we project the operatorial Dyson-like equation (6.11) on the "basis" introduced in (6.20):

$$\begin{aligned} \tilde{\chi}_{gg',\Lambda\Lambda'}^{\sigma\sigma'}(\omega) &= \tilde{\chi}_{0gg,\Lambda\Lambda'}^{\sigma\sigma'}(\omega) \\ &+ \sum_{g'''} \sum_{\sigma'',\sigma'''} \sum_{\Lambda'',\Lambda'''} \tilde{\chi}_{0gg,\Lambda\Lambda''}^{\sigma\sigma''}(\omega) \tilde{K}_{gg''',\Lambda''\Lambda'''}^{\sigma''\sigma'''}(\omega) \tilde{\chi}_{g''',\Lambda'''\Lambda'}^{\sigma'''\sigma'}(\omega) \end{aligned} \quad (6.26)$$

where we have used  $\chi_{0gg'}^{\sigma\sigma'} = \chi_{0gg'}^{\sigma\sigma'} \delta_{gg'}$ . We are interested in  $\tilde{K}$ , the projection of the kernel on the same "basis" functions as in (6.20). One notices that, unlike  $\chi_0$ ,  $\tilde{K}$  is not diagonal in the initial states. We plug in (6.25) the expansions of type (6.20) for both  $\chi_0$  and  $\chi$  and identify with (6.26). One obtains:

$$\begin{aligned} \tilde{K}_{gg',\Lambda\Lambda'}^{\sigma\sigma'}(\omega) &= \int d^3r \int d^3r' K^{\sigma\sigma'}(\vec{r}, \vec{r}', \omega) \\ &\times \phi_g^{\dagger}(\vec{r}) \Psi_{\Lambda}^{\sigma}(\vec{r}, \omega + E_g) \phi_{g'}^{\sigma'}(\vec{r}') \Psi_{\Lambda'}^{\sigma'\dagger}(\vec{r}', \omega + E_{g'}) \end{aligned} \quad (6.27)$$

As a technical detail, note the difference with (6.20) in terms of hermitian conjugate factors. In this sense, the form of  $\tilde{K}$  both in reference [101] (eq. 11) and in [9] (eq. 26) is not general (but nevertheless correct in the case of kernels that take only real values).

In its most general form, the TDDFT kernel can be split into a classical Coulomb (Hartree) term  $f_H$  and an exchange-correlation contribution  $f_{xc}$ :

$$K^{\sigma\sigma'}(\vec{r}, \vec{r}', \omega) = f_H^{\sigma\sigma'}(\vec{r}, \vec{r}') + f_{xc}^{\sigma\sigma'}(\vec{r}, \vec{r}', \omega) \quad (6.28)$$

where  $f_H$  is local and independent of spin, and expressed in Hartree units (for a rigorous proof please refer to the appendix):

$$f_H^{\sigma\sigma'}(\vec{r}, \vec{r}') = \frac{1}{|\vec{r} - \vec{r}'|} \quad (6.29)$$

In the following we shall discuss several approximations for the exchange-correlation part of the kernel  $f_{xc}$ , and the physics they imply.

### 6.2.5 The local fields effect

The local fields (LF) effect are due to the internal polarization of the sample when penetrated by the X-rays and are a consequence of the atomic structure of the sample. The physical phenomenon that gives the local fields effect is simply the re-arrangement of the electrons in the sample, when subjected to the electromagnetic field.

The local fields picture introduces the concept of electron and holes and allows some electron-electron (hole-hole) interaction. The electron-hole pairs create an internal electric field which opposes the one of the electromagnetic wave. In other words, the local fields are responsible for the screening of the X-ray field. The local fields are long-ranged and their effect next to the absorber's nucleus is minimum [126]. Therefore the screening they introduce is not proper to the core hole, but to the X-ray external field. The RPA-LF approximation to the TDDFT consists in imposing  $f_{xc}^{\sigma\sigma'}(\vec{r}, \vec{r}', \omega) = 0$ . The corresponding TDDFT kernel reads:

$$K^{\sigma\sigma'}(\vec{r}, \vec{r}', \omega) = \frac{1}{|\vec{r} - \vec{r}'|} \quad (6.30)$$

### 6.2.6 The adiabatic local density approximation

A straightforward way to add some exchange and correlation effects to the RPA-LF description is "to recycle" the LSDA to the time-dependent situation. This method goes under the name of adiabatic local density approximation (ALDA) or the time dependent local (spin) density approximation (TDLSDA). The adiabatic approximation excludes the memory effects, and the exchange-correlation potential depends uniquely on the density in the ground state (i.e. at  $t = 0$ ):

$$v_{xc}[n](\vec{r}, t) = v_{xc}[n(t)](\vec{r})|_{n=n(t=0)} \quad (6.31)$$

where  $v_{xc}[n]$  is provided in references [51] and [52] (see section 3.1.2). The corresponding exchange-correlation kernel gives:

$$f_{xc}^{\sigma\sigma'}(\vec{r}t, \vec{r}'t') = \left. \frac{\delta v_{xc}[n(t), \sigma](\vec{r})}{\delta n_{\sigma'}(\vec{r}', t')} \right|_{n(t=0)} \quad (6.32)$$

One sees that  $f_{xc}^{\sigma\sigma'}$  generates a potential that is local both in space and in time, and that may mix the spin channels. It follows that:

$$K^{\sigma\sigma'}(\vec{r}, \vec{r}', \omega) = \frac{1}{|\vec{r} - \vec{r}'|} + f_{xc}^{\sigma\sigma'}(\vec{r}) \delta(\vec{r} - \vec{r}') \quad (6.33)$$

The Fourier transformed  $\delta(t - t')$  term in (6.32) will give no  $\omega$  dependence, i.e. the TDLSDA kernel is independent of energy. The TDLSDA kernel may indirectly integrate an  $\omega$  dependence, provided one uses the Hedin correction for the exchange-correlation potential, as described in section 3.1.2. The TDLSDA has the same fundamental characteristics as its ground state equivalent, the LSDA. It is spatially local, as the potential  $v_{xc}$  depends exclusively on the density in the very same position.

The time dependent equivalent of the LDA inherits the same pathologies as its parent's [19]. For finite systems, the main limitation of the TDLSDA is given by the ill behaving asymptotic behaviour of the local functionals. At very large distances, the real Coulomb potential decays as  $1/r$ , whereas the L(S)DA total potential decays exponentially (like the density) and does not cancel the former. In infinite systems, the worrying feature of the TDLSDA exchange-correlation kernel is its dependence on the local density. Therefore the TDLSDA works in systems where the electrons are rather delocalized, i.e. where no dramatic variations of the potential occur. It follows that

TDLSDA overestimates delocalization. Only non-local functionals may account correctly for charge transfer, thus TDLSDA fails to predict localized charges. Moreover, TDLSDA cannot predict bound excitons [84]. For optical excitations, the TDLDA gives reasonable results in most of the cases in finite systems, but not in extended ones [19]. It has been argued [19] that the case of core electron spectra is in many regards similar to the situation of finite systems. For a detailed discussion, please refer to section 6.4.

We draw attention to the fact that, with a view towards accuracy, we implemented the TDLSDA, and not the TDLDA, kernel. The exchange-correlation potential given by the TDLSDA in the spin unpolarized case is equal to the TDLDA one. Note that this is not the case for the exchange-correlation kernels.

Compared to the RPA-LF, the TDLSDA brings the local (short-range) interaction between electrons and holes as an extra ingredient. The core hole is a localized entity. To achieve a minimum description of its interactions, one should use a non-local, and eventually frequency dependent, exchange-correlation potential (and kernel).

### 6.2.7 The restricted adiabatic approximation

The restricted TDL(S)DA is more or less an interpolation between the RPA-LF and the TDL(S)DA. The idea is to use the TDLSDA correlation for the kernel elements that connect identical states, and the RPA-LF for the rest:

$$K^{\sigma\sigma'}(\vec{r}, \vec{r}', \omega) \Big|_{gg'} = \frac{1}{|\vec{r} - \vec{r}'|} + \delta_{gg'} f_{xc}^{\sigma\sigma'}(\vec{r}) \delta(\vec{r} - \vec{r}') \quad (6.34)$$

This kernel was first introduced by Ankudinov, Nesvizhskii and Rehr [7] on a claimed BSE justification and is supposed of providing a better description of the core hole. According to Ankudinov and Rehr [9], should  $f_{xc}$  describe the core hole, the latter's localisation determines the spherical symmetry of the screened potential. Therefore  $f_{xc}$  only couples states with identical total momentum  $j$ . For a detailed discussion of the pertinence of this choice of the kernel, please refer to section 6.4. In [7], the kernel in (6.34) is called the dynamical TDLDA, due to a supposed energy dependence. We nevertheless prefer another nomenclature, as the kernel in (6.34) depends on the energies of the initial states, and not on  $\omega$ , the photon's energy.

One could equally try using the exchange-correlation contribution only between the states of equal energy (the second restricted TDL(S)DA):

$$K^{\sigma\sigma'}(\vec{r}, \vec{r}', \omega) \Big|_{gg'} = \frac{1}{|\vec{r} - \vec{r}'|} + \delta(E_g - E'_g) f_{xc}^{\sigma\sigma'}(\vec{r}) \delta(\vec{r} - \vec{r}') \quad (6.35)$$

In practice, the results of the second restricted TDL(S)DA are extremely close to the restricted TDL(S)DA ones. We therefore choose not to pursue in this direction.

### 6.2.8 The limitations of these kernels

The resonances of  $\chi_0$  in (6.18) are infinitely narrow ( $\epsilon \rightarrow 0$ ) and are placed at the single particle excitation energies of the system. On the contrary, those of  $\chi$  (issued from a "perfect" calculation) have a finite width and are described by poles in the complex plane, whose real part gives the excitation energies whereas the imaginary one is related

to the excitation lifetime. Generally speaking,  $\chi$  has more poles than  $\chi_0$  does. The singularities of  $\chi_0$  are related to the single particle excitations in the system, whereas the extra ones introduced by  $\chi$  account for the multi-electron excitations (double, triple etc. or collective).

The approximations we made for the exchange-correlation kernel cannot possibly add extra peaks to the spectrum (missing in the IPA calculation) other than plasmon ones. To see double excitations (two different electrons in an excited state), it is mandatory to have an energy dependent kernel [68]. This is not the case in our calculations. We recall that the energy dependence of the restricted TDLSDA kernel is trivial and thus unable to reproduce such sophisticated features. Therefore, our implementation of the TDDFT is unable to feature peaks due to the multi-electron excitations. To our knowledge, this limitation concerns all the present TDDFT calculations for extended systems.

Physically, an energy dependence of the exchange-correlation kernel means that it describes memory effects, i.e. the exchange-correlation functional depends on the density at a previous time. It has been shown that a time (energy) dependent exchange-correlation kernel is not pertinent unless it is nonlocal [38]. At the present time and to our knowledge, no such functional has been implemented in an X-ray absorption calculation.

None of the kernels we introduced describes the core hole explicitly. Moreover, its interactions were not taken into account directly, although the energy dependence of the restricted TDLSDA may be seen as a substitute of it [7]. An explicit treatment of the core hole effect implies having a kernel that describes the electron - hole interaction non-locally, in both space and time (the excitonic effect). At the moment, this is possible either by exploiting the BSE formalism [105] for the localized exciton, or, in a lesser extent, by appealing to the extremely recent (and still to be tested and implemented) TDLDA+U non-local functional [63]. We recall that for the time being no exchange-correlation kernel that includes the multiplet effect is available.

## 6.2.9 The spherical harmonics expansion

This section introduces quantities that are specific to the FDMNES implementation of the TDDFT method. We use the spherical harmonics development of the Hartree potential, as proposed in reference [3]:

$$\frac{1}{|\vec{r} - \vec{r}'|} = \sum_{\Lambda_0} \frac{4\pi}{2l_0 + 1} \frac{r_{<}^{l_0+1}}{r_{>}^{l_0}} Y_{\Lambda_0}^*(\Omega) Y_{\Lambda_0}(\Omega') \quad (6.36)$$

where  $r_{<} = \min(r, r')$  and  $r_{>} = \max(r, r')$ .

We stress upon the idea that this TDDFT method requires that the ground state resolution of the SE is performed with a real potential, due to its inability to treat the singular solution. Therefore all the radial functions are real and we drop the cc. for the radial functions. The contributions in (6.28) give:

$$\tilde{K}_{gg',\Lambda\Lambda'}^{\sigma\sigma'}(\omega) = \tilde{f}_{H_{gg',\Lambda\Lambda'}}^{\sigma\sigma'}(\omega) + \tilde{f}_{xc_{gg',\Lambda\Lambda'}}^{\sigma\sigma'}(\omega) \quad (6.37)$$

where, with the aid of (6.36) and (6.27):

$$\begin{aligned}
\tilde{f}_{H_{gg'}, \Lambda\Lambda'}^{\sigma\sigma'}(\omega) &= c_{g\Lambda_g}^\sigma c_{g'\Lambda_{g'}}^{\sigma'} \sum_{\Lambda_0} \frac{4\pi}{2l_0+1} \int d\Omega' Y_{\Lambda_0}(\Omega') Y_{\Lambda_{g'}}(\Omega') Y_{\Lambda'}^*(\Omega') \\
&\times \int d\Omega Y_{\Lambda_0}^*(\Omega) Y_{\Lambda_g}^*(\Omega) Y_{\Lambda}(\Omega) \\
&\times \left( \int_0^R dr r^2 b_{\Lambda}^\sigma(r, \omega + E_g) b_{\Lambda_g}^\sigma(r) \int_0^r dr' r'^2 b_{\Lambda_{g'}}^{\sigma'}(r') b_{\Lambda'}^{\sigma'}(r', \omega + E_{g'}) \frac{r'^{l_0+1}}{r^{l_0}} \right. \\
&+ \left. \int_0^R dr r^2 b_{\Lambda}^\sigma(r, \omega + E_g) b_{\Lambda_g}^\sigma(r) \int_r^R dr' r'^2 b_{\Lambda_{g'}}^{\sigma'}(r') b_{\Lambda'}^{\sigma'}(r', \omega + E_{g'}) \frac{r'^{l_0}}{r'^{l_0+1}} \right)
\end{aligned} \tag{6.38}$$

and

$$\begin{aligned}
\tilde{f}_{xc_{gg'}, \Lambda\Lambda'}^{\sigma\sigma'}(\omega) &= c_{g\Lambda_g}^\sigma c_{g'\Lambda_{g'}}^{\sigma'} \int d\Omega Y_l^m(\Omega) Y_{l_g}^{m_g*}(\Omega) Y_{l'}^{m'*}(\Omega) Y_{l_{g'}}^{m_{g'}}(\Omega) \\
&\times \int_0^R dr r^2 b_{\Lambda}^\sigma(r, \omega + E_g) b_{\Lambda_g}^\sigma(r) b_{\Lambda_{g'}}^{\sigma'}(r) b_{\Lambda'}^{\sigma'}(r, \omega + E_{g'}) f_{xc}^{\sigma\sigma'}(r)
\end{aligned} \tag{6.39}$$

The expression in (6.39) is valid for the TDLSDA, whereas the restricted schemes involve an extra  $\delta_{gg'}$  factor, and  $\delta(E_g - E_{g'})$  respectively. All these kernels are hermitian. For the explicit form of  $f_{xc}$  please check the appendix.

The series in (6.36) can be cut at a maximum value of  $l_0 = l_g + l_{max}$ , according to the selection rules for the Gaunt coefficients in (6.38). The evaluation of the integrals of angular products in (6.39) is less customary and is detailed in the appendix.

### 6.2.10 The renormalisation of the response function

We underline the fact that the TDDFT provides a calculation recipe to include the many body interactions, to an extent dictated by the kernel, in the response function. The renormalisation in (6.11) is actually a matrix equation of the form:

$$\hat{\chi} = (\hat{1} - \hat{\chi}_0 \hat{K})^{-1} \hat{\chi}_0 \tag{6.40}$$

where all the quantities are operators.

While  $\tilde{\chi}_0$  is diagonal over the initial states  $g$ , it is not the case for the kernel  $\tilde{K}$ . Consequently, the many body response function  $\tilde{\chi}$  may cross different initial states. This effect gets to be seen on the spectra if one calculates two edges that are close in energy (less than 50 eV of difference), such as the  $L_{2,3}$  edges of the  $3d$  elements. In this case, the overlap between the matrix elements of the real parts of  $\tilde{\chi}_0$  (figure 6.3) determines a transfer of spectral weight in the imaginary parts of  $\tilde{\chi}$ . Subsequently, the branching ratio is modified.

Calculating two edges close in energy all by employing the approximation (6.18) to the Adler-Wiser equation is referred to as the double pole approximation [10, 99]. Physically, this approximation is valid if two transitions are strongly coupled to each other ( $L_2$  and the  $L_3$  of the  $3d$  elements) but not to the rest of the spectrum. In other words, the approximation we employed is a three level problem [99].

Generally speaking, the poles of the response function indicate the values of the excitation energies in the system, unless they are forbidden by symmetry. In the resonant

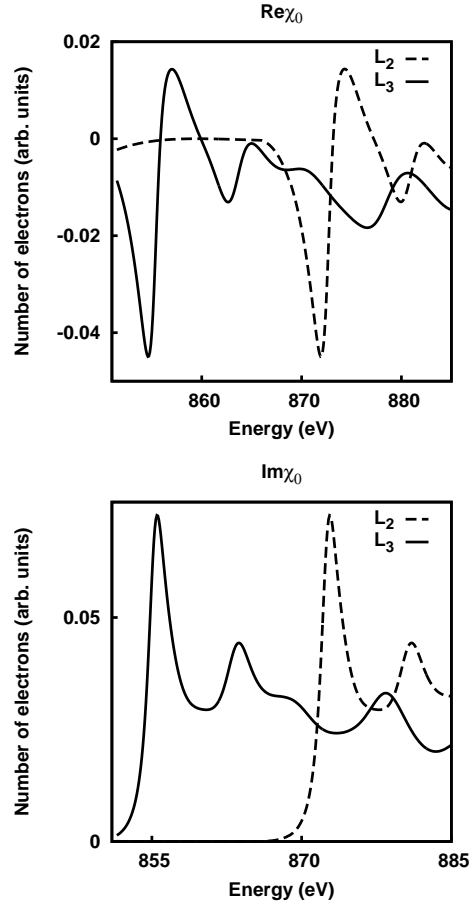


Figure 6.3: Calculated real and imaginary parts of  $\chi_0$  for the  $L_{2,3}$  edges of pure nickel.  $\Re\chi_0$  is similar to  $f'$ , whereas  $\Im\chi_0$  indicates the absorption peaks before the multiplication with the manifold of the corresponding initial states.

case, and in the IPA picture, these are the difference between the final state's energy and the core level's one. Similar to the optical frequencies range case, our method does not seem to detect any significant shift: the poles of  $\chi$  are situated at more or less the same position as the ones of  $\chi_0$ .

Note that the kernel's elements are zero for the  $\Lambda$  states whose mixing is prohibited by the symmetry constraints. For instance, the kernel matrix elements connecting the states with  $l = 0$  and  $l = 1$  in a material possessing the inversion symmetry are zero. Moreover, there is no symmetry lowering due to the many body effects, nor are the selection rules altered (at least in the local approximations for the kernel).

### 6.2.11 Extensions of the adiabatic approximation

In the resonant regime, the interaction with the core hole is a strong, if not essential, effect. A proper treatment of the core hole requires the description of the excitonic effect (the electron-hole interaction) into our calculation. Rigorously, this may be done by appealing to a BSE method [105] whose computational cost is extremely high.

Ideally, one should construct a method that follows the BSE spirit all by keeping the computational simplicity of the TDDFT calculation.

**The Bethe Salpeter equation** A complete description of the excitonic effects can be obtained by solving the BSE, originally introduced by H. Bethe and E. Salpeter in 1951 [97]. We shall be very brief on the description of the formalism, as it is secondary to the purpose of this manuscript. For more details, please refer to the reference [84]. The BSE deals with two particle Green functions  $L_0$  and  $L$ , whose poles indicate the two particle excitation energies in the system. In one of its most usual operatorial forms, the BSE reads:

$$L = L_0 + L_0(v - W)L \quad (6.41)$$

where  $L$  stands for the interacting two particle Green function, whereas

$$L_0(x_1, x_2, x_3, x_4, \omega) = \sum_{ij} (f_j - f_i) \frac{\phi_i^*(x_1) \phi_j(x_2) \phi_i(x_3) \phi_j^*(x_4)}{\omega - (E_i - E_j)} \quad (6.42)$$

is the non-interacting one. Here  $x = (\vec{r}\sigma)$  and  $f_i$  is the occupation number of orbital  $i$ . Note that contrary to the TDDFT renormalisation in (6.11), the BSE involves four-point quantities, the main reason for its computational heaviness.  $v$  stands for the bare Coulomb interaction, whereas  $W$  is the screened electron-hole interaction. Moreover,  $\chi_0$  and  $f_H$  are the two point contractions of  $L_0$  and  $v$ , respectively:

$$\chi_0(x_1, x_3, \omega) = -L_0(x_1, x_2, x_3, x_4, \omega) \delta(x_1 - x_2) \delta(x_3 - x_4) \quad (6.43)$$

by confronting (6.18) and (6.42). A similar equation connects  $v$  to  $f_H$ . In reference [19] authors stress upon the fact that  $\chi_0$  is calculated from the Kohn-Sham wavefunctions, whereas  $L_0$  is issued by the many body perturbation theory and is usually calculated in the GW quasiparticle approximation. Consequently, (6.43) is valid only if the two quantities are calculated from the same approximation. The subtraction in (6.41) indicates the attractive character of the screened interaction. In (6.41) the screened interaction  $W$  is assigned the same task as the exchange-correlation kernel  $f_{xc}$  in the TDDFT formalism: to describe all interaction effects beyond the local fields.

**TDDFT versus BSE** Several attempts to reconcile the TDDFT and BSE methods have been reported (see, for instance [94, 109]). BSE and TDDFT equations have been proved to be formally equivalent. The exact form of this equivalence has been found for a local exchange-correlation kernel [84]. It is equally possible to derive a TDDFT exchange-correlation kernel based on the BSE calculations. This has been done for optical frequencies and is known as the Nanoquanta kernel [19, 44, 109].

**The strength of the core hole interaction** Taking the limit  $W \rightarrow 0$  in (6.41) reduces the complexity of the problem to the calculation of the local field effects. Depending on the strength of the core hole interaction, one can distinguish several regimes. If it is weak, the local fields dominate, and the application of (6.41) to the calculation of X-ray core spectroscopy implies a total screening effect lower than the one suggested by the RPA-LF. If the interaction is strong, it may overcome the local field effects.

### The extended TDLSDA calculation scheme

In 2005, Ankudinov, Takimoto and Rehr [9] proposed a calculation scheme claimed to be a TDDFT-BSE procedure submitted to certain approximations. In this work, we use the spirit of the method proposed in [9] and adapt it to our own implementation. The purpose is to study it in great detail and to analyze to what extent it is capable of describing the core hole. Although it was originally baptized as TDDFT-BSE [9], we shall call it the extended TDLSDA method, for reasons that will become clearer further in the manuscript.

Ankudinov, Takimoto and Rehr [9] propose a correction that is related to the screened interaction  $\mathcal{W}$ . The corresponding TDDFT kernel reads:

$$\hat{\Theta} = \hat{K} + \hat{\mathcal{W}} \quad (6.44)$$

where  $K \equiv f_H$  is the usual RPA-LF kernel and  $\mathcal{W}$  is the two point contraction of  $W$ . Note that performing a TDDFT calculation by the use of  $\hat{\Theta}$  is rigorously equivalent with the two steps method introduced in [9]. In reference [9] the authors distinguish between the cases where  $\hat{K}$  is calculated in the RPA-LF or in the TDLSDA. For the latter, they subtract  $f_{xc}$  from  $\mathcal{W}$ . We chose not to discuss this second method, as it yields results that are quasi-identical to the first one's.

The authors of [9] expect that calculating the absorption cross section by using  $\hat{\Theta}$  would include some effect due to the core hole interaction, which would justify the TDDFT-BSE name. We believe that this particular choice of the kernel cannot describe the core hole properly. Our arguments are to be revealed in the rest of the current section.

Similarly to  $f_{xc}$ ,  $\mathcal{W}$  of the BSE is subjected to approximations. In the following paragraphs we discuss the approximations introduced by Ankudinov, Takimoto and Rehr [9], who tried to integrate  $\mathcal{W}$  within the TDDFT framework.

**The RPA screened interaction** Most usually the BSE schemes take the screened interaction  $W$  as frequency independent:

$$\mathcal{W} = \epsilon^{-1} f_H \quad (6.45)$$

where we chose to show the two points form, dealt with by the TDDFT, and not the four points form in the BSE framework.  $\epsilon$  is the dielectric matrix calculated in the RPA [19]:

$$\epsilon = \hat{1} - \hat{K} \hat{\chi}_0 \quad (6.46)$$

Note the different order of terms, as compared to (6.40).  $K$  is the usual TDDFT kernel.

$$\mathcal{W} = (\hat{1} - \hat{K} \hat{\chi}_0)^{-1} f_H \quad (6.47)$$

This approximation on  $\mathcal{W}$  is usually referred to as the statically screened RPA interaction. By employing (6.44) with  $K = f_H$  and (6.47) the renormalisation equation (6.40) gives:

$$\hat{\chi} = \left( \hat{1} - \hat{\chi}_0 f_H - \hat{\chi}_0 (\hat{1} - f_H \hat{\chi}_0)^{-1} f_H \right)^{-1} \hat{\chi}_0 \quad (6.48)$$



Note that according to (6.45)  $\mathcal{W}$  is local, static and positive, whereas  $W$  from (6.41) is non-local, frequency dependent and preceded by a  $-$  sign.

Mathematically, it can be proven that the extended TDLSDA with RPA screened interaction always enhances the local fields. In (6.44) the two kernels  $f_H$  and  $\mathcal{W}$  have identical signs, whereas this is not the case of the genuine BSE (6.41). Should we take  $\mathcal{W}$  with the opposite sign in (6.47), the corresponding extended TDLSDA scheme gives identical results to the IPA calculations, meaning that the opposite sign Coulomb interaction cancels. To understand this behaviour, one could iterate (6.46):

$$\epsilon = \lim_{n \rightarrow \infty} (1 + f_H \hat{\chi}_0 + (f_H \hat{\chi}_0)^2 + \dots + (f_H \hat{\chi}_0)^n) \quad (6.49)$$

and plug it into (6.48):

$$\hat{\chi}_N = (1 - \hat{\chi}_0 f_H \mp \lim_{n \rightarrow \infty} (\hat{\chi}_0 f_H + (\hat{\chi}_0 f_H)^2 + \dots + (\hat{\chi}_0 f_H)^n)^{-1} \hat{\chi}_0 \quad (6.50)$$

where  $\mp$  stands for a positive  $\mathcal{W}$  (as proposed originally in equation 6.47) and for a negative one, respectively. Our calculations show that the contribution of the terms whose  $n > 1$  in (6.50) is negligible. In the first case of figures (positive  $\mathcal{W}$ ) we actually evaluate:

$$\hat{\chi}_N = (1 - 2\hat{\chi}_0 f_H)^{-1} \hat{\chi}_0 \quad (6.51)$$

whereas a negative  $\mathcal{W}$  yields directly  $\chi_N = \chi_0$ , validating our observations. These arguments show that, at least for some simple materials, the extended TDLSDA scheme employing (6.47) gives results that are identical to the ones obtained by a simple RPA-LF calculation whose Hartree kernel  $f_H$  has been doubled with respect to its initial value. We verified this conclusion with several  $L_{2,3}$  calculations and we think it is a general one. Rigorously, one is not allowed to iterate (6.46), as some of the concerned matrix elements are not less smaller than 1. Still, these are just a minority and our argument stays qualitatively correct.

All the arguments above have been verified numerically: an extended TDDFT calculation in the limit of the RPA screened interaction (6.47) yields results that are identical to the ones issued from a RPA-LF calculation where all values of the kernel matrix elements have been doubled.

**The locally screened interaction** By analogy with the Hartree potential, a more intuitive guess on  $\mathcal{W}$  gives:

$$\Delta V(\vec{r}) = \int d^3 r' n(\vec{r}') \mathcal{W}(\vec{r}, \vec{r}') \quad (6.52)$$

where

$$\Delta V(\vec{r}) = V_{exc}(\vec{r}) - V_0(\vec{r}) \quad (6.53)$$

is the fully screened core hole potential, i.e. the difference between the absorber's potential with and without the core hole, respectively. Note that both  $\Delta V(\vec{r})$  and  $\mathcal{W}(r, r')$  are negative.

Within this scheme, we employ the approximation that the short-ranged screened interaction  $\mathcal{W}$  takes significant values only in the space extension of the core orbital. Moreover, both the core potential  $\Delta V(\vec{r})$  and its density  $|\phi_g^\sigma(\vec{r}')|^2$  are taken as spherical. In other words, (6.52) becomes:

$$\Delta V(\vec{r}) = \int d^3r' |\phi_g^\sigma(\vec{r}')|^2 W(\vec{r}, \vec{r}') \quad (6.54)$$

This is a very strong approximation. The dependence of  $\Delta V(r)$  on the initial state  $g$  and spin  $\sigma$  is suppressed, due to the very spherical approximation. Similar to (6.27) the TDDFT kernel derived from  $\mathcal{W}$  reads:

$$\begin{aligned} \tilde{\mathcal{K}}_{gg', \Lambda\Lambda'}^\sigma(\omega) &= \int d^3r \int d^3r' \mathcal{W}(\vec{r}, \vec{r}', \omega) \\ &\times \phi_g^{\sigma\dagger}(\vec{r}) \Psi_\Lambda^\sigma(\vec{r}, \omega + E_g) \phi_{g'}^\sigma(\vec{r}') \Psi_{\Lambda'}^{\sigma\dagger}(\vec{r}', \omega + E_{g'}) \end{aligned} \quad (6.55)$$

The fact that  $\Delta V(r)$  is diagonal in the initial state variable implies the very same feature in the kernel's  $\mathcal{K}$ 's behaviour. It follows that the screened interaction  $\mathcal{W}$  has some trivial energy dependence, in the sense that its matrix elements depend on the energy of the edge designated by the  $g$  initial state. One could re-write (6.54) in form:

$$\Delta V(r) = \int d^3r' \phi_g^{\sigma\dagger}(\vec{r}') \phi_g^\sigma(\vec{r}') \mathcal{W}(\vec{r}, \vec{r}') \quad (6.56)$$

One could wish to merge (6.55) and (6.56). To do so, the only possible way is to assume a local character for  $W$ :

$$\mathcal{W}(\vec{r}, \vec{r}') = \tilde{\mathcal{W}}(\vec{r}) \delta(\vec{r} - \vec{r}') \quad (6.57)$$

We stress the fact that this is yet another way to take into account the core hole, locally. The local character of the approximation places it outside the BSE framework. We recall that the justification for its introduction is a technical (the need to merge equations 6.55 and 6.56) and not a physical one. By employing (6.55), (6.56) and (6.57) one gets:

$$\tilde{\mathcal{K}}_{\Lambda\Lambda'}^{g\sigma}(\omega) = \int d^3r \Delta V(r) \Psi_\Lambda^\sigma(\vec{r}, \omega + E_g) \Psi_{\Lambda'}^{\sigma\dagger}(\vec{r}', \omega + E_{g'}) \delta_{gg'} \quad (6.58)$$

$$\begin{aligned} \tilde{\mathcal{K}}_{\Lambda\Lambda'}^{g\sigma}(\omega) &= \int dr r^2 \Delta V(r) b_\Lambda^\sigma(\vec{r}, \omega + E_g) b_{\Lambda'}^\sigma(\vec{r}, \omega + E_{g'}) \delta_{gg'} \\ &\times \int d\Omega Y_\Lambda(\Omega) Y_{\Lambda'}^*(\Omega) \end{aligned} \quad (6.59)$$

The normalization relation for the spherical harmonics gives:

$$\tilde{\mathcal{K}}_\Lambda^{g\sigma}(\omega) = \int dr r^2 \Delta V(r) b_\Lambda^{\sigma 2}(\vec{r}, \omega + E_g) \quad (6.60)$$

meaning that the TDDFT kernel describing the core hole interaction in the local approximation is diagonal in the  $\Lambda$ ,  $g$  and  $\sigma$  variables. Physically, it means that the

present approximation for  $\mathcal{W}$  prevents the core hole interaction from coupling states with different  $(l, m)$  quantum numbers, i.e.  $\mathcal{W}$  has a  $s$  wave character. This reminds us of the form of the restricted TDLSDA approximation described previously.

This result can be retrieved in a close form in Ankudinov, Takimoto and Rehr [9]. Nonetheless, the derivation in [9] raises several problems. First, the authors start from a different form of the matrix formulation of  $\mathcal{K}$ : eq. 28 in [9] introduces an inaccurate dependence on  $\vec{r}$  and  $\vec{r}'$  (check our equation 6.55 for comparison). Due to this inaccuracy, they no longer need to suppose the local character of  $\mathcal{W}$  and can merge their equivalent forms (6.55) and (6.56) directly. Consequently, we reach the same result as the authors of [9], but we make an extra assumption (the locality of  $\mathcal{W}$ ). Given the local character of the exchange-correlation kernel, we chose not to pursue in this direction.

**About the so-called TDDFT-BSE method** From this point of view, performing the extended TDLSDA scheme by choosing the statically screened RPA interaction  $\mathcal{W}$  has no profound physical meaning, as it yields results that are identical to the ones one would obtain by the mere multiplication by a factor 2 of the Hartree kernel matrix elements. We therefore question the appropriateness of the method introduced by Ankudinov, Takimoto and Rehr [9] that concerns the RPA screened interaction (6.47). We equally disagree with the original nomenclature in [9] of the TDDFT methods concerning the RPA screened interaction (6.47) and the locally screened one (6.55). We find that calling this method TDDFT-BSE is unfit: a local approximation (in both cases  $\mathcal{K}$  is local) should not be introduced in a BSE context.

### 6.3 Implementation

Any TDDFT calculation requires a previous ground state one. This is why the implementation of the TDDFT method within the FDMNES code is modular. From the user's point of view, it is a completely separate module, whose call is optional (*via* a keyword). In our implementation, the TDDFT calculation accompanies, but does not alter, the single particle calculation (see the flow-chart in figure 3.1). Consequently, besides the usual output files, an extra one containing the TDDFT-corrected absorption cross section is generated.

The underlying ground state calculation, either self-consistent or not, is equally meant to provide us the Fermi level, the knowledge of which is essential for the calculation of  $\chi_0$ . Note that this feature would not have been available without the previously implemented self-consistent loop.

The ground state calculation can be performed either in the MST, or by following a full potential scheme (FDM). The latter is to be preferred if the MT approximation is questionable for the calculated compound. We recall that a FDM ground state calculation is limited to rather small cluster radii. Moreover, in practice, integrating the spin-orbit coupling into a ground state, FDM calculation is not feasible due to the enormous calculation time it would require.

Let the calculation of some neighbour edges, like the  $L_{2,3}$  or the  $M_{4,5}$ . As long as a single particle calculation is concerned, one defines the same energy grid  $\{E\}$  around

each edge, in units of photoelectron (and not photon) energies. Next, one performs two separate, consecutive calculations, which differ only in terms of photon energies and initial states.

To evaluate  $\chi_0(\omega)$  with the aid of (6.23) we will be using  $\Im\tau_{\Lambda\Lambda'}^{\sigma\sigma'}(E)$  and  $Z_{g\Lambda}^\sigma(E)$  from the single particle calculation. The energy dependence of  $\Im\tau_{\Lambda\Lambda'}^{\sigma\sigma'}$  points to some photoelectron energy  $E$ , whereas  $\chi_0$  depends on the photons' energy  $\omega$ . Thus, for a TDDFT calculation where two edges are involved, it is mandatory to construct an extended energy grid that will explicitly contain the two edges.

This new grid is built automatically from the initial ones, which were user-defined. We superpose the two initial grids, which we previously shifted by a quantity corresponding to the energy difference between the two edges. We keep the meshing of the initial grids and at their crossing we give priority to the mesh of the shifted one. The reason for this choice is that the density of the point energies is supposed to be higher in the beginning of the initial grid (i.e. next to the edge), than at its end. One should insure that the initial grid is large enough to cover the distance between the edges and that the mesh is accurate enough around the low part of the energy edge.

To get the values of  $\chi_0$  on the extended grid, according to (6.23), we need to evaluate integrals of the following kind:

$$B(\omega) = \int_{E_F}^{\infty} dE \frac{A(E)}{\omega - (E - E_g) + i\epsilon} \quad (6.61)$$

where  $A(E) = \Im\tau_{\Lambda\Lambda'}^{\sigma\sigma'}(E) Z_{g\Lambda'}^{\sigma'}(E) Z_{g\Lambda}^\sigma(E)$ . By separating the real from the imaginary parts one gets:

$$\begin{aligned} B(\omega) &= \int_{E_F}^{\infty} dE A(E) \frac{\omega - (E - E_g)}{\left(\omega - (E - E_g)\right)^2 + \epsilon^2} \\ &- i \int_{E_F}^{\infty} dE A(E) \frac{\epsilon}{\left(\omega - (E - E_g)\right)^2 + \epsilon^2} \end{aligned} \quad (6.62)$$

In practice, the upper limit of the integral is taken some 1000 eV above the last point in the energy grid, instead of  $\infty$ . The missing values in  $A(E)$  are taken as the extrapolation of the imaginary part of the atomic structure factor  $f''$ , with the corresponding units. The physical reason one needs a large extension of the grid is that, although  $\Im A(E)$  are very localized structures around the edge energies,  $\Re A(E)$  are extended. Note that this procedure of calculating the real part of the susceptibility is proper to our implementation. The other existing methods (see the implementation details in [101] and [7]) use the Kramers-Kronig relations to do so.

One can evaluate (6.62) either by taking into account a finite  $\epsilon$  ( $\approx 0.1\text{eV}$ ), or by taking the limit  $\epsilon \rightarrow 0$ . In practice the two give similar results. For the latter, one can use the following representation of the Dirac  $\delta$  function:

$$\lim_{\epsilon \rightarrow 0} \frac{1}{\pi} \frac{\epsilon}{x^2 + \epsilon^2} = \delta(x) \quad (6.63)$$

Consequently, after discretisation, (6.62) becomes:

$$B(\omega) = -\frac{1}{2} \left( \sum_i A(E_i) \log \frac{\omega - (e_2 - E_g)}{\omega - (e_1 - E_g)} \right) - i\pi A(\omega + E_g) \Theta(\omega + E_g - E_F)$$

Here  $i$  is the mesh index running over the  $E$  energies and  $A(E_i)$  is considered constant in the energy interval limited by:

$$e_1 = \frac{1}{2}(E_{i-1} + E_i); \quad e_2 = \frac{1}{2}(E_i + E_{i+1}) \quad (6.64)$$

The above evaluation of the integral in (6.23) enables us to determine  $\chi_0(\omega)$ . Note that we obtain a  $\chi_0$  representation of each edge  $g$ , whose imaginary parts' unique peaks are similar in form but shifted in energy (see figure 6.3). The two different peaks have identical heights, as the difference in the spectral weight of the absorption peaks is due to the sum on the initial states, a later step in the calculation.

We evaluate the  $c_{g,\Lambda_g}^\sigma$  according to the prescription in section 3.1.1. From this point on, we are interested in running the TDDFT calculation in the extended energy grid exclusively.

We introduce a first energy loop to calculate the radial wavefunctions  $b_l(r)$  in the new grid, then calculate the kernel  $\tilde{K}$ , on the basis of (6.38) and (6.39). A second loop is required for the matrix inversion in (6.40) and the calculation of  $\tilde{\chi}$ . Should we perform the extended TDLSDA scheme, we use the same loop to calculate  $\mathcal{W}$ . We use the same loop equally to determine the transition matrix tensors (2.16), (2.17) and (2.18). As we previously stressed upon, the main idea behind this particular TDDFT method is that we can treat  $\tilde{\chi}$  and  $\tau$  on equal footing. Once we get  $\tilde{\chi}$  we re-use the single particle implementation in the code that was meant for  $\tau$  and calculate the tensors in the usual FDMNES' way. This procedure is extremely convenient, as we get to "recycle" the ancient structure of FDMNES and keep the powerful feature of the tensor analysis.

One great advantage of the TDDFT calculation is that it is not time consuming. Most of the computational time goes into the matrix inversion in (6.40). A remarkable fact is that the TDDFT calculation time does not scale with the radius of the cluster. Due to the approximation for resonant regimes to the Adler-Wiser equations in (6.18),  $\chi_0$  only takes significant values inside the absorbing atom. This means that the matrix inversion (6.40) is limited to the spacial range of the absorber, and thus the computation time required for the TDDFT method is nearly independent of the size of the calculation cluster.

## 6.4 Results

To test the pertinence of our method, we calculated the TDDFT corrections for the  $L_{2,3}$  absorption spectra of the bulk transitional elements. We used large clusters of calculation (7Å) and the cut-off level issued from our self-consistent procedure. The experimental data issue from references [41] and [98]. The former is used as reference by Schwitalla and Ebert [101] and Ankudinov, Nesvizhskii and Rehr [7]. Whenever available, we prefer the more recent data in [98], for the reason it has better experimental resolution.

In our series of calculations, we included calcium and scandium, due to their available  $3d$  states, and excluded zinc, whose  $3d$  levels are full. For all these elements we compared the single particle calculations to the TDDFT ones (RPA-LF, TDLSDA, restricted TDLSDA), for identical broadening. In order not to artificially alter the branching ratio we chose a broadening that does not depend on the energy. According

to section 3.1.6 this corresponds to  $\Gamma_{max} = 0$ . Concerning the spectral width of the core level, we take the same tabulated values of  $\Gamma_{hole}$  (see equation 3.10) for both the  $L_2$  and the  $L_3$  structures. We calculate the branching ratio by a simple ratio of the maxima of the intensities of the  $L_3$  and  $L_2$  structures.

Unless specified otherwise, the TDDFT results we present are issued from fully relativistic calculations preceded by a non-excited IPA (scheme a) self-consistent loop. All calculations showed for the magnetic  $3d$  elements (iron, cobalt, nickel) include the spin polarisation.

In figures 6.4 - 6.7 and 6.13 we confront the IPA and TDDFT calculations (more specifically, LSDA and TDLSDA) to experimental data, for the  $L_{2,3}$  edges of the  $3d$  elements. TDDFT definitely improves on the one-body calculations, for the first half of the  $3d$  series, both in terms of branching ratio and general shape of the spectra. The experimental data was normalized to match the high energy spectrum of the calculations. Neither the IPA nor the TDDFT calculations were normalized, which allows one to observe the eventual energy shift and the mismatch at high energies. The TDDFT corrections have little influence for the second half of the  $3d$  series, and are sometimes worse than the IPA ones (see the case of iron and cobalt in figure 6.7).

A rough comparison between the LSDA and the TDLSDA calculations gives rise to some general remarks. Firstly, the two seem to meet at high energies. When this superposition is not perfect (see figures 6.4 and 6.7) we suspect an artefact of the calculation. Secondly, the TDDFT spectra are beneath the IPA ones (see figures 6.4 - 6.7, 6.13 and 6.9). The two behaviour are consequences of the fact that the TDDFT corrections indicate the change in the screening response when the many-body effects are turned on. The higher the screening of the X-ray field, the lesser the area beneath the absorption spectrum. The screening we calculate in this TDDFT way is intra-atomic. It is known [105] that the screening effects do have a band contribution. Its calculation is beyond the performance of our method. The screening effects are visible only in the near-edge region. Therefore, we expect the two types of calculations to converge at high energies.

For the first elements of the  $3d$  series, the calculated  $L_3$  edges are broader and down shifted in energy with respect to the experimental ones. This effect disappears at higher atomic numbers, where the concerned states are occupied anyway. We believe that, for reasons we do not understand yet, the first  $d$  states above the Fermi level are not available to the spectroscopy. We recall that the degeneracy of the  $d$  states is lifted by the crystal field, resulting in a double structure at the  $L_3$  ( $L_2$ ) edge. It is therefore natural that the double structure appears in the LSDA calculation, where one probes a projection of the density of states. Moreover, it seems that the local TDDFT approximation does not succeed in erasing the first of these structures. The same behaviour has been observed by Schwitalla and Ebert [101].

In the following we shall discuss in what way the different ingredients of the calculation (cluster size, spin-orbit coupling, choice of the kernel, convolution procedure) affect the TDDFT results.

**The cluster size** We checked that our TDDFT procedure had no intrinsic artefacts due to the size of the calculation cluster, provided it contained at least one atomic shell around the absorbing atom. As we explained in section 6.3, the effect of the TDDFT is

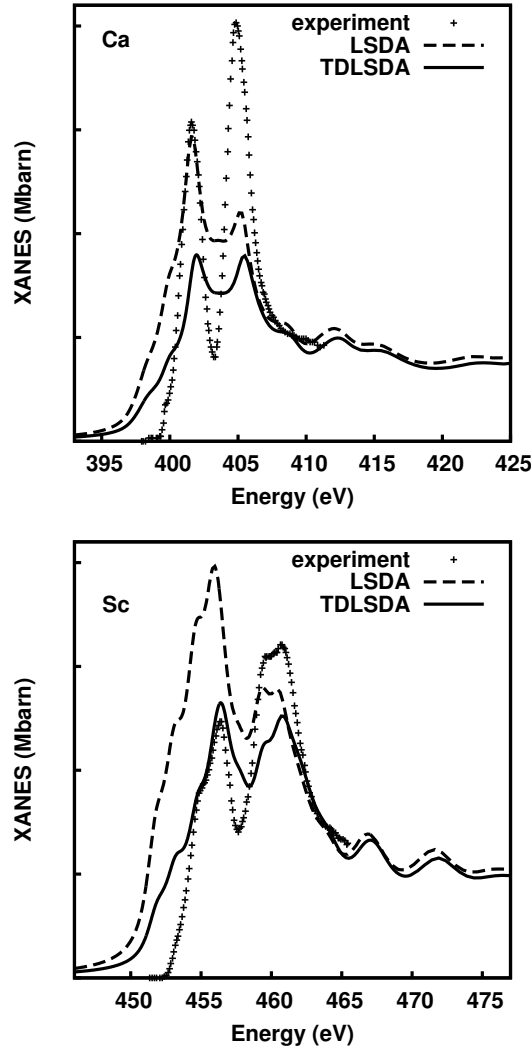


Figure 6.4: One body LSDA (dashes) and TDLSDA calculations (solid) versus experiment [41] for calcium and scandium at the  $L_{2,3}$  edges. TDLSDA improves on the LSDA calculations, but not enough to give a satisfactory agreement with the experiment in terms of general shape of the spectra. Both calculations seem to underestimate the onset of the  $L_3$  edge.

localized around the absorbing atom. Therefore, when increasing the cluster's radius, the form of the TDDFT spectrum follows accurately the band modulations of the IPA one (see figure 6.8). It follows that most of the change brought in by the TDDFT is independent of the size of the cluster. The difference between the IPA and TDDFT calculations of absorption in vanadium is roughly the same, whether one deals with a single atom or with a cluster.

**The spin-orbit coupling** We performed two different sets of calculations, with and without the spin-orbit coupling (see table 6.1). One notices an intrinsic TDDFT effect linked to the fact of having considered the coupling (for the specific changes in the

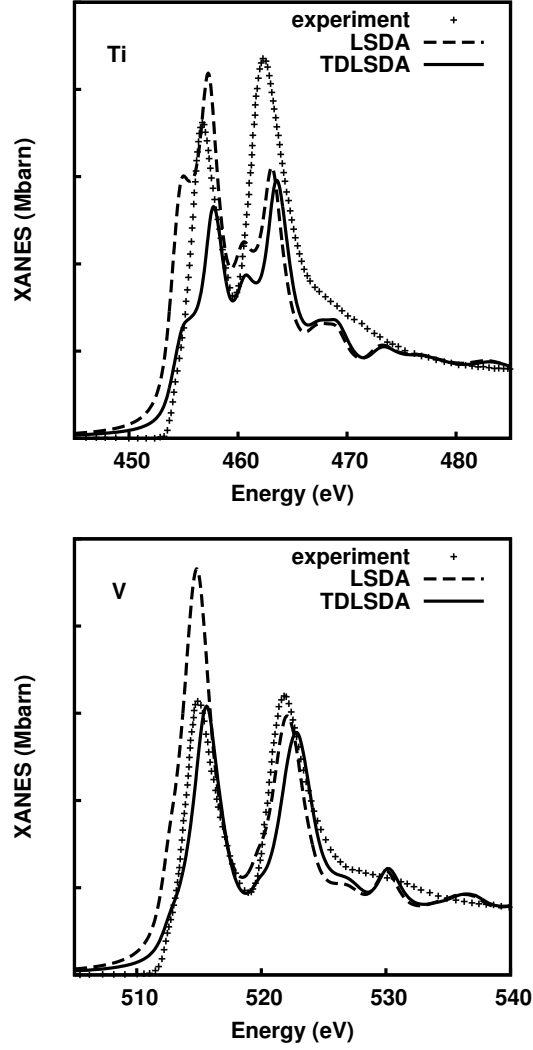


Figure 6.5: One body LSDA (dashes) and TDLSDA calculations (solid) versus experiment [98] for titanium and vanadium at the  $L_{2,3}$  edges. TDLSDA calculations are definitely better than the LSDA ones. Similar to the calcium and scandium case, both TDDFT calculations seem to underestimate the onset of the  $L_3$  edge.

formulae, please check the appendix). Even if for the first elements of the series the spin-orbit coupling makes no difference in terms of the IPA calculations, the TDDFT ones are seriously affected (see figure 6.10). We checked that this extra difference is due to the non-diagonal (in terms of spin) elements of the Coulomb kernel matrix elements. From this point on, for the sake of accuracy, we will be discussing only the calculations that include the spin-orbit coupling.

We draw attention upon a specific difference with respect to the TDDFT procedure introduced by Ankudinov, Nesvizhskii and Rehr [7]. The TDDFT scheme introduced by these authors assumes for convenience that the response function  $\chi(\vec{r}, \vec{r}')$  has spherical symmetry [7,9], i.e. its projection on the spherical harmonics basis is independent of  $m$ .



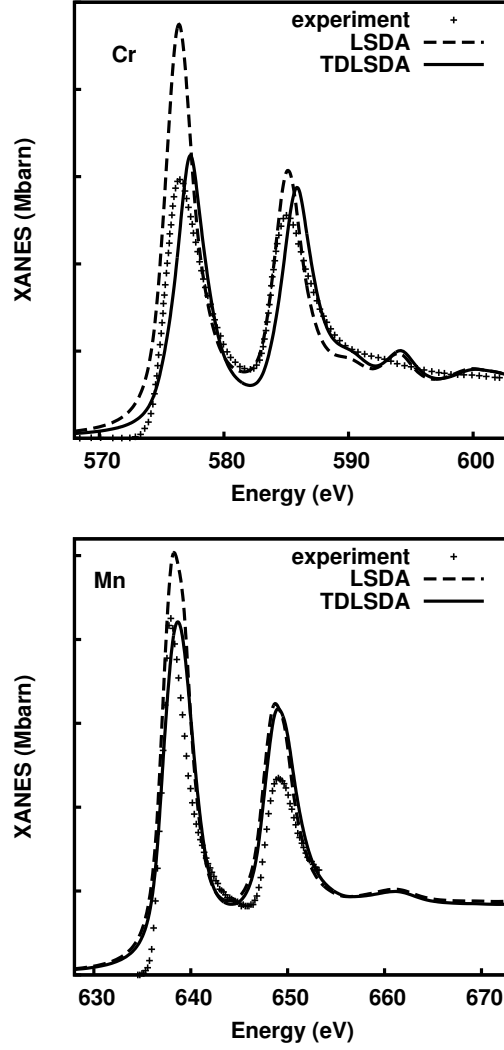


Figure 6.6: One body LSDA (dashes) and TDLSDA calculations (solid) versus experiment [98] for chromium and manganese at the  $L_{2,3}$  edges.

This means that only the spherical contribution of the TDDFT corrections are being considered. On the other hand, our implementation does not make any assumption. The spherical approximation breaks down particularly in the presence of the spin-orbit coupling, when the development of  $\chi(\vec{r}, \vec{r}')$  on the spherical basis will contain some  $\mathfrak{S}\tau_{l,m\uparrow}^{l,m+1\downarrow}$  factor.

**The various local kernels** One can see (figures 6.9 and 6.11) that the various exchange-correlation kernels that we tested (RPA-LF, TDLSDA, restricted TDLSDA) give quasi-identical results. This result is in agreement with the findings of Schwitalla and Ebert [101] and turns to be valid equally for TDDFT calculations on complex structures (for instance, transition elements oxides). From the physics' point of view, this means that the local fields effect is important for X-ray absorption calculations,

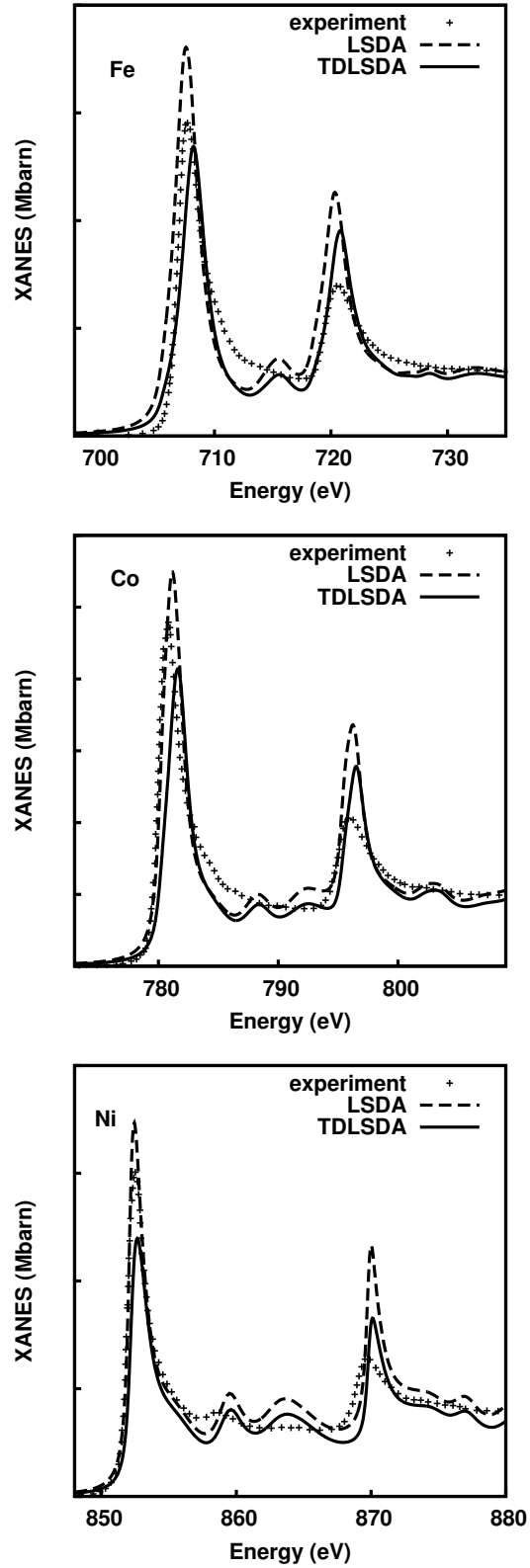


Figure 6.7: One body LSDA (dashes) and TDLSDA calculations (solid) versus experiment [98] for iron, cobalt and nickel at the  $L_{2,3}$  edges. In so far the branching ration is concerned, the TDLSDA corrections are negligible for nickel, and worsen the LSDA results for iron and cobalt.

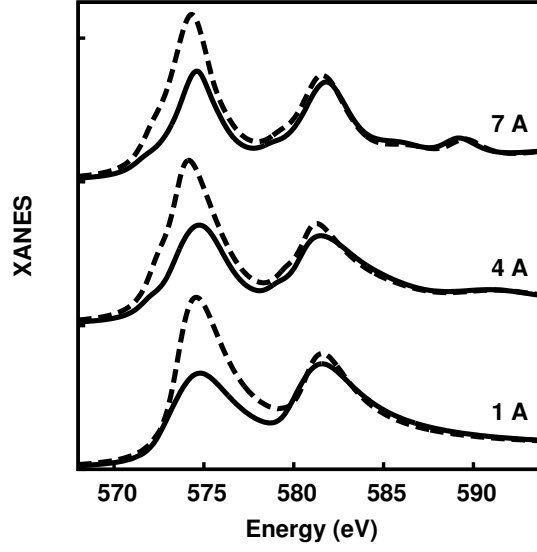


Figure 6.8: The absorption at the  $L_{2,3}$  edges of vanadium, for different sizes of the calculation cluster: 1 Å (a single atom), 4 Å (15 atoms) and 7 Å (113 atoms). The TDDFT spectra (solid) are always beneath the corresponding IPA (dashes) ones. Spectra corresponding to different radii are vertically shifted for convenience.

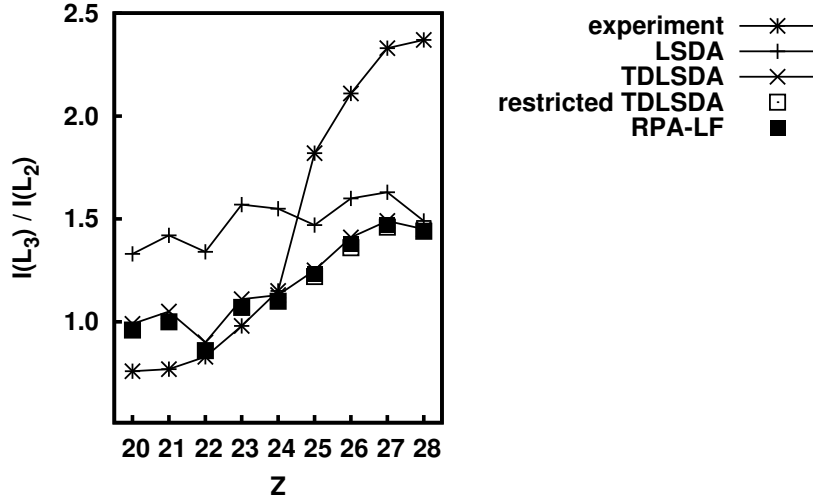


Figure 6.9: The  $L_{2,3}$  branching ratios: the TDDFT corrections improve the IPA calculations for the first elements of the  $3d$  series. The different local exchange-correlation kernels (RPA-LF, TDLSA and restricted TDLSA) give quasi-identical results. This figure has been made with the data in table 6.1.

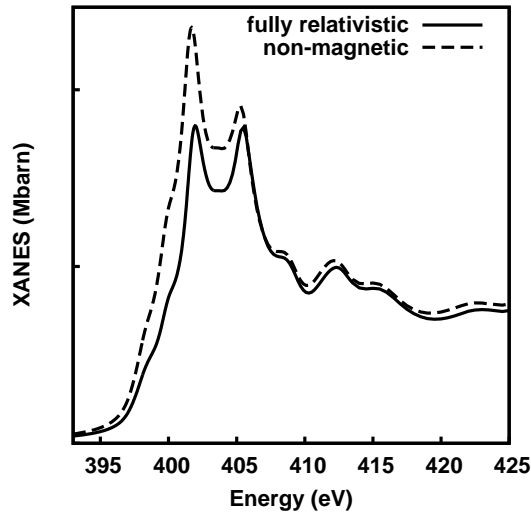


Figure 6.10: TDDFT calculations of the  $L_{2,3}$  edges of calcium: with (solid) and without (dashes) the spin-orbit coupling. The difference between the two spectra seems to come mainly from the non-diagonal (in terms of spin) elements of the Coulomb kernel matrix elements.

Method	Ca		Sc		Ti	
	SO	no SO	SO	no SO	SO	no SO
IPA	1.33	1.31	1.42	1.42	1.34	1.34
RPA-LF	0.96	1.16	1.00	1.21	0.86	0.72
TDLSDA	0.99	1.23	1.05	1.30	0.90	0.83
restricted TDLSDA	0.96	1.17	1.00	1.25	0.85	0.76
Experiment	0.76 <sup>1</sup>		0.77 <sup>1</sup>		0.83 <sup>2</sup>	
Method	V		Cr		Mn	
	SO	no SO	SO	no SO	SO	no SO
IPA	1.57	1.58	1.55	1.55	1.64	1.55
RPA-LF	1.07	1.26	1.10	1.21	1.24	1.29
TDLSDA	1.11	1.29	1.13	1.22	1.26	1.32
restricted TDLSDA	1.07	1.25	1.10	1.19	1.25	1.30
Experiment	0.98 <sup>2</sup>		1.15 <sup>2</sup>		1.82 <sup>1</sup>	
Method	Fe		Co		Ni	
	SO	no SO	SO	no SO	SO	no SO
IPA	1.60	1.76	1.63	1.71	1.49	1.39
RPA-LF	1.38	1.40	1.47	1.49	1.44	1.32
TDLSDA	1.41	1.39	1.49	1.43	1.45	1.35
restricted TDLSDA	1.36	1.38	1.46	1.44	1.44	1.34
Experiment	2.11 <sup>2</sup>		2.33 <sup>2</sup>		2.37 <sup>2</sup>	

Table 6.1: The  $L_{2,3}$  branching ratio, experimental and calculated. SO stands for spin-orbit calculation. <sup>1,2</sup> issue from experimental data taken from references [41] and [98] respectively.

Ca	Sc	Ti	V	Cr	Mn	Fe	Co	Ni	Cu
1.29	1.36	1.43	1.50	1.56	1.63	1.00	0.80	0.60	0.60

Table 6.2: The values (in eV) of the convolution parameter  $\Gamma$  one has used to calculate the branching ratio in table 6.1.

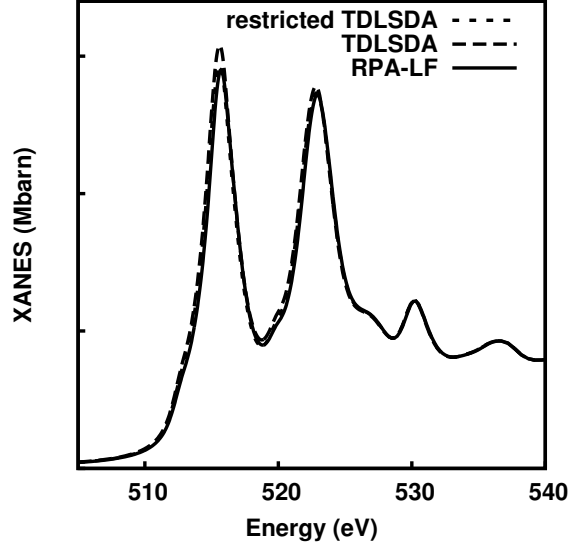


Figure 6.11: TDDFT calculations of the  $L_{2,3}$  edges of vanadium. Three distinct local approximations for the exchange-correlation kernel have been tested: RPA-LF, TDLSDA and restricted TDLSDA. They all yield similar results.

whereas the local part of the electron-hole interaction is negligible. We draw attention to the fact that this is different from the optical frequency range, where the inclusion of the local exchange-correlation kernel generates an effect no longer negligible. It appears that in the X-ray range the interaction with the core hole has an extremely pronounced non-local character. Consequently, we argue that the use of a non-local exchange-correlation kernel is mandatory for accurate TDDFT X-ray absorption calculations.

Our results disagree with the ones of Rehr and Ankudinov [92]. They find about 50 *per cent* difference between the branching ratio calculated in RPA-LF with respect to the TDLSDA one. They equally find an excellent match between the restricted TDLSDA calculated and the experimental branching ratio at the  $L_{2,3}$  branching ratio of the  $3d$  elements. In our view such an agreement cannot be obtained by employing a local approximation on the exchange-correlation kernel, as the core hole effect is an essential ingredient of the description of X-ray absorption spectroscopy.

For the first half of the  $3d$  series, our calculations show a reduction of about 25 *per cent* of the TDDFT calculation with respect to the IPA one, in terms of  $L_{2,3}$  branching ratios. For the first half of the  $3d$  series, our results are in good agreement with the ones of Schwitalla and Ebert [101]. These authors obtain a TDDFT correction that reduces slightly with the increasing atomic number. In our case, this tendency is stronger and leads to an almost zero effect in the case of nickel.

Note that, contrary to the alternative TDDFT X-ray absorption implementations, ours does not perform any Kramers-Kronig transformation and therefore is numerically more stable.

**TDDFT on excited atoms** All the TDDFT calculations described above have been performed on an underlying ground state calculation. We also tried to insert the final state rule in this preliminary calculation. We described a cluster with a fully screened core hole, and calculated  $\hat{\chi}_0$  accordingly. Such a procedure is not rigorously justified, as the Adler-Wiser equations (6.18) require the wavefunctions  $\Psi_\Lambda$  to be calculated in the ground state. Nevertheless, the sometimes poor agreement with the experiment of the rigorous calculations may justify some deviations from this rule. Quantitatively, this procedure turned up to worsen the agreement with the experiment, therefore we chose not to pursue this direction.

**The broadening in  $\chi_0$**  There are two basic ways to apply the broadening to the spectra. The standard procedure is to evaluate  $\chi_0$  by taking the limit  $\epsilon \rightarrow 0$ , then calculate absorption by means of  $\chi$  and broaden the spectra at the very end. The alternative is to broaden  $\chi_0$  directly, by employing  $\epsilon = \Gamma_{hole}$  and  $\Gamma_{max} = 0$ . Under these terms no further convolution is needed. Performing a TDDFT calculation with a broadened ground-state response function is somehow un-orthodox, as the decay phenomena should not appear in the fundamental state. Despite this, such an *ad-hoc* prescription actually works, and the two procedures are equivalent in terms of results.

**TDDFT and the convolution procedure** In the previous results we have shown, the convolution of the  $L_{2,3}$  spectra is identical and energy independent (for the specific values, please check table 6.2). We feel that this is the best way to put into perspective the genuine improvement that TDDFT brings to the branching ratio. Note that a TDDFT calculation with a better (and frequency dependent) kernel should yield the correct width of the  $L_2$  and  $L_3$  structures. If this is not the case (for instance, for kernels that are local and energy independent), it should be accepted as such and one should not tempt to correct this by convoluting with different  $L_2$  and  $L_3$  widths. The interpretation of the TDDFT calculation of the  $L_{2,3}$  spectra is very delicate. A change in the convolution procedure may lead to completely different conclusions.

In figure 6.12 (above) we show the TDLSDA calculations of the  $L_{2,3}$  edges of nickel, for two distinct, energy independent, convolution parameters. One can see that the spectrum convoluted by  $\Gamma = 1.3$  eV gives a poor agreement with the experiment at the very beginning of the  $L_3$  edge. In this sense, we fit  $\Gamma$  such as the  $L_3$  edge is perfectly modelled, and use the same convolution value for all energies (figure 6.12 above). It is obvious that this procedure, though favourable for the first edge, cannot describe accurately the second one. Experimentally, the  $L_2$  structure is broader than the  $L_3$  one: as the energy of the  $2p_{1/2}$  states is lower than the one of  $2p_{3/2}$ , there are more mechanisms to fill it and thus its life time is shorter.

One might argue that an energy dependent convolution is required in order to account for this different experimental broadening. We therefore tried to convolute the  $L_2$  structure with twice the value of the  $L_3$  width (figure 6.12 below) and thus we get an undeniable improvement of the agreement between the TDDFT calculation and the

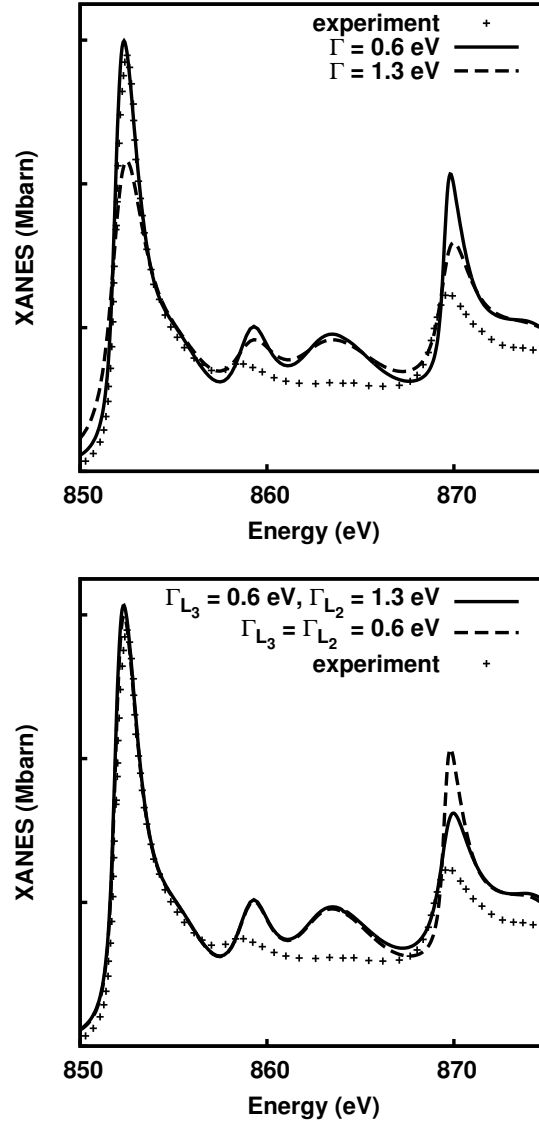


Figure 6.12: The experimental [98] and TDDFT calculated absorption at the  $L_{2,3}$  edges of nickel. Above, the TDDFT calculations correspond to two distinct energy independent, convolution parameters  $\Gamma$ . One prefers the  $\Gamma$  that reproduces the  $L_3$  edge best (solid). Below, we show TDDFT calculations corresponding to two convolution procedures: energy independent (solid) and different  $L_2$  and  $L_3$  broadening widths (dashes). The latter impedes one to distinguish what is the actual improvement brought in by the TDDFT scheme.

experiment. In this spirit, one could find a perfect agreement, provided the two broadening parameters were conveniently chosen. We argue that such procedure, though tempting, is to be avoided, whether the two widths are taken from experimental data (tabulated values) or are calculated *ab initio* (for instance, *via* a GW calculation). In the first case of figures, i.e. tabulated values, the success of the convoluted TDDFT spectrum is due to a fitting procedure and not to the TDDFT procedure itself. Moreover, such procedure cannot be general: for the same chemical element, the two widths depend on the atomic environment (for instance, the widths of nickel in pure nickel and in nickel oxide are different). In the second case of figures (*ab initio* calculated widths) one should clearly distinguish to what extent the improvement is due to the particular choice of the TDDFT kernel, or to the GW approximation. To conclude with, we argue that in order to analyse the effect of the TDDFT calculation, the broadening parameters  $\Gamma$  need to be the same at both edges, contrary to the procedure employed by Ankudinov, Nesvizhskii and Rehr [7].

**TDDFT and the energy shift** As we previously mentioned in section 6.2.10, we do not observe any genuine energy shift between the IPA and the TDDFT calculations, although an apparent one may be observed. In some cases the first structures in the IPA spectrum are strongly diminished or nearly suppressed, which induces an apparent shift between the TDDFT and the IPA calculations.

Scherz et al. [99] start from the work of [10] and propose an effective, element dependent, exchange-correlation kernel meant to describe the experimental  $L_{2,3}$  branching ratio of the  $3d$  elements. They construct a kernel starting from the very experimental data, then run a non-relativistic TDDFT calculation in the double pole approximation that uses the very same kernel. Although their method is not general, as it is based more or less on a fit procedure, it has the great merit to provide insight into the TDDFT mechanisms that allow the change in the positions and intensities of peaks. Scherz et al. [99] do obtain a shift: it is due to the fact that the diagonal (in terms of initial states) elements of the kernel have significantly different values when the states belong to either the  $L_2$  or to the  $L_3$  transitions. This is not the case of the kernels we are employing.

**TDDFT and the delocalized  $L_{2,3}$  edges** All the  $L_{2,3}$  edges of the  $3d$  elements are partially localized structures, with the exception of copper (figure 6.13). This seems to be a general feature of the calculation of delocalized edges: the TDDFT corrections, in the limit of local approximations, bring very little improvement on the IPA calculations.

The  $3d$  levels of copper are almost full. Therefore, the absorption spectra is tributary mostly to the  $4d$  transitions. It follows that the effect of the mixing when the transitions concern delocalized levels is weak.

**TDDFT and the cut-off level** There is an inherent advantage of the TDDFT calculations on the final state rule ones: the former introduce no ambiguity in the calculation of the cut-off level. In the TDDFT case, the cut-off is the Fermi level of the ground state calculation. In the case of final state rule calculations, the Fermi level (a one body, ground state concept) loses its meaning and the cut-off is calculated as the energy where the integrated  $d$  DOS equals the nominal  $d$  electrons on the absorbing



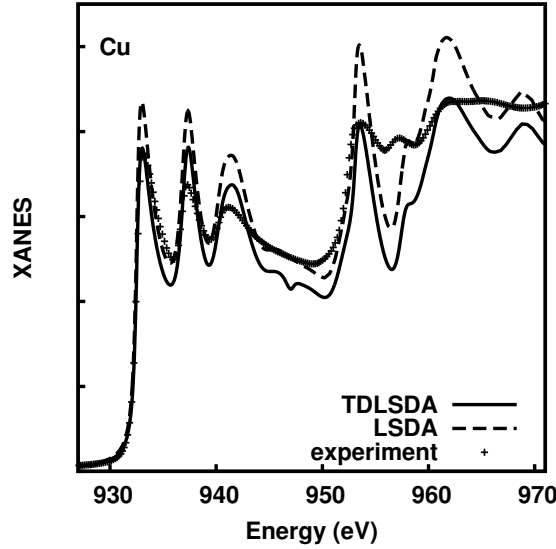


Figure 6.13: One body LSDA (dashes) and TDLSA calculations (solid) versus experiment for copper at the  $L_{2,3}$  edges. Both calculations were run on a 9 Å cluster (248 atoms) and the value of the broadening parameter is 0.6 eV. It appears that for delocalized edges, the TDLSA corrections are negligible.

atom. This means that the photoelectron takes part in the screening process and is absent from the  $3d$  levels. Such a procedure to determine the cut-off is justified by our aiming at a better agreement with the experiment, but is still theoretically ambiguous. On the contrary, the RPA-LF does not encounter such problems: the only impeding factor to the precise identification of the cut-off level are the non-spherical effects. For the  $3d$  simple elements at the  $L_{2,3}$  edges, we found that TDDFT calculations are to be preferred to the final state rule ones.

**TDDFT and the mixing of transition channels** We noticed that performing a TDDFT calculation at a single edge, whether completely delocalized (the  $K$  edge of the  $3d$  elements) or not (the  $L_2$  or the  $L_3$  edges of the  $3d$  elements), yields practically the same values as its IPA correspondent. It follows that our method can only account for the local fields or exchange-correlation effects through the mechanism of the mixing of transitions, which occurs when one solves (in a single calculation) some adjacent edges, like the  $L_{2,3}$  edges of the  $3d$  elements. Moreover, one can see that the correction brought in by the TDDFT procedure reduces while the atomic number, and thus the energy distance between  $L_2$  and  $L_3$ , increase. Although in principle the TDDFT correction should also affect the isolated edges, we never managed to have a quantitative effect. We believe this is a consequence of the local approximation on the exchange-correlation kernel.

The available transitions (single particle excitations) in the X-ray range are sparser than the ones of the optical frequencies. The core spectroscopy involves initial levels that are rather far from one another. For instance, a  $L_2$  calculation does not need to take into account the possible transitions from the  $2s$  level of the absorber. On the

other hand, it needs to account for the ones from  $2p_{3/2}$ , which are a lot closer (a few eV).

Therefore, using our TDDFT implementation for the calculation of a single  $L_2$  ( $L_3$ ) edge of a  $3d$  element does not make any sense. In such a case, the approximation we made to the Adler Wiser equation (6.18) no longer stands. One is allowed to select a few transition channels (the  $g$  states instead of all the occupied states) provided they are isolated from the rest of the spectrum. This is not the case for a single  $L_2$  ( $L_3$ ) transition.

We analysed in detail the mechanism of the mixing. We banned the mixing between the cross-edge transitions in (6.40), by artificially setting to zero the kernel elements connecting the  $2p_{1/2}$  and the  $2p_{3/2}$  states. In this way we only allowed the intra-edge mixing, corresponding to the crossing of the  $2p_{1/2}$ , or of the  $2p_{3/2}$  states, respectively. Under these conditions, we get results that are similar to the IPA. It follows that only the inter-edge mixing contribute to the change in the branching ratio, in the limit of the local approximation. This conclusion is in perfect agreement with the findings of Scherz et al. [99].

## 6.5 Conclusions and perspectives

We presented a detailed study of adiabatic TDDFT methods applied to X-ray absorption at the  $L_{2,3}$  edges. The work presented in this chapter is at its beginning and further refinement is to be expected. We have shown that although the TDDFT with local kernels provides an improvement with respect to the IPA calculations, there is still an essential ingredient missing from our TDDFT scheme. We think that the same as for the optical region, at X-ray frequencies the core hole effects are essential in order to get a satisfactory agreement with the experimental data. It has been argued [19] that the TDLSDA is supposed to give satisfactory results for core spectroscopy. Our results invalidate this statement, thus a non local (and eventually frequency dependent) exchange-correlation kernel is imperative for a TDDFT calculation of core spectroscopies. In other words, one needs a kernel that can describe the excitonic effects.

There are clear shortcomings of the TDDFT calculations on extended systems, at the present moment. The most stringent ones concern some specific aspects of the spectra, like the prediction of multiplet and excitonic lines, or the correct position of  $E_2 - E_2$  structures at  $K$  edges. It is still unclear to what extent the limitations of the underlying DFT-LDA ground state calculation affect the performance of the TDDFT calculation. In so far the latter is concerned, the exchange-correlation kernel accounting for all the many body effects (including multiplets) has not been derived yet. It follows that the TDDFT calculations on extended systems encounter huge limitations for strongly correlated materials.

Our conclusion is in reasonable agreement with the work of Schwitalla and Ebert [101] on local fields effects. On the other hand, our results contradict the findings of Ankudinov, Nesvizhskii and Rehr [7], who pretend to have achieved a perfect agreement with the experimental values of the  $L_{2,3}$  branching ratios for the  $3d$  elements, all by employing a local kernel (the restricted TDLSDA). Moreover, our results indicate that all the local exchange-correlation kernels we employed (RPA-LF, TDLSDA, restricted TDLSDA) yield similar results, which goes against the findings in reference [7]. We

equally disagree with Ankudinov, Takimoto and Rehr [9], who claim to have developed a mixed TDDFT-BSE calculation scheme.

It follows that the X-ray absorption community lacks a convenient calculation tool that is able to account for the core hole. One of the perspectives of this work include the implementation of a genuine, BSE derived, TDDFT kernel which is supposed to describe the excitonic effects. Second, we wish to test the way in which our TDDFT procedure couples to the LSDA+U ground state calculations. The calculation of the  $L_{2,3}$  edges of correlated materials is expected to benefit from this *duo*.

## Chapter 7

# A study of the colossal magnetoresistive $\text{Pr}_{0.6}\text{Ca}_{0.4}\text{MnO}_3$ perovskite

### 7.1 The context of the study

The manganites <sup>1</sup> are perovskites of type  $\text{Re}_x\text{A}_{1-x}\text{MnO}_3$ , where Re is a trivalent rare earth (Pr, La, Nd, Sm etc.) and A a divalent alkali element (Ba, Ca, Sr) yielding a partially filled Mn 3*d* band. For particular values of doping, manganites exhibit the colossal magnetoresistance effect, which encouraged extensive research work aiming at elucidating the origins of this extraordinary transport property.

The manganites have rich phase diagrams that show a (classical) critical point around the same value of the doping  $x$ . It follows that in the vicinity of this point, the balance between the various degrees of freedom (spin, orbital or charge) is very sensitive to external conditions like pressure, magnetic and electric fields or variations of temperature or doping. The colossal magnetoresistance effect exhibited by manganites at half-doping is believed to be a consequence of the interplay between the orbital and spin degrees of freedom. Its mechanism is as follows: while the ground state of these manganites is insulating and antiferromagnetic, applying an external magnetic field destroys the orbital order. The emerging state is metallic and ferromagnetic, thus with a drop in resistivity.

To understand and control the phase transition it is imperative to unambiguously determine the ground state of the half-doped manganites. At room temperature, these materials have a single manganese site (of formal charge 3.5). At low temperature, three distinct manganese sites appear:  $\text{Mn}_1$ ,  $\text{Mn}_2$  and  $\text{Mn}_3$  (see figure 7.1). The first and simplest microscopic model for the low temperature phase was introduced in the early '50s by Goodenough, who proposed a charge ordered model in the form of a checkerboard pattern of the  $\text{Mn}^{3+}$  and  $\text{Mn}^{4+}$  [46]. In this model,  $\text{Mn}_1$  and  $\text{Mn}_2$  correspond to the 3+ formal charge and are subjected to the Jahn-Teller effect (i.e. the lifting of

---

<sup>1</sup> Although the term *manganite* is unanimously agreed upon in material science, its use is inaccurate. In inorganic nomenclature, the manganite is a mineral, whereas any negatively charged molecular entity with manganese as the central atom is called a *manganate*.

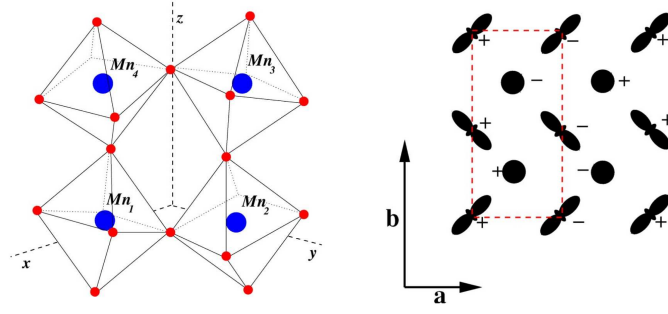


Figure 7.1: On the left, the  $\text{Pr}_{0.6}\text{Ca}_{0.4}\text{MnO}_3$  unit cell in the high temperature phase. The octahedra are formed by the oxygen atoms and are centred around the manganese. For simplicity, the Ca/Pr atoms are not shown. All octahedra are equivalent. On the right, a sketch of the ground state in the original Goodenough model. The filled eights represent the occupied  $e_g$  orbital on the  $\text{Mn}_{3+}$  sites, whereas the closed circles represent the isotropic  $\text{Mn}_{4+}$ . The + and - signs indicate the relative orientations of the spin. The rectangle marks the unit cell for the orbital order, whereas the whole picture represents the unit cell when considering the additional magnetic ordering. The images have been taken from reference [47].

orbital degeneracy following the distortion of the oxygen octahedron centred around the manganese atom).  $\text{Mn}_3$  is isotropic and bears the  $4+$  formal charge.

At the present moment we know that the Goodenough model is not accurate: recent X-ray studies at the  $K$  edge of manganese [47, 54] go against the hypothesis of the charge separation. Nevertheless, the picture of the Jahn-Teller / isotropic manganese atoms holds. One therefore needs to refine the classical Goodenough model towards a more realistic description of the ground state of manganites. The RXD experimental technique is particularly suitable for this task, as it gets to probe the orbital, magnetic and eventual charge order by a clever choice of the scattering vector. In the particular case of  $\text{Pr}_{0.6}\text{Ca}_{0.4}\text{MnO}_3$  several resonant scattering experimental studies, either at the  $K$  edge [47, 48] or at the  $L_{2,3}$  edges [110, 115], exist. To our knowledge, the only theoretical interpretations of the latter are based on multiplet calculations. We believe that our *ab initio* calculation schemes can be used to gain more insight into these experiments.

Calculating the manganese  $L_{2,3}$  edges in manganites is a very delicate task and requires an approach that goes beyond the one body picture. To acquire better knowledge of the material, we chose to begin with the calculation of the  $K$  edge. The next step is to run our TDDFT calculation schemes at the  $L_{2,3}$  edges. We underline the fact that this is the first application of a TDDFT method to a RXD spectrum calculation. Consequently, we pay particular attention to the polarization effect and its eventual alteration in the many-body framework.

In its low temperature phase,  $\text{Pr}_{0.6}\text{Ca}_{0.4}\text{MnO}_3$  crystallizes in the  $Pbnm$  spacegroup [90], which contains three distinct manganese atoms:  $\text{Mn}_1$ ,  $\text{Mn}_2$  and  $\text{Mn}_3$  (see figure 7.1). The orientation of the spins remains unknown and its determination is one of the tasks of the calculations.

## 7.2 The resonant X-ray diffraction study

The low temperature phase of  $\text{Pr}_{0.6}\text{Ca}_{0.4}\text{MnO}_3$  is antiferromagnetic, of propagation vector (100). All through this manuscript, the indices correspond to the low temperature unit cell (the experimental studies generally refer to the high temperature unit cell). The orbital order spans in the perpendicular direction, with the propagation vector (010). The only resonant contributions to the magnetic (100) and orbital (010) reflections come from  $\text{Mn}_1$  and  $\text{Mn}_2$ .

An important aspect to be discussed is that at the  $K$  edge, the (010) reflection probes the Jahn-Teller distortion, and not the orbital ordering. This issue was long debated upon in the late '90s. The final resolution is that at  $K$  edge one sees the coupling between the  $p$  states and the  $t_{2g}$  states issued from the Jahn Teller effect [12, 14]. Should one have no distortion but ordered  $d$  orbitals, the coupling between these and the  $p$  states is too weak to yield a signal at the (010) position. Consequently, we did not describe any orbital ordering in the input of the calculation. A structure that has the Jahn Teller distortion is sufficient to yield a good agreement with the experimental data.

At the  $L_{2,3}$  edges, the distinction between the Jahn Teller distortion and the orbital order no longer makes sense, as one probes directly the  $d$  orbitals. The Jahn-Teller distortion breaks the symmetry of the  $t_{2g}$  orbitals, and this asphericity propagates with the (010) periodicity - the orbital ordering. The orbital ordering needs to be explicitly described as input only when it is not associated to the Jahn-Teller effect, as in the case of  $\text{NdMg}$  (see section 3.2).

The (020) and (060) reflections measure the difference between the Jahn-Teller manganese atoms  $\text{Mn}_1$  and  $\text{Mn}_2$  and the isotropic  $\text{Mn}_3$  (see table 7.1). For historical reasons, they are called charge order reflections, as they are supposed to account for the charge separation between the  $\text{Mn } 3+$  and  $\text{Mn } 4+$  of the Goodenough model. Experimental data unambiguously reject this hypothesis [128]: in  $\text{Pr}_{0.6}\text{Ca}_{0.4}\text{MnO}_3$  the charge order peak in the  $\sigma - \sigma$  configuration vanishes at  $\phi = \pi/2$  azimuth, i.e. when the incoming  $\sigma$  polarization is along  $\text{Oz}$ . Such setup, which is insensitive to the Jahn-Teller distortion contained in the  $x\text{Oy}$  plane, is supposed to reveal the difference in the structure factors of the two kinds of manganese, if any. Of course, this conclusion should be taken with care, i.e. some slight charge ordering may be compatible with the experimental resolution.

The (020) and (060) reflections can only be measured at the  $K$  edge. At the lower energy  $L_{2,3}$  edges these points lie outside the Ewald sphere. Nonetheless, the charge ordering phenomena (if any) is the same whatever the edge and it is unnecessary to measure it at the  $L_{2,3}$  edges.

## 7.3 Tensor analysis

In this section we shall deal with the azimuthal dependence of the reflections we are interested in, at both  $K$  and  $L_{2,3}$  edges. Calculations show that  $\text{Mn}_1$  and  $\text{Mn}_2$  have quasi-identical electronic structures.

Mn <sub>1</sub>							Mn <sub>3</sub>						
Position			010	100	020	Op.sym.	Position			020	Op.sym.		
0.	0.	0.	1	1	1	E	0.241	0.25	0.	-1	E		
0.5	0.	0.	1	-1	1	TE	0.241	0.25	0.5	-1	m <sub>z</sub>		
0.	0.	0.5	1	1	1	TC <sub>2z</sub>	0.259	0.75	0.	-1	Ti		
0.5	0.	0.5	1	-1	1	C <sub>2z</sub>	0.259	0.75	0.5	-1	TC <sub>2z</sub>		
Mn <sub>2</sub>							0.741	0.25	0.	-1	TE		
Position			010	100	020	Op.sym.	0.741	0.25	0.5	-1	Tm <sub>z</sub>		
0.	0.5	0.	-1	1	1	E	0.759	0.75	0.	-1	i		
0.5	0.5	0.	-1	-1	1	TE	0.759	0.75	0.5	-1	C <sub>2z</sub>		
0.	0.5	0.5	-1	1	1	TC <sub>2z</sub>							
0.5	0.5	0.5	-1	-1	1	C <sub>2z</sub>							

Table 7.1: Positions, Bragg factors and symmetry operations for the non-equivalent manganese atoms.

Let  $D_1$  ( $D_2$ ) the tensor describing the prototypical Mn<sub>1</sub> (Mn<sub>2</sub>) atom:

$$D_1 = \begin{pmatrix} a_1 & d_1 & e_1 \\ d_1^* & b_1 & f_1 \\ e_1^* & f_1^* & c_1 \end{pmatrix} \quad (7.1)$$

The symmetry operations in table 7.1 transform the tensor in the following way:

$$TED_1 = \begin{pmatrix} a_1 & d_1^* & e_1^* \\ d_1 & b_1 & f_1^* \\ e_1 & f_1 & c_1 \end{pmatrix} \quad (7.2)$$

$$C_{2z}D_1 = \begin{pmatrix} a_1 & d_1 & -e_1 \\ d_1^* & b_1 & -f_1 \\ -e_1^* & -f_1^* & c_1 \end{pmatrix} \quad (7.3)$$

$$TC_{2z}D_1 = \begin{pmatrix} a_1 & d_1^* & -e_1^* \\ d_1 & b_1 & -f_1^* \\ -e_1 & -f_1 & c_1 \end{pmatrix} \quad (7.4)$$

and the equivalent for the  $D_2$  transformations. On the basis of the principles expound in section 2.2.1 and similarly to the calculation in section 3.2.2, the amplitudes of the (010), (100) and (020) scatterings give:

$$A_{010} = 4 \begin{pmatrix} a_1 - a_2 & \Re d_1 - \Re d_2 & 0 \\ \Re d_1 - \Re d_2 & b_1 - b_2 & 0 \\ 0 & 0 & c_1 - c_2 \end{pmatrix} \quad (7.5)$$

$$A_{100} = 4 \begin{pmatrix} 0 & 0 & i(\Im e_1 + \Im e_2) \\ 0 & 0 & i(\Im f_1 + \Im f_2) \\ -i(\Im e_1 + \Im e_2) & -i(\Im f_1 + \Im f_2) & 0 \end{pmatrix} \quad (7.6)$$

$$A_{020} = 4 \begin{pmatrix} a_1 + a_2 - 2a_3 & \Re d_1 + \Re d_2 - 2\Re d_3 & 0 \\ \Re d_1 + \Re d_2 - 2\Re d_3 & b_1 + b_2 - 2b_3 & 0 \\ 0 & 0 & c_1 + c_2 - 2c_3 \end{pmatrix} \quad (7.7)$$

The origin of (010) and (020) being electrical, their amplitude tensor elements are real. On the contrary, the (100) is magnetic, thus its amplitude contains purely imaginary terms. This discussion is general and applies to both  $K$  and  $L_{2,3}$  edges. It is important to mention that the actual values of the general tensor (7.1) depend on the choice of the edge, as the majority, dipolar probed states are not the same. As a consequence, the magnetic reflection (100) cannot be seen at the  $K$  edge: the magnetism carried by the  $d$  orbitals yields tensor elements that are too weak. For the rest of the reflections, there is no need to describe the magnetism for the  $K$  edge calculations and one could stick to a general tensor (7.1) with real elements.

## 7.4 Results at the $K$ edge

The  $K$  edge of  $\text{Pr}_{0.6}\text{Ca}_{0.4}\text{MnO}_3$  is rather easy to calculate: we performed non-magnetic MST calculations on a cluster of 157 atoms (7.65 Å). We did not describe any charge or orbital ordering for the manganese atoms, as input data (see the explanations above).  $\text{Pr}_{0.6}\text{Ca}_{0.4}\text{MnO}_3$  is a solid state solution: the insertion of Ca in the  $\text{PrMnO}_3$  matrix is not periodic. We perform two distinct calculations for  $\text{PrMnO}_3$  and  $\text{CaMnO}_3$  by using the same crystallographic structure [90], then convolute the resulting diffraction amplitudes with a weight of 0.6 and 0.4.

In the calculations, the indexation of reflection obeys the low temperature unit cell. To retrieve the experimental indexes one must divide by  $h$  and  $k$  by a factor of 2. In figures 7.2 and 7.3 we compare calculations and experimental data for the charge and orbital reflections, respectively. The agreement is rather good. We succeed in reproducing the global shapes of the spectra, as well as the spectral details at the 6542 eV in the charge order spectra. On the contrary, the localized structures around 6562 eV for the (020) and 6568 eV for (060) are not well resolved by our calculations. At the very same energies, very discrete shoulders appear in the (030) spectrum, and are equally missed by our calculation. The simulations equally overestimate the intensity of the signal after the edge, for the charge order reflections, and underestimates it for the orbital order ones.

Calculations predict a narrower orbital order spectral line than the one that is actually measured (figure 7.3). We believe that this is a consequence of the experimentalists having used different monochromators for the (020) and (030) outgoing polarization analysis. Consequently, there are two distinct experimental resolutions, whereas in the calculations we used a single one.

From (7.5) and (7.6), and after the multiplication with the incoming and outgoing polarizations, we get to calculate the azimuthal dependence of the diffracted intensity. We set the origin of the azimuth  $\phi$  along the  $Oz$  axis, or, equivalently, when the sigma polarization  $\epsilon_\sigma$  is contained in the  $xOy$  plane. At zero azimuth and  $K$  edge we calculate:

$$\frac{I_{010}^{\sigma\pi}}{I_{010\phi=0}^{\sigma\sigma}} = \frac{\cos^2 \theta_B (\Re d_1 - \Re d_2)}{(a_1 - a_2)^2} \gg 1 \quad (7.8)$$

as  $a_1 \approx a_2$  due to the similarity in the  $p$  states of  $\text{Mn}_1$  and  $\text{Mn}_2$ . This means that calculations predict that orbital order scatterings occur in the  $\sigma - \pi$  channel exclusively. This result disagrees with the experimental data in reference [128] (figure 7 -



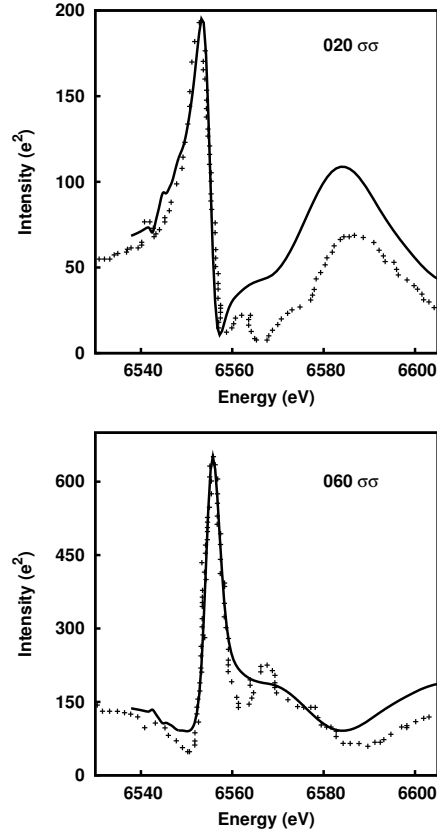


Figure 7.2: The charge order reflections (020) and (060) in the dominant  $\sigma - \sigma$  channel: theory (solid) and experiments from reference [47] (dots). The experimental data were scaled to the maximum of the diffraction peak.

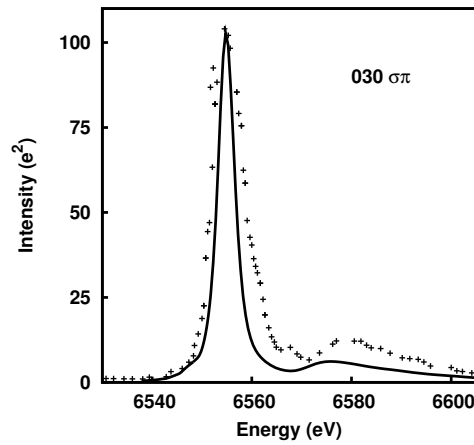


Figure 7.3: The orbital order reflection (030) in the dominant  $\sigma - \pi$  channel: theory (solid) and experiments from reference [47] (dots). The experimental data were scaled to the maximum of the diffraction peak.

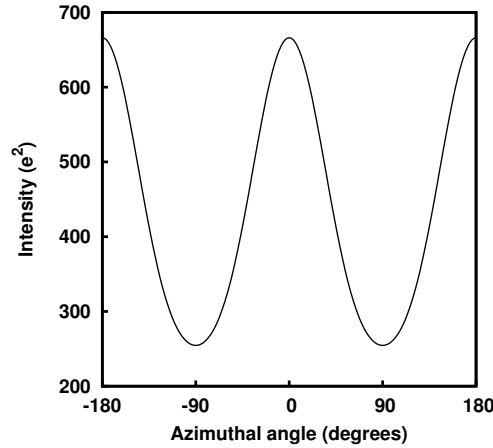


Figure 7.4: The azimuthal dependence of the calculated charge order reflection (060) in the dominant  $\sigma - \sigma$  channel. The experimental data in [128] show a cancellation of the intensity at  $\phi = 90$ , which proves the absence of the charge ordering. The larger the calculation radii, the higher the minimum in  $\phi = 90$ . We conclude that this is an artefact of the calculation, as it overestimates the difference in electronic structure between the  $\text{Mn}_1$  and  $\text{Mn}_2$ , on one hand, and  $\text{Mn}_3$ , on the other hand.

the experimental reflections are indexed based on the high temperature unit cell). At the  $K$  edge, the measured (030)  $\sigma - \sigma$  scattering is not negligible (the 010 was not measured), as there is experimental evidence for non-resonant Thomson scattering. This is probably due to the fact that the spacegroup used in the calculations and suggested in the literature [90] is not accurate enough, and thus the real symmetry is lower than the one which was used.

The dominant contribution to the (030) scattering is in the  $\sigma - \pi$  channel. The calculations show a very good agreement with the experimental data (figure 7.3). Contrary to the (010) and (030) orbital order reflections, the dominant scattering channel for the charge order (020) and (060) reflections is the  $\sigma - \sigma$ :

$$\frac{I_{020}^{\sigma\pi}}{I_{020}^{\sigma\sigma}_{\phi=0}} = \frac{\cos^2 \theta_B (\Re d_1 + \Re d_2 - \Re d_3)}{(a_1 + a_2 - 2a_3)^2} \ll 1 \quad (7.9)$$

in agreement with the experiment [47]. We obtain a non-zero minimum for the (060)  $\sigma - \sigma$  at  $\phi = 90$  (see figure 7.4). The calculations predict a ratio  $I_{020}^{\sigma\sigma}(\phi = 90)/I_{020}^{\sigma\sigma}(\phi = 0)$  between 0.1 (for a cluster radius of 5.65 Å) and 0.3 (for 7.65 Å) instead of the zero (in the limits of the experimental resolution) obtained in [128]. We mention that the data in [128] are not corrected for self-absorption. The value of the ratio of the intensities at the two azimuths should not depend on the radius of the cluster, once convergence with respect to the cluster size has been achieved. We believe that its overestimation is an artefact of the calculation. The MT approximation enhances the difference in electronic structure between the  $\text{Mn}_1$  and  $\text{Mn}_2$ , on one hand, and  $\text{Mn}_3$ , on the other hand.

Our calculations predict a charge ordering, even if in the input all the manganese atoms were described with the same atomic configuration. In a sense, this is to be

expected, in both experiment and simulation, while  $\text{Mn}_1$ ,  $\text{Mn}_2$  and  $\text{Mn}_3$  are on different sites. The reason for the disagreement is to be looked for either in the experiment (resolution problems, misalignment, lack of polarisation analysis) or in the calculations (as explained above).

Experimentally, no traces of the structural phase transition have been noticed on the (020)  $\sigma - \pi$  reflection [47]. Note that the (020) is forbidden in the high temperature phase, where all the manganese atoms are equivalent. Measuring a signal requires some kind of asphericity (enhanced by the resonant regime): one measures the difference between two atoms that are connected by a symmetry operation other than the identity. This phenomenon is called the Templeton effect. One might say that if the (020)  $\sigma - \pi$  reflection intensity is not altered in the phase transition point, it is insensitive to the Jahn-Teller distortion.

Above the phase transition (no periodicity of the distorted octahedra), a simple calculation gives:

$$I_{020}^{\sigma\pi}|_{HT} = 16d^2 \cos^2 \theta_B \quad (7.10)$$

whereas below the transition point (in temperature):

$$I_{020}^{\sigma\pi}|_{LT} = 16(d_1 + d_2 - d_3)^2 \cos^2 \theta_B \quad (7.11)$$

HT (LT) stands for high (low) temperature and  $d$  is the  $xy$  general tensor element for the manganese atom in HT. At the  $K$  edge one is allowed to take  $d_1 \approx -d_2$ : when neglecting the  $d$  orbitals contribution,  $\text{Mn}_1$  and  $\text{Mn}_2$  are connected by a  $m_x$  mirror. The isotropic  $\text{Mn}_3$  is barely affected by the structural transition, thus we approximate  $d_3 \approx d$ . Within these approximations, we obtain an overestimated factor 4 in favour of the LT phase. We therefore plead that the Jahn-Teller distortion affects the (020)  $\sigma - \pi$  indirectly, *via* the change in the  $xy$  tensor element for the isotropic manganese. This explains why the reflection is not dramatically increased at the transition point.

In the reflections we studied, the E2-E2 contribution is minimal. Although the RXD spectra calculations agree very well with the experimental data in terms of shape and intensities, they are placed at a too high energy (not shown here). To get our reference, we superposed the experimental and calculated XANES signal. This effect is most probably a screening issue: the final state rule fails. We chose not to proceed in the direction of trying partial screening, as the calculations provide a most satisfactory analysis of the RXD spectra, which are not expected to be altered by a potential energy shift.

## 7.5 Results at the $L_{23}$ edges

In this chapter, we use some unpublished data of K.J. Thomas et. al. [115]. In this experiment, the (010) and (100) reflections were measured at the  $L_{2,3}$  edges of manganese, on a single crystal. The incoming photons were  $\pi$  polarized and no polarisation analysis was performed on the outgoing beams. The orbital reflection (010) was measured with the crystal  $c$  axis in the scattering plane, whereas the magnetic (100) was measured with  $c$  perpendicular to the scattering plane. In our calculations, the origin of the azimuthal angle is along  $c$  ( $Oz$ ). This gives  $\Psi = 0$  for the orbital reflection and  $\Psi = 90$  for the magnetic one.

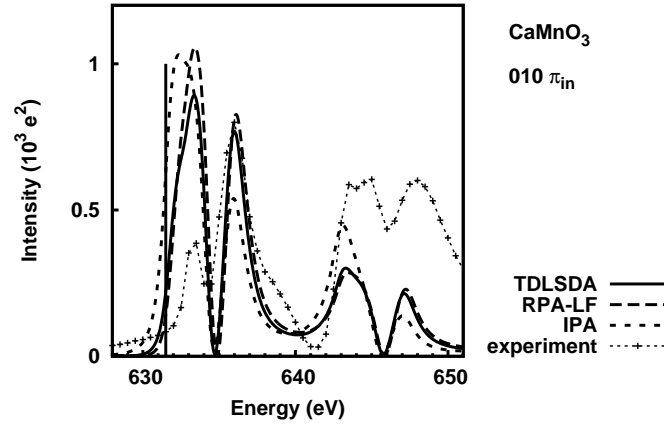


Figure 7.5: TDLSA (solid), RPA-LF (long dashes) and IPA (short dashes) calculations of the orbital (010) incoming  $\pi$  reflection. The calculations were performed on  $\text{CaMnO}_3$ , whereas the experimental data (line with points) was taken on  $\text{Pr}_{0.6}\text{Ca}_{0.4}\text{MnO}_3$ . The Fermi level of  $\text{Mn}_1$  and  $\text{Mn}_2$  is indicated with a vertical line. The best agreement is given by the TDLSA calculation: the first structure in the spectrum is shifted from 631.5 eV in the IPA calculation to 632.2 eV in the TDLSA one, following the trend in the experiment.

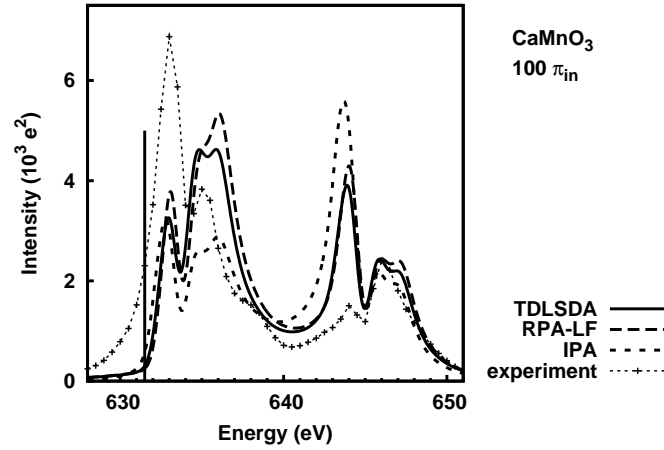


Figure 7.6: TDLSA (solid), RPA-LF (long dashes) and IPA (short dashes) calculations of the magnetic (100) incoming  $\pi$  reflection. The calculations were performed on  $\text{CaMnO}_3$ , whereas the experimental data (line with points) was taken on  $\text{Pr}_{0.6}\text{Ca}_{0.4}\text{MnO}_3$ . The Fermi level of  $\text{Mn}_1$  and  $\text{Mn}_2$  is indicated with a vertical line. The best agreement is given by the TDLSA calculation: the intensity of the structure at 644 eV decreases, whereas its position is shifted by 0.2 eV with respect to its IPA counterpart.

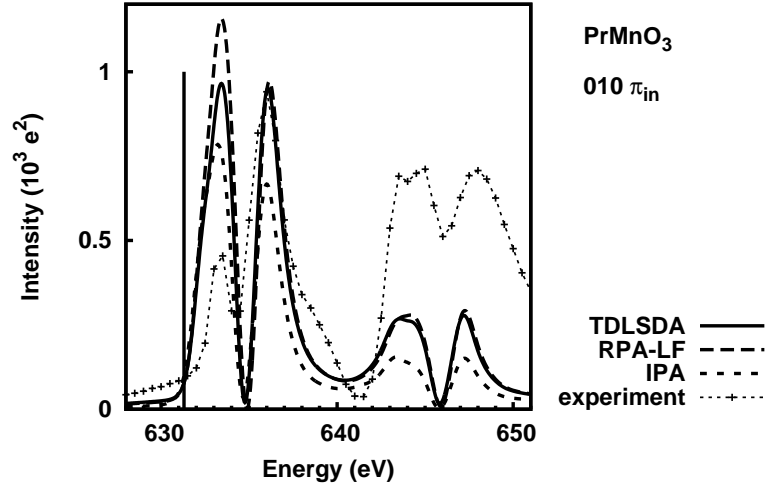


Figure 7.7: TDLSA (solid), RPA-LF (long dashes) and IPA (short dashes) calculations of the orbital (010) incoming  $\pi$  reflection. The calculations were performed on  $\text{PrMnO}_3$ , whereas the experimental data (line with points) was taken on  $\text{Pr}_{0.6}\text{Ca}_{0.4}\text{MnO}_3$ . The Fermi level of  $\text{Mn}_1$  and  $\text{Mn}_2$  is indicated with a vertical line. The TDLSA improves the intensity of the structure at 644 eV.

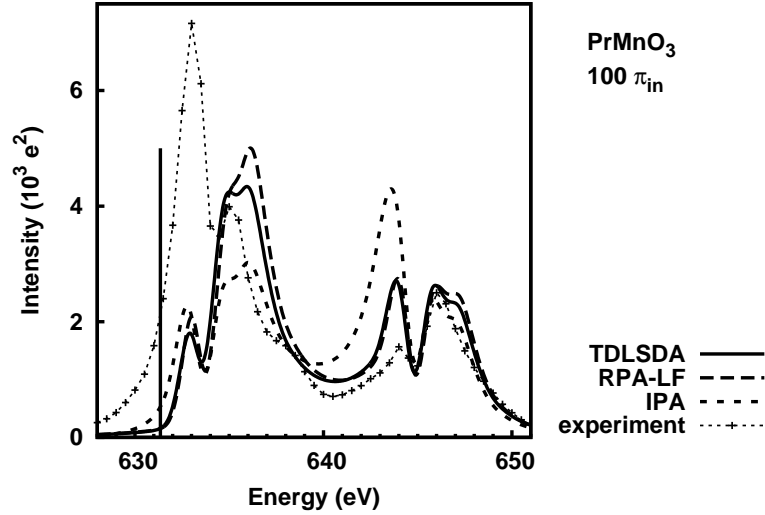


Figure 7.8: TDLSA (solid), RPA-LF (long dashes) and IPA (short dashes) calculations of the magnetic (100) incoming  $\pi$  reflection. The calculations were performed on  $\text{PrMnO}_3$ , whereas the experimental data (line with points) was taken on  $\text{Pr}_{0.6}\text{Ca}_{0.4}\text{MnO}_3$ . The Fermi level of  $\text{Mn}_1$  and  $\text{Mn}_2$  is indicated with a vertical line.

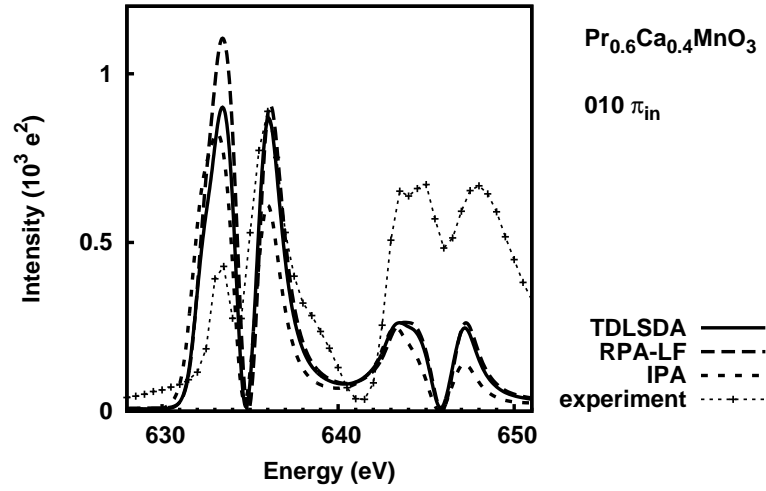


Figure 7.9: TDLSA (solid), RPA-LF (long dashes), IPA (short dashes) calculations and experimental data (line with points) on the magnetic (010) incoming  $\pi$  reflection at the  $L_{2,3}$  edges of Mn in  $\text{Pr}_{0.6}\text{Ca}_{0.4}\text{MnO}_3$ . The TDLSA improves the intensity of the structure at 644 eV.

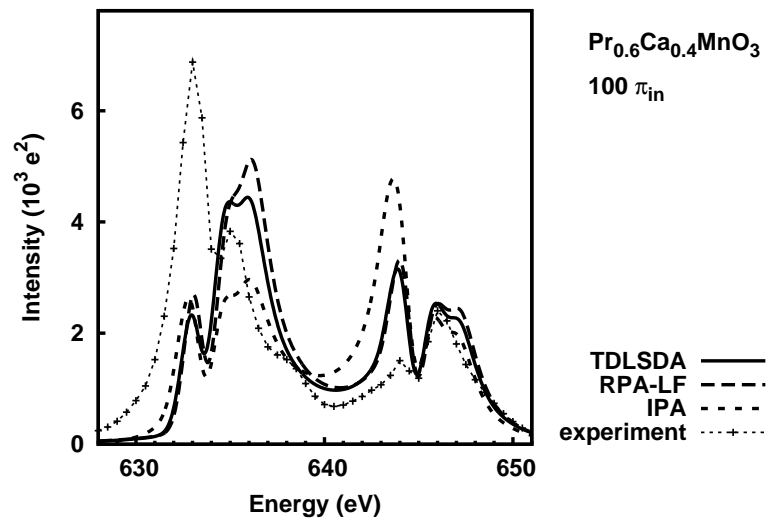


Figure 7.10: TDLSA (solid), RPA-LF (long dashes), IPA (short dashes) calculations and experimental data (line with points) on the magnetic (100) incoming  $\pi$  reflection at the  $L_{2,3}$  edges of Mn in  $\text{Pr}_{0.6}\text{Ca}_{0.4}\text{MnO}_3$ .

The experimental data should be looked at with extreme precaution. First, the crystal used in the experiment is twinned. Due to the close values of  $a$  and  $b$  the (010) and (100) reflections are not well resolved in the  $k$  space, which may bias the values of the measured intensities. Second, the magnetic reflection spectrum shown in [115] ( $c$  axis normal to the scattering plane) indicates intensities that are two orders of magnitude higher than the ones of the orbital reflection. Experiments on powders refute this finding [110] which leads us to the conclusion that this fact is either an experimental artefact, or a feature linked to the particular azimuth. Our calculations support the former, which lead us to scale all the experimental data in a convenient way.

All the calculations were performed on a 6.13 Å cluster (87 atoms) and convoluted with the energy independent, tabulated values [60]. In this work we will discuss the improvement brought by the TDDFT calculations (RPA-LF and TDLSDA) upon the IPA ones. We chose not to show the restricted TDLSDA data, which is quasi-identical to the TDLSDA. We equally chose not to show the extended TDLSDA results, due both to the lack of foundation of this method, as explained in chapter 6, and to the poor agreement with the experimental data.

The TDDFT results introduced in this section are original in the sense that this is the first application of a TDDFT method to the calculation of RXD spectra. Generally speaking, the corrections suggested by the TDDFT are more spectacular for RXD than they are for XANES. A peculiar feature in the measured spectra [115], and that cannot be explained in the IPA picture, is that the magnetic reflection is shifted by 0.7 eV towards the low energies, with respect to the orbital one. In the following we will show how the TDDFT partially succeeds in modelling this shift.

There is a lot of experimental evidence (on both  $\text{Pr}_{0.6}\text{Ca}_{0.4}\text{MnO}_3$  and other manganites, regardless of the choice of the edge) proving that the (010) and (100) scatterings take significant values only in the rotated  $\sigma - \pi$  or  $\pi - \sigma$  channels [47, 110]. Our calculations support this finding: the (010) and (100)  $\pi - \pi$  intensities are negligible.

As a starting point we used the magnetic structure in reference [90]. All the calculations we show include the spin-orbit coupling and are not self-consistent. In figures 7.5 and 7.6, on one hand, and 7.7 and 7.8, on the other hand, we compare the experimental data with the calculations on  $\text{CaMnO}_3$  and  $\text{PrMnO}_3$ , respectively. An extra shift (0.5 eV to the higher energies) has been employed for the latter. The partial agreement is different in the two cases. For  $\text{CaMnO}_3$ , the TDDFT succeeds in shifting the peak at 635 eV in the IPA (010) spectrum by 0.7 eV towards the higher energies. This is exactly the quantity needed to obtain a perfect agreement. Unfortunately,  $\text{PrMnO}_3$  does not reproduce the same behaviour. Consequently, the convolution of two, with a weight favourable to the  $\text{PrMnO}_3$  (0.6) yields only a small fraction ( $\approx 20\%$ ) of the required shift (figures 7.9 and 7.10). Both in terms of intensities and shifts, we estimate that the TDLSDA gives the best results of all the three calculations (the second best being the RPA-LF). The TDLSDA constantly improves the intensity of the structure at 644 eV in the magnetic (100) spectrum.

In figures 7.5, 7.6 we pictured the Fermi level of  $\text{Mn}_1$  and  $\text{Mn}_2$  by a vertical line. The Fermi levels corresponding to the two different calculation clusters (centered around  $\text{Mn}_1$  and  $\text{Mn}_2$  respectively) are calculated in the first step of the calculation, according to the procedure featured in chapter 4. We recall that  $\text{Mn}_3$  does not participate in the

concerned reflections, as well as the fact that  $\text{Mn}_1$  and  $\text{Mn}_2$  are quasi-identical, thus with similar Fermi levels. One can see that in the cases of both  $\text{CaMnO}_3$  and  $\text{PrMnO}_3$  the Fermi level is placed in the gap (more precisely, it is at the very beginning of the  $d$  band, but this is a calculation artefact). This was to be expected, as both materials have a Mott insulating low temperature phase. It follows that the calculations might benefit from a LSDA+U calculation followed by a TDDFT one. We are currently working on this issue.

Our calculations on  $\text{CaMnO}_3$  and  $\text{PrMnO}_3$ , with and without the spin-orbit coupling (not shown here) indicate that the contribution of the latter is minimal. This was to be expected, as the  $3d$  orbital moment is quenched in the  $3d$  systems. Small differences do exist, and surprisingly they are more important in the orbital than in the magnetic spectrum. If no coupling and for the (010) reflection, the most stringent effect is the modification of the azimuthal dependence, as compared to the IPA calculation. Such an effect is to be expected when two or more elements of the atomic tensor contribute to the azimuthal dependence. The TDDFT brings an individual correction for both of them, and this may alter the azimuthal dependence.

## 7.6 Conclusions and perspectives

In this chapter we confronted calculations to the resonant diffraction experimental data on  $\text{Pr}_{0.6}\text{Ca}_{0.4}\text{MnO}_3$ , at both the  $K$  and  $L_{2,3}$  edges of manganese. The agreement is far better at the former than it is at the latter. Many body effects are important at the  $L_{2,3}$  edges of Mn in  $\text{Pr}_{0.6}\text{Ca}_{0.4}\text{MnO}_3$ , thus we decided to employ the TDDFT method to improve upon the IPA calculation. We stress the fact that this is a very audacious pursuit, as  $\text{Pr}_{0.6}\text{Ca}_{0.4}\text{MnO}_3$  is an alloy containing two different magnetic materials, each of them having three non-equivalent manganese atoms.

This work shows the first results of a TDDFT calculation method applied to the RXD technique. These first results are encouraging, but there is still room for improvement. The TDLSDA correction only achieves in partially reproducing the energy shift between the (100) and (010) reflections. Further improvements are needed to get the entire shift. Work in progress consists in using the Hubbard correction U for the  $3d$  orbitals of manganese, in the ground state calculation that precedes the TDLSDA one. Although we do expect a change for the better, we strongly believe that only by improving the TDDFT kernel can we obtain a satisfactory agreement with the experimental spectra.





## Chapter 8

# Conclusions and Perspectives

The present work is aiming at a better *ab initio* description of X-ray absorption spectroscopy. Research efforts were invested in three distinct directions: setting up a self-consistent procedure, the implementation of an LSDA+U calculation scheme and the establishment of a TDLSDA procedure adapted to the core spectroscopies energy range. In spite of the fact that all these procedures are well established in more "standard" cases (reciprocal space calculations, optical frequencies ...), the X-ray community lacks a detailed study of their applicability for core spectroscopies. A major purpose of this work is to answer to these questions. At a higher level, we wish to investigate the interplay of the theoretical developments mentioned above: performing a TDDFT calculation preceded by self-consistent, real space, ground state LSDA+U one.

In the following we will sum up our major conclusions. The main advantage in performing a real space, X-ray absorption, self-consistent calculation is that it gives a reasonable estimate of the Fermi level. Technical constraint forced us to implement the self-consistent procedure in the MT approximation. Consequently, self-consistency in itself is less important than the full potential feature. The effect of self-consistency is very little for absorption spectra at  $K$  edges. Nevertheless, one needs to use this feature in the case of a LSDA+U calculation, which is very sensitive to the electronic structure. The TDLSDA calculation gives a better agreement than the IPA one, at the  $L_{2,3}$  edges of both simple ( $3d$  elements) and complex materials (manganites). Nevertheless, for a satisfactory agreement, one should improve the TDDFT kernel. It appears that the pertinent description of the core hole is essential for the X-ray absorption spectroscopy calculations. It follows that only a non-local and, ideally, frequency dependent, kernel is a suitable candidate for this task.

This work set up the tools and a methodology to calculate XANES, RXD and XMCD spectra behind the one body picture. Its natural continuation would be to exploit the methods established and tested within this Ph.D. work in order to explore interesting physics.



# Résumé en français

Les spectroscopies autour des seuils d'absorption X sont d'excellents moyens d'analyse de l'environnement de l'atome absorbeur sur le plan géométrique, électronique ou magnétique. A très basse énergie (domaine du XANES pour X-ray Absorption Near Edge Structure), les données expérimentales prises au synchrotron sont encore souvent mal interprétées par les modèles théoriques en vigueur alors que c'est là qu'elles sont le plus riches en informations sur le matériau étudié. L'interprétation de ces phénomènes est un enjeu important pouvant s'appliquer à l'étude des matériaux les plus divers qu'ils soient d'intérêts physiques (magnétisme, conduction ..), chimiques (catalyse ...) ou même biologiques. Ce travail a pour but l'amélioration des méthodes existantes et l'implémentation de nouvelles méthodes de calcul des transitions électroniques, applicable au XANES, à la diffraction résonnante et au dichroïsme. Parmi les nombreuses techniques de calcul, les plus répandues sont celles dites "monoélectroniques" utilisant la fonctionnelle densité (DFT) et les méthodes de type multiplet. Les premières réussissent généralement à reproduire les seuils K, alors que les multiplets sont plutôt appropriés pour les seuils  $L_{2,3}$  et  $M_{4,5}$ . La tendance actuelle est de s'orienter vers des méthodes de calcul qui fonctionnent dans les deux cas. Parmi celles-ci nous mentionnons les méthodes de calcul basées sur la théorie de la fonctionnelle densité dépendante du temps (TDDFT), l'équation Bethe-Salpeter (BSE) et la méthode multicanal.

**Le but de ce travail** Les outils actuels de simulation des spectroscopies d'absorption (absorption X, diffraction résonnante, dichroïsme circulaire magnétique) manquent souvent de précision dans la description des spectres expérimentaux. Les travaux présentés dans le cadre de cette thèse ont pour but de diminuer l'écart entre l'expérience et la théorie. Tous ces développements théoriques ont été intégrés dans le code FDMNES. J'ai contribué à l'amélioration des méthodes de calcul existantes, l'implémentation de la procédure autocohérente, et au développement de nouvelles méthodes: la procédure LDA+U et la méthode TDDFT. Des nombreux calculs sur des composés modèles ont été effectués, afin de tester l'exactitude et la solidité de nos méthodes. Les résultats des calculs FDMNES ont été comparés à ceux issus d'autres méthodes ou codes de calcul. Il n'existe pas une technique unique de calcul, qui soit appropriée pour toutes les classes de matériaux. En conséquence, une autre direction de ce travail était de tester les limites de chaque méthode présentée dans le cadre de cette thèse. Grâce à cette étude, nous sommes en mesure de proposer des options de calcul par défaut, ce qui aide des utilisateurs moins expérimentés de ces simulations. Des calculs sur des composés complexes ont également été effectués et les données expérimentales ont été interprétées.

**Le but du manuscrit** L'intérêt principal de ce manuscrit est d'introduire le lecteur aux techniques *ab initio* de calcul des spectroscopies d'absorption de rayons X. Le formalisme et ses limites en terme d'approximations sont expliqués, l'implémentation des méthodes est décrite en détail puis illustrée par des exemples parlants. L'autocohérence dans l'approche monoélectronique et la méthode LDA+U puis la TDDFT sont successivement présentées. Les succès et les failles de chaque de ces méthodes ainsi que leur domaine d'applicabilité sont discutés. Pour quelques composés spécifiques (NdMg, manganates) les résultats des plusieurs méthodes de calcul sont décrits en spécifiant laquelle est la plus appropriée par rapport aux données expérimentales et pourquoi.

**La structure du manuscrit** La première partie de ce manuscrit (les deux premiers chapitres et la première section du troisième) constituent une introduction générale au domaine et au code FDMNES. Le reste du manuscrit contient les développements théoriques réalisés pendant cette thèse. Les paragraphes suivants résument le contenu de chaque chapitre.

**Introduction** Le premier chapitre est une introduction aux techniques expérimentales - l'absorption X (XANES), la diffraction résonnante (RXD) et le dichroïsme magnétique circulaire (XMCD)- et aux méthodes de calcul correspondantes. Je donne une vue d'ensemble sur l'utilisation des techniques synchrotron dans de nombreux directions de la science de matériaux et des sciences du vivant. En particulier, je décris les avantages des techniques rayons X par rapport à leurs équivalents en neutrons. Finalement je présente l'état de l'art dans les méthodes de calcul actuellement utilisées pour la simulation de ces spectroscopies. Une distinction entre les méthodes dites monoélectroniques (à un corps) et basées sur la théorie de la fonctionnelle densité (DFT) et les méthodes atomiques (multiplets, interaction des configuration, diagonalization exacte) est faite. Ces techniques sont complémentaires: les premières donnent des résultats satisfaisants lorsque la structure électronique des états d'arrivée est plutôt délocalisée, alors que les deuxièmes fonctionnent lorsque les états d'arrivée sont localisés (atomiques). Les techniques DFT sont *ab initio*, i.e. elles n'introduisent pas de paramètres fondamentaux, alors que les multiplets et les techniques de diagonalization exacte utilisent un Hamiltonien où les différentes interactions ont été quantifiées de manière paramétrisée. Il existe également des modèles de bande qui vont au delà de l'approximation monoélectronique - les méthodes TDDFT ou BSE. La clé d'une description raisonnable de l'absorption X est d'aller vers des méthodes qui incluent la description atomique dans les modèles de bande. Dans ce sens nous mentionnons la procédure LDA+U et le calcul basé sur la théorie dynamique du chaps moyen (DMFT) couplée à l'approximation de la densité locale (LDA).

**Aspects fondamentaux de l'interaction des rayons X avec la matière** Le deuxième chapitre est dédié aux aspects fondamentaux de l'interaction des rayons X avec la matière. En premier lieu, les formules de base du processus de l'absorption (la section efficace d'absorption et celle de diffusion) sont déduites en utilisant les outils de la seconde quantification. Dans la suite du chapitre le formalisme tensoriel pour la description des spectroscopies mentionnées est exposé, en intégrant les simplifications introduites par la description des symétries locales. Finalement, les éléments de base

de la résolution de la structure électronique du solide sont présentés.

**FDMNES et le calcul monoélectronique** Le troisième chapitre traite de la méthode monoélectronique du calcul FDMNES. L'organigramme général du code est présenté, ainsi que chaque étape en particulier: le calcul des états atomiques, le calcul du potentiel, la résolution de l'équation de Schrödinger radiale et de la structure électronique, le calcul des tenseurs et la convolution finale. Dans la dernière partie du chapitre 3 je présente une application du calcul monoélectronique à l'étude RXD de l'ordre magnétique et quadrupolaire dans NdMg, aux seuils  $L_{2,3}$  du neodyme.

**La procédure autocohérente** Le quatrième chapitre contient l'étude de la procédure autocohérente pour le calcul de l'absorption X. Je présente les détails de l'implémentation, ainsi que les résultats sur des composés simples (le cuivre aux seuils  $K$  et  $L_{2,3}$ , la même chose pour les éléments de transition) ou plus complexes (le  $\text{TiO}_2$ , le BN et le CaO, tous au seuil  $K$ ). La conclusion générale est que l'autocohérence a très peu d'influence sur la forme des spectres d'absorption. Néanmoins, l'information la plus importante que l'on obtient est une estimation pertinente de la position du niveau de Fermi. L'identification de celui-ci est essentielle pour l'élimination des états occupés, et donc pour obtenir un bon accord avec les spectres expérimentaux. Quantitativement, l'estimation est assez exacte pour les structures compactes, mais peut être imprécise pour les matériaux où les effets non-sphériques sont importants. Dans ce même cas des structures compactes, le calcul autocohérent de la structure électronique peut être effectué sur un rayon d'agrégat plus petit que celui utilisé pour le calcul de l'absorption. Des contraintes techniques ont imposé que l'autocohérence dans FDMNES soit implémentée dans le cadre de l'approximation *muffin-tin*. Nos résultats sur BN et CaO indiquent que les calculs non autocohérents mais sans aucune approximation pour le potentiel (méthode des différences finies) sont meilleurs que ceux auto-cohérents, mais utilisant l'approximation *muffin-tin*. Jusqu'ici, cette discussion a été contrainte aux calculs du seuil  $K$ . Il est assez délicat de conclure sur les seuils  $L_{2,3}$ , car l'accord avec les données expérimentales est assez mauvais, que l'on soit autocohérent ou pas, en raison des effets multiélectroniques. Bien que l'auto-cohérence fournit une densité d'états électroniques plus fiable, cela ne suffit pas pour avoir un accord satisfaisant. De manière générale, l'introduction d'une procédure autocohérente n'est pas un but en soi, mais une étape nécessaire pour d'autres développements théoriques telle la méthode TDDFT ou la procédure LDA+U.

**La méthode LDA+U** Le cinquième chapitre se préoccupe de la procédure de calcul LDA+U, ou la correction de Hubbard. Cette méthode est censée améliorer la description des orbitales corrélées, i.e. les  $3d$  des éléments de transition ou les  $4f$  des terres rares. L'esprit de cette méthode est de rajouter des corrections atomiques (le terme U) pour les orbitales mentionnées tout en gardant la description de bande (LDA) pour le reste. Je présente les fondements de cette méthode, les détails de l'implémentation et quelques résultats préliminaires sur les seuils  $K$  et  $L_{2,3}$  du manganèse dans  $\text{LaMnO}_3$ . Nous avons constaté que les résultats de la LDA+U sont extrêmement sensibles au taux d'occupation de l'orbitale corrélée, d'où la nécessité d'effectuer un calcul autocohérent en amont. On pourrait penser que la correction que la LDA+U apporte à la LDA est

plus importante aux seuils  $L_{2,3}$ , où on sonde directement les orbitales corrélés, qu'au seuil  $K$ . Nos résultats montrent cependant un changement de la forme du spectre XANES même pour un seuil  $K$ . Toujours-est-il que plus de tests seront nécessaires avant de conclure sur le sujet de la LDA+U appliquée à l'absorption X. La correction U arrive à ouvrir le *gap* autour du niveau de Fermi dans  $\text{LaMnO}_3$  et donc à décrire la physique de ce matériau (un isolant de Mott), ce qui constitue une faille de la LDA.

**Au delà de l'approche monoélectronique** Le sixième chapitre contient l'aspect le plus important de ce travail de thèse - la méthode TDDFT appliquée à l'absorption X. Les bases de cette théorie sont introduites, ainsi que l'implémentation de la méthode dans le code FDMNES. Bien que ce ne soit pas la première fois qu'une méthode TDDFT ait été appliquée à l'absorption X, les études précédentes ne sont pas claires. Nos travaux ont pour but d'étudier dans quelle mesure l'approximation locale de la TDDFT (TDLDA) est appropriée au calcul des spectroscopies de cœur. Nos résultats montrent que malgré le fait que la TDLDA améliore nettement les résultats du calcul monoélectronique des seuils  $L_{2,3}$  des éléments de transition, un élément essentiel manque dans cette description: le trou de cœur. Nous concluons que comme pour l'absorption optique, la description de l'effet excitonique est une condition nécessaire pour avoir un bon accord avec l'expérience. En conséquence, la continuation de ce travail implique l'amélioration du noyau TDDFT en vue de l'inclusion de ces effets.

**L'étude RXD du  $\text{Pr}_{0.6}\text{Ca}_{0.4}\text{MnO}_3$**  Le septième et dernier chapitre contient l'étude RXD du  $\text{Pr}_{0.6}\text{Ca}_{0.4}\text{MnO}_3$  aux seuils  $K$  et  $L_{2,3}$  du manganèse. Bien que les simulations du seuil  $K$  donnent un bon accord avec l'expérience, les seuils  $L_{2,3}$  sont assez mal reproduits aussi bien en monoélectronique qu'en TDLDA. La TDLDA apporte une amélioration par rapport au monoélectronique, mais cette amélioration n'est pas suffisante. Nous estimons que seule une amélioration du noyau de la TDDFT peut donner un accord satisfaisant. Nous soulignons le fait que ce calcul constitue la première application d'une méthode TDDFT au calcul de RXD. Ce matériau est compliqué également par le fait qu'il nécessite deux calculs indépendants (les seuils  $L_{2,3}$  du manganèse dans  $\text{CaMnO}_3$  et  $\text{PrMnO}_3$ ) dont chacun implique le calcul de trois atomes non-équivalents.

**Perspectives** Ce travail eut pour but l'amélioration des descriptions *ab initio* des spectroscopies d'absorption X. Des efforts ont été investis dans trois directions préférentielles: la mise au point d'une procédure autocohérente, l'implémentation de la méthode LDA+U et l'établissement d'une méthode de calcul basée sur l'approximation locale de la TDDFT. Malgré le fait que tous ces éléments sont déjà établis dans des cas plus standards (calculs dans l'espace réciproque, fréquences optiques) la communauté des rayons X manque d'une étude détaillée de leur applicabilité pour les spectroscopies de cœur. L'intérêt de cette thèse est de répondre à ces questions. Pour la suite, nous envisageons de regarder l'interaction entre les outils mentionnés, par des calculs TDLDA précédés de calculs autocohérents LSDA+U de l'état fondamental. Il faudra aussi améliorer la prise en compte de l'effet du trou de cœur par l'introduction d'un noyau d'échange-corrélation non locale et dépendant de temps. Enfin la continuation de cette thèse consistera en l'application des méthodes mises au point au calcul de composés complexes.

# Appendices

The norm of the radial solution . . . . .	133
The radial solution of the Dirac equation . . . . .	134
The physical quantities in the presence of the spin-orbit coupling . . . . .	135
The Hartree kernel . . . . .	136
The TDLSDA exchange-correlation kernel . . . . .	137
The generalized Gaunt coefficient . . . . .	138
Equations of the TDDFT with the spin-orbit coupling . . . . .	139

## The norm of the radial solution

This appendix describes the normalization procedure for the radial wavefunction that is employed by FDMNES. If no spin-orbit coupling, the eigenfunctions of (2.29) can be expanded around each atom core. Consequently:

$$\tilde{\phi}(\vec{r}) = \sum_l \sum_{m=-l}^l a_{lm}(E) \tilde{b}_{lm}(r, E) Y_l^m(\hat{r}) \quad (1)$$

where  $Y_l^m(\hat{r})$  are the complex spherical harmonics. Let

$$\tilde{\phi}_l(r, E) = a_l(E) \tilde{b}_l(r, E) \quad (2)$$

the radial part of the SE regular solution. Note that the energy dependence is contained mainly in the  $a_l$  coefficient. The following procedure holds for each  $m \in (-l, l)$  and thus we make no further reference to the  $m$  quantum number. We want to normalize the radial wavefunctions in order to match the stationary solution of the SE in the vacuum:

$$\phi_{vac}(r, E) = \sqrt{\frac{k}{\pi}} (j_l(kr) - i t_l h_l^+(kr)) \quad (3)$$

where  $t_l$  is the atomic, energy dependent, scattering amplitude,  $k = \sqrt{E}$ ,  $j_l(kr)$  the Bessel function and  $h_l^+(kr)$  the retarded (outgoing) Haenkel function. This second term accounts for the scattered waves whereas the  $\frac{k}{\pi}$  factor normalizes to the density of states in the vacuum. In practice we impose the continuity at the MT radius  $r_{MT}$  of the two wavefunctions (the free and the atomic) and of their first order derivatives:

$$a_l(E) \tilde{b}_l(r_{MT}, E) = \sqrt{\frac{k}{\pi}} (j_l(kr_{MT}) - i t_l h_l^+(kr_{MT})) \quad (4)$$

$$a_l(E) \tilde{b}_l'(r_{MT}, E) = \sqrt{\frac{k}{\pi}} (j_l'(kr_{MT}) - i t_l h_l^{+'}(kr_{MT})) \quad (5)$$



yielding:

$$\frac{a_l}{t_l} = -\frac{1}{\pi r_{MT}^2} \sqrt{\frac{k}{\pi}} W^{-1}(j_l, b_l)|_{r=r_{MT}} \quad (6)$$

where  $W(f, g) = fg' - f'g$  is the wronskian. We choose the norm as:

$$b_l(r, E) = \frac{a_l}{t_l} \tilde{b}_l(r, E) \quad (7)$$

yielding:

$$\phi_l(r) = a_l(E) b_l(r, E) \quad (8)$$

which means that  $h_l^+$  and  $\phi_l(r)$  match. This normalization corresponds to one state *per Rydberg*. A similar procedure is employed for the normalisation of the solutions of the Dirac equation, where we perform a distinct calculation for each spin population.

### The radial solution of the Dirac equation

After the elimination of the small components, the Dirac equation gives [122]:

$$\begin{aligned} & \left( -\nabla^2 + V(\vec{r}) - E - \frac{\alpha^2}{4} (V(\vec{r}) - E)^2 \right. \\ & \left. - \frac{\alpha^2}{4} \frac{1}{1 - \frac{\alpha^2}{4} (V(\vec{r}) - E)} (\nabla V(\vec{r}) \nabla + i \vec{\sigma} (\nabla V(\vec{r}) \times \nabla)) \right) \Psi(\vec{r}) = 0 \end{aligned} \quad (9)$$

where  $\alpha$  is the fine structure constant and  $\vec{\sigma}$  are the Pauli matrices ( $i = 1, 2, 3$ ):

$$\sigma_1 = \begin{pmatrix} 0 & 1 \\ 1 & 0 \end{pmatrix}; \quad \sigma_2 = \begin{pmatrix} 0 & -i \\ i & 0 \end{pmatrix}; \quad \sigma_3 = \begin{pmatrix} 1 & 0 \\ 0 & -1 \end{pmatrix} \quad (10)$$

The first three terms of (9) are the same as those of the Schrödinger equation, whereas the rest are relativistic ones. The forth term induces an energy shift (with respect to the non-relativistic case) and the last is the quantitative spin-orbit coupling. The solution  $\Psi(\vec{r})$  is a two component spinor:

$$\Psi(\vec{r}) = \begin{pmatrix} \Psi_{\uparrow}(\vec{r}) \\ \Psi_{\downarrow}(\vec{r}) \end{pmatrix} \quad (11)$$

and the potential  $V(\vec{r})$  is spin polarised:

$$V(\vec{r}) = \begin{pmatrix} V_{\uparrow}(\vec{r}) \\ V_{\downarrow}(\vec{r}) \end{pmatrix} \quad (12)$$

The Dirac equation (9) contains no approximation, and is valid for a potential of arbitrary symmetry. Note that the spin-orbit term in (9) is proportional to the gradient of the potential. It follows that there can be no spin-flip in a region of

constant potential, like the interstitial space between the MT spheres. The radial solution of (9) is a system of two coupled equations:

$$\begin{cases} \left( -\frac{d^2}{dr^2} + G_{Ol\uparrow}(\vec{r}) + mG_{SO\uparrow}(\vec{r}) \right) u_{l,m,\uparrow}(r) \\ + \sqrt{(l-m)(l+m+1)} G_{SO\uparrow}(\vec{r}) u_{l,m+1,\downarrow}(r) = 0 \\ \sqrt{(l-m)(l+m+1)} G_{SO\downarrow}(\vec{r}) u_{l,m,\uparrow}(r) \\ + \left( -\frac{\partial^2}{\partial r^2}(\vec{r}) + G_{Ol\downarrow}(r) - (m+1) G_{SO\downarrow}(\vec{r}) \right) u_{l,m+1,\downarrow}(r) = 0 \end{cases}$$

where  $(\sigma = \uparrow, \downarrow)$ :

$$G_{Ol\sigma} = V_\sigma(\vec{r}) - E + \frac{l(l+1)}{r^2} - \frac{\alpha^2}{4} (V_\sigma(\vec{r}) - E)^2 - \frac{\alpha^2}{4} \frac{1}{1 - \frac{\alpha^2}{4} (V_\sigma(\vec{r}) - E)} \frac{\partial V_\sigma(\vec{r})}{\partial r} \left( \frac{d}{dr} - \frac{1}{r} \right) \quad (13)$$

$$(14)$$

and

$$G_{SO\sigma} = \frac{\alpha^2}{4} \frac{1}{1 - \frac{\alpha^2}{4} (V_\sigma(\vec{r}) - E)} \quad (15)$$

### The physical quantities in the presence of the spin-orbit coupling

If one takes into account the spin-orbit coupling, and still for a real potential, the spin polarised quantities in section 2.3.5 become:

$$\begin{aligned} \rho_{l,m+\frac{1}{2}-\sigma}^{l',m'+\frac{1}{2}-\sigma}(r, \sigma) &= -\frac{1}{\pi} \Im \sum_{ss'} \int_0^{E_F} dE b_{l',m'+\frac{1}{2}-\sigma,\sigma}^{s'}(r, E) \\ &\times \tau_{l,m+\frac{1}{2}-s,s}^{l',m'+\frac{1}{2}-s',s'}(E) b_{l,m+\frac{1}{2}-\sigma,\sigma}^s(r, E) \end{aligned} \quad (16)$$

$$\begin{aligned} \delta_\sigma(E) &= -\frac{1}{\pi} \Im \int d^3r \sum_{ss'} \sum_{l,m} \\ &\times b_{l,m+\frac{1}{2}-\sigma,\sigma}^{s'}(r, E) \tau_{l,m+\frac{1}{2}-s,s}^{l,m+\frac{1}{2}-s,s}(E) b_{l,m+\frac{1}{2}-\sigma,\sigma}^s(r, E) \end{aligned} \quad (17)$$

$$N_\sigma = \int d^3r \sum_{l,m} \rho_{l,m+\frac{1}{2}-\sigma}^{l,m+\frac{1}{2}-\sigma}(r, \sigma) \quad (18)$$

$$\begin{aligned} \sigma(\omega) &= \frac{\pi\omega}{\epsilon_0 c} \left( \frac{e}{\hbar} \right)^2 \sum_g \sum_{\sigma\sigma'} \sum_{lms} \sum_{l'm's'} \Im \tau_{l,m+\frac{1}{2}-s,s}^{l',m'+\frac{1}{2}-s',s'} \\ &\times \left( \int d^3r \phi_g^{\sigma*}(\vec{r}) O^*(\vec{\epsilon}, \vec{r}) b_{l,m+\frac{1}{2}+\sigma,\sigma}^s(r) Y_l^{m+\frac{1}{2}+\sigma}(\hat{r}) \right) \\ &\times \left( \int d^3r \phi_g^{\sigma'}(\vec{r}) O(\vec{\epsilon}, \vec{r}) b_{l',m'+\frac{1}{2}+\sigma,\sigma}^{s*}(r) Y_{l'}^{m'+\frac{1}{2}+\sigma'+*}(\hat{r}) \right) \end{aligned} \quad (19)$$

$$\begin{aligned}
f'(\omega) - if''(\omega) &= \frac{m\omega^2}{\hbar^2} \sum_{\sigma\sigma'} \sum_g \sum_{lms} \sum_{l'm's'} \int_{E_F}^{\infty} dE \frac{\Im \tau_{l,m+\frac{1}{2}-s,s'}^{l',m'+\frac{1}{2}-s',s'}}{\omega - (E - E_g) + i\Gamma(E)} \\
&\times \left( \int d^3r \phi_g^{\sigma*}(\vec{r}) O_{out}^*(\vec{\epsilon}, \vec{r}) b_{l',m'+\frac{1}{2}+\sigma,\sigma}^{s'}(r) Y_{l'}^{m'+\frac{1}{2}+\sigma'}(\hat{r}) \right) \\
&\times \left( \int d^3r \phi_g^{\sigma}(\vec{r}) O_{in}(\vec{\epsilon}, \vec{r}) b_{l,m+\frac{1}{2}+\sigma,\sigma}^s(r) Y_l^{m+\frac{1}{2}+\sigma*}(\hat{r}) \right) \quad (20)
\end{aligned}$$

For a potential taking complex values, the same quantities as above can be deduced from the following propagator [116]:

$$\begin{aligned}
\mathcal{G}_{\sigma\sigma'}(\vec{r}, \vec{r}') &= \sum_{l,m} \sum_{l',m'} \sum_{s,s'} b_{l',m'+\frac{1}{2}-\sigma',\sigma'}^{s'}(r', E) Y_{l'}^{m'+\frac{1}{2}-\sigma'}(\hat{r}') \\
&\times \left( \tau_{l,m+\frac{1}{2}-s,s}^{l',m'+\frac{1}{2}-s',s'}(E) - \delta_{ll'} t_{l,m+\frac{1}{2}-s,s}^{l',m'+\frac{1}{2}-s',s'}(E) \right) b_{l,m+\frac{1}{2}-\sigma,\sigma}^s(r, E) Y_l^{m+\frac{1}{2}-\sigma}(\hat{r}) \\
&- \sum_{l,m} \sum_s s_{l,m+\frac{1}{2}-\sigma',\sigma'}^s(r_<, E) Y_l^{m+\frac{1}{2}-\sigma',\sigma'}(\hat{r}_<) \\
&\times t_{l,m+\frac{1}{2}-s,s}^{l,m+\frac{1}{2}-s,s}(E) s_{l,m+\frac{1}{2}-\sigma,\sigma}^s(r_>, E) Y_l^{m+\frac{1}{2}-\sigma,\sigma}(\hat{r}_>) \quad (21)
\end{aligned}$$

We underline the fact that the propagator  $\mathcal{G}$  crosses the spins, i.e. it couples some *up* and *down* elements. For an explanation of the physical meaning of a complex potential, please refer to section 3.1.6.

### The Hartree kernel

The total classical energy of a charged system is:

$$\mathcal{E} = \sum_{\sigma\sigma'} \int d^3r \int d^3r' \frac{n_{\sigma}(\vec{r}) n_{\sigma'}(\vec{r}')}{|\vec{r} - \vec{r}'|} \quad (22)$$

If one assimilates the charge distributions with Dirac functions, one gets the energy of a two charge system. One equally has:

$$\mathcal{E} = \frac{1}{2} \sum_{\sigma} \int d^3r V(\vec{r}, \sigma) n_{\sigma}(\vec{r}) \quad (23)$$

where  $V$  is the Hartree (classical) potential. The Hartree potential is the functional derivative of the total energy:

$$V(\vec{r}, \sigma) = \frac{\delta \mathcal{E}}{\delta n_{\sigma}(\vec{r})} \quad (24)$$

which yields:

$$V(\vec{r}, \sigma) = \sum_{\sigma'} \int d^3r' \frac{n_{\sigma'}(\vec{r}')}{|\vec{r} - \vec{r}'|} \quad (25)$$

Note that the Hartree potential is independent of spin:  $V(\vec{r}, \uparrow) = V(\vec{r}, \downarrow)$ . More explicitly:

$$V(r) = \int d^3r' \frac{n_{\uparrow}(\vec{r}')}{|\vec{r} - \vec{r}'|} + \int d^3r' \frac{n_{\downarrow}(\vec{r}')}{|\vec{r} - \vec{r}'|} \quad (26)$$

The kernel of the Hartree term:

$$f(\vec{r}, \sigma, \sigma') = \frac{\delta V(\vec{r}, \sigma)}{\delta n_{\sigma'}(\vec{r})} \quad (27)$$

which gives:

$$f_H(\vec{r}, \uparrow, \uparrow) = f_H(\vec{r}, \downarrow, \downarrow) = f_H(\vec{r}, \uparrow, \downarrow) = \frac{1}{|\vec{r} - \vec{r}'|} \quad (28)$$

or

$$f_H(\vec{r}, \sigma, \sigma') = \frac{1}{|\vec{r} - \vec{r}'|} \quad (29)$$

### The TDLSDA exchange-correlation kernel

Let the parameters [78]:

$$c_P = 0.045; \quad c_F = \frac{c_P}{2}; \quad r_P = 21; \quad r_F = 2^{\frac{4}{3}} r_P \quad (30)$$

and the following notations ( $\sigma = \uparrow, \downarrow$ ):

$$x^{\sigma} = \frac{n^{\sigma}}{n^{\uparrow} + n^{\downarrow}}; \quad \left(n^{\uparrow} + n^{\downarrow}\right)^{-1} = \frac{4\pi}{3} r_S^3 \quad (31)$$

$$\mu_c^{P,F} = -c_{P,F} \ln \left(1 + \frac{r_{P,F}}{r_S}\right); \quad \epsilon_c^{P,F} = -c_{P,F} f \left(1 + \frac{r_S}{r_{P,F}}\right) \quad (32)$$

$$\nu_C = \frac{4}{3} \frac{1}{2^{\frac{1}{3}} - 1} (\epsilon_C^F - \epsilon_C^P) \quad (33)$$

where

$$f(y) = (1 + y^3) \ln \left(1 + \frac{1}{y}\right) + \frac{1}{2}y - y^2 - \frac{1}{3} \quad (34)$$

By using the form of the exchange-correlation potential in reference [86], the exchange-correlation kernel reads (we omit the  $\vec{r}$  dependence for convenience):

$$f_{xc}^{\sigma} = \frac{\delta V_{xc}^{\sigma}}{\delta n^{\sigma}} \quad (35)$$

$$\begin{aligned}
f_{xc}^\sigma = & - \frac{4\pi r_S^2}{9} \left\{ \left( 2(1-x)(2x)^{-\frac{2}{3}} + 2x^{\frac{1}{3}} \right) \left( \frac{18}{\pi^2} \right)^{\frac{1}{3}} + \frac{c_P r_P}{1 + \frac{r_P}{r_S}} \right. \\
& + \frac{4}{3} \frac{1}{1 - 2^{-\frac{1}{3}}} \left( x^{\frac{4}{3}} + (1-x)^{\frac{4}{3}} - x^{\frac{1}{3}} \right) r_S^2 \\
& \times \left[ + \frac{c_F}{r_F} \left( 3 \left( \frac{r_S}{r_F} \right)^2 \ln \left( 1 + \frac{r_F}{r_S} \right) - \frac{r_F}{r_S} + \frac{3}{2} - 3 \frac{r_S}{r_F} \right) \right. \\
& \quad \left. - \frac{c_P}{r_P} \left( 3 \left( \frac{r_P}{r_F} \right)^2 \ln \left( 1 + \frac{r_P}{r_S} \right) - \frac{r_P}{r_S} + \frac{3}{2} - 3 \frac{r_P}{r_F} \right) \right] \\
& + \frac{1}{1 - 2^{-\frac{1}{3}}} \left( x^{\frac{4}{3}} + (1-x)^{\frac{4}{3}} - 2^{-\frac{1}{3}} \right) \left( \frac{c_F r_F}{1 + \frac{r_F}{r_S}} - \frac{c_P r_P}{1 + \frac{r_P}{r_S}} \right) \\
& + 2^{\frac{1}{3}} r_S \nu_C (1-x) \left( 4x^{\frac{1}{3}} - 4(1-x)^{\frac{1}{3}} + x^{-\frac{2}{3}} \right) \\
& \left. + \frac{4}{1 - 2^{-\frac{1}{3}}} r_S (\mu_C^F - \mu_C^P) (1-x) \left( -x^{\frac{1}{3}} + (1-x)^{\frac{1}{3}} \right) \right\} \quad (36)
\end{aligned}$$

### The generalized Gaunt coefficient

Starting from the known Gaunt coefficients [123]:

$$G_3(L_1, L_2, L_3) = \int d\Omega Y_{L_1}^*(\Omega) Y_{L_2}(\Omega) Y_{L_3}(\Omega) \quad (37)$$

we want to calculate:

$$G_4(L_1, L_2, L_3, L_4) = \int d\Omega Y_{L_1}^*(\Omega) Y_{L_2}(\Omega) Y_{L_3}^*(\Omega) Y_{L_4}(\Omega) \quad (38)$$

where  $L = (l, m)$ . One can always expand:

$$Y_{L_1}^*(\Omega) Y_{L_2}(\Omega) = \sum_L c_{L_1 L_2}^L Y_L(\Omega) \quad (39)$$

Should one multiply (39) by  $Y_{L'}(\Omega)$  and integrate with respect of  $d\Omega$ :

$$c_{L_1 L_2}^L = G_3(L_2, L_1, L) \quad (40)$$

after using the fact that  $G_3$  s are real. (39) becomes:

$$Y_{L_1}^*(\Omega) Y_{L_2}(\Omega) = \sum_L G_3(L_2, L_1, L) Y_L(\Omega) \quad (41)$$

One can re-write (41) in the form:

$$Y_{L_3}^*(\Omega) Y_{L_4}(\Omega) = \sum_{L'} G_3(L_4, L_3, L) Y_{L'}(\Omega) \quad (42)$$

From (41) and (42) one obtains:

$$G_4(L_1, L_2, L_3, L_4) = \sum_L G_3(L_2, L_1, L) G_3(L_4, L_3, L) \quad (43)$$

## Equations of the TDDFT with the spin-orbit coupling

This appendix introduces the equations of chapter 6, adapted for a non zero spin-orbit coupling for the final states. This is meant to be a technical section and we therefore skip the detailed comments of the formulae. Please refer to section 6 for a detailed explanation. The main difference with the zero coupling limit consists in the appearance of two extra summations over the two solutions  $s$  and  $s'$  of the SE, as introduced in section 2.3.1. Note that in this case  $\chi_0$  is no longer diagonal with respect to the spin variable. The initial wavefunctions are:

$$\phi_g(\vec{r}) = \sum_{\sigma} \phi_g^{\sigma}(\vec{r}) \zeta_{\sigma} = \sum_{\sigma} c_{\Lambda_g^{\sigma}} b_g(r) Y_{\Lambda_g^{\sigma}}(\hat{r}) \zeta_{\sigma} \quad (44)$$

where  $\Lambda_g^{\sigma} = (l_g, m_g + \frac{1}{2} - \sigma, \sigma)$  is the set of quantum numbers characterizing the initial states and  $\zeta_{\sigma}$  the spin eigenfunction. One can see that each initial state  $\phi_g(\vec{r})$  is a sum of the two spin contributions, weighted by the Clebsch-Gordon coefficients  $c_{\Lambda_g^{\sigma}}$ . The final state wavefunction can be written as [57]:

$$\Psi_f(\vec{r}, E) = \sum_{\sigma} \sum_{\Lambda_s} a_{\Lambda_s}^f(E) \Psi_{\Lambda_{\sigma}}^s(\vec{r}, E) \zeta_{\sigma} \quad (45)$$

Here  $s$  is the index over the solution and by convention we take it either  $\frac{1}{2}$  or  $-\frac{1}{2}$ , i.e. the same values as for the spin projection  $\sigma$ .  $\Lambda_s = (l, m + \frac{1}{2} - s, s)$  and  $\Lambda_{\sigma} = (l, m + \frac{1}{2} - \sigma, \sigma)$  are set of quantum numbers describing the final state.  $a_{\Lambda_s}^f(E)$  is the multiple scattering amplitude of the  $\Lambda_{\sigma}$  contribution to the  $s$  component of the final state wavefunction:

$$\Psi_{\Lambda_{\sigma}}^s(\vec{r}, E) = b_{\Lambda_{\sigma}}^s(r, E) Y_{\Lambda_{\sigma}}(\hat{r}) \quad (46)$$

where the summation over  $\Lambda_s$  implies:

$$\sum_{\Lambda_s} \equiv \sum_{lms} \quad (47)$$

and  $m$  obeys the constraint  $-l \leq m + \frac{1}{2} - s \leq l$ . A similar remark can be made on the  $\Lambda_{\sigma}$  summation.

The fully relativistic Adler-Wiser equation [84] reads:

$$\chi_0^{\sigma\sigma'}(\vec{r}, \vec{r}', \omega) = \lim_{\epsilon \rightarrow 0} \sum_g \int_{E_F}^{\infty} dE \sum_f \frac{\phi_g^{\sigma}(\vec{r}) \Psi_f^{\dagger}(\vec{r}, E) \Psi_f(\vec{r}', E) \phi_g^{\sigma'\dagger}(\vec{r}')}{\omega - (E - E_g) + i\epsilon} \quad (48)$$

where  $f$  are the final states of the same energy  $E$ . We stress the fact that the energies  $\omega$  and  $E$  are expressed into different scales: the former describes the photon, whereas the latter belongs to the photoelectron.  $E_g$  is the Kohn-Sham energy of the  $g$  state, i.e. the expectation value of the DFT local density approximation hamiltonian  $\mathcal{H}_{LDA}$ :

$$E_g = \frac{\langle \phi_g | \mathcal{H}_{LDA} | \phi_g \rangle}{\langle \phi_g | \phi_g \rangle} \quad (49)$$

By exploiting the optical theorem:

$$\sum_f a_{\Lambda'_s}^f(E) a_{\Lambda_s}^f(E) = -\Im \tau_{\Lambda_s \Lambda'_s}(E) \quad (50)$$

the AdlerWiser equation (48) can be simplified to:

$$\begin{aligned} \chi_0^{\sigma\sigma'}(\vec{r}, \vec{r}', \omega) &= -\frac{1}{\pi} \sum_{gg'} \sum_{\Lambda_s \Lambda'_s} \lim_{\epsilon \rightarrow 0} \int_{E_F}^{\infty} dE \delta_{gg'} \\ &\times \frac{\phi_g^\sigma(\vec{r}) \Psi_{\Lambda_\sigma}^{s\dagger}(r, E) \Im \tau_{\Lambda_s \Lambda'_s}(E) \Psi_{\Lambda'_\sigma}^{s'}(\vec{r}', E) \phi_{g'}^{\sigma'\dagger}(\vec{r}')}{\omega - (E - E_g) + i\epsilon} \end{aligned} \quad (51)$$

We are considering an expansion of the following kind:

$$\begin{aligned} \chi_0^{\sigma\sigma'}(\vec{r}, \vec{r}', \omega) &= \sum_{gg'} \delta_{gg'} \phi_g^\sigma(\vec{r}) \phi_{g'}^{\sigma'\dagger}(\vec{r}') \sum_{\Lambda_s \Lambda'_s} \\ &\times \tilde{\chi}_{0gg', \Lambda_s \Lambda'_s}^{\sigma\sigma'}(\omega) \Psi_{\Lambda_\sigma}^{s\dagger}(\vec{r}, \omega + E_g) \Psi_{\Lambda'_\sigma}^{s'}(\vec{r}', \omega + E_{g'}) \end{aligned} \quad (52)$$

We recall that:

$$\begin{aligned} \sigma(\omega) &= -\frac{4\pi\omega}{c} \int d^3r \int d^3r' \sum_{\sigma\sigma'} \sum_{gg'} \sum_{\Lambda_s \Lambda'_s} O^*(\omega, \vec{r}') O(\omega, \vec{r}) \\ &\times \phi_{g'}^{\sigma'\dagger}(\vec{r}') b_{\Lambda_\sigma}^s(r) Y_{\Lambda_\sigma}^*(\hat{r}) \Im \tau_{\Lambda_s \Lambda'_s} b_{\Lambda'_\sigma}^{s'}(r') Y_{\Lambda'_\sigma}(\hat{r}') \phi_g^\sigma(\vec{r}) \end{aligned} \quad (53)$$

One can treat the projection of the susceptibility  $\tilde{\chi}$  and the multiple scattering amplitudes  $\tau$  on equal footing:

$$\tilde{\chi}_{0g, \Lambda_s \Lambda'_s}^{\sigma\sigma'} \equiv \tau_{\Lambda_s \Lambda'_s} \quad (54)$$

Let:

$$\tilde{\chi}_{0gg', \Lambda_s \Lambda'_s}^{\sigma\sigma'}(\omega) = -\delta_{gg'} \int_{E_F}^{\infty} \frac{dE}{\pi} \frac{\Im \tau_{\Lambda_s \Lambda'_s}(E)}{\omega - (E - E_g) + i\epsilon} \frac{Z_{g'\Lambda'_\sigma}^{s'}(E) Z_{g\Lambda_\sigma}^s(E)}{Z_{g'\Lambda'_\sigma}^{s'}(\omega + E_{g'}) Z_{g\Lambda_\sigma}^s(\omega + E_g)} \quad (55)$$

an equivalent form of the equivalence in (54) where:

$$Z_{g\Lambda_\sigma}^s(E) = \int_0^R dr r^2 b_g(r) b_{\Lambda_\sigma}^s(r, E) \quad (56)$$

In the  $|r\rangle$  representation (6.11) re-writes as:

$$\begin{aligned} \chi^{\sigma\sigma'}(\vec{r}, \vec{r}', \omega) &= \chi_0^{\sigma\sigma'}(\vec{r}, \vec{r}', \omega) + \sum_{\sigma''\sigma'''} \int d^3r'' \int d^3r''' \\ &\times \chi_0^{\sigma\sigma''}(\vec{r}, \vec{r}'', \omega) K^{\sigma''\sigma'''}(\vec{r}'', \vec{r}''') \chi^{\sigma'''\sigma'}(\vec{r}''', \vec{r}', \omega) \end{aligned} \quad (57)$$

We project the operatorial Dyson-like equation (6.11) on the "basis" introduced in (52):

$$\tilde{\chi}_{gg', \Lambda_s \Lambda'_s}^{\sigma\sigma'}(\omega) = \tilde{\chi}_{0gg', \Lambda_s \Lambda'_s}^{\sigma\sigma'}(\omega) + \sum_{g'''} \sum_{\sigma''\sigma'''} \sum_{\Lambda_s'' \Lambda_s'''} \tilde{\chi}_{0gg, \Lambda_s \Lambda_s''}^{\sigma\sigma''}(\omega) \tilde{K}_{gg''', \Lambda_s'' \Lambda_s'''}^{\sigma''\sigma'''}(\omega) \tilde{\chi}_{g''', \Lambda_s'' \Lambda_s'''}^{\sigma'''\sigma'}(\omega) \quad (58)$$

$$\begin{aligned}
\tilde{K}_{gg',\Lambda_s\Lambda'_s}^{\sigma\sigma'}(\omega) &= \int d^3r \int d^3r' K^{\sigma\sigma'}(\vec{r},\vec{r}',\omega) \\
&\times \phi_g^{\sigma\dagger}(\vec{r}) \Psi_{\Lambda_\sigma}^s(\vec{r},\omega+E_g) \phi_{g'}^{\sigma'}(\vec{r}') \Psi_{\Lambda'_\sigma}^{s'\dagger}(\vec{r}',\omega+E_{g'})
\end{aligned} \tag{59}$$

$$K^{\sigma\sigma'}(\vec{r},\vec{r}',\omega) = f_H^{\sigma\sigma'}(\vec{r},\vec{r}') + f_{xc}^{\sigma\sigma'}(\vec{r},\vec{r}',\omega) \tag{60}$$





# Bibliography

- [1] M. Amara, I. Aviani, S. E. Luca, D. Dufeu, P. Lethuillier, and R. M. Galéra. *J. Magn. Magn. Mater.*, 226-230:1005–1007, 2001.
- [2] M. Amara, R. M. Galéra, P. Morin, and J. F. Berar. Observation of quadrupolar x-ray diffraction peaks in NdMg. *Journal of Physics: Condensed Matter*, 10(47):L743–L748, 1998.
- [3] J. Angyan, I. Greber, and M. M. Spherical harmonic expansion of short-range screened coulomb interactions. *J. Phys. A*, 39:8613–8630, 2006.
- [4] V. Anisimov, F. Aryasetiawan, and A. Liechtenstein. First principles calculations of the electronic structure and spectra of strongly correlated systems: the LDA+U method. *J. Phys.: Condens. Matter*, 9:767–808, 1997.
- [5] V. I. Anisimov, I. V. Solovyev, M. A. Korotin, M. T. Czyżyk, and G. A. Sawatzky. Density-functional theory and nio photoemission spectra. *Phys. Rev. B*, 48(23):16929–16934, Dec 1993. doi:10.1103/PhysRevB.48.16929.
- [6] V. I. Anisimov, J. Zaanen, and O. K. Andersen. Band theory and Mott insulators: Hubbard U instead of Stoner I. *Phys. Rev. B*, 44(3):943–954, Jul 1991. doi:10.1103/PhysRevB.44.943.
- [7] A. L. Ankudinov, A. I. Nesvizhskii, and J. J. Rehr. Dynamic screening effects in x-ray absorption spectra. *Phys. Rev. B*, 67(11):115120, Mar 2003. doi:10.1103/PhysRevB.67.115120.
- [8] A. L. Ankudinov, B. Ravel, J. J. Rehr, and S. D. Conradson. Real-space multiple-scattering calculation and interpretation of x-ray-absorption near-edge structure. *Phys. Rev. B*, 58(12):7565–7576, Sep 1998. doi:10.1103/PhysRevB.58.7565.
- [9] A. L. Ankudinov, Y. Takimoto, and J. J. Rehr. Combined Bethe-Salpeter equations and time-dependent density-functional theory approach for x-ray absorption calculations. *Phys. Rev. B*, 71(16):165110, Apr 2005. doi:10.1103/PhysRevB.71.165110.
- [10] H. Appel, E. K. U. Gross, and K. Burke. Excitations in time-dependent density-functional theory. *Phys. Rev. Lett.*, 90(4):043005, Jan 2003. doi:10.1103/PhysRevLett.90.043005.

- [11] F. Aryasetiawan, K. Karlsson, O. Jepsen, and U. Schönberger. Calculations of Hubbard  $U$  from first-principles. *Phys. Rev. B*, 74(12):125106, Sep 2006. doi:10.1103/PhysRevB.74.125106.
- [12] P. Benedetti, J. van den Brink, E. Pavarini, A. Vigliante, and P. Wochner. Ab initio calculation of resonant x-ray scattering in manganites. *Phys. Rev. B*, 63(6):060408, Jan 2001. doi:10.1103/PhysRevB.63.060408.
- [13] M. Benfatto, S. Della Longa, and C. R. Natoli. The MXAN procedure: a new method for analysing the XANES spectra of metalloproteins to obtain structural quantitative information. *J. Synchrotron Rad.*, 10:51–57, 2003.
- [14] M. Benfatto, Y. Joly, and C. R. Natoli. Critical Reexamination of the Experimental Evidence of Orbital Ordering in  $\text{LaMnO}_3$  and  $\text{La}_{0.5}\text{Sr}_{1.5}\text{MnO}_4$ . *Phys. Rev. Lett.*, 83(3):636–639, Jul 1999. doi:10.1103/PhysRevLett.83.636.
- [15] N. Binggeli and M. Altarelli. Orbital ordering, Jahn-Teller distortion, and resonant x-ray scattering in  $\text{KCuF}_3$ . *Phys. Rev. B*, 70(8):085117, Aug 2004. doi:10.1103/PhysRevB.70.085117.
- [16] M. Blume. Magnetic scattering of x rays. *J. Appl. Phys.*, 57:3615, 1985.
- [17] Y. Bodenthin, U. Staub, M. García-Fernández, M. Janoschek, J. Schlappa, E. I. Golovenchits, V. A. Sanina, and S. G. Lushnikov. Manipulating the Magnetic Structure with Electric Fields in Multiferroic  $\text{ErMn}_2\text{O}_5$ . *Phys. Rev. Lett.*, 100(2):027201, Jan 2008. doi:10.1103/PhysRevLett.100.027201.
- [18] M. Bolte, G. Meier, B. Krüger, A. Drews, R. Eiselt, L. Bocklage, S. Bohlens, T. Tyliczszak, A. Vansteenkiste, B. Van Waeyenberge, K. W. Chou, A. Puzic, and H. Stoll. Time-resolved x-ray microscopy of spin-torque-induced magnetic vortex gyration. *Phys. Rev. Lett.*, 100(17):176601, Apr 2008. doi:10.1103/PhysRevLett.100.176601.
- [19] S. Botti, A. Schindlmayr, R. Del Sole, and L. Reining. Time dependent density functional theory for extended systems. *Rep. Prog. Phys.*, 70:357–407, 2007.
- [20] L. Braicovich, L. J. P. Ament, V. Bisogni, F. Forte, C. Aruta, G. Balestrino, N. B. Brookes, G. M. De Luca, P. G. Medaglia, F. M. Granozio, M. Radovic, M. Salluzzo, J. van den Brink, and G. Ghiringhelli. Dispersion of Magnetic Excitations in the Cuprate  $\text{La}_2\text{CuO}_4$  and  $\text{CaCuO}_2$  Compounds Measured Using Resonant X-Ray Scattering. *Phys. Rev. Lett.*, 102(16):167401, Apr 2009. doi:10.1103/PhysRevLett.102.167401.
- [21] L. Braicovich, J. van den Brink, V. Bisogni, M. M. Sala, L. J. P. Ament, N. B. Brookes, G. M. De Luca, M. Salluzzo, T. Schmitt, V. N. Strocov, and G. Ghiringhelli. Magnetic Excitations and Phase Separation in the Underdoped  $\text{La}_{2-x}\text{Sr}_x\text{CuO}_4$  Superconductor Measured by Resonant Inelastic X-Ray Scattering. *Phys. Rev. Lett.*, 104(7):077002, Feb 2010. doi:10.1103/PhysRevLett.104.077002.
- [22] H. Bruus and K. Flensberg. *Many Body Quantum Theory in Condensed Matter Physics*. Oxford, 2004.

- [23] O. Bunău, R. M. Galéra, Y. Joly, M. Amara, S. E. Luca, and C. Detlefs. Resonant magnetic and multipolar scattering at the neodymium  $L_{2,3}$  absorption edges in the antiferroquadrupolar phase of NdMg. *Phys. Rev. B*, 81(14):144402, Apr 2010. doi:10.1103/PhysRevB.81.144402.
- [24] O. Bunău and Y. Joly. Self-consistent aspects of x-ray absorption calculations. *J. Phys.: Condens. Matter*, 21:345501, 2009.
- [25] K. Burke. The abc of the density functional theory. <http://dft.uci.edu/materials/bookABCDFT/gamma/g1.pdf>, 2007.
- [26] D. Cabaret, E. Gaudry, M. Taillefumier, P. Saintavit, and F. Mauri. XANES calculation with an efficient non muffin-tin method: Application to the angular dependence of the Al K-edge in corundum. *Physica Scripta*, T115:131–133, 2005.
- [27] L. Campbell, L. Hedin, J. J. Rehr, and W. Bardyszewski. Interference between extrinsic and intrinsic losses in x-ray absorption fine structure. *Phys. Rev. B*, 65(6):064107, Jan 2002. doi:10.1103/PhysRevB.65.064107.
- [28] J. Chakhalian, J. W. Freeland, H. Habermeier, G. Cristiani, G. Khaliullin, M. van Veenendaal, and B. Keimer. Orbital reconstruction and covalent bonding at an oxide interface. *Science*, 318:1114–1117, 2007.
- [29] V. Chembrolu, J. P. Strachan, X. W. Yu, A. A. Tulapurkar, T. Tyliczszak, J. A. Katine, M. J. Carey, J. Stöhr, and Y. Acremann. Time-resolved x-ray imaging of magnetization dynamics in spin-transfer torque devices. *Phys. Rev. B*, 80(2):024417, Jul 2009. doi:10.1103/PhysRevB.80.024417.
- [30] J. Coey and M. Viret. Mixed-valence manganites. *Advances in Physics*, 48:167–293, 1999.
- [31] C. Cohen-Tannoudji, B. Diu, and F. Laloe. *Quantum Mechanics*. Hermann, 2005.
- [32] R. Coldea, S. M. Hayden, G. Aeppli, T. G. Perring, C. D. Frost, T. E. Mason, S.-W. Cheong, and Z. Fisk. Spin Waves and Electronic Interactions in  $\text{La}_2\text{CuO}_4$ . *Phys. Rev. Lett.*, 86(23):5377–5380, Jun 2001. doi:10.1103/PhysRevLett.86.5377.
- [33] F. de Bergevin and M. Brunel. *Phys. Lett. A*, 39:141, 1972.
- [34] F. de Groot. Multiplet effects in x-ray spectroscopy. *Coordination Chemistry Reviews*, 249(1-2):31 – 63, 2005. doi:10.1016/j.ccr.2004.03.018.
- [35] F. de Groot. Ligand and metal x-ray absorption in transition metal complexes. *Inorganica Chimica Acta*, 361:850–856, 2008.
- [36] J. Diamond. Symmetry and the scattered wave model. *Chem. Phys. Lett.*, 20:63–66, 1973.

- [37] D. Dill and J. Dehmer. Electron-molecule scattering and molecular photoionization using the multiple scattering method. *The Journal of Chemical Physics*, 61(2):692–699, 1974.
- [38] J. F. Dobson. Harmonic-potential theorem: Implications for approximate many-body theories. *Phys. Rev. Lett.*, 73(16):2244–2247, Oct 1994. doi:10.1103/PhysRevLett.73.2244.
- [39] S. L. Dudarev, G. A. Botton, S. Y. Savrasov, C. J. Humphreys, and A. P. Sutton. Electron-energy-loss spectra and the structural stability of nickel oxide: An LSDA+U study. *Phys. Rev. B*, 57(3):1505–1509, Jan 1998. doi:10.1103/PhysRevB.57.1505.
- [40] H. Ebert. *Electronic Structure and Physical Properties of Solids*, volume 535, chapter Fully relativistic band structure calculations for magnetic solids. Formalism and Application, page 191. Springer Berlin, 2000.
- [41] J. Fink, T. Müller-Heinzerling, B. Scheerer, W. Speier, F. U. Hillebrecht, J. C. Fuggle, J. Zaanen, and G. A. Sawatzky. 2p absorption spectra of the 3d elements. *Phys. Rev. B*, 32(8):4899–4904, Oct 1985. doi:10.1103/PhysRevB.32.4899.
- [42] D. Foulis.  
<http://www.esrf.eu/UsersAndScience/Experiments/TBS/SciSoft/OurSoftware/fpx>.
- [43] J. W. Freeland, J. Chakhalian, A. V. Boris, J.-M. Tonnerre, J. J. Kavich, P. Yordanov, S. Grenier, P. Zschack, E. Karapetrova, P. Popovich, H. N. Lee, and B. Keimer. Charge transport and magnetization profile at the interface between the correlated metal  $\text{CaRuO}_3$  and the antiferromagnetic insulator  $\text{CaMnO}_3$ . *Phys. Rev. B*, 81(9):094414, Mar 2010. doi:10.1103/PhysRevB.81.094414.
- [44] M. Gatti, V. Olevano, L. Reining, and I. V. Tokatly. Transforming nonlocality into a frequency dependence: A shortcut to spectroscopy. *Phys. Rev. Lett.*, 99(5):057401, Aug 2007. doi:10.1103/PhysRevLett.99.057401.
- [45] A. Gonis and W. Butler. *Multiple Scattering in Solids*. Springer-Verlag New York Inc., 2000.
- [46] J. B. Goodenough. Theory of the Role of Covalence in the Perovskite-Type Manganites  $[\text{La}, \text{M}(\text{II})]\text{MnO}_3$ . *Phys. Rev.*, 100(2):564–573, Oct 1955. doi:10.1103/PhysRev.100.564.
- [47] S. Grenier, J. P. Hill, D. Gibbs, K. J. Thomas, M. v. Zimmermann, C. S. Nelson, V. Kiryukhin, Y. Tokura, Y. Tomioka, D. Casa, T. Gog, and C. Venkataraman. Resonant x-ray diffraction of the magnetoresistant perovskite  $\text{Pr}_{0.6}\text{Ca}_{0.4}\text{MnO}_3$ . *Phys. Rev. B*, 69(13):134419, Apr 2004. doi:10.1103/PhysRevB.69.134419.
- [48] S. Grenier, J. P. Hill, V. Kiryukhin, W. Ku, Y.-J. Kim, K. J. Thomas, S.-W. Cheong, Y. Tokura, Y. Tomioka, D. Casa, and T. Gog.  $d-d$  Excitations in Manganites Probed by Resonant Inelastic X-Ray Scattering. *Phys. Rev. Lett.*, 94(4):047203, Feb 2005. doi:10.1103/PhysRevLett.94.047203.

- [49] K. Hatada, K. Hayakawa, M. Benfatto, and C. Natoli. Full potential multiple scattering for core electron spectroscopies. *J. Phys: Condes. Matter*, 21:104206, 2009.
- [50] M. W. Haverkort, Z. Hu, A. Tanaka, W. Reichelt, S. V. Streltsov, M. A. Korotin, V. I. Anisimov, H. H. Hsieh, H.-J. Lin, C. T. Chen, D. I. Khomskii, and L. H. Tjeng. Orbital-Assisted Metal-Insulator Transition in VO<sub>2</sub>. *Phys. Rev. Lett.*, 95(19):196404, Nov 2005. doi:10.1103/PhysRevLett.95.196404.
- [51] L. Hedin and B. Lundqvist. Explicit local exchange correlation potentials. *J. Phys. C: Solid State Phys.*, 4:2064–2083, 1971.
- [52] L. Hedin and U. von Barth. A local exchange correlation potential for spin polarized case. *J. Phys. C: Solid State Phys.*, 5:1629–1642, 1972.
- [53] C. Henderson, G. Cressey, and S. Redfern. Geological applications of synchrotron radiation. *Radiation Physics and Chemistry*, 45:459–481, 1995.
- [54] J. Herrero-Martín, J. García, G. Subías, J. Blasco, and M. C. Sánchez. Structural origin of dipole x-ray resonant scattering in the low-temperature phase of Nd<sub>0.5</sub>Sr<sub>0.5</sub>MnO<sub>3</sub>. *Phys. Rev. B*, 70(2):024408, Jul 2004. doi:10.1103/PhysRevB.70.024408.
- [55] H. Ikeno, F. M. De Groot, E. Stavitski, and I. Tanaka. Multiplet calculations of L<sub>2,3</sub> x-ray absorption near-edge structures for 3d transition-metal compounds. *Journal of Physics: Condensed Matter*, 21(10), 2009.
- [56] Y. Joly. X-ray absorption near edge structure calculations beyond the muffin-tin approximation. *Phys. Rev. B*, 63:125120–125129, 2001.
- [57] Y. Joly. Interaction matter - polarized light. In E. Beaupaire, H. Bulou, F. Scheurer, and J. Kappler, editors, *Magnetism and Synchrotron Radiation*, pages 77–126. Springer, 2010.
- [58] W. Kohn and L. J. Sham. Self consistent equations including exchange and correlation effects. *Phys. Rev. A*, 140:1133–1138, 1965.
- [59] G. Kotliar, S. Y. Savrasov, K. Haule, V. S. Oudovenko, O. Parcollet, and C. A. Marianetti. Electronic structure calculations with dynamical mean-field theory. *Rev. Mod. Phys.*, 78(3):865–951, Aug 2006. doi:10.1103/RevModPhys.78.865.
- [60] M. O. Krause and J. H. Oliver. Natural widths of atomic k and l levels, k alpha x-ray lines and several kll auger lines. *J. Phys. Chem. Ref. Data*, 8:329–338, 1979.
- [61] P. Krüger. Multichannel multiple scattering calculation of L<sub>2,3</sub> -edge spectra of TiO<sub>2</sub> and SrTiO<sub>3</sub> : Importance of multiplet coupling and band structure. *Phys. Rev. B*, 81(12):125121, Mar 2010. doi:10.1103/PhysRevB.81.125121.
- [62] P. Krüger and C. R. Natoli. X-ray absorption spectra at the Ca L<sub>2,3</sub> edge calculated within multichannel multiple scattering theory. *Phys. Rev. B*, 70(24):245120, Dec 2004. doi:10.1103/PhysRevB.70.245120.

- [63] C.-C. Lee, H. Hsueh, and W. Ku. Dynamical linear response of TDDFT with LDA+U functional: strongly hybridized Frenkel excitons in NiO. arXiv:1002.1101v1, accepted for publication in *Phys. Rev. B (Rapid Comm.)*., 2010.
- [64] Z. Levine. Magnetic dichroism at the giant dipole resonance of Fe and Mn via time-dependent density-functional theory. *J. Phys. B: At. Mol. Opt. Phys.*, 31:3155–3166, 1998.
- [65] A. I. Liechtenstein, V. I. Anisimov, and J. Zaanen. Density-functional theory and strong interactions: Orbital ordering in Mott-Hubbard insulators. *Phys. Rev. B*, 52(8):R5467–R5470, Aug 1995. doi:10.1103/PhysRevB.52.R5467.
- [66] F. Löhl, V. Arsov, M. Felber, K. Hacker, W. Jalmuzna, B. Lorbeer, F. Ludwig, K.-H. Matthiesen, H. Schlarb, B. Schmidt, P. Schmüser, S. Schulz, J. Szewinski, A. Winter, and J. Zemella. Electron bunch timing with femtosecond precision in a superconducting free-electron laser. *Phys. Rev. Lett.*, 104(14):144801, Apr 2010. doi:10.1103/PhysRevLett.104.144801.
- [67] T. Maier, M. Jarrell, T. Pruschke, and M. H. Hettler. Quantum cluster theories. *Rev. Mod. Phys.*, 77(3):1027–1080, Oct 2005. doi:10.1103/RevModPhys.77.1027.
- [68] N. Maitra, F. Zhang, R. Cave, and K. Burke. Double excitations within time-dependent density functional theory linear response. *Journal of Chemical Physics*, 120(13):1601–1612, 2004. doi:10.1063/1.1651060.
- [69] M. Mannini, F. Pineider, P. Saintavrit, C. Danieli, E. Otero, C. Sciancalepore, A. Talarico, M. Arrio, A. Cornia, D. Gatteschi, and R. Sessoli. Magnetic memory of a single-molecule quantum magnet wired to a gold surface. *Nature Materials*, 8:194–197, 2009.
- [70] M. Marques, U. C., F. Noguiera, A. Rubio, K. Burke, and E. Gross. *Time Dependent Density Functional Theory*. Springer, 2004.
- [71] R. Martin. *Electronic Structure - Basic Theory and Practical Methods*. Cambridge University Press, 2004.
- [72] E. Materials. 871, El Cerro Blvd., Danville, CA 94526 USA.
- [73] L. F. Mattheiss. Energy bands for solid argon. *Phys. Rev.*, 133(5A):A1399–A1403, Mar 1964. doi:10.1103/PhysRev.133.A1399.
- [74] A. Mihelic. [www.p-ng.si/arcon/xas/xanes/xanes-theory.pdf](http://www.p-ng.si/arcon/xas/xanes/xanes-theory.pdf), 2002.
- [75] A. Mirone, S. Dhési, and G. van der Laan. Spectroscopy of  $\text{La}_{0.5}\text{Sr}_{1.5}\text{MnO}_4$  orbital ordering: a cluster many-body calculation. *The European Physics Journal B*, 53(1):23–28, 2006.
- [76] A. Mirone, M. Sacchi, and S. Gota. Ligand-field atomic-multiplet calculations for arbitrary symmetry. *Phys. Rev. B*, 61(20):13540–13544, May 2000. doi:10.1103/PhysRevB.61.13540.

- [77] H. Modrow, S. Bucher, J. J. Rehr, and A. L. Ankudinov. Calculation and interpretation of  $K$ -shell x-ray absorption near-edge structure of transition metal oxides. *Phys. Rev. B*, 67(3):035123, Jan 2003. doi:10.1103/PhysRevB.67.035123.
- [78] V. L. Moruzzi, J. F. Janak, and A. R. Williams. *Calculated Electronic Properties of Metals*. Pergamon Press Inc., 1978.
- [79] K. Namikawa, M. Ando, T. Nakajima, and H. Kawata. X-ray resonance magnetic scattering. *Journal of the Physical Society of Japan*, 54:4099–4102, 1985.
- [80] C. R. Natoli, D. K. Misemer, S. Doniach, and F. W. Kutzler. First-principles calculation of x-ray absorption-edge structure in molecular clusters. *Phys. Rev. A*, 22(3):1104–1108, Sep 1980. doi:10.1103/PhysRevA.22.1104.
- [81] C. R. Natoli, D. K. Misemer, S. Doniach, and F. W. Kutzler. First-principles calculation of x-ray absorption-edge structure in molecular clusters. *Phys. Rev. A*, 22(3):1104–1108, Sep 1980. doi:10.1103/PhysRevA.22.1104.
- [82] F. Nolting and al. Direct observation of the alignment of the ferromagnetic spins by antiferromagnetic spins. *Nature*, 405:767–769, 2000.
- [83] P. Nozières and C. T. de Dominicis. Singularities in the x-ray absorption and emission of metals. iii. one-body theory exact solution. *Phys. Rev.*, 178(3):1097–1107, Feb 1969. doi:10.1103/PhysRev.178.1097.
- [84] G. Onida, L. Reining, and A. Rubio. Electronic excitations: density-functional versus many-body green’s-function approaches. *Rev. Mod. Phys.*, 74(2):601–659, Jun 2002. doi:10.1103/RevModPhys.74.601.
- [85] P. Blaha, K. Schwarz, G. Madsen, D. Kvasnicka, and J. Luitz. *An augmented plane wave + local orbital program for calculating crystal properties*. TU Wien, 2001.
- [86] J. P. Perdew and Y. Wang. Accurate and simple analytic representation of the electron-gas correlation energy. *Phys. Rev. B*, 45:13244–13249, 1992.
- [87] A. G. Petukhov, I. I. Mazin, L. Chioncel, and A. I. Lichtenstein. Correlated metals and the  $LDA + U$  method. *Phys. Rev. B*, 67(15):153106, Apr 2003. doi:10.1103/PhysRevB.67.153106.
- [88] B. Poumellec, R. Cortes, G. Tourillon, and J. Berthon. Angular Dependence of the Ti  $K$  Edge in Rutile  $TiO_2$ . *Physica Status Solidi (B)*, 164:319–326, 1991.
- [89] T. Privalov, F. Gel’mukhanov, and H. Ågren. Role of relaxation and time-dependent formation of x-ray spectra. *Phys. Rev. B*, 64(16):165115, Oct 2001. doi:10.1103/PhysRevB.64.165115.
- [90] P. Radaelli, D. Cox, M. Marezio, and S. Cheong. Charge, orbital and magnetic ordering in  $La_{0.5}Ca_{0.5}MnO_3$ . *Phys. Rev. B*, 55(5):3015, 1997.
- [91] J. J. Rehr. Excited state electronic structure and the theory of x-ray spectra. *J. Phys.: Condens. Matter*, 15:647–654, 2003.



- [92] J. J. Rehr and A. Ankudinov. Time dependent density functional theory calculations of x ray absorption. *International Journal of Quantum Chemistry*, 95:487–492, 2003.
- [93] J. J. Rehr and A. Ankudinov. Progress in the theory and interpretation of xanes. *Coordination Chemistry Reviews*, 249:131–140, 2005.
- [94] L. Reining, V. Olevano, A. Rubio, and G. Onida. Excitonic effects in solids described by time-dependent density-functional theory. *Phys. Rev. Lett.*, 88(6):066404, Jan 2002. doi:10.1103/PhysRevLett.88.066404.
- [95] F. Rodolakis, P. Hansmann, J.-P. Rueff, A. Toschi, M. W. Haverkort, G. Sangiovanni, A. Tanaka, T. Saha-Dasgupta, O. K. Andersen, K. Held, M. Sikora, I. Alliot, J.-P. Itié, F. Baudelet, P. Wzietek, P. Metcalf, and M. Marsi. Inequivalent Routes across the Mott Transition in  $V_2O_3$  Explored by X-Ray Absorption. *Phys. Rev. Lett.*, 104(4):047401, Jan 2010. doi:10.1103/PhysRevLett.104.047401.
- [96] E. Runge and E. K. U. Gross. Density-functional theory for time-dependent systems. *Phys. Rev. Lett.*, 52(12):997, Mar 1984. doi:10.1103/PhysRevLett.52.997.
- [97] E. E. Salpeter and H. A. Bethe. A relativistic equation for bound-state problems. *Phys. Rev.*, 84(6):1232–1242, Dec 1951. doi:10.1103/PhysRev.84.1232.
- [98] A. Scherz. Ph.d. dissertation in freie universitat berlin. <http://www-ssrl.slac.stanford.edu/stohr>, 2004.
- [99] A. Scherz, E. K. U. Gross, H. Appel, C. Sorg, K. Baberschke, H. Wende, and K. Burke. Measuring the kernel of time-dependent density functional theory with x-ray absorption spectroscopy of 3d transition metals. *Phys. Rev. Lett.*, 95(25):253006, Dec 2005. doi:10.1103/PhysRevLett.95.253006.
- [100] G. Schütz, W. Wagner, W. Wilhelm, P. Kienle, R. Zeller, R. Frahm, and G. Materlik. Absorption of circularly polarized x rays in iron. *Phys. Rev. Lett.*, 58(7):737–740, Feb 1987. doi:10.1103/PhysRevLett.58.737.
- [101] J. Schwitalla and H. Ebert. Electron Core-Hole Interaction in the X-Ray Absorption Spectroscopy of 3d Transition Metals. *Phys. Rev. Lett.*, 80(20):4586–4589, May 1998. doi:10.1103/PhysRevLett.80.4586.
- [102] M. Seah and W. Dench. National Physics Laboratory, Div. of Chemical Standards, Teddington, Middlesex, 1978.
- [103] D. Seibilleau. Spectroscopies - an introduction. In E. Beaupaire, H. Bulou, F. Scheurer, and J. Kappler, editors, *Magnetism: Synchrotron Radiation Approach*, pages 1–44. Springer, 2004.
- [104] J. Shim, K. Haule, and G. Kotliar. X-ray absorption branching ratio in actinides: LDA+DMFT approach. *EPL*, 85:17007, 2009. doi:10.1209/0295-5075/85/17007.

- [105] E. Shirley, J. Soininen, and J. J. Rehr. Modelling core-hole screening in core-exciton spectroscopies. *Physica Scripta*, T115:31–34, 2005.
- [106] E. L. Shirley. Ab initio inclusion of electron-hole attraction: Application to x-ray absorption and resonant inelastic x-ray scattering. *Phys. Rev. Lett.*, 80(4):794–797, Jan 1998. doi:10.1103/PhysRevLett.80.794.
- [107] M. Sikora, A. Juhin, T.-C. Weng, P. Saintavit, C. Detlefs, F. de Groot, and P. Glatzel. Strong  $K$ -edge Magnetic Circular Dichroism Observed in Photon-in–Photon-out Spectroscopy. *Phys. Rev. Lett.*, 105(3):037202, Jul 2010. doi:10.1103/PhysRevLett.105.037202.
- [108] G. Smolentsev, G. Guilera, M. Tromp, S. Pascarelli, and A. Soldatov. Local structure of reaction intermediates probed by time-resolved x-ray absorption near edge structure spectroscopy. *Journal of Chemical Physics*, 130:174508, 2009.
- [109] F. Sottile, V. Olevano, and L. Reining. Parameter-free calculation of response functions in time-dependent density-functional theory. *Phys. Rev. Lett.*, 91(5):056402, Jul 2003. doi:10.1103/PhysRevLett.91.056402.
- [110] U. Staub, M. García-Fernández, Y. Bodenthin, V. Scagnoli, R. A. De Souza, M. Garganourakis, E. Pomjakushina, and K. Conder. Orbital and magnetic ordering in  $\text{Pr}_{1-x}\text{Ca}_x\text{MnO}_3$  and  $\text{Nd}_{1-x}\text{Sr}_x\text{MnO}_3$  manganites near half doping studied by resonant soft x-ray powder diffraction. *Phys. Rev. B*, 79(22):224419, Jun 2009. doi:10.1103/PhysRevB.79.224419.
- [111] M. Stener, G. Fronzoni, and M. de Simone. Time dependent density functional theory of core electrons excitations. *Chemical Physics Letters*, 373(1-2):115 – 123, 2003. doi:10.1016/S0009-2614(03)00543-8.
- [112] J. Stohr and H. Siegmann. *Magnetism - From Fundamentals to Nanoscale Dynamics*. Springer, 2006.
- [113] M. Taillefumier, D. Cabaret, A.-M. Flank, and F. Mauri. X-ray absorption near-edge structure calculations with the pseudopotentials: Application to the  $K$  edge in diamond and  $\alpha$ -quartz. *Phys. Rev. B*, 66(19):195107, Nov 2002. doi:10.1103/PhysRevB.66.195107.
- [114] K. Terakura, A. R. Williams, T. Oguchi, and J. Kübler. Transition-Metal Monoxides: Band or Mott Insulators. *Phys. Rev. Lett.*, 52(20):1830–1833, May 1984. doi:10.1103/PhysRevLett.52.1830.
- [115] K. J. Thomas, J. P. Hill, S. Grenier, Y.-J. Kim, P. Abbamonte, L. Venema, A. Rusydi, Y. Tomioka, Y. Tokura, D. F. McMorrow, G. Sawatzky, and M. van Veenendaal. Soft x-ray resonant diffraction study of magnetic and orbital correlations in a manganite near half doping. *Phys. Rev. Lett.*, 92(23):237204, Jun 2004. doi:10.1103/PhysRevLett.92.237204.
- [116] T. A. Tyson, K. O. Hodgson, C. R. Natoli, and M. Benfatto. General multiple-scattering scheme for the computation and interpretation of

- x-ray-absorption fine structure in atomic clusters with applications to SF<sub>6</sub>, GeCl<sub>4</sub>, and Br<sub>2</sub> molecules. *Phys. Rev. B*, 46(10):5997–6019, Sep 1992. doi:10.1103/PhysRevB.46.5997.
- [117] G. van der Laan. Studying spintronics materials with soft x-ray resonant scattering. *Current Opinion in Solid State and Materials Science*, 10:120–127, 2006.
- [118] R. Vedrinskii, V. Kraizman, A. Novakovich, S. Elyafi, S. Bocharov, T. Kirchner, and G. Drager. Experimental and theoretical studies of fine structure in polarized Ni K x-ray absorption spectra of NiO single crystals. *Phys. Status Solidi B*, 226:203–217, July 2001.
- [119] D. D. Vvedensky, D. K. Saldin, and J. B. Pendry. An update of DLXANES, the calculation of X-ray absorption near-edge structure. *Computer Physics Communications*, 40(2-3):421 – 440, 1986. doi:10.1016/0010-4655(86)90122-0.
- [120] W. G. Waddington, P. Rez, I. P. Grant, and C. J. Humphreys. White lines in the  $L_{2,3}$  electron-energy-loss and x-ray absorption spectra of 3d transition metals. *Phys. Rev. B*, 34(3):1467–1473, Aug 1986. doi:10.1103/PhysRevB.34.1467.
- [121] G. Williams. <http://xray.uu.se/hypertext/EBindEnergies>.
- [122] J. H. Wood and A. M. Boring. Improved pauli hamiltonian for local-potential problems. *Phys. Rev. B*, 18(6):2701–2711, Sep 1978. doi:10.1103/PhysRevB.18.2701.
- [123] Y.-l. Xu. Fast evaluation of the gaunt coefficients. *Mathematics of Computation*, 65:1601–1612, 1996. doi:10.1090/S0025-5718-96-00774-0.
- [124] A. N. Yaresko, V. N. Antonov, H. Eschrig, P. Thalmeier, and P. Fulde. Electronic structure and exchange coupling in  $\alpha'$ -NaV<sub>2</sub>O<sub>5</sub>. *Phys. Rev. B*, 62(23):15538–15546, Dec 2000. doi:10.1103/PhysRevB.62.15538.
- [125] J. Zaanen, G. A. Sawatzky, J. Fink, W. Speier, and J. C. Fuggle.  $L_{2,3}$  absorption spectra of the lighter 3d transition metals. *Phys. Rev. B*, 32(8):4905–4913, Oct 1985. doi:10.1103/PhysRevB.32.4905.
- [126] A. Zangwill and P. Soven. Density-functional approach to local-field effects in finite systems: Photoabsorption in the rare gases. *Phys. Rev. A*, 21(5):1561–1572, May 1980. doi:10.1103/PhysRevA.21.1561.
- [127] K. Zhang, E. A. Stern, J. J. Rehr, and F. Ellis. Double electron excitation in atomic Xe. *Phys. Rev. B*, 44(5):2030–2039, Aug 1991. doi:10.1103/PhysRevB.44.2030.
- [128] M. v. Zimmermann, C. S. Nelson, J. P. Hill, D. Gibbs, M. Blume, D. Casa, B. Keimer, Y. Murakami, C.-C. Kao, C. Venkataraman, T. Gog, Y. Tomioka, and Y. Tokura. X-ray resonant scattering studies of orbital and charge ordering in Pr<sub>1-x</sub>Ca<sub>x</sub>MnO<sub>3</sub>. *Phys. Rev. B*, 64(19):195133, Oct 2001. doi:10.1103/PhysRevB.64.195133.